

A MEASUREMENT OF THE  $W\gamma$  CROSS SECTION AT  $\sqrt{S} = 8$  TEV IN  $PP$   
COLLISIONS WITH THE CMS DETECTOR

by

Ekaterina Avdeeva

A DISSERTATION

Presented to the Faculty of  
The Graduate College at the University of Nebraska  
In Partial Fulfilment of Requirements  
For the Degree of Doctor of Philosophy

Major: Physics & Astronomy

Under the Supervision of Professor Ilya Kravchenko

Lincoln, Nebraska

May, 2017

A MEASUREMENT OF THE  $W\gamma$  CROSS SECTION AT  $\sqrt{S} = 8$  TEV IN  $PP$   
COLLISIONS WITH THE CMS DETECTOR

Ekaterina Avdeeva, Ph.D.

University of Nebraska, 2017

Adviser: Someone

Abstract goes here.

# Contents

<b>Contents</b>	<b>iii</b>
<b>1 Introduction</b>	<b>1</b>
1.1 Fundamental Particles and Interactions . . . . .	4
1.2 Electroweak Interactions . . . . .	8
1.3 Strong Interactions . . . . .	13
1.4 Physics of Proton-Proton Collisions . . . . .	15
1.5 Open Questions of the Standard Model . . . . .	17
<b>2 <math>W\gamma</math> Production Theory and Former Experimental Results</b>	<b>19</b>
2.1 Electroweak Theory of the Standard Model . . . . .	20
2.2 Cross Section and Luminosity . . . . .	29
2.3 Standard Model $W\gamma$ Production . . . . .	32
2.4 Anomalous $W\gamma$ Production . . . . .	37
2.5 A brief history of $W\gamma$ measurements . . . . .	41
<b>3 Experimental Setup</b>	<b>46</b>
3.1 Large Hadron Collider . . . . .	47
3.2 Compact Muon Solenoid . . . . .	53
3.2.1 Introduction . . . . .	53

3.2.2	Magnet . . . . .	55
3.2.3	Tracking System . . . . .	56
3.2.4	Electromagnetic Calorimeter . . . . .	57
3.2.5	Hadron Calorimeter . . . . .	57
3.2.6	Muon System . . . . .	58
3.2.7	Triggering and Data Aquisition . . . . .	60
3.2.8	Particle Flow Algorithm of Event Reconstruction . . . . .	61
<b>4</b>	<b>CMS Tracker Alignment</b>	<b>67</b>
4.1	Approach . . . . .	69
4.2	Selected Results on Alignment of the Tracking System with 2015 Data	73
4.2.1	Geometry Comparison . . . . .	74
4.2.2	Distributions of Medians of Unbiased Track-Hit Residuals . .	75
4.2.3	Cosmic Track Splitting Validation . . . . .	76
4.2.4	Primary Vertex Validation . . . . .	77
<b>5</b>	<b><math>W\gamma</math> Cross Section Measurement</b>	<b>80</b>
5.1	Event and Object Selection . . . . .	83
5.1.1	Event Level Selection . . . . .	83
5.1.2	Object Selection . . . . .	84
5.1.3	Selected Events . . . . .	85
5.2	Background Subtraction . . . . .	88
5.2.1	Jets $\rightarrow \gamma$ Background Estimation and Subtraction . . . . .	88
5.2.2	$e \rightarrow \gamma$ Background Estimation and Subtraction for the Electron Channel . . . . .	90
5.2.3	Other Backgrounds . . . . .	91
5.2.4	$P_T^\gamma$ Spectra before and after the Background Subtraction . . . . .	92

5.3	Detector Resolution Unfolding . . . . .	97
5.4	Acceptance X Efficiency . . . . .	103
5.5	Systematic Uncertainties . . . . .	105
5.5.1	Uncertainties due to Jets $\rightarrow \gamma$ Data-Driven Background Estimation . . . . .	105
5.5.2	Other sources of the systematic uncertainties . . . . .	107
5.5.3	Results . . . . .	110
5.6	Cross Section . . . . .	113
.1	APPENDIX: $Z\gamma$ FSR and ISR Plots . . . . .	116
.2	APPENDIX: Studies of $E_T^{miss}$ Dependence of Templates . . . . .	125
.3	APPENDIX: Template Fit Plots, $W\gamma$ , Data . . . . .	131
.4	APPENDIX: MC closure Check . . . . .	145
.5	APPENDIX: Template Fit Plots, $W\gamma$ , MC closure . . . . .	151
.6	APPENDIX: Template Fit Plots, MC Closure $W+jets$ and $W\gamma$ Only . . . . .	165
.7	APPENDIX: Fit Plots of $M_{e\gamma}$ . . . . .	182
.8	APPENDIX: Fit Plots of $M_{e\gamma}$ without $M_T^W$ cut . . . . .	193
.9	APPENDIX: Tables for $e \rightarrow \gamma$ Background Estimation . . . . .	204
.10	APPENDIX: Electron-photon invariant mass. Data vs MC plots . . . . .	207
.11	APPENDIX: Correlation Matrices for Different Sources of the Systematic Uncertainties . . . . .	213
.12	APPENDIX: Code and Software . . . . .	218
.13	APPENDIX: ZGamma Check . . . . .	220
.14	APPENDIX: Template Fit Plots, $Z\gamma$ , Data . . . . .	229
.15	APPENDIX: Template Fit Plots, $Z\gamma$ , MC Closure . . . . .	243
<b>Bibliography</b>		<b>258</b>

# Chapter 1

## Introduction

Elementary particle physics describes fundamental particles and their interactions. Fundamental particles are the smallest constituents of our Universe. When examined at smaller scales, the substances around us consist of molecules, molecules consist of atoms. In an atom there is a nucleus made of neutrons and protons and some number of electrons occupying orbits around the nucleus. Protons and neutrons have a structure while an electron is not known to have any internal structure, therefore, an electron is an example of a particle which is considered to be fundamental.

Interactions of elementary particles are described by quantum field theories which incorporate principles of the quantum mechanics and the special theory of relativity. The set of such theories, including quantum electrodynamics (QED), quantum chromodynamics (QCD) and the theory of weak interactions is called the Standard Model (SM). Current observations have proved the SM to be an accurate description of elementary particle interactions.

However, there are several experimental observations that are not described by the SM such as effects of gravity, dark matter, dark energy, matter/antimatter

asymmetry and others. Therefore, the SM is not a complete theory of particle interactions. There are several SM extensions offered by theorists as well as radically new theories waiting for experimental confirmation or exclusion.

Some SM extensions and new theories predict the existence of heavy particles with masses lying beyond experimentally reachable energies. The search of these particles is a priority in particle physics. One source of highly energetic elementary particles is cosmic rays. The most energetic particles ever observed came from this source. However, cosmic rays are totally uncontrollable and such highly energetic particles are rare. If we want to produce a large number of particles in a given energy range, we need to use a particle accelerator. A large amount of data allows experimentalists to perform a statistical analysis and increase the probability of finding a new particle if it exists.

Symmetric colliding beams is the most effective way to produce as heavy particles as possible given the energies of the colliding particles. Compared to experiments colliding a single beam at a fixed target, in the case of a symmetric collision the total momentum of two colliding particles is zero and, therefore, much larger fraction of energy can transfer to a mass of a new particle. The Large Hadron Collider (LHC) is one such collider with the highest energy in the world. It can produce the most massive particles to probe physics beyond the SM (BSM).

The Compact Muon Solenoid (CMS) is one of two general-purpose detectors at the LHC. It is placed at one of four collision points. CMS has a broad physics program including searches for the BSM physics as well as the precision measurements of the parameters of the SM itself. The measurement of this dissertation is a SM measurement with CMS data collected in 2012 in  $pp$  collisions of LHC with beam energies of 4 TeV. The result can be compared to the SM prediction. Certain BSM theories predict a deviation of the result of this measurement from its SM

value, therefore, with this measurement, in addition to testing the SM, we also search for a new physics.

The rest of this chapter gives general introductory information about the SM while Ch. 2 concentrates on the theory of the SM and BSM  $W\gamma$  production and also discusses previous measurements of this process. Chapter 3 describes LHC and CMS in more details. Chapter 4 explains one specific detail of the CMS operation that is the spacial alignment of the tracking detector of charged particles. Finally, Ch. 5 describes the details of the measurement of this dissertation and reports the results.

## 1.1 Fundamental Particles and Interactions

The SM describes interactions of elementary particles. There are four fundamental interactions: electromagnetic, strong, weak and gravitational. The gravity is not included into the SM but its effect on particles is negligible compared to the other forces which makes it possible to develop a theory of the particle physics and conduct experiments even without having the gravity included into the model.

All fundamental elementary particles in the SM can be split into three categories by their spins. There are fermions which possess spin  $s=1/2$ , there are gauge bosons which are vector particles ( $s=1$ ) and there is the Higgs boson which is a scalar particle ( $s=0$ ).

The fermions are arranged into three generations, each generation consists of a quark with charge  $Q=+2/3$  (up, charm, and top quarks), a quark with  $Q=-1/3$  (down, strange, and bottom quarks), a charged lepton with  $Q=-1$  (electron, muon, and tau-lepton) and a neutrino (electron, muon, and tau neutrinos) which is electrically neutral. Each quark can carry any of three colors: red, blue, or green. Additionally, each fermion has its antiparticle. Therefore, the total number of fundamental fermions is  $(6(\text{leptons}) + 6(\text{quarks}) \cdot 3(\text{colors})) \cdot 2(\text{to include antiparticles}) = 48$ .

Corresponding particles in different generations have the same charges, spins and interaction properties but masses of particles increase with generation. These mass differences lead to different decay properties because a particle A can decay to particles B and C only if their masses relate as  $m_A > m_B + m_C$ . Thus, an electron is a stable particle, a muon decays as  $\mu^- \rightarrow e^- + \bar{\nu}_e + \nu_\mu$ , a tau-lepton, as the heaviest charged lepton, has the largest number of decay channels amongst the charged leptons:  $\tau^- \rightarrow \mu^- + \bar{\nu}_\mu + \nu_\tau$ ,  $\tau^- \rightarrow e^- + \bar{\nu}_e + \nu_\tau$ ,  $\tau^- \rightarrow \nu_\tau + \text{quarks}$ .

In addition to fermions, the SM includes gauge bosons which are interaction mediators. They are called mediators because fermions interact with each other by exchanging them. For example, two charged fermions can interact with each other by exchanging a photon. Such interaction is called electromagnetic interaction and a photon is a mediator for the electromagnetic interaction. Similarly, a gluon is a mediator for strong interactions, and  $W^\pm$  and  $Z^0$  bosons are mediators for weak interactions.  $W^\pm$  and  $Z^0$  bosons are massive while a photon and a gluon are massless particles.

The last SM particle is the Higgs boson. The Higgs boson is a scalar neutral particle which is playing a critical role in the electroweak symmetry breaking. The Higgs mechanism explains how  $W$  and  $Z$  bosons become massive particles.

All the particles are summarized in Fig. 1.1. These and only these fundamental particles and their antiparticles have been discovered by now. However, there are many composite particles which are called hadrons. Hadrons can consist of three quarks (baryons), quark and antiquark (meson), or three antiquarks (antibaryons). Hadrons always possess an integer charge.

Most of the particles are short-lived and decay within microseconds. The only stable particles are protons and antiprotons, electrons and positrons, neutrinos and antineutrinos, photons, and, in some sense, gluons. However, if a particle cannot decay, it does not mean that it would live forever. There are many different kinds of reactions in which particles can disappear. Antiprotons and positrons would immediately annihilate with protons and electrons, photons can be absorbed by charged particles, electrons and protons can scatter to produce neutrons and neutrinos and many other reactions are possible.

In this dissertation, the study of  $pp \rightarrow W\gamma + X \rightarrow l\nu\gamma$  process where  $\ell = e, \mu$  is presented. The  $W\gamma$  production with leptonic  $W$  decays proceeds through one of

the following three processes: the initial state radiation where a photon is emitted from one of the incoming partons, the final state radiation where a photon is radiated off the charged lepton from the  $W$  boson decay, and, finally, the triple gauge coupling (TGC) where a photon is emitted from the  $W$  boson. Many BSM theories predict an enhancement of the TGC production over the SM value and, therefore, the experimental search for such an enhancement is a good test for such theories.

Therefore, the focus of this study is an interaction between a photon and a  $W$  boson however many other SM particles are relevant too. Thus, a charged lepton and a neutrino appear as the final state particles, a quark and an antiquark appear as initial state particles and all fundamental particles except the Higgs boson participate in various background processes. Subsequent chapters describe these particle interactions in more details.

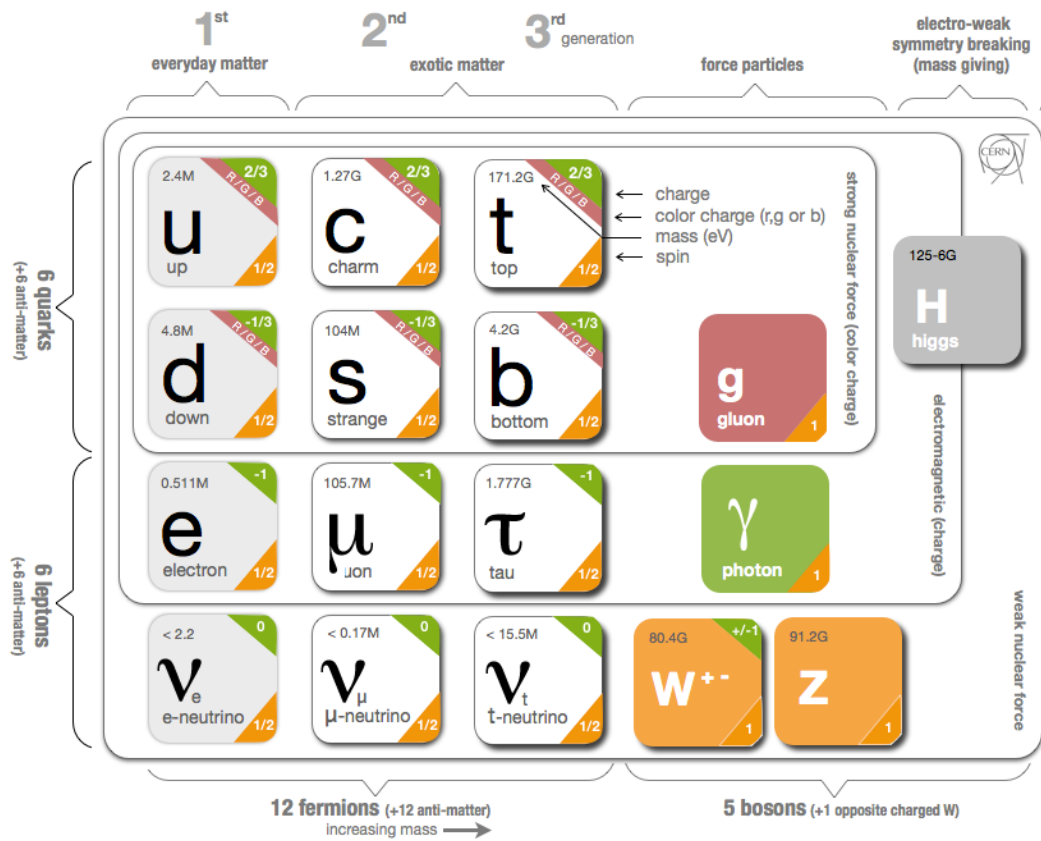


Figure 1.1: Standard Model Particles and Interactions. Source of the figure: [57].

## 1.2 Electroweak Interactions

All electrically charged particles participate in electromagnetic interactions. The theory of electromagnetic interactions is called quantum electrodynamics (QED). All electromagnetic interactions are mediated by a photon, a spin-one electrically neutral massless particle, and can be reduced to one elementary process (Fig. 1.2, left). This process represents a charged fermion radiating or absorbing a photon. Such elementary process itself is forbidden by the energy conservation law but this element is a base of an actual process. For example, the Bhabha scattering,  $e^+e^- \rightarrow e^+e^-$ , occurs through  $e^+e^-$  annihilation with further production of a new  $e^+e^-$  pair (Fig. 1.2, middle) or through exchange of a photon between the positron and the electron (Fig. 1.2, right). Both cases involve nothing except the electromagnetic elementary process (Fig. 1.2, left). Such graphical representations of the particle physics processes are called Feynman diagrams.

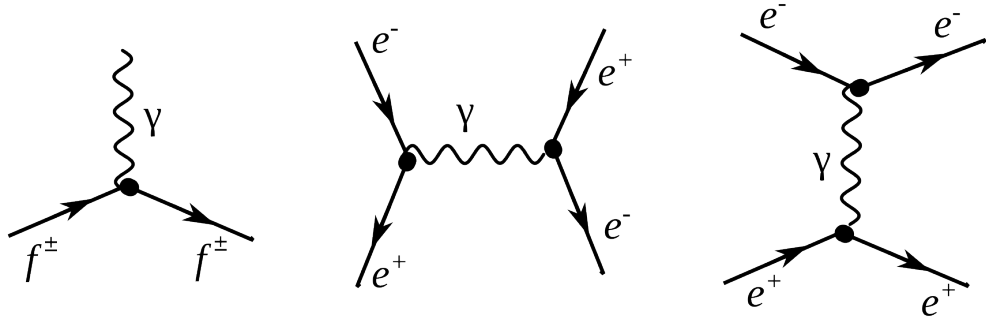


Figure 1.2: Electromagnetic interactions. Left: a photon radiation off a charged fermion, middle and right: Bhabha scattering.

As for the weak interactions, there are two kinds of them: neutral (mediated by a Z boson) and charged (mediated by a  $W^\pm$  boson). Elementary processes with W and Z bosons are shown in Fig. 1.3. Because the electric charge must be conserved

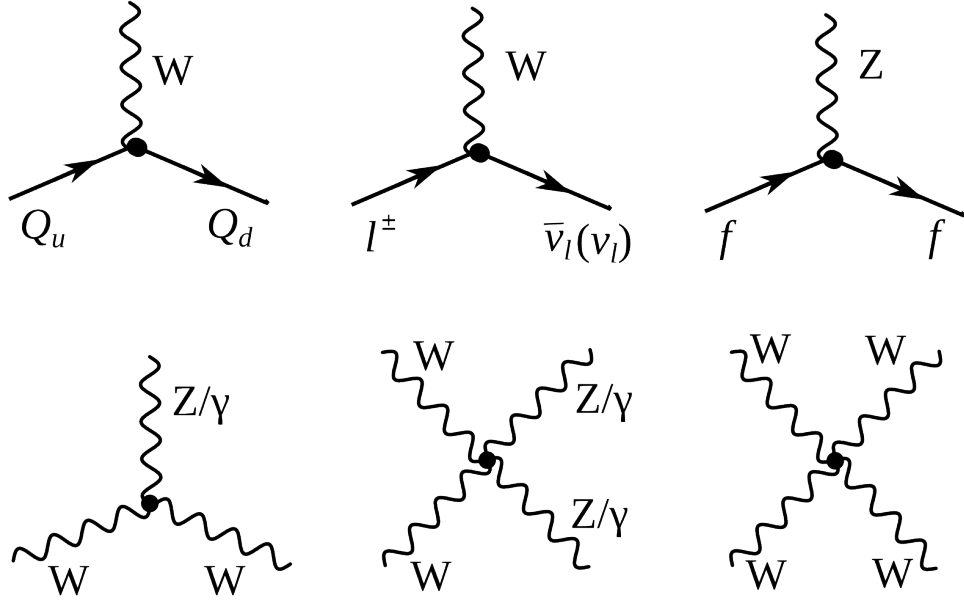


Figure 1.3: Weak elementary processes and gauge couplings. Top left: a quark with charge  $Q=+2/3$  enters, emits a  $W$  boson, and a quark with charge  $Q=-1/3$  escapes. Top middle: a charged lepton enters, emits a  $W$  boson, and a neutrino or antineutrino escapes conserving a lepton flavor number. Top right: a fermion enters, emits a  $Z$  boson and escapes. Bottom left: TGC couplings  $WW\gamma$  and  $WWZ$ . Bottom middle: QGC couplings  $WW\gamma\gamma$ ,  $WWZ\gamma$  and  $WWZZ$ . Bottom right: QGC coupling  $WWWW$ .

at any vertex, a particle radiating or absorbing a  $W$  boson converts to a different particle. Thus, a charged lepton converts to a neutrino (or vice versa) as shown in Fig. 1.3, top middle. Each lepton carries a lepton flavor number (Tab. 1.1). Lepton flavor is conserved in any interaction, thus an electron radiating a  $W$  boson always converts to an electron neutrino, a muon converts to a muon neutrino etc.

From top left diagram in Fig. 1.3 we see that if a quark with  $Q=+2/3$  enters, then a quark with  $Q=-1/3$  escapes and, therefore, the flavor of the quark is changed. The charged weak interaction is the only interaction which changes a quark flavor. The probability of each of three quarks with  $Q=-1/3$  to be born

Table 1.1: Lepton Flavor Number

particles	$L_e$	$L_\mu$	$L_\tau$
$e^-, \nu_e$	+1	0	0
$e^+, \bar{\nu}_e$	-1	0	0
$\mu^-, \nu_\mu$	0	+1	0
$\mu^+, \bar{\nu}_\mu$	0	-1	0
$\tau^-, \nu_\tau$	0	0	+1
$\tau^+, \bar{\nu}_\tau$	0	0	-1

is determined by the Cabibbo-Kobayashi-Maskawa matrix which relates mass eigenstates  $d, c$  and  $b$  to weak eigenstates  $d', c'$  and  $b'$  (Eq. 1.1). Absolute values of the matrix elements are all known (Eq. 1.2) and are the highest for the quark of the same generation as the initial state quark. In the particular case shown in the top left diagram in Fig. 1.3,  $u$  is the initial state quark and  $d$  has the highest probability to be produced after an interaction with a  $W$  boson but  $s$  and  $b$  can also be produced if there is enough energy.

$$\begin{pmatrix} d' \\ s' \\ b' \end{pmatrix} = \begin{pmatrix} V_{ud} & V_{us} & V_{ub} \\ V_{cd} & V_{cs} & V_{cb} \\ V_{td} & V_{ts} & V_{tb} \end{pmatrix} \begin{pmatrix} d \\ s \\ b \end{pmatrix} \quad (1.1)$$

$$\begin{pmatrix} |V_{ud}| & |V_{us}| & |V_{ub}| \\ |V_{cd}| & |V_{cs}| & |V_{cb}| \\ |V_{td}| & |V_{ts}| & |V_{tb}| \end{pmatrix} = \begin{pmatrix} 0.97 & 0.23 & 0.00 \\ 0.23 & 0.97 & 0.04 \\ 0.01 & 0.04 & 1.00 \end{pmatrix} \quad (1.2)$$

An elementary process of a neutral weak interaction is an emission a  $Z$  boson off a fermion line (right top diagram in Fig. 1.3). Diagrams with a  $Z$  boson are very similar to ones with a photon except a photon can only be radiated off a charged particle but a  $Z$  boson can also be radiated off a neutrino or antineutrino.

The bottom diagrams in Fig. 1.3 are gauge bosons coupling diagrams including self-coupling of a  $W$  boson, its interaction with a  $Z$  boson and its electromagnetic radiation of a photon. Charge-conserving TGC and quartic gauge couplings (QGC) containing two or four  $W$  bosons are all possible in the SM:  $WWZ$ ,  $WW\gamma$ ,  $WWZZ$ ,  $WWZ\gamma$ ,  $WW\gamma\gamma$ , and  $WWWW$ .

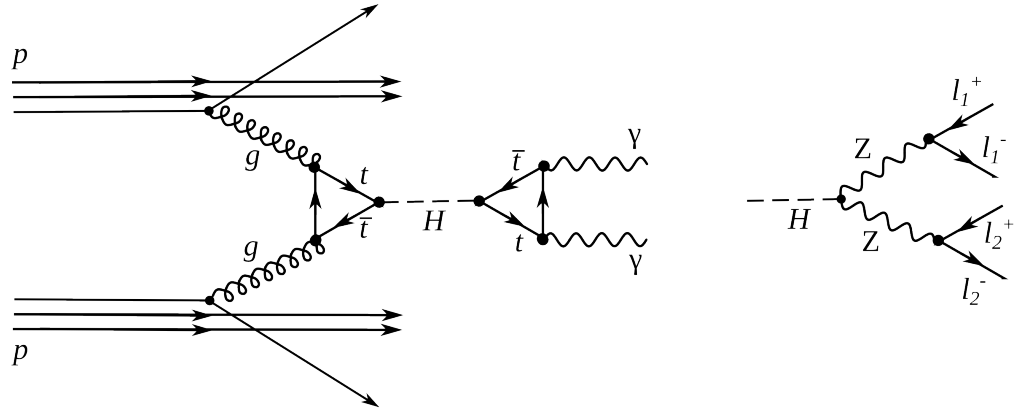


Figure 1.4: The Higgs boson production and decay. Left:  $H \rightarrow \gamma\gamma$ , right:  $H \rightarrow ZZ \rightarrow 4l$ .

Electromagnetic and weak interactions are unified by the electroweak Glashow-Weinberg-Salam (GWS) theory which is based on  $SU(2) \times U(1)$  symmetry.  $SU(2)$  is the symmetry of weak isospin which generates three bosons:  $W^1$ ,  $W^2$  and  $W^3$ .  $U(1)$  is the symmetry of the weak hypercharge and generate one neutral boson  $B$ .  $W^1$  and  $W^2$  are mixed to create  $W^+$  and  $W^-$  mediators while  $W^3$  and  $B$  are mixed to create a  $Z$  boson and a photon. Therefore, the GWS theory considers electromagnetic and weak forces as different manifestations of the electroweak force. The electroweak theory is discussed in greater details in Ch. 2.

Weak interactions are mediated by heavy bosons ( $M_W = 80$  GeV,  $M_Z = 91$  GeV) while electromagnetic interactions are mediated by a massless photon, thus, the electroweak symmetry is broken. To explain this phenomenon, the Higgs

mechanism was introduced. The mechanism predicted an existence of an additional boson: the Higgs boson. The Higgs boson was a missing piece of the SM for many years and was finally discovered in 2012 at LHC by ATLAS and CMS collaborations through the processes shown in Fig. 1.4 [18], [13].

The measurement in this dissertation is an electroweak measurement because the process involves a  $W$  boson. It includes an interaction of a  $W$  boson with leptons and quarks as well as the TGC  $WW\gamma$ . Thus, the measurement is a good test of the SM electroweak theory.

### 1.3 Strong Interactions

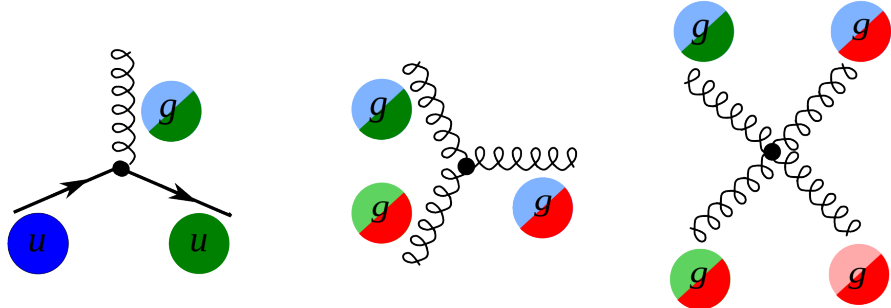


Figure 1.5: Elementary processes of strong interactions

The third fundamental force after the electromagnetic and weak ones is the strong force. The strong force is responsible for gluing protons and neutrons together in the nuclei as well as for forming protons and neutrons themselves. The strong interactions occur by exchanging gluons which are spin-one massless electrically neutral particles.

The elementary strong processes are shown in Fig. 1.5. There are three elementary processes:  $qqg$ ,  $ggg$  and  $gggg$ , all are involving particles with color charges. Thus, gluons couple to quarks and self-couple. Color charges must be conserved at each elementary process of the strong interaction. Each quark possesses one of three colors at a time, and there are eight types of gluons to cover all possible color exchanges.

The coupling constant of the strong interaction depends on the distance between interacting particles: it becomes larger as the distance becomes larger and smaller as the distance becomes smaller. As the distance approaches zero, the coupling constant approaches zero too, and, thus, in the asymptotic limit two quarks located at the same place do not interact. This property is called asymptotic freedom.

On the other hand, when the distance between quarks becomes larger, the coupling constant also becomes larger. This property confines quarks to always stay in the color neutral combinations (hadrons), it forbids the existence of free quarks. A combination becomes color neutral when there is the same amount of color and anticolor or if there is the same amount of each of the three colors. Thus, mesons are comprised of a quark and an antiquark with the opposite color charges, and baryons are composed of three quarks: red, green and blue one. Examples of baryons include such well-known particles as a proton and a neutron.

The asymptotic freedom and the confinement are properties that are specific to strong interactions. The theory of strong interactions is called the quantum chromodynamics (QCD) which is a quantum field theory invariant under  $SU(3)$  color transformations. When the coupling constant is much less than one  $\alpha_s \ll 1$ , the perturbative approach can be used to compute observables.

The  $W\gamma$  process being measured in this dissertation is not intended to test QCD, but a good understanding of QCD is essential for performing this measurement because the QCD corrections to the Feynman diagrams of the process are large and have to be taken into account when producing simulation. In addition, QCD describes the dynamics of quarks and gluons within colliding protons and predicts probabilities of one or another quark-antiquark pair to interact. Physics of proton-proton collisions is discussed in Ch. 1.4.

## 1.4 Physics of Proton-Proton Collisions

Consider a  $pp$  collision at LHC. The proton energies are so high that each proton behaves as a complex structure. A proton is a baryon, it consists of three quarks:  $uud$ . These three quarks are called valence quarks. They interact with each other by exchanging gluons which produce virtual  $q\bar{q}$  pairs (Fig. 1.6). Such virtual quarks are also called sea quarks.

Any parton, quark, antiquark or gluon, from one proton can interact with any parton from another proton. Probabilities  $f_i(x, Q^2)$  of any particular constituent  $i$  to interact are described partially by QCD and partially by experimental measurements and depend on the momentum transfer  $Q$  and the momentum fraction of a specific parton  $x$ . These probabilities are called parton distribution functions (PDFs).

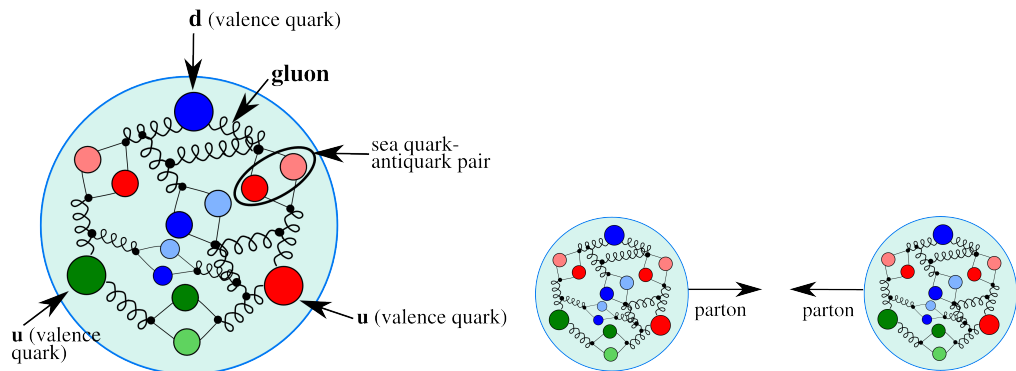


Figure 1.6: The proton structure (left) and the proton-proton collision (right).

For large  $Q^2$  and  $x$  gluon-gluon interactions have the largest probabilities to occur (Fig. 1.7). However, gluons do not couple directly to a  $W$  boson, thus, in the  $W\gamma$  measurement we are mostly interested in quark-antiquark pairs which would have a total charge corresponding to the charge of a  $W$  boson ( $\pm 1$ ). Since

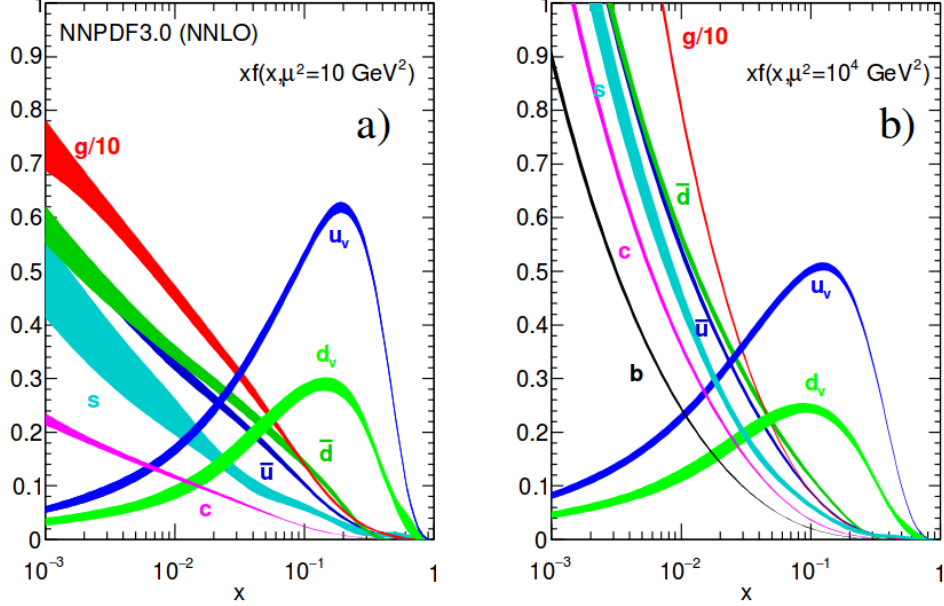


Figure 1.7: Parton distribution functions [43].

we have  $u$  and  $d$  as valence quarks and we know that the probability to couple to the same generation quark in charged weak interactions is the highest, most of the  $W$  bosons are created by  $u\bar{d}$  and  $d\bar{u}$  pairs however other  $q\bar{q}'$  combinations with the total charges of  $\pm 1$  are also possible. As we look for events containing  $W\gamma$  we also have other events mimicking our process. Such background events can be produced by any pair of partons.

## 1.5 Open Questions of the Standard Model

While the SM is an accurate description of all particle physics experimental results, there are certain phenomena which are not included into the SM. In this subsection we discuss some of them.

The gravitational interactions do not fit into the SM. It is the open question whether the quantum theory of gravity is possible and whether there is a mediator of the gravitational interactions. Also, it is not known why the gravitational force is so much weaker than the other forces. One possible explanation comes from a theory which predicts extra spatial dimensions beyond the three we experience (e.g. the string theory). In this case, it is possible that the gravitational force is shared with other dimensions and only a fraction is available in our three dimensions.

Another mystery of the universe is its composition: it is known from the studies of the gravitational effects that our universe consists of dark energy by 68%, of dark matter by 27% and of baryon matter only by 5% [42]. The dark energy resists the gravitational attraction and accelerates the expansion of the universe, and is not detectable by any effects except gravitational. The understanding of dark energy is a question of general relativity rather than particle physics. The dark matter, however, likely consists of particles and therefore is a subject of particle physics. It does not radiate and that is why it cannot be detected by telescopes. The nature of the dark matter is not known but its constituents must be very stable to remain since the Big Bang. The theory of the supersymmetry which is unifying fundamental particles and mediators predicts many of new heavy particles and the lightest supersymmetric particle, the neutralino, is a good candidate for dark matter.

One more open question is the reason for the matter/antimatter asymmetry.

Matter and antimatter should have been created in the same amount at the moment of the Big Bang. Most of it has annihilated but because of asymmetry, there was more matter than antimatter which led to the state of the Universe we observe now. There is a phenomenon of the CP-violation in weak interactions observed and described which predicts the asymmetry at a certain level. However, the effect of the CP-violation is not large enough to account for the observed amount of the matter and, therefore, the total matter/antimatter asymmetry remains unexplained.

The measurement of the photon transverse momentum spectrum ( $P_T^\gamma$ ) of the  $W\gamma$  process has a goal to both test the SM and search for the BSM physics. The low  $P_T^\gamma$  region is not expected to be affected by any new physics and must agree well with the SM predictions while the high  $P_T^\gamma$  region may indicate an existence of new physics if there is an enhancement over the SM predictions. The excess would be indirect evidence of the BSM particles like supersymmetric particles or additional gauge bosons which could be part of the explanation of the dark matter presence or difference in magnitudes of different interactions. More theoretical details about the SM description of  $W\gamma$  process as well as possible BSM physics are given in Ch. 2.

## Chapter 2

# **$W\gamma$ Production Theory and Former Experimental Results**

Chapter 2 provides deeper theoretical background for the measurement of this dissertation and discusses former experimental results. The derivation of the electroweak Lagrangian is described in Ch. 2.1, including the appearance of triple gauge coupling (TGC) and quartic gauge coupling (QGC) terms. Then concepts of the cross section and the luminosity are discussed in Ch. 2.2. More specific details regarding the SM cross section of  $W\gamma$  are summarized in Ch. 2.3. Possible causes and potential effects of anomalous TGC (aTGC) are explained in Ch. 2.4. Finally, Ch. 2.5 lists former physics experiments which probed the same aTGC vertex which is probed in the measurement of this dissertation including measurements of exactly the same process at lower LHC beam energy.

## 2.1 Electroweak Theory of the Standard Model

To develop a quantum field theory, we start with the Lagrangian of free fermions. In order to describe a system with a conserved physical quantity, the Lagrangian is required to satisfy a local invariance with respect to a certain transformation. For instance, a conservation of electric charge requires local invariance under  $U(1)$  transformation for the QED Lagrangian [46]. The requirement of local invariance introduces an interaction between one or more new vector fields and our free fermions. The new vector fields are mediators of an interaction conserving the physical quantity. To provide a full description for a new boson field, in addition to the interaction term we introduce an invariant term for the kinetic energy of the boson. Such an approach allows us to derive a Lagrangian which is locally invariant with respect to a certain gauge transformation and contains interacting fermions as well as interaction mediators.

The SM is a quantum field theory invariant under the local  $SU(3)_C \times SU(2)_L \times U(1)_Y$  transformation [46]. The SM Lagrangian includes all observed quantum fields and their interactions.

The part of the SM Lagrangian based on the  $SU(3)_C$  symmetry is called QCD or the theory of strong interactions. QCD has three types of charges which are called colors: red, blue, and green. To be a subject of the strong interaction, a fermion must possess a color charge. Quarks and antiquarks are such fermions. The requirement to satisfy the gauge invariance with respect to  $SU(3)_C$  transformations generates eight massless gluons, and the non-abelian nature of the  $SU(3)$  group generates self-interactions of gluons including three-gluon and four-gluon vertices.

The part of the SM Lagrangian based on the  $SU(2)_L \times U(1)_Y$  symmetry is the foundation of the unified theory of electroweak interactions.  $SU(2)_L$  reflects

transformations in the weak isospin space of left-handed fermions ([28], Ch. 9) while  $U(1)_Y$  reflects transformations in a weak hypercharge space of all fermions. The requirement of the local gauge invariance generates four massless vector bosons which are mediators of electromagnetic and weak interactions. The non-abelian structure of the  $SU(2)$  group generates gauge boson self-couplings the same way as self-interactions of gluons appear in QCD.

Mass terms for the vector bosons would violate the gauge invariance of the electroweak Lagrangian, however it is experimentally known that the mediators of weak interactions are heavy particles with masses  $M_W = 80$  GeV and  $M_Z = 91$  GeV. A possible solution of this discrepancy is the mechanism of Spontaneous Symmetry Breaking.

The mechanism of Spontaneous Symmetry Breaking and the appearance of the mass terms for  $W$  and  $Z$  bosons is realized by introducing an additional doublet of scalar fields. After that, the Lagrangian is transformed in such a way that  $W$  and  $Z$  bosons acquire masses through their interactions with a new particle: the Higgs boson ( $H$ ). A photon does not couple to the Higgs boson remaining a massless particle and leaving QED symmetry group  $U(1)$  to be unbroken.

The measurement in this dissertation provides a test for the electroweak sector of the SM. We will retrace the steps of the derivation of the electroweak part of the SM Lagrangian starting from the terms for free fermions. The resulting Lagrangian accommodates electroweak gauge bosons and their self-couplings. One of these self-couplings,  $WW\gamma$ , is the primary focus of our measurement.

It is experimentally known that the dynamics of weak interactions depend on particle chirality ([28], chapter 4.4.1). In particular, a  $W$  boson couples to left-handed fermions and right-handed antifermions only. Given different properties of left-handed and right-handed fermions, they are treated differently by the

electroweak theory.  $SU(2)$  doublets are introduced for the wave functions of left-handed fermions while  $SU(2)$  singlets are introduced for the wave functions of right-handed fermions. Equations 2.1 and 2.2 show wave functions for the first generation fermions. Wave functions for the other two generations are constructed the same way.

$$\psi_1(x) = \begin{pmatrix} u \\ d' \end{pmatrix}_L, \psi_2(x) = u_R, \psi_3(x) = d'_R. \quad (2.1)$$

$$\psi_1(x) = \begin{pmatrix} \nu_e \\ e^- \end{pmatrix}_L, \psi_2(x) = \nu_{eR}, \psi_3(x) = e^-_R. \quad (2.2)$$

The state  $d'$  in Eq. 2.1 is a weak eigenstate which is a linear combination of the mass eigenstates of the  $d$ ,  $c$  and  $b$  quark wave functions and is determined by the quark mixing matrix,  $V$ , which is also called Cabibbo-Kobayashi-Maskawa matrix [46]:

$$\begin{pmatrix} d' \\ c' \\ b' \end{pmatrix} = V \begin{pmatrix} d \\ c \\ b \end{pmatrix} \quad (2.3)$$

To derive the unified electroweak Lagrangian, we start with the free fermion terms:

$$L_0 = \sum_{j=1}^3 i\bar{\psi}_j(x)\gamma^\mu\partial_\mu\psi_j(x), \quad (2.4)$$

where  $\gamma^\mu$  are Dirac matrices ([28], chapter 7.1) and  $\psi_j(x)$  are wave functions determined by Eqs. 2.1 and 2.2.

The wave function  $\psi_1$  changes under the  $SU(2)_L \times U(1)_Y$  transformations in

the following way:

$$\psi_1(x) \rightarrow e^{iy_1\beta} U_L \psi_1(x), \quad (2.5)$$

while the wave functions  $\psi_{(2,3)}(x)$  are singlets of  $SU(2)_L$  and are affected only by  $U(1)$  transformations:

$$\psi_{(2,3)}(x) \rightarrow e^{iy_{(2,3)}\beta} \psi_{(2,3)}(x). \quad (2.6)$$

The transformation in the weak isospin space is defined as  $U_L \equiv e^{i\sigma_i \alpha_i / 2}$  where  $\sigma_i$  are Pauli matrices ([28], chapter 4.2.2). Phases  $\alpha_i(x)$  and  $\beta(x)$  in Eqs. 2.5 and 2.6 are arbitrary functions of  $x$ , and  $y_{(1,2,3)}$  are weak hypercharges which are named analogous to electric charges in QED.

In order for the Lagrangian to satisfy the local  $SU(2)_L \times U(1)_Y$  invariance, partial derivatives in Eq. 2.4 have to be substituted with covariant derivatives:

$$D_\mu \psi_1(x) = [\partial_\mu - ig\tilde{W}_\mu(x) - ig'y_1 B_\mu(x)] \psi_1(x) \quad (2.7)$$

$$D_\mu \psi_{(2,3)}(x) = [\partial_\mu - ig'y_{(2,3)} B_\mu(x)] \psi_{(2,3)}(x) \quad (2.8)$$

where  $g, g'$  are arbitrary constants,

$$\tilde{W}_\mu(x) \equiv \frac{\sigma_i}{2} W_\mu^i(x) = \frac{1}{\sqrt{2}} \begin{pmatrix} \sqrt{2}W_\mu^3 & (W_\mu^1 - iW_\mu^2)/\sqrt{2} \\ (W_\mu^1 + iW_\mu^2)/\sqrt{2} & -W_\mu^3 \end{pmatrix}, \quad (2.9)$$

$B_\mu, W_\mu^1, W_\mu^2, W_\mu^3$  are four vector bosons that arise from the requirement that the Lagrangian is invariant under local  $SU(2)_L \times U(1)$  transformations.

The Lagrangian becomes:

$$L_0 \rightarrow L = \sum_{j=1}^3 i\bar{\psi}_j(x)\gamma^\mu D_\mu \psi_j(x) \quad (2.10)$$

To make new vector bosons physical fields it is necessary to add terms for their kinetic energies:

$$L_{KIN} = -\frac{1}{4}B_{\mu\nu}B^{\mu\nu} - \frac{1}{4}W_{\mu\nu}^i W_i^{\mu\nu} \quad (2.11)$$

where  $B_{\mu\nu} \equiv \partial_\mu B_\nu - \partial_\nu B_\mu$ ,  $W_{\mu\nu}^i \equiv \partial_\mu W_\nu^i - \partial_\nu W_\mu^i + g\epsilon^{ijk}W_\mu^j W_\nu^k$

Off-diagonal terms of  $\tilde{W}_\mu$  are wave functions of charged vector bosons

$$W^\pm = (W_\mu^1 \mp iW_\mu^2)/\sqrt{2} \quad (2.12)$$

while  $W_\mu^3$  and  $B_\mu$  are neutral fields which are mixtures of a  $Z$  boson and a photon determined by:

$$\begin{pmatrix} W_\mu^3 \\ B_\mu \end{pmatrix} \equiv \begin{pmatrix} \cos \theta_W & \sin \theta_W \\ -\sin \theta_W & \cos \theta_W \end{pmatrix} \begin{pmatrix} Z_\mu \\ A_\mu \end{pmatrix} \quad (2.13)$$

where  $\theta_W$  is the electroweak mixing angle and  $A_\mu$  is a photon field.

In order to be consistent with QED, terms involving  $A_\mu$  in the electroweak Lagrangian must be equal to the corresponding terms in the QED Lagrangian [46]:

$$L_{QED} = i\bar{\psi}(x)\gamma^\mu \partial_\mu \psi(x) - m\bar{\psi}(x)\psi(x) + qA_\mu(x)\bar{\psi}(x)\gamma^\mu \psi(x) - \frac{1}{4}F_{\mu\nu}(x)F^{\mu\nu}(x), \quad (2.14)$$

where  $q$  is electric charge of  $\psi(x)$  field,  $F_{\mu\nu} \equiv \partial_\mu A_\nu - \partial_\nu A_\mu$ .

This requirement relates  $g$ ,  $g'$ ,  $\theta_W$  and  $e$  as  $g \sin \theta_W = g' \cos \theta_W = e$  and provides an expression for weak hypercharges:  $y = q - t_3$ , where  $q$  is the electric charge and  $t_3$  is the  $z$ -component of the weak isospin. This results in  $y_1 = 1/6$ ,  $y_2 = 2/3$ , and  $y_3 = -1/3$  for quarks and  $y_1 = -1/2$ ,  $y_2 = 0$ , and  $y_3 = -1$  for leptons. A right-handed neutrino has a weak hypercharge of  $y_2 = 0$ . It also does not have an electric charge, and as a right-handed fermion has  $t_3 = 0$ , therefore, it does not couple to a  $W$  boson. Thus, a right-handed neutrino does not participate in any SM interaction.

Writing  $\tilde{W}_\mu$  in Eq. 2.11 explicitly, we obtain triple gauge coupling (TGC) and quartic gauge coupling (QGC) terms:

$$L_{TGC} = -\frac{g}{4}(\partial_\mu W_\nu^i - \partial_\nu W_\mu^i)\epsilon^{ijk}W^{\mu j}W^{\nu k} - \frac{g}{4}\epsilon^{ijk}W_\mu^jW_\nu^k(\partial^\mu W^{\nu i} - \partial^\nu W^{\mu i}) \quad (2.15)$$

$$L_{QGC} = -\frac{g^2}{4}\epsilon^{ijk}\epsilon^{ilm}W_\mu^jW_\nu^kW_\lambda^{\mu l}W^{\nu m} \quad (2.16)$$

Substituting expressions for  $W_\mu^i$  and  $B_\mu$  determined by Eqs. 2.12 and 2.13 into Eqs. 2.15 and 2.16 we receive charged TGC and QGC terms in the Lagrangian (those involving two or four  $W$  bosons) in the forms of Eqs. 2.17 and 2.20, but all neutral TGC and QGC terms (those not involving any  $W$  bosons) cancel out.

Equation 2.17 involves  $WWZ$  (Eq. 2.18) and  $WW\gamma$  (Eq. 2.19) interactions:

$$L_{TGC} = L_{TGC}^{(1)} + L_{TGC}^{(2)}, \quad (2.17)$$

$$L_{TGC}^{(1)} = -ie \cot \theta_W (W^{-\mu\nu} W_\mu^+ Z_\nu - W^{+\mu\nu} W_\mu^- Z_\nu + W_\mu^- W_\nu^+ Z^{\mu\nu}), \quad (2.18)$$

$$L_{TGC}^{(2)} = -ie (W^{-\mu\nu} W_\mu^+ A_\nu - W^{+\mu\nu} W_\mu^- A_\nu + W_\mu^- W_\nu^+ A^{\mu\nu}). \quad (2.19)$$

Equation 2.20 involves  $WWWW$  (Eq. 2.21),  $WWZZ$  (Eq. 2.22),  $WWZ\gamma$  (Eq. 2.23), and  $WW\gamma\gamma$  (Eq. 2.24) interactions:

$$L_{QGC} = L_{QGC}^{(1)} + L_{QGC}^{(2)} + L_{QGC}^{(3)} + L_{QGC}^{(4)}, \quad (2.20)$$

$$L_{QGC}^{(1)} = -\frac{e^2}{2 \sin^2 \theta_W} (W_\mu^+ W^{-\mu} W_\nu^+ W^{-\nu} - W_\mu^+ W^{\mu} W_\nu^- W^{-\nu}), \quad (2.21)$$

$$L_{QGC}^{(2)} = -e^2 \cot^2 \theta_W (W_\mu^+ W^{-\mu} Z_\nu Z^\nu - W_\mu^+ Z^\mu W_\nu^- Z^\nu), \quad (2.22)$$

$$L_{QGC}^{(3)} = -e^2 \cot \theta_W (2W_\mu^+ W^{-\mu} Z_\nu A^\nu - W_\mu^+ Z^\mu W_\nu^- A^\nu - W_\mu^+ A^\mu W_\nu^- Z^\nu), \quad (2.23)$$

$$L_{QGC}^{(4)} = -e^2 (W_\mu^+ W^{-\mu} A_\nu A^\nu - W_\mu^+ A^\mu W_\nu^- A^\nu). \quad (2.24)$$

In the measurement of this dissertation we probe  $WW\gamma$  coupling (Eq. 2.19).

The unified electroweak Lagrangian discussed above involves kinetic energy terms for fermions and gauge bosons as well as interactions of fermions with gauge bosons, TGC, and QGC. However, this Lagrangian does not contain any

mass terms. Because left-handed and right-handed wave functions transform differently under the electroweak symmetry, adding fermion mass terms of  $\frac{1}{2}m_f^2\bar{\psi}\psi$  would violate the Lagrangian invariance and, therefore, fermion mass terms are forbidden by the  $SU(2) \times U(1)$  symmetry requirement. Mass terms for gauge bosons also would violate the Lagrangian invariance just as a photon mass term  $\frac{1}{2}m^2A^\mu A_\mu$  would violate  $U(1)$  invariance of  $L_{QED}$  [28]. Therefore, Lagrangian  $L$  in Eq. 2.10 contains massless particles only.

However, it is known from experiments that the  $Z$  and  $W$  bosons as well as fermions are massive particles and, therefore, our theory should accommodate their masses. To introduce masses into the electroweak Lagrangian, an  $SU(2)_L$  doublet of complex scalar fields  $\phi(x)$  is added to the Lagrangian:

$$\phi(x) \equiv \begin{pmatrix} \phi^{(+)}(x) \\ \phi^{(0)}(x) \end{pmatrix} \quad (2.25)$$

By selecting a special gauge of  $\phi(x)$  it is possible to spontaneously break electroweak symmetry, generate a new scalar particle, the Higgs boson [46], and introduce mass terms for  $W$  and  $Z$  bosons and charged fermions through their couplings to the Higgs boson. The strength of the coupling constant is proportional to the square of the particle's mass, therefore, heavier particles are more likely to interact with  $H$ , and massless particles do not couple to  $H$ .

The mechanism of generating a fermion's mass involves both left-handed and right-handed components of the fermion. If our hypothesis that right-handed neutrinos do not exist is right, then the Higgs mechanism does not generate neutrino masses. However, from the experiments of neutrino oscillations, neutrinos are known to have masses even though they are orders of magnitude smaller than those of other fermions. Several hypotheses have been offered to resolve this

contradiction however at the moment the mechanism for neutrinos to acquire masses remain unknown [43].

In this dissertation, we study an electroweak process  $W\gamma \rightarrow l\nu_l\gamma$  and probe the TGC vertex  $WW\gamma$  (Eq. 2.19). To do that, we measure the differential cross section of  $W\gamma \rightarrow l\nu_l\gamma$  with respect to the photon transverse momentum. The concept of the cross section in particle physics is discussed in the next chapter.

## 2.2 Cross Section and Luminosity

In this dissertation we measure the total cross section of the process  $pp \rightarrow l\nu_l\gamma + X$  and its differential cross section in transverse momentum of the photon. A cross section in particle physics is an interaction probability per unit flux of incident particles [37]. It can be interpreted as an area which must be crossed by an incident particle in order to interact with a scattering center, or, in case of a differential cross section, area  $d\sigma$  within which an incident particle must appear to be scattered off by an angle  $d\theta$  (Fig. 2.1). The relationship between  $d\sigma$  and  $d\theta$  gives us the expression for a differential cross section  $d\sigma/d\theta$ . Integrating over  $d\theta$ , we obtain the total cross section  $\sigma$ . The cross section concept illustrated in Fig. 2.1 is generalized to be an effective area, and is generalized for two (or more) particle interactions rather than a light particle scattering off a stationary center.

The angle  $\theta$  here is used only as an illustration of a concept of differential cross section. In particle physics we measure a differential cross section with respect to a parameter  $X$  which can be a parameter of one of final state particles or of a system of final state particles. For example, a cross section could be measured as a function of the transverse momentum of a final state photon  $P_T^\gamma$ , the invariant mass of two final state leptons  $m_{ll}$ , or even discreet observables such as the number of jets associated with the process  $N_{jets}$ .

In the scenario illustrated in Fig. 2.1, the number of particles passing through the area  $\sigma$  per unit time is

$$N = L \cdot \sigma, \quad (2.26)$$

where  $L$  is the flux of incident particles and is called luminosity. For colliding beams, the luminosity is determined by collisions frequency, the number of col-

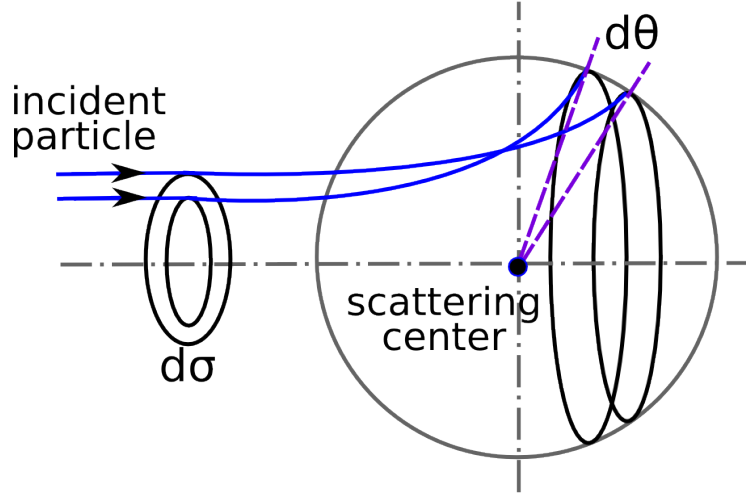


Figure 2.1: Illustration of the differential cross section concept in the classical case.

liding particles in each beam, and beams cross sections. The cross section  $\sigma$  of a specific process can be determined from an experiment as  $\sigma = N/L$ .

A cross section can be computed theoretically using the following expression:

$$\sigma = \frac{W_{fi}}{F} N_{fs}, \quad (2.27)$$

where  $W_{fi}$  is a transition probability between final and initial states of the system per unit spatial volume,  $F$  is the initial flux, and  $N_{fs}$  is the density of final states ([29], chapter 4.3). The initial flux in this expression is determined as number of incident particles per unit volume multiplied by their velocity and by the number of target particles per unit volume.

The formula for the cross section relevant for our measurement, two particles to three final state particles scattering  $1 + 2 \rightarrow 3 + 4 + 5$ , is determined by the Fermi's Golden Rule [28]:

$$\sigma = \frac{1}{4\sqrt{(p_1 p_2)^2 - (m_1 m_2)^2}} \int |M|^2 (2\pi)^4 \delta^4(p_1 + p_2 - p_3 - p_4 - p_5) \prod_{j=3}^5 \frac{1}{2\sqrt{\bar{p}_j^2 + m_j^2}} \frac{d^3 \bar{p}_j}{(2\pi)^3}, \quad (2.28)$$

where  $p_i$  are four-momenta and  $\bar{p}_i$  are three momenta of the initial state and the final state particles,  $m_i$  are masses of particles,  $M$  is the process amplitude determined by the dynamics of the particles interaction. All possible momenta of the final state particles is called the phase space.

During proton-proton collisions at high energy, the hard scattering process occurs between partons in the protons, as discussed in Ch. 1.4. Therefore, the cross section of a process  $pp \rightarrow X + Y$  has two ingredients: PDFs and a partonic cross section  $\sigma_{ab \rightarrow X}$ . The partonic cross section is described by perturbative QCD while PDFs require non-perturbative computations and are determined, in part, from experiments (Fig. 1.7). According to the QCD factorization theorem [30]:

$$\sigma(pp \rightarrow X + Y) = \sum_{a,b} \int dx_a dx_b f_a(x_a, Q^2) f_b(x_b, Q^2) \sigma(ab \rightarrow X). \quad (2.29)$$

In the case of  $W\gamma$  process,  $X$  is  $l\nu\gamma$ ,  $ab$  are  $q_i\bar{q}_j$  or  $q_j\bar{q}_i$ .  $Q^2$  is the large momentum scale that characterizes hard scattering,  $f_a$  and  $f_b$  are PDFs,  $x_a$  and  $x_b$  are fractions of momenta of the partons. In the next sections we will discuss the computation of partonic cross sections of the  $W\gamma$  process and possible BSM effects.

## 2.3 Standard Model $W\gamma$ Production

A  $W$  boson in proton-proton collisions can be produced in the processes  $q\bar{q}' \rightarrow W$  where  $q$  and  $\bar{q}'$  are a quark and an antiquark which have a total charge of  $+1$  if producing a  $W^+$  boson or  $-1$  if producing a  $W^-$  boson. The processes  $u\bar{d} \rightarrow W^+$  and  $d\bar{u} \rightarrow W^-$  are the most likely to occur because  $u$  and  $d$  are valence quarks in a proton. There are twice as many  $u$  quarks in a proton as  $d$  quarks, therefore,  $W^+$  is produced twice more frequently than  $W^-$ . Antiquarks  $\bar{d}$  and  $\bar{u}$  come from the sea  $q\bar{q}$  pairs of the other proton.

Once created, a  $W$  boson decays immediately, its lifetime is  $\simeq 10^{-25}$  s. In an experiment one detects its decay products rather than the  $W$  boson itself. Decay modes of a  $W$  boson include  $W^\pm \rightarrow l^\pm \nu_l (\bar{\nu}_l)$  where  $l^\pm = e^\pm, \mu^\pm$  or  $\tau^\pm$  with branching fractions of 11% per a leptonic channel [43]. The remaining 67% account for various  $W \rightarrow q\bar{q}'$  decays. In this dissertation we only consider  $W^\pm \rightarrow \mu^\pm \nu_\mu (\bar{\nu}_\mu)$  and  $W^\pm \rightarrow e^\pm \nu_e (\bar{\nu}_e)$  channels.

A photon can be emitted from any charged particle of the process: a quark, an antiquark, a charged lepton or a  $W$  boson (Fig. 2.2, top). A quark and an antiquark are initial state particles and, therefore, if one of them radiates a photon, we refer to the process as initial state radiation (ISR). A muon or an electron is a final state particle and if it radiates a photon, we call such a process final state radiation (FSR). Finally, a  $W$  boson is a gauge boson and if it radiates a photon, the process has a vertex with three gauge bosons:  $WW\gamma$ , and we call such process the triple gauge coupling (TGC). We cannot distinguish between these processes experimentally because we detect final state particles only.

The electroweak Lagrangian is described in Chapter 2.1. It is possible to derive equations of motion from the Lagrangian for any fields involved [28]. However, in

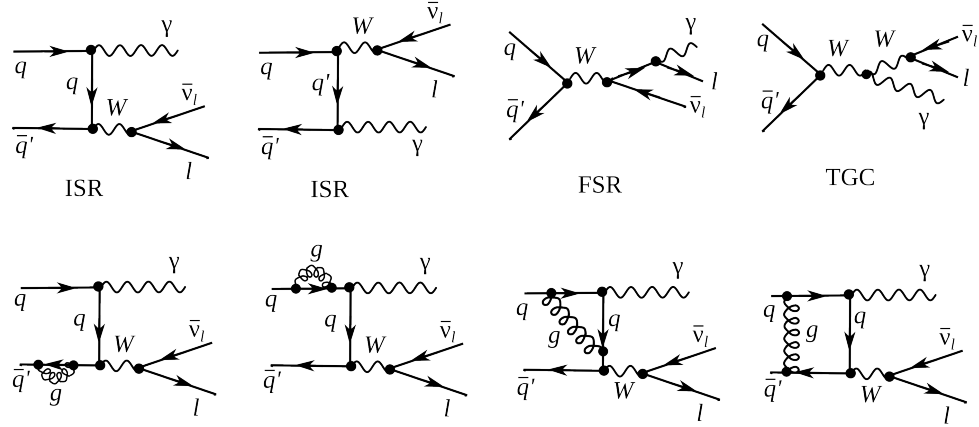


Figure 2.2: Feynman diagrams of  $W\gamma$  production. Top: LO diagrams, bottom: several examples of NLO in QCD.

a quantum field theory equations of motion cannot be solved exactly and, therefore, the perturbative approach is used if a coupling constants is  $g \ll 1$ .

To represent the process graphically Feynman diagrams were invented. Also the diagrams can be used to calculate the process amplitude  $M$  in Eq. 2.28 because they are determined by Lagrangian terms relevant to the process. There are an infinite number of Feynman diagrams corresponding to any specific process and the total amplitude of the process is a sum of individual amplitudes of each diagram and it is not technically possible to take into account all of them. Each vertex introduces a factor in the amplitude of the process that is proportional to the coupling constant. If the coupling constant is  $g \ll 1$ , the perturbative approach arranges all the diagrams by orders of contribution, and, therefore, the Feynman diagrams with fewer vertices would give a significantly larger contribution to the amplitude. In Fig. 2.2 examples of the Leading Order (LO) and the Next-to-Leading Order (NLO) Feynman diagrams are shown (top and bottom diagrams respectively).

At LO, the  $W\gamma$  process is represented by four Feynman diagrams including one FSR, one TGC and two ISR diagrams. Each LO diagram has three vertices. The first calculation of the  $W\gamma$  process with necessary expressions can be found in [59].

The NLO corrections to the amplitude of the  $W\gamma$  process that are shown in Fig. 2.2 are QCD corrections only, which include gluon loops at the same quark line and exchange of a gluon between two different quark lines, however, QED and weak NLO diagrams are also possible. QED corrections involve radiations of extra photons by charged particles, exchange of photons between different charged particles or a photon can be radiated and absorbed by the same charged particle forming a loop. Similarly, weak corrections involve extra virtual  $W$  or  $Z$  bosons. The QCD corrections are the largest among the discussed correction types because the QCD coupling constant is the largest.

A theoretical cross section in particle physics is compared to a measurement result to test the predictions of the model. Also the theoretical cross section is used for producing simulated data. In a simulation, a large set of  $pp$  collisions resulting in a physics process of interest is modeled to create a data set that mimics real data. A typical simulation consists of two parts: the generation of the process and the simulation of particles paths through the detector. The first stage contains a collection of events with final state particles with kinematic quantities distributed according to theoretical predictions for a given process. This stage relies on the theory including the cross section and also all dynamics of the process. The second stage simulates the interaction with media during propagation of particles through the model of the detector as well as the response of detector electronics. In its final form, a simulated dataset has the same format and content of detector signals for each event as real data, and can undergo the same reconstruction and analysis

procedure as real data would.

The most precise theoretical  $W\gamma$  cross section available is the Next-to-Next-to-Leading Order (NNLO) cross section in QCD [61]. The effects of the NNLO correction over the NLO correction and over the LO result are shown in Fig. 2.3 for the transverse mass of the final state particles  $m_T^{l\nu\gamma}$  and for the rapidity difference between a charged lepton and a photon  $\Delta_{l\gamma}$ . The NNLO and NLO theoretical predictions for the photon transverse momentum  $p_T^\gamma$  are overlaid with the 7 TeV ATLAS result. The contribution from higher order corrections is estimated to be  $\pm 4\%$ . However, the NNLO theoretical result was published only recently, in 2015, and no NNLO  $W\gamma$  simulation is available at this time. The simulation used in this analysis is LO + up to two hadronic jets simulation which was found to give the same predictions as the NLO result.

Certain BSM theories predict an enhancement of the contribution from the TGC diagram over the SM prediction. The discussion of these BSM effects and how they affect the  $W\gamma$  process takes place in Ch. 2.4.

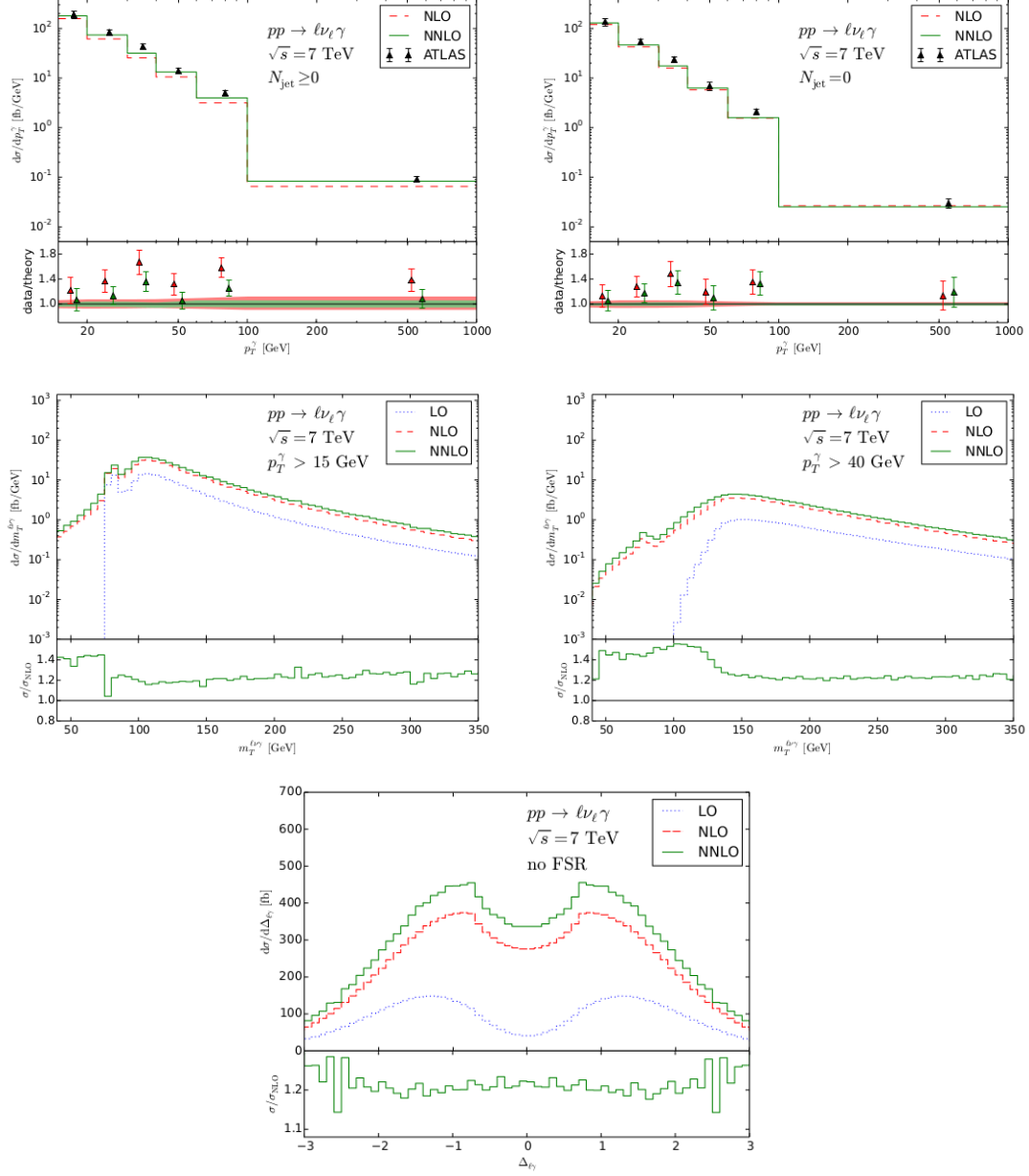


Figure 2.3: Theory spectra. Top: NLO and NNLO  $p_T^\gamma$  spectra of  $W\gamma \rightarrow l\nu\gamma$  at  $\sqrt{s} = 7$  TeV overlaid with ATLAS data for  $N_{jet} \geq 0$  (left) and  $N_{jet} = 0$  (right). Middle: LO, NLO and NNLO  $m_T^{l\nu\gamma}$  spectra of  $W\gamma \rightarrow l\nu\gamma$  at  $\sqrt{s} = 7$  TeV for  $P_T^\gamma > 15$  GeV (left) and  $P_T^\gamma > 40$  GeV (right). Bottom: LO, NLO and NNLO  $\Delta_{l\gamma}$  spectra of  $W\gamma \rightarrow l\nu\gamma$  at  $\sqrt{s} = 7$  TeV.

## 2.4 Anomalous $W\gamma$ Production

Most BSM physics theories predict the existence of particles with masses lying beyond the discovered energy range. If their masses are not accessible even at the accelerators with the highest energies, the direct detection of such particles is not possible. However, loops of heavy particles can affect diagrams of productions of lighter particles. They would give additional contributions to TGC and QGC couplings and, therefore, to the amplitudes to the processes involving TGC and QGC productions. There would be a different number of events produced in the process than one would expect based on SM predictions as shown in Fig. 2.5.

TGC and QGC couplings can be probed by precision measurements of SM processes of diboson and triboson productions because these processes can occur through TGC and QGC. TGC and QGC are represented by vertices with three and four bosons (Fig. 2.4). As discussed in Ch. 2.1, charged TGC and QGC are possible at tree level in the SM while neutral TGC and QGC are not.

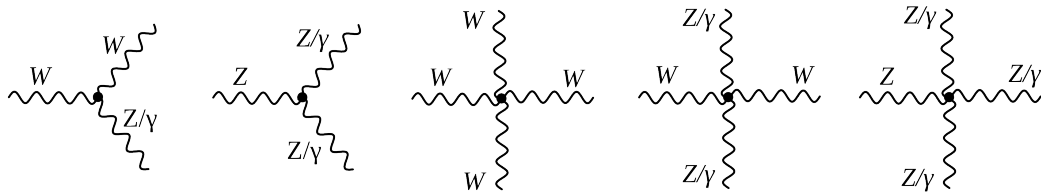


Figure 2.4: Charged TGC (first), neutral TGC (second), charged QGC (third and fourth), and neutral QGC (fifth) vertices.

To account for the effects from the potential loops of heavy particles, we introduce an effective Lagrangian with arbitrary values of coupling constants which can be reduced to the SM Lagrangian if these constants would have their SM values. Introducing the effective Lagrangian makes searches model-independent

because we do not specify particles that form the loops but instead just check whether there is a deviation from the SM prediction in measured observables.

In  $W\gamma$  measurement we can probe  $WW\gamma$  vertex. The most general Lorentz invariant Lagrangian terms of  $WW\gamma$  interaction takes the following form [58]:

$$iL_{eff}^{WW\gamma} = iL_{eff(1)}^{WW\gamma} + iL_{eff(2)}^{WW\gamma} + iL_{eff(3)}^{WW\gamma}, \quad (2.30)$$

where

$$iL_{eff(1)}^{WW\gamma} = e[g_1^\gamma A^\mu (W_{\mu\nu}^- W^{+\nu} - W_{\mu\nu}^+ W^{-\nu}) + \kappa_\gamma W_\mu^+ W_\nu^- A^{\mu\nu} + \frac{\lambda_\gamma}{m_W^2} A^{\mu\nu} W_\nu^{+\rho} W_{\rho\mu}^-], \quad (2.31)$$

$$iL_{eff(2)}^{WW\gamma} = e[ig_5^\gamma \epsilon_{\mu\nu\rho\sigma}((\partial^\rho W^{-\mu}) W^{+\nu} - W^{-\mu} (\partial^\rho W^{+\nu})) A^\sigma + ig_4^\gamma W_\mu^- W_\nu^+ (\partial^\mu A^\nu + \partial^\nu A^\mu)], \quad (2.32)$$

$$iL_{eff(3)}^{WW\gamma} = e[\frac{\tilde{\kappa}_\gamma}{2} W_\mu^- W_\nu^+ \epsilon^{\mu\nu\rho\sigma} A_{\rho\sigma} - \frac{\tilde{\lambda}_\gamma}{2m_W^2} W_{\rho\mu}^- W_\nu^{+\mu} \epsilon^{\nu\rho\alpha\beta} A_{\alpha\beta}], \quad (2.33)$$

where  $e$  is the absolute value of the electron charge,  $A^\mu$  is the photon field,  $W^{\pm\mu}$  are the fields of the  $W^\pm$  bosons,  $W_{\mu\nu} = \partial_\mu W_\nu - \partial_\nu W_\mu$ ,  $A_{\mu\nu} = \partial_\mu A_\nu - \partial_\nu A_\mu$ ,  $m_W$  is the mass of the  $W$  boson,  $g_1^\gamma$ ,  $\kappa_\gamma$ ,  $\lambda_\gamma$ ,  $g_5^\gamma$ ,  $g_4^\gamma$ ,  $\tilde{\kappa}_\gamma$ , and  $\tilde{\lambda}_\gamma$  are constants.

Despite seven constants in the extended Lagrangian, only  $\lambda_\gamma$  and  $\kappa_\gamma$  are considered in the aTGC searches. The rest of the constants are fixed to their SM values based on the following considerations. The constants  $g_1^\gamma = 1$  and  $g_5^\gamma = 0$  are fixed to make the Lagrangian obey the electromagnetic gauge invariance for the on-shell photons. The non-zero value of  $g_4^\gamma$  also violates C and P conserva-

tions, and non-zero values of  $g_4^\gamma$ ,  $\kappa_\gamma$ ,  $\tilde{\lambda}_\gamma$  violate the CP conservation law. Such violation parametrizations are not considered in charged TGC measurements, thus, constants  $g_4^\gamma$ ,  $\kappa_\gamma$ , and  $\tilde{\lambda}_\gamma$  are fixed to zero.

The SM values of  $\lambda_\gamma$  and  $\kappa_\gamma$  are  $\lambda_\gamma = 0$  and  $\kappa_\gamma = 1$ . For convenience, the deviation from the SM value is introduced  $\Delta\kappa_\gamma \equiv \kappa_\gamma - 1$ . These two parameters are tested in  $WW\gamma$  aTGC searches because non-zero values of these parameters would not violate any fundamental law.

The most significant effects of aTGC would appear at high energy scales. Figure 2.5 shows this effect in  $P_T^\gamma$  spectrum of 7 TeV  $W\gamma \rightarrow \mu\nu\gamma$  measurement. As seen in Fig. 2.5, the spectrum with non-zero values of aTGC constants at low  $P_T^\gamma$  coincides with the SM prediction but for higher  $P_T^\gamma$  the disagreement appears.

A common approach to aTGC searches is to measure the spectrum of a kinematic parameter highly correlated with the energy of a final state particle or a system of final state particles. For  $W\gamma$  process, the most sensitive variable is  $P_T^\gamma$ . Examining this spectrum allows us to probe and constrain aTGC coupling constants. Chapter 2.5 reviews the experimental results to date on constraining aTGC coupling constants of the  $WW\gamma$  vertex.

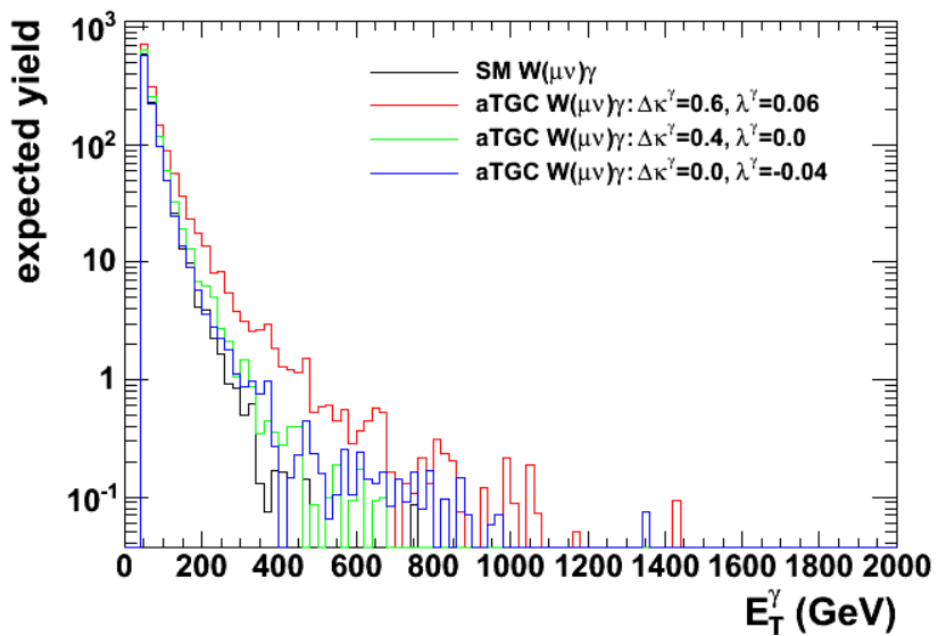


Figure 2.5: Distributions of  $P_T^\gamma$  in simulated  $W\gamma \rightarrow \mu\nu\gamma$  events with different values of aTGC constants at LHC energy of  $\sqrt{s} = 7$  TeV. Source of figure: [56].

## 2.5 A brief history of $W\gamma$ measurements

aTGC parameters of the  $WW\gamma$  vertex can be probed in measurements of  $W\gamma$ ,  $WW$ ,  $WZ$  processes. Limits on the  $\Delta\kappa_\gamma$  and  $\lambda_\gamma$  constants obtained by different experiments are summarized in Fig. 2.6. The summary includes the combination results from Do [20] and LEP [32] as well as results of several individual measurements by ATLAS and CMS including  $W\gamma$  at  $\sqrt{s} = 7$  TeV [47], [48],  $WW$  at  $\sqrt{s} = 7$  and 8 TeV [49], [11], [12], and  $WV$  at  $\sqrt{s} = 7$  and 8 TeV [4], [10] measurements.

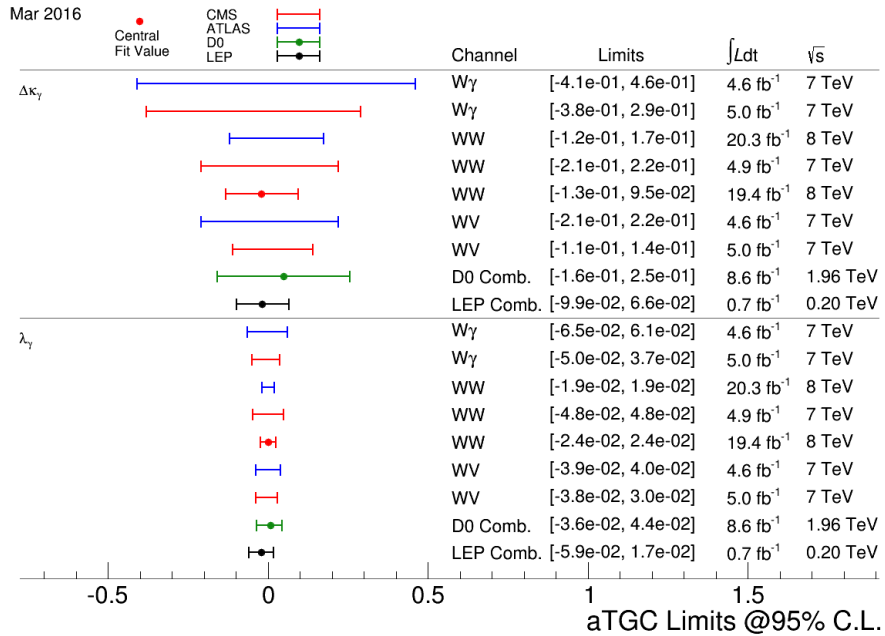


Figure 2.6: Summary of limits on the  $WW\gamma$  aTGC coupling constants. Figure from [62].

The most recent measurements of  $W\gamma$  production were performed by CMS [48] and ATLAS [47] collaborations with  $pp$  collisions at  $\sqrt{s} = 7$  GeV collected in 2011. Both collaborations considered two channels:  $W\gamma \rightarrow \mu\nu\gamma$  and  $W\gamma \rightarrow e\nu\gamma$ .

Diboson processes are rare in  $pp$ -collisions and analysts have to filter out events of their interest from many processes which are more likely to happen. To do

that, a variety of selection criteria are applied which reject most of the background events to increase the signal fraction in the selected sample as much as possible. However, even after all possible selection criteria are applied, the majority of selected events are still background events and it is not possible to reduce the background any further without also significantly reducing signal.

The major source of such irreducible background is the fake photon background where hadronic jets are misidentified as photons. Such events originate mostly from  $W+jets$ , but  $Z+jets$  and  $t\bar{t}+jets$  events contribute to this source of background as well. In the electron channel there is one more significant background that is the fake photon background where electron is misidentified as a photon. Such events are coming from  $Z+jets$  events. For the muon channels this background is small. Other sources of backgrounds for both channels include real- $\gamma$ , fake lepton + real photon and fake lepton + fake photon backgrounds. The major source of real- $\gamma$  background is the  $Z\gamma$  process where a final state lepton and a photon mimics the  $W\gamma$  final state. Fake lepton + real photon background originates from the  $\gamma+jets$  process where a jet is misidentified as a lepton. Fake lepton + fake photon backgrounds come from dijet and multijet events where one of the jets is misidentified as a lepton and the other one is misidentified as a photon. The probability of a jet to be misidentified as a lepton is very small, therefore fake lepton + real photon and fake lepton + fake photon backgrounds are negligible.

$P_T^\gamma$  spectra are measured because this variable is the most sensitive to the potential aTGC. The  $P_T^\gamma$  spectra of the selected events in data superimposed with selected events in the simulation of the signal and estimated background contribution for the muon and electron channels are shown in Fig. 2.7 for CMS and in Fig. 2.8 for ATLAS measurement. Both measurements show a good agreement between data and the simulation.

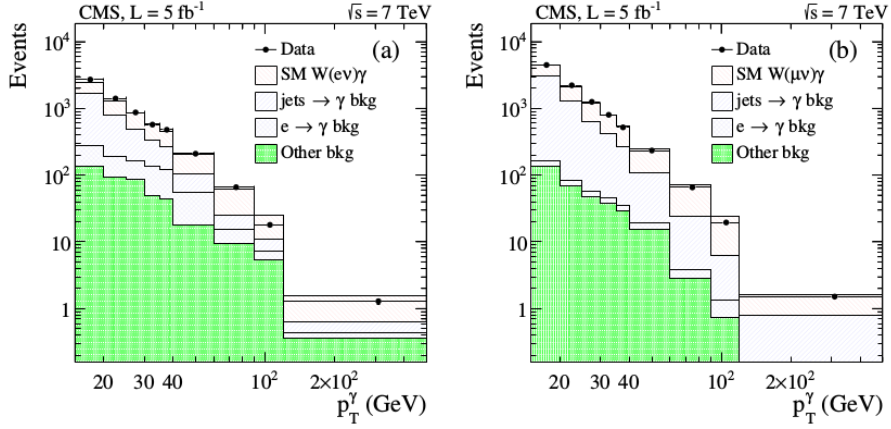


Figure 2.7: The distribution of the  $p_T^\gamma$  of  $W\gamma$  candidates in the analysis of 7 TeV CMS data. Data vs signal MC + background estimates. Left:  $W\gamma \rightarrow e\nu\gamma$ , right:  $W\gamma \rightarrow \mu\nu\gamma$  [48].

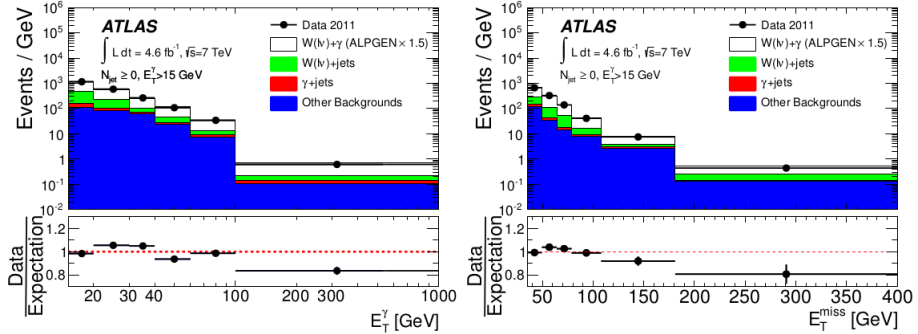


Figure 2.8: The distribution of the photon transverse momentum (left) and missing transverse momentum (right) of  $W\gamma$  candidates in the analysis of 7 TeV ATLAS data. Data vs signal MC + background estimates [47].

The phase space restrictions of  $W\gamma$  measurements come from the considerations of the detector acceptance, reducing heavily background-dominated regions and theoretical considerations such as to avoid divergence of the cross section and to reduce ISR and FSR contributions to the cross section.

CMS provides measurements of the  $P_T^\gamma$  spectrum, the total cross section within the phase spaces of  $\Delta R > 0.7$ ,  $P_T^\gamma > 15$  GeV,  $P_T^\gamma > 60$  GeV and  $P_T^\gamma > 90$  GeV.

ATLAS, in addition to the  $P_T^\gamma$  spectrum, total cross section and limits, provides the differential cross section and cross section with different number of associated jets. The phase space restrictions for ATLAS measurement include requirements on charged lepton kinematics  $P_T^l > 25$  GeV,  $|\eta_l| < 2.47$ , requirements on the transverse momentum of a neutrino  $P_T^\nu > 35$  GeV, photon kinematics  $P_T^\gamma > 15$  GeV,  $|\eta^\gamma| < 2.37$ , photon isolation fraction  $\epsilon_h^P < 0.5$  and lepton-photon separation  $\Delta R(l, \gamma) > 0.7$ . For the differential cross section in number of associated jets, the requirements on jets kinematics and jets separation from leptons and photons are also applied:  $E_T^{jet} > 30$  GeV,  $|\eta^{jet}| < 4.4$ ,  $\Delta R(e/\mu/\gamma, jet) > 0.3$ . No evidence of new physics is observed.

The estimated cross sections with any number of associated jets for  $P_T^\gamma > 15$  GeV are

$$\sigma(pp \rightarrow W\gamma \rightarrow l\nu\gamma) = 37.0 \pm 0.8 \text{ (stat.)} \pm 4.0 \text{ (syst.)} \pm 0.8 \text{ (lumi.) pb} \quad (2.34)$$

and

$$\sigma(pp \rightarrow W\gamma \rightarrow l\nu\gamma) = 2.77 \pm 0.03 \text{ (stat.)} \pm 0.33 \text{ (syst.)} \pm 0.14 \text{ (lumi.) pb} \quad (2.35)$$

for CMS and ATLAS respectively. The results agree with NLO MCFM [39] predictions of  $31.81 \pm 1.8$  pb for the phase space used by CMS and of  $1.96 \pm 0.17$  pb for the phase space used by ATLAS.

In addition to the cross sections, both CMS and ATLAS provide limits on aTGC coupling constants  $\Delta\kappa_\gamma$  and  $\lambda_\gamma$ . To do that, samples with non-zero aTGC coupling

constants are generated, run through the whole reconstruction and selection procedures, and compared to the measured results of  $P_T^\gamma$  spectra. The results on one-dimensional limits are quoted in Fig. 2.6 while the results on two-dimensional limits can be found in [47], [48].

In this dissertation we are measuring total and differential  $d\sigma/dP_T^\gamma$  cross section. While the aTGC limits are not derived in this dissertation, the measured differential cross section can be used to derive them. The measurement details and results are described in Chapter 5.

# Chapter 3

## Experimental Setup

The measurement of this dissertation is based on data collected by the Compact Muon Solenoid (CMS) detector from the Large Hadron Collider (LHC) proton-proton ( $pp$ ) collisions in 2012. Thus, the experimental setup for this measurement includes the LHC and the CMS detector that are described in Ch. 3.1 and Ch. 3.2 respectively.

### 3.1 Large Hadron Collider

The LHC [33], [35], [36] is the largest particle accelerator and the most ambitious particle physics research facility ever built. The LHC accelerates two particle beams up to near the speed of light. The beams travel in opposite directions, each in its own beam pipe, in ultrahigh vacuum. The beam is made up of discrete protons. The bunches are accelerated by varying electromagnetic fields, focused by superconducting quadrupole magnets and steered by dipole magnets. The bunches collide at fixed collision points where particle detectors are placed. Particles are produced in the collisions and registered by the detectors for various BSM searches as well as for precision SM measurements.

The LHC is located in the tunnel originally built for the LEP accelerator. The LEP was decommissioned to make room for the LHC. The tunnel is about 27 km in circumference, located at the Swiss-French boundary up to 100 meters underground.

Before entering LHC, particle beams go through several stages of acceleration, and the LHC is the final machine of the chain of the CERN's accelerator complex (Fig. 3.1). Protons are extracted from hydrogen atoms, are accelerated by Linac2 to energies of 5 MeV, and are then injected into the Proton Synchrotron Booster (PSB) where they reach energies of 1.4 GeV. After that, protons are sent to PS and Super PS (SPS) where they are accelerated up to 25 GeV and 450 GeV respectively. Finally, protons enter the LHC and are accelerated to reach their collision energies of several TeV per beam. Besides protons, the complex also accelerates and collides lead ions. However, in this dissertation we analyze data from  $pp$  collisions only.

Six detectors are installed at the LHC to detect products of hadron collisions and to perform the measurements of the LHC physics program. There are two

## CERN's Accelerator Complex

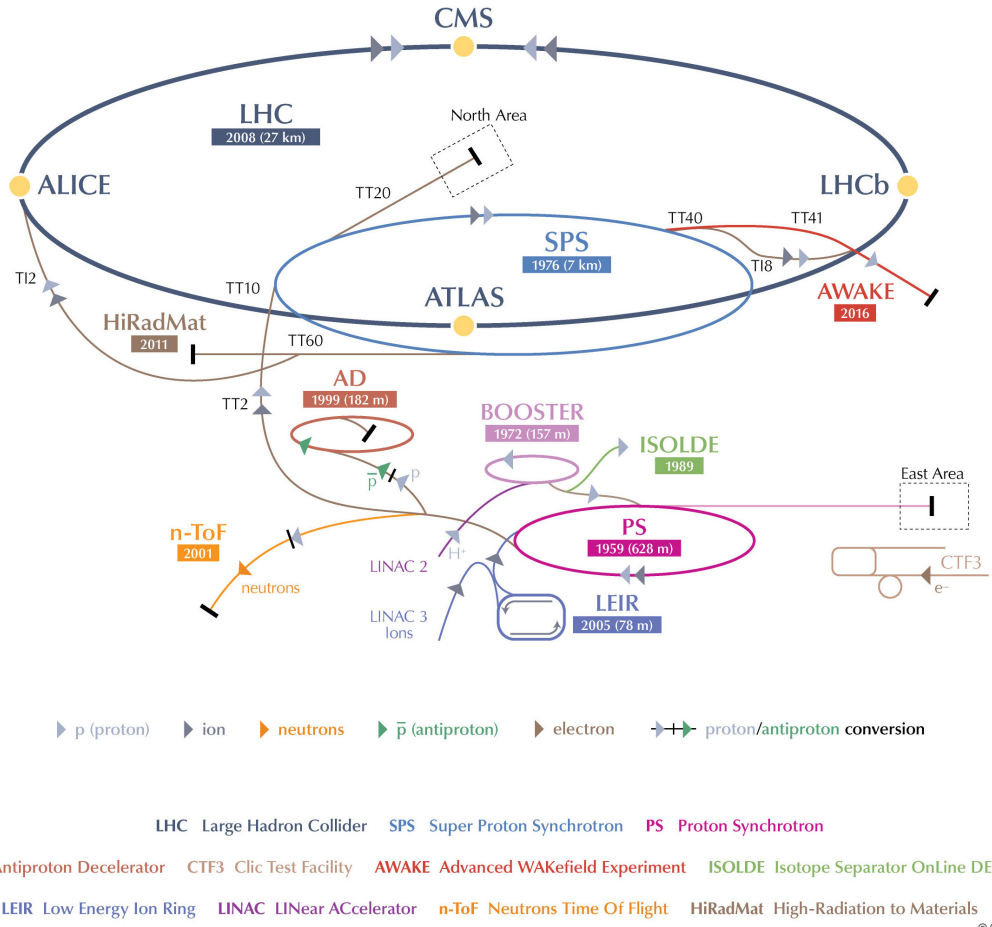


Figure 3.1: CERN's accelerator complex [22].

general purpose detectors: ATLAS and CMS. There is LHCb which specializes in the physics of B-mesons, and ALICE which is designed to detect products of heavy ion collisions. Also there are two relatively small detectors: LHCf and TOTEM which are installed close to the ATLAS and CMS collision points respectively.

The design energy of the LHC is  $\sqrt{s} = 14$  TeV which corresponds to 7 TeV per beam. However, it takes years to reach the design energy, and, meanwhile, several

lower energy points were probed. In 2010-2011 the LHC operated at an energy of 3.5 TeV per beam which was already higher than the energy of any other collider. In 2012 the energy increased up to 4 GeV. In 2013-2014 the LHC was shut down for upgrades. Collisions were restarted at 6.5 TeV in 2015 and continued at this energy in 2016.

All critical measurements performed at lower energies are also repeated at higher energies because the ability to probe higher energy scales increases our chances for a discovery. Precision SM measurements of cross section need to be done at all energies and compared to the theory since the cross sections evolve with energy. The cross sections of many interesting processes increase with energy because in a collision of higher energy hadrons more partons can participate in the interaction. This enabling the observation of rarer processes. Cross sections of various productions in  $pp$  collisions and their energy dependencies are shown in Fig. 3.2.

In addition to the beam energy, there are many other collider parameters. A brief summary of them is available in Tab. 3.1. One of the most critical parameters of an accelerator is the ability to produce a large number of interesting collisions which is determined by the luminosity (Ch. 2.2). The instantaneous luminosity is determined by the following expression [43]:

$$L = f \frac{n_1 n_2}{4\pi\sigma_x\sigma_y} \quad (3.1)$$

where  $n_1$  and  $n_2$  are numbers of particles in colliding bunches,  $f$  is a frequency of collisions,  $\sigma_x$  and  $\sigma_y$  characterize sizes of overlapping parts of colliding beams in horizontal and vertical directions. Instantaneous luminosity multiplied by a cross section of a process gives an event rate (Eq. 2.26). To determine the integrated

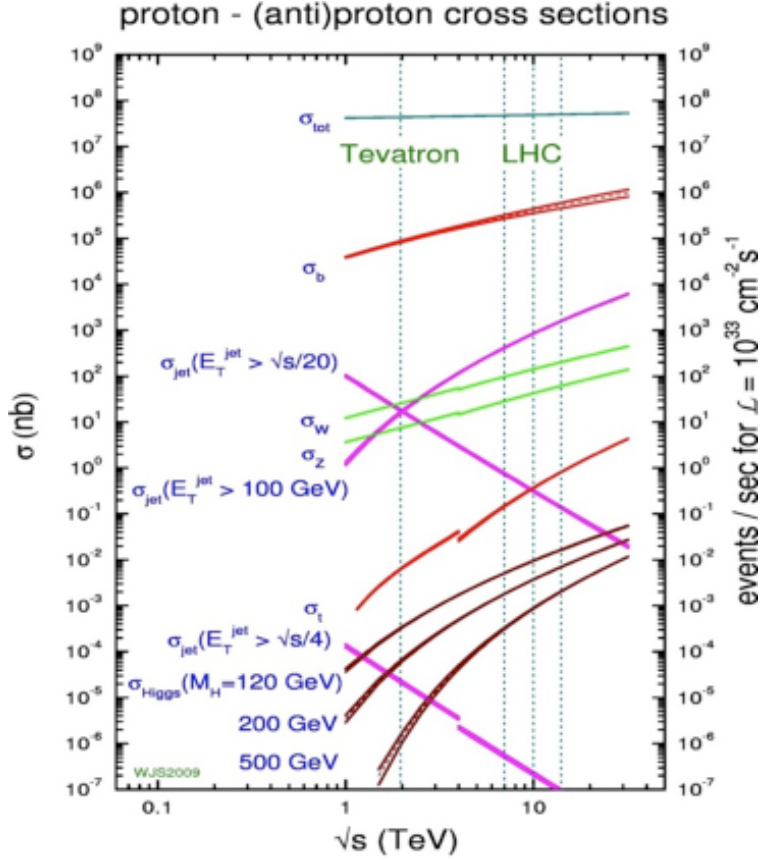


Figure 3.2: Cross sections of various productions in  $pp$  collisions [51].

luminosity, one has to integrate the instantaneous luminosity over time:

$$L_{int} = \int L dt \quad (3.2)$$

With the integrated luminosity, one can compute the total number of events of interest over the full period of data taking. Thus the integrated luminosity of a data sample is a measure of the size of the data sample.

The LHC's luminosity is higher than that of any previous collider. The integrated luminosity of the LHC for  $pp$  collisions for different years of the operation is shown in Fig. 3.3. Run I of the LHC operation covers run periods of 2010-2012. While running at the energy of  $\sqrt{s} = 7$  TeV, LHC delivered  $45 \text{ pb}^{-1}$  and  $6.1 \text{ fb}^{-1}$

of data in 2010 and 2011 year respectively. In 2012 the working energy of LHC was  $\sqrt{s} = 8$  TeV, and the integrated luminosity was  $L_{int} = 23.3 \text{ fb}^{-1}$ . After a long shutdown, LHC was upgraded for Run II, to operate on  $\sqrt{s} = 13$  TeV in 2015 and delivered  $4.2 \text{ fb}^{-1}$  of data by the end of 2015. In 2016 LHC continued operating at  $\sqrt{s} = 13$  TeV and delivered the integrated luminosity of  $41.1 \text{ fb}^{-1}$  [34].

The measurement of this dissertation is performed at the energy of 4 TeV per beam or the center of mass energy  $\sqrt{s} = 8$  TeV with  $19.6 \text{ fb}^{-1}$  of data. The same process was measured at  $\sqrt{s} = 7$  TeV with about four times less data by both CMS and ATLAS. These measurements are discussed in greater detail in Ch. 2.5.

Table 3.1: Main parameters of LHC [33]

Circumference	27 km
Dipole operating temperature	1.9 K
Number of magnets	9593
Number of main dipoles	1232
Number of main quadrupoles	392
Number of RF cavities	8 per beam
Nominal energy, protons	7 TeV
Nominal energy, lead ions	2.76 TeV per nucleon
Peak magnetic dipole field	8.33 T
Min. distance between bunches	7 m
Design luminosity	$10^{34} \text{ cm}^{-2} \text{ s}^{-1}$
No. of bunches per proton beam	2808
No. of protons per bunch (at start)	$1.1 \times 10^{11}$
No. of collisions per second	600 millions



Figure 3.3: LHC integrated luminosity by year [23].

## 3.2 Compact Muon Solenoid

### 3.2.1 Introduction

CMS is a general-purpose detector designed for detecting various highly energetic particles which are produced in  $pp$  collisions at the LHC [5]. CMS has a broad program with goals of direct and indirect searches of BSM physics including supersymmetric particles as well as precision measurements of various SM parameters.

The CMS detector is cylindrically symmetric with the particle beam as the central axis. Cartesian, cylindrical and spherical coordinates are all used to describe the CMS geometry, depending on the context. The  $x$ -axis of the CMS points towards the center of the LHC while the  $y$ -axis points vertically up. The orientation of the  $z$ -axis corresponds to the counterclockwise direction of the LHC beam (Fig. 3.4). Cylindrical coordinates are defined as  $r = \sqrt{x^2 + y^2}$ ,  $\phi = \arctan(y/x)$ . Instead of the polar angle  $\theta$ , it is more convenient to use the pseudorapidity  $\eta = -\ln \tan \theta/2$ . A pseudorapidity ranges from  $\eta = -\infty$  to  $\eta = +\infty$  for directions parallel to the beam axis with the value of  $\eta = 0$  for a direction perpendicular to the beamline. This variable is convenient for measurements because a distribution of a massless particle in  $\eta$  is nearly flat. The acceptance of the CMS in  $\eta$  is limited and varies from  $|\eta| < 2.4$  to  $|\eta| < 5.3$  depending on a subdetector (Fig. 3.5, top).

The detector consists, from inner to the outer layer, of a tracking system, an electromagnetic calorimeter (ECal), a hadronic calorimeter (HCal), a magnet and a muon system. Having the tracking system, ECal and HCal inside of a large solenoid makes the detector compact. A slice of CMS in the  $r - \phi$  plane is shown in Fig. 3.6.

When a heavy particle is produced in a collision, it decays immediately, and

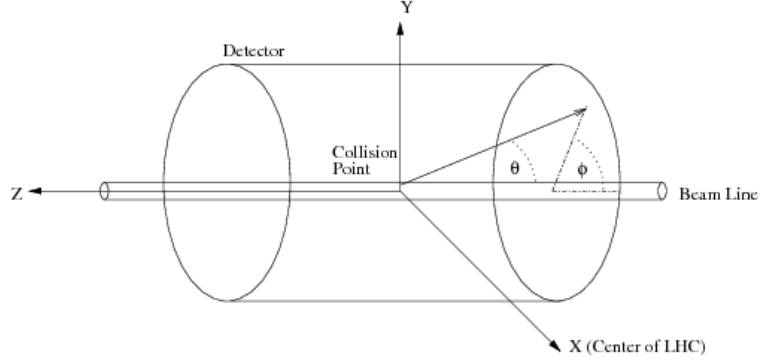


Figure 3.4: CMS coordinate system.

we detect its long-living decay products including electrons, photons, muons, neutral or charged hadrons. Depending on the trace left by the particle in different subdetectors we can identify the particle. Electrons and positrons leave curved tracks, trajectories of charged particles, in the tracking system and then induce showers in the electromagnetic calorimeter (ECal). Photons induce the same electromagnetic showers in the ECal, however, as neutral particles, they do not leave tracks in the tracking system. Hadrons normally travel through the ECal undisturbed and induce a hadronic shower in the hadronic calorimeter (HCal). Charged and neutral hadrons can be distinguished from each other by checking whether they leave a track in the tracking system or not. Muons are the only particles which penetrate through the ECal, the HCal and the magnet and leave tracks in the CMS muon system. Neutrinos are not directly detected by CMS.

All subdetectors are essential for the  $W\gamma$  measurement, and the remainder of this chapter describes the subdetectors in greater details. Muons and electrons which we have as final state particles are both affected by the CMS magnetic field, allowing the tracking system and the muon system to measure their trajectory parameters and momenta. In this dissertation we use the information of the

primary vertex, the collision point, determined by the tracking system, to select our events. The tracking system also provides us information about electron trajectories and momenta in the electron channel and distinguishes between electrons and photons. The ECal is necessary to identify electrons and photons and to measure all kinematic parameters of photons. The HCal is also used for electron and photon identification: the energy deposit in the HCal left by an electron or a photon must be very small compared to the energy deposit left in the ECal. The muon system is essential for muon reconstruction and identification.

### 3.2.2 Magnet

A magnetic field in a particle detector is necessary to measure momenta of charged particles by track curvatures. The higher the momentum is, the less a particle trajectory is affected by the magnetic field. In CMS, the tracking system measures momenta of all charged particles. Also, the muon system measures momenta of muons.

The CMS magnet is placed between the HCal and the muon system. The magnet is made of superconducting wires. An electric current flowing in the wires creates a uniform field of  $B = 4\text{T}$  inside the solenoid, for the tracking system, and also provides a smaller magnetic field of a certain configuration outside the solenoid, for the muon system. The stronger field in the tracking system is necessary because of higher track density and smaller size relative to the muon system.

### 3.2.3 Tracking System

The tracking system measures track geometry including particle trajectories, locations of primary and secondary vertices, and momenta of charged particles. It needs to disturb particles as little as possible so that they can pass through. Therefore, just a few measurements must be enough to reconstruct the track. The accuracy of a measurement of each hit, position measurement, is  $10 \mu\text{m}$ .

The tracking system consists of silicon pixels and silicon strips (Fig. 3.7). Tracks that originate from proton collisions, collision tracks, start at the center and then cross the layers of the tracking system. Tracks are straight in the  $r - z$  plane and curved by the magnetic field in the  $r - \phi$  plane. The acceptance of the tracker system in the  $r - z$  plane is geometrically limited by the absolute value of the pseudorapidity  $|\eta| \leq 2.5$ .

The pixel tracker is the closest subsystem of CMS to the collision point. Thus it experiences the largest particle flux: at 8 cm from the collision point the flux is about  $10 \text{ million}/(\text{cm}^2\text{s})$ , and the pixel detector with its 65 millions sensors is capable of reconstructing all these tracks. It consists of three layers of cylinders in the barrel with radii of 4 cm, 7 cm and 11 cm which are referred as barrel pixel subdetectors (BPIX) and four disks in the endcap, two disks at each side, which are referred as forward pixel subdetector (FPIX).

The strip tracker is placed right outside the pixel tracker and occupies the detector volume up to 130 cm around the beam axis. The strip tracker consists of four parts: the tracker inner barrel (TIB), the tracker inner disks (TID), the tracker outer barrel (TOB) and the tracker endcap (TEC) as shown in Fig. 3.7. In the strip tracker, there are over 15,000 sensitive modules with a total number of 10 million strips. Each sensitive module consists of a set of sensors, its support structure, and

readout elements.

### 3.2.4 Electromagnetic Calorimeter

The ECal is a layer between the tracking system and the HCal. It is made of high-density lead tungstate crystals arranged in a barrel section and two endcap sections. The crystals work as scintillators. When electrons and photons pass through it, scintillators produce light proportional to the particle's energy. The scintillated light then is amplified by photomultipliers. After that, signals are digitized and taken away by fiber optic cables.

The ECal measures the energy of electrons and photons and parameters of their trajectories. In order to distinguish between electrons and photons, it is necessary to perform matching to the track in the tracking system. If there is a track, then the particle is an electron (or positron), otherwise the particle is a photon.

It is important for the ECal to be able to distinguish between high energetic photons and pairs of lower energetic photons e.g. from a  $\pi^0$  decay. It is especially difficult in the endcap sections where the angle between two photon trajectories is small. For this reason, ECal preshower (PS) which have 15 times smaller granularity are located in front of the endcaps. The preshower provide extra spatial precision.

### 3.2.5 Hadron Calorimeter

The HCal measures the energy of charged and neutral hadrons. Also, it plays a key role in the indirect detection of invisible particles like neutrinos.

Invisible particles leave no record in CMS detector. They are detected by

missing transverse energy ( $E_T^{miss}$ ) that is determined as

$$E_T^{miss} = -|\sum \mathbf{P}_T|, \quad (3.3)$$

where the summation covers all visible particles in the event. Therefore, for precise measurement of  $E_T^{miss}$  it is important to capture the full energy release of all visible particles. For this purpose, HCal is designed to stop all hadrons passing through.

The HCal consists of the barrel, endcap and forward parts: HB, HE and HF in Fig. 3.5, top, respectively. Its acceptance extends to  $|\eta| = 3.0$  for endcaps and to  $|\eta| = 5.3$  for forward HCal.

The HCal is a sampling calorimeter. It consists of alternating layers of absorbers and scintillators. When a hadron hits an absorber, it induces a hadronic shower. The light produced by the shower is collected on optic fibers and passed to the readout system. The total amount of light released in a certain region of the HCal is a measure of hadron's energy. In addition to the energy, the HCal also reconstructs the trajectory of the hadron.

### 3.2.6 Muon System

Muons, unlike other visible particles, are not stopped by CMS calorimeters. Muons are the only particles that are registered in the muon system which is placed outside the magnet and which is the largest part of the CMS detector.

There are four concentric layers of muon detectors (stations) and iron return yoke between them. Muons induce several hits in the muon stations which are later fitted and matched to the tracking system measurements to provide the best possible resolution in the measurements of the muon's trajectory and momentum.

There are three types of muon chambers used in the CMS muon system: drift

tubes (DTs), cathode strip chambers (CSCs) and resistive plate chambers (RPCs) (Fig. 3.8). Overall, there are 1400 muon chambers including 250 DTs, 540 CSCs and 610 RPCs.

The system of DTs measures positions of muons in the barrel. Each DT chamber is about 2 m by 2.5 m in size. A chamber consists of 12 layers of aluminum which are arranged in groups of four. There are up to 60 DTs in a layer. The middle group of layers measures z-coordinate and two other groups determine the perpendicular coordinate. The DT's volume is filled with a gas, and there is a wire inside. The DT's width is 4 cm. When a charged particle passes through the volume, it ionizes atoms, and the wire receives an electric charge. The position along the wire is registered, and the distance of the muon away from the wire is calculated providing measurements of two coordinates of the position of the muon.

CSCs are placed in the endcap regions. CSCs are arrays of anode wires crossed by copper cathode strips placed in a gas volume. When a charged particle penetrates the gas volume, it ionizes the gas. Electrons drift to the wires while ions move to the strips, and charge pulses are induced on wires as well as on strips. Strips are perpendicular to wires. Thus we measure two coordinates for each particle.

RPCs are parallel capacitors made of high-resistivity plastic plates with a space between them filled with gas. RPCs provide quick measurements of muon momenta and are used for triggering. A muon passing through the RPC ionizes gas atoms. Released electrons ionize more atoms inducing an avalanche. Electrodes receive signal and pass it to external strips that provide a quick measure of the muon's momentum.

### 3.2.7 Triggering and Data Aquisition

At peak luminosity, CMS experiences forty million proton-proton collisions per second that come in bunches separated by 25 ns. It is not technically feasible to readout all these events. Moreover, we do not need most of these events for a physics measurement because most of them have not resulted from interesting physics process. We have resources to store about one hundred events out of forty million, and that is why we need a trigger system that quickly decides what the best one hundred events are.

If the triggers were too loose, and we would select one hundred events too quickly, e.g., in 1/10 s, then CMS would not be able to process the remaining 90% of events provided by LHC in a given second and we would lose 90% of potentially interesting events.

If the triggers were too strict, we would select, e.g., ten events per second, not one hundred and lose CMS's potential to store and process data by 90% which would significantly reduce our chances for discovery and increase statistical uncertainties for precision measurements.

Thus, the challenge of the trigger system is to select the best one hundred events per second and do so quickly to be able to process every single event. To achieve this goal, a two-level trigger system was developed consisting of the Level 1 trigger (L1T) and the High Level Trigger (HLT) as shown in Fig. 3.9.

L1T is a hardware based trigger (Fig. 3.10). It uses information from the ECal, HCal and muon system. L1T reduces the frequency of coming events from 40 MHz to 100 kHz. Events that did not pass the L1T are lost forever while events that pass the L1T are temporarily stored to get checked by the HLT.

HLT is a software-based trigger. It uses information from all subdetectors

and runs quick reconstruction and identification algorithms to determine types of particles and their kinematics. It reduces the number of events to 100 Hz. Events that did not pass HLT are lost forever. Events that pass HLT are arranged into appropriate datasets depending on HLT selection criteria they passed and stored for physics measurements.

### 3.2.8 Particle Flow Algorithm of Event Reconstruction

A particle flow algorithm is used by CMS to identify and reconstruct stable particles [44]. It processes the information from all CMS subdetectors and identifies and reconstructs each stable particle in an event individually. The list of particles include muons, electrons, photons, charged and neutral hadrons. Each type of particles leaves its specific trace in the CMS detector as shown in Fig. 3.6. After reconstruction of individual stable particles, jets are built, missing transverse energy  $E_T^{miss}$  is determined, certain short-lived particles are reconstructed based on the list of individual stable particles in the event.

One particle can induce several different particle-flow elements in different subdetectors. The linking algorithm links these elements together producing blocks of elements. Usually, a block has between one and three elements. Links can be connections between the tracking system and PS, ECal or HCal, between PS and ECal, between ECal and HCal, and between a tracking system and a muon system.

In each block, muons are considered first. A link between charged tracks in the tracking and muon systems comprise a global muon which produces one “particle-flow muon”. The corresponding track in the tracking system is removed from the block and corresponding energy deposits are subtracted from ECal and HCal. Then electrons are reconstructed and identified using the tracking system

and ECal. The corresponding tracks and ECal clusters are removed from the block. Remaining tracks and clusters are considered more carefully to identify charged hadrons, neutral hadrons, and photons.

When all particles in the event are reconstructed and identified,  $E_T^{miss}$  is determined.  $E_T^{miss}$  is used in physics measurements as a measure of  $P_T$  of neutrinos and other invisible particles in the event. Fake  $E_T^{miss}$  can originate from particles that did not fall into the detector acceptance, particles that they did not reach the tracking system because their momenta was too low and, therefore, track curvature was too high, momenta mismeasurement, particle misidentification, cosmic rays particles, and machine background.

In the measurement of this dissertation particle flow muons, electrons, photons, and  $E_T^{miss}$  are used for all the major steps of the cross section measurement including event selection, background subtraction, various corrections, and determination of phase space restrictions and bin boundaries. Each step is described in greater details in Ch. 5.

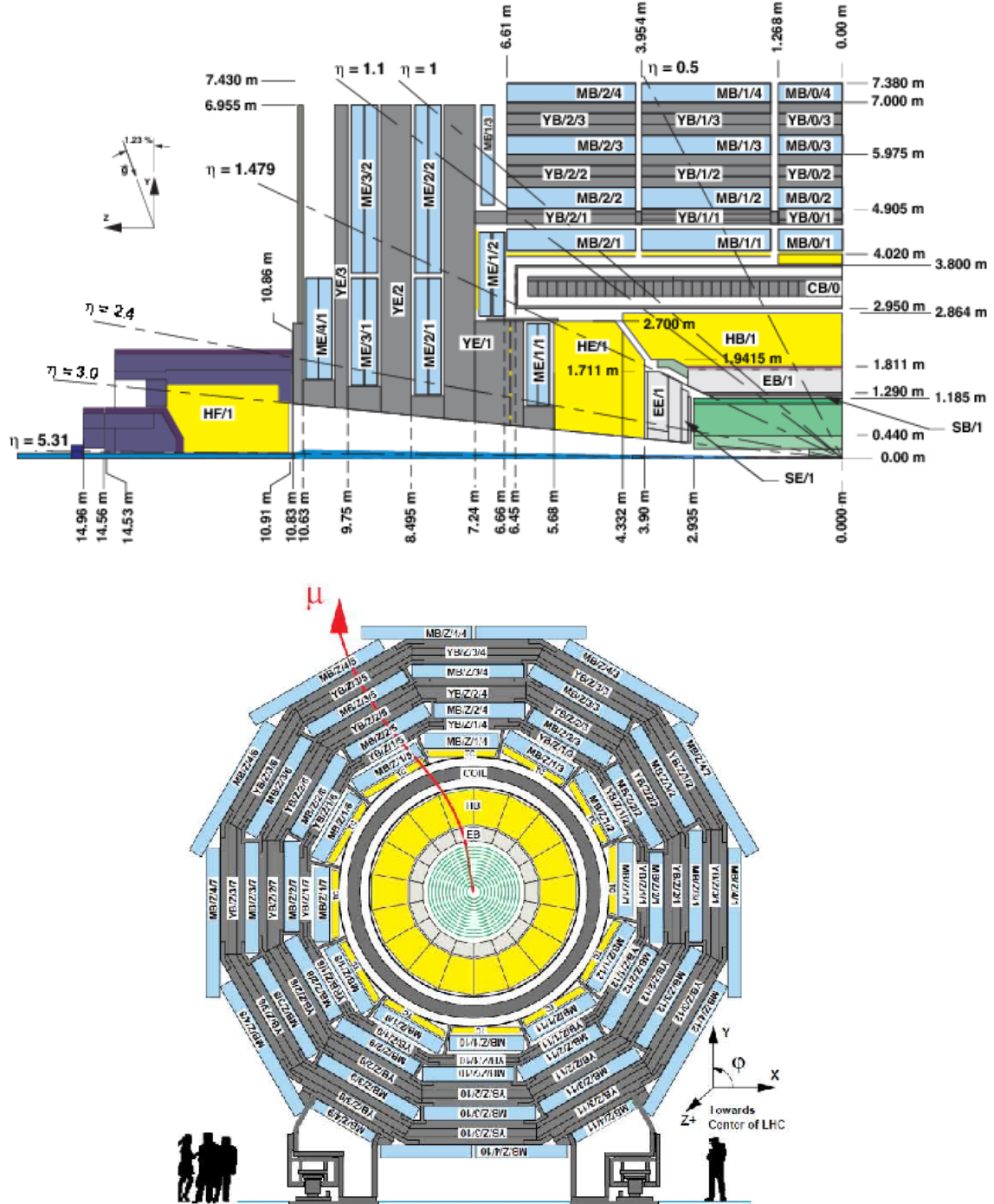


Figure 3.5: CMS detector, schematic view. Top:  $r-z$  plane, bottom:  $r-\phi$  plane at  $z=0$  [8].

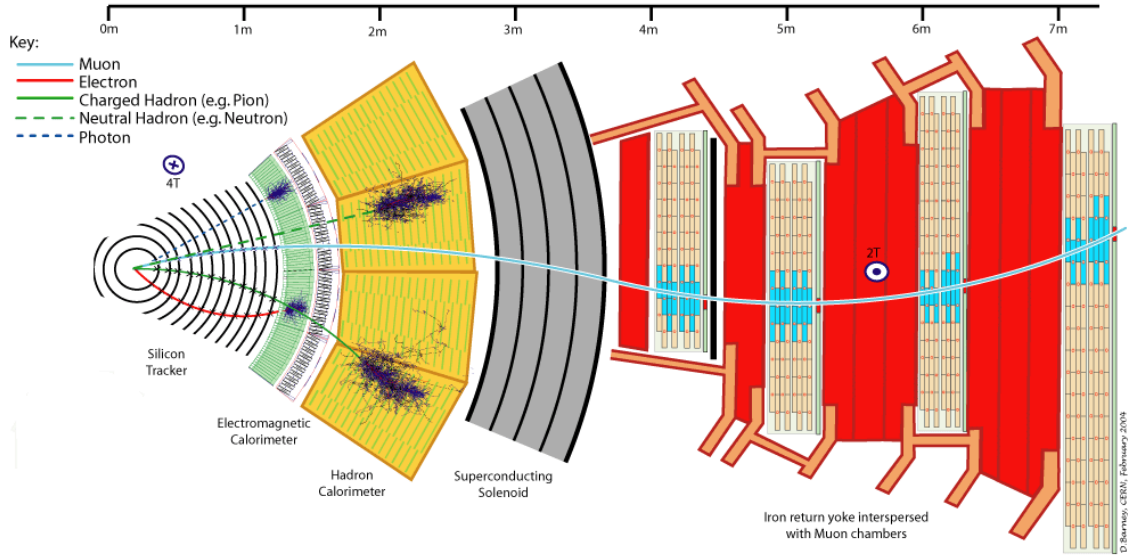


Figure 3.6: CMS detector, a schematic view of a segment in the  $r - \phi$  plane at  $z = 0$ . Traces left by muons, electrons, photons, charged and neutral hadrons in different subdetectors are shown.

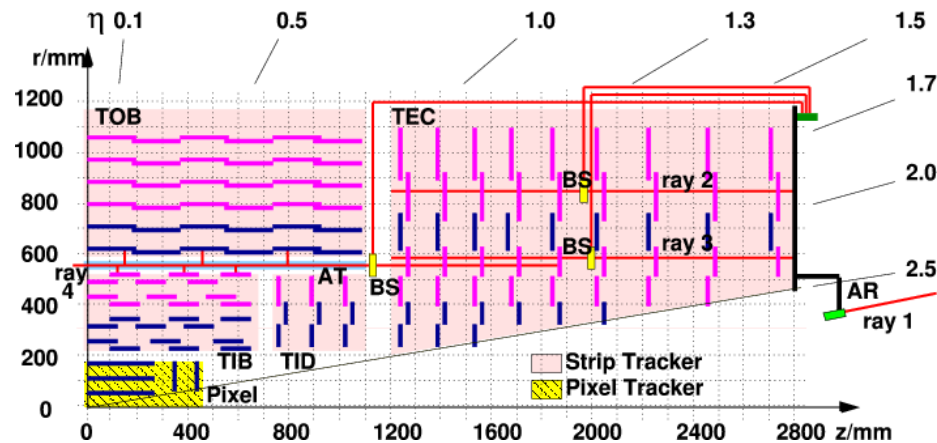


Figure 3.7: Slice of the CMS tracking system in the  $r - z$  plane.

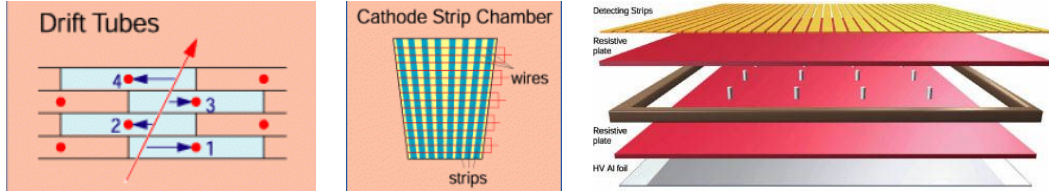


Figure 3.8: Components of the CMS muon system. Left to right: drift tubes (DTs), cathode strip chambers (CSCs), resistive plate chambers (RPCs).

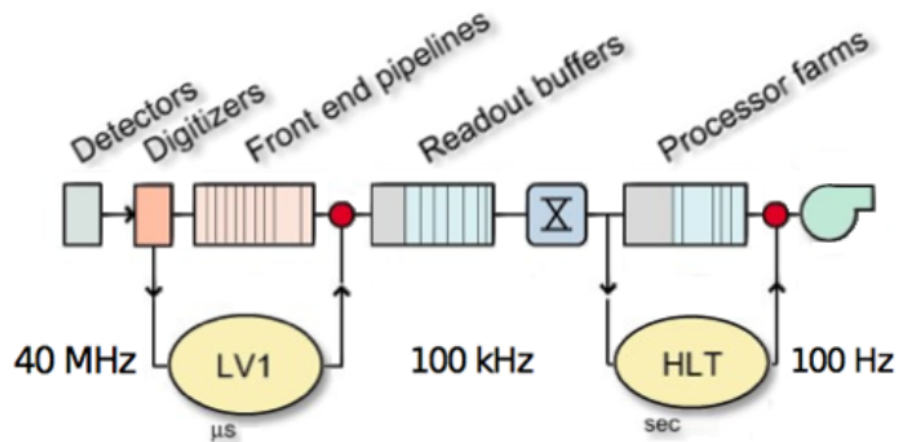


Figure 3.9: Two-level CMS trigger system.

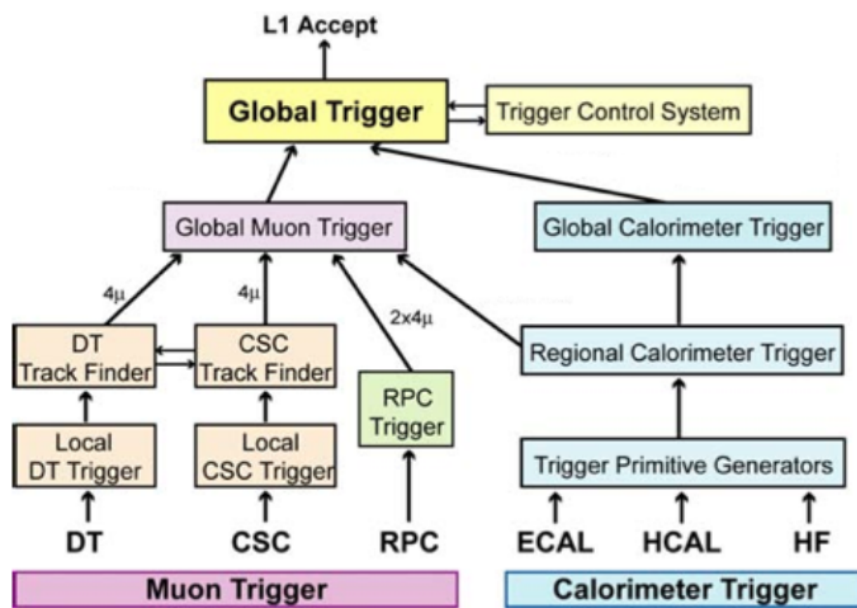


Figure 3.10: Level 1 CMS trigger system.

# Chapter 4

## CMS Tracker Alignment

In the presence of a constant magnetic field, a charged particle has a helical trajectory which can be parametrized by five constants in three dimensions. While a charged particle travels through a tracking system, the tracking system detects hits. A reconstruction algorithm determines the track parameters by fitting the positions of hits assuming the helical trajectory. That allows to reconstruct the full geometry of the track as well as to determine a particle momentum, and whether the particle came from the point of the  $p\bar{p}$  collision or decay of a secondary particle.

High precision track reconstruction is necessary for accurate measurements of particle kinematics. Better hit resolution and location uncertainty lead to the higher precision of a measurement of the track parameters. The location uncertainty depends on our knowledge of the positions and orientations in the space of the tracking system modules. For example, the hit resolution in the CMS pixel detector is  $\sim 10 \mu\text{m}$  in the  $r - \phi$  plane and  $\sim 30 \mu\text{m}$  in the longitudinal direction [15]. When the modules of the pixel detector are mounted, their positions are known with precision of  $\sim 200 \mu\text{m}$ . Thus, we need to know positions of modules an order of magnitude times better than they are known when mounted. The procedure for

the determination of the module locations and orientations is called the tracker alignment. The approach used for the tracking alignment in CMS is described in Ch. 4.1.

The procedure of tracker alignment is essential for the momenta measurement of all charged particles including electrons and muons that are the final state particles of the measurement of this dissertation as well as the determination of the position of the primary vertex. The measurement of this dissertation is based on data collected in 2012 while the author of this dissertation participated in the alignment of the tracking system in 2015 (Ch. 4.2). The results of 2015 alignment are not used for the measurement of this dissertation but are used for all CMS physics measurements of 2015 data including  $W\gamma$  measurement at  $\sqrt{s} = 13$  TeV.

## 4.1 Approach

The concept of track-based alignment can be illustrated in the example of the alignment of a toy tracker (Fig. 4.1-4.2). A charged particle crosses a toy tracker of six flat equidistant modules. Because real geometry of the tracker differs from the ideal one, hits are recorded at the places different from the design ideal places. We record and process a large number of tracks to determine positions and orientations of the modules.

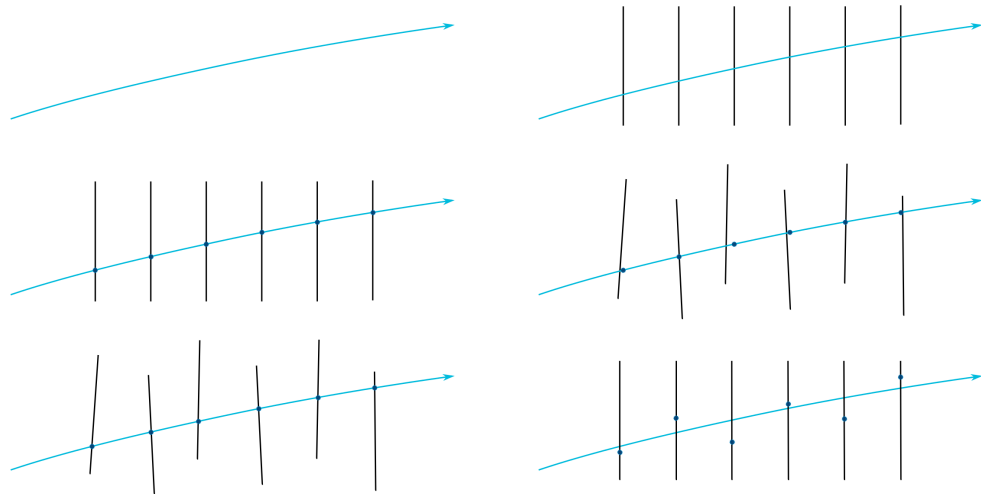


Figure 4.1: The alignment of a toy tracker, part 1 [1]. When a charged particle passing through a detector (top left), it crosses a toy tracker which consists of six flat equidistant modules (top right). If the modules were placed exactly at their designed positions, we would observe the hits exactly at the points where the track crosses modules of ideal geometry (middle left). However, in reality, the positions and tilts of the modules are different from ones suggested by the ideal geometry (middle right). Hits, indeed, are recorded at the places where modules are mounted, not at the design ideal places (bottom left). If we assumed a tracker to be ideal and a track to be smooth, we would see that our hits are off-track (bottom right).

The tracker alignment problem is a least squares problem. The expression to minimize is the following:

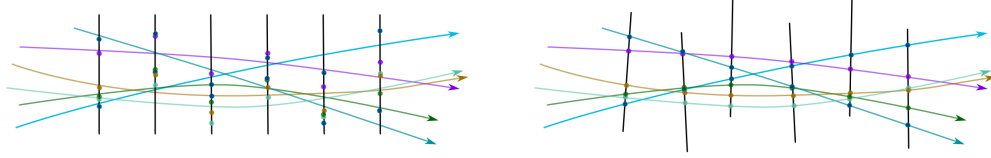


Figure 4.2: The alignment of a toy tracker, part 2 [1]. We record a large number of tracks and take into account them all to determine the alignment parameters by minimizing residuals between measured and predicted hits.

$$\chi^2(\mathbf{p}, \mathbf{q}) = \sum_j^{tracks} \sum_i^{hits} \left( \frac{m_{ij} - f_{ij}(\mathbf{p}, \mathbf{q}_j)}{\sigma_{ij}} \right)^2, \quad (4.1)$$

where  $\mathbf{p}$  are parameters describing the tracker geometry,  $\mathbf{q}_j$  are parameters of the  $j^{th}$  track,  $m_{ij} - f_{ij}$  are residuals (distances between the measured hit and a position predicted by the track fit),  $\sigma_{ij}$  is the Gaussian error of the measurement.

In CMS, we have two alignment algorithms: Millepede-II [40] and HIP [31]. Millepede-II performs a simultaneous fit of all alignment parameters and all track parameters while HIP performs iterative fits of alignment parameters  $\mathbf{p}$  and track parameters  $\mathbf{q}_j$ .

We can align the large substructures with respect to the global CMS coordinate system and individual modules with respect to the coordinate systems of their substructures. The parameters to align large substructures include three coordinates to determine location and three angles to determine orientation of the substructure. At the module level, we align positions and rotations with respect to the positions and angles of the corresponding large structure (Fig. 4.3). Also at the module level, we align for surface deformations which are described by three parameters per sensor (Fig. 4.4).

In addition to particles originating from  $pp$  collisions of the LHC, CMS also

detects muons that originate from interactions of cosmic particles with the Earth's atmosphere. Tracks left by these two types of particles in the tracking system are referred as collision and cosmic tracks respectively. We need both types of tracks for the alignment.

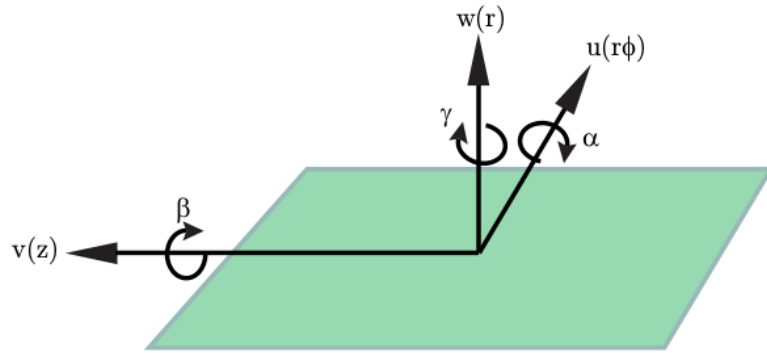


Figure 4.3: Alignment local parameters [2].

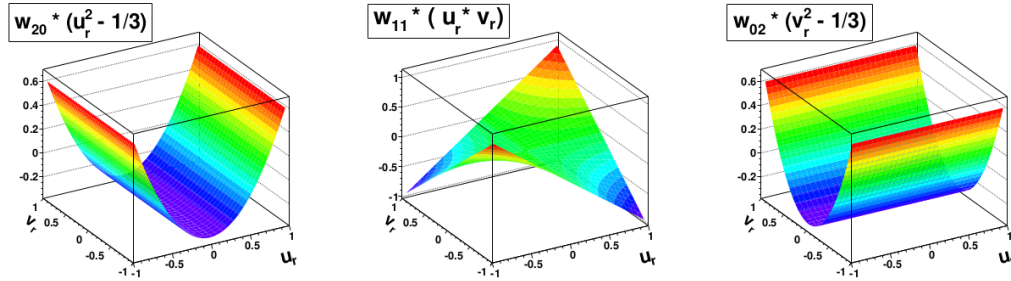


Figure 4.4: Surface deformations [14].

It is necessary to align a part of the tracking system whenever we suspect a physical change in a location or an orientation of this part. First of all, whenever a part of the CMS tracker is taken out and placed back, we need to realign it. Also whenever a magnet is turned on and off, different parts of the tracking system shift with respect to one another. Pixel half barrels are not screwed firmly, and

are moving along each other on rails, therefore, they need to be aligned every 15 minutes. Realignment is also necessary when modules are replaced or when the temperature changes.

After the procedure of the tracking system alignment is performed, we validate the results. Chapter 4.2 discusses various tools of alignment validation using the example of the tracking system alignment based on the 2015 data.

## 4.2 Selected Results on Alignment of the Tracking System with 2015 Data

Different data-taking periods in 2015 include the following periods:

- cosmic ray data with CMS magnetic field of  $B = 0\text{T}$ ;
- cosmic ray data at  $B = 3.8\text{T}$ ;
- $pp$  collision data at  $B = 0\text{T}$ ;
- $pp$  collision data at  $B = 3.8\text{T}$ .

Only  $pp$  collision data at  $B = 3.8\text{T}$  are used for physics measurements and the three other periods are preliminary. During the preliminary periods we make sure that all parts of the detector work properly and also perform the preliminary alignment of the tracking system. Periods of  $pp$  collisions are interfilled with cosmic ray data-taking when LHC does not provide any collision data. This interfill cosmic ray data are also used for the tracker alignment.

Different data-taking periods correspond to different detector geometries particularly due to changes of the magnetic field. Thus, alignment constants were derived separately for each of the data-taking periods using the alignment results of the previous period of data-taking as a starting point. Both Millepede-II and HIP algorithms were used to perform the alignment.

The first alignment of the tracker corrected for the displacements that took place between the Run I and Run II. Cosmic ray data with magnetic field turned on ( $B = 3.8\text{T}$ ) and off ( $B = 0\text{T}$ ) were used for this alignment. The modules in certain parts of BPIX were repaired during the shutdown, and all pixel subdetectors were moved within the tracker.

After the cosmic ray data taking periods, the magnetic field was turned off again, and the first collisions were detected with  $B = 0\text{T}$ . This change in the magnetic field caused movements in the tracking system that has the strongest effect in the pixel subdetectors. The alignment performed using  $B = 0\text{T}$  collisions and cosmic ray data recovers the tracker performance in the ability to reconstruct kinematic parameters of charged particles. When the magnetic field was turned back on, the large substructures of BPIX and FPIX have displaced again, and, thus, the tracking system was aligned again to recover these displacements.

Validation of tracking system alignment tools include geometry comparison tool (Ch. 4.2.1), validation using distribution of median residuals (Ch. 4.2.2), cosmic track splitting validation (Ch. 4.2.3), and primary vertex validation (Ch. 4.2.4). Full results of the first alignment with Run II data are available at [3].

### 4.2.1 Geometry Comparison

Geometry comparison visualizes differences in positions of modules between two different geometries of the CMS tracking system. Figure 4.5 shows the comparison between positions of the FPIX modules between Run I and Run II geometries. Each dot in the figure corresponds to one module. Four clusters of red dots (Fig. 4.5, left) and shifted parts at  $(\phi < -\pi/2, \phi > \pi/2)$  and  $(-\pi/2 < \phi < \pi/2)$  (Fig. 4.5, right) represent displacements of four half-disks by 4.5 and 5.5 mm at the  $-z$  side of the FPIX. At the  $+z$  side of the FPIX small relative movements of individual modules are observed only. For more intuitive visualization, the three-dimensional plot of the pixel detector is produced (Fig. 4.6).

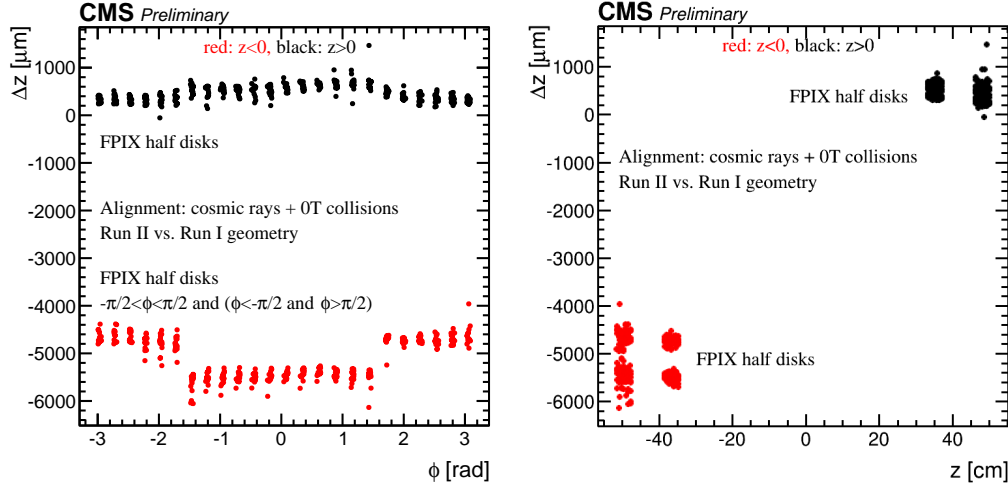


Figure 4.5: Comparison of Run II and Run I positions of the modules in the FPIX of the CMS tracking system. Positions are determined with the Millepede-II and HIP algorithms using cosmic ray data collected with the magnetic field of  $B = 0\text{T}$  and  $B = 3.8\text{T}$  magnetic field in the CMS solenoid. The difference  $\Delta z$  (Run II - Run I) is plotted as a function of  $z$  (left) and  $\phi$  (right) in global coordinates.

#### 4.2.2 Distributions of Medians of Unbiased Track-Hit Residuals

Besides geometry comparison, we also have distributions of medians of unbiased track-hit residuals (DMR) validation tool. Each track from a given dataset is refitted using prepared alignment constants, and the hit for each module is predicted from all other hits of the track. After that, DMRs of all modules in a given subdetector are plotted on the same histogram. The width of the prepared DMR is a measure of the statistical precision of the derived alignment results.

The DMRs are plotted for the local  $x$ - (Fig. 4.7, left) and  $y$ -directions (Fig. 4.7, right) in the BPIX. The blue line shows the DMR for Run I while the green line shows the aligned geometry. The RMS values show that performance of the aligned geometry is improved by a factor of 10 over the Run I geometry. Because of physical changes in the detector, the Run I geometry is not expected to work

# CMS Preliminary

Alignment: cosmic rays + 0T collisions

Run II vs. Run I geometry, shift x 5

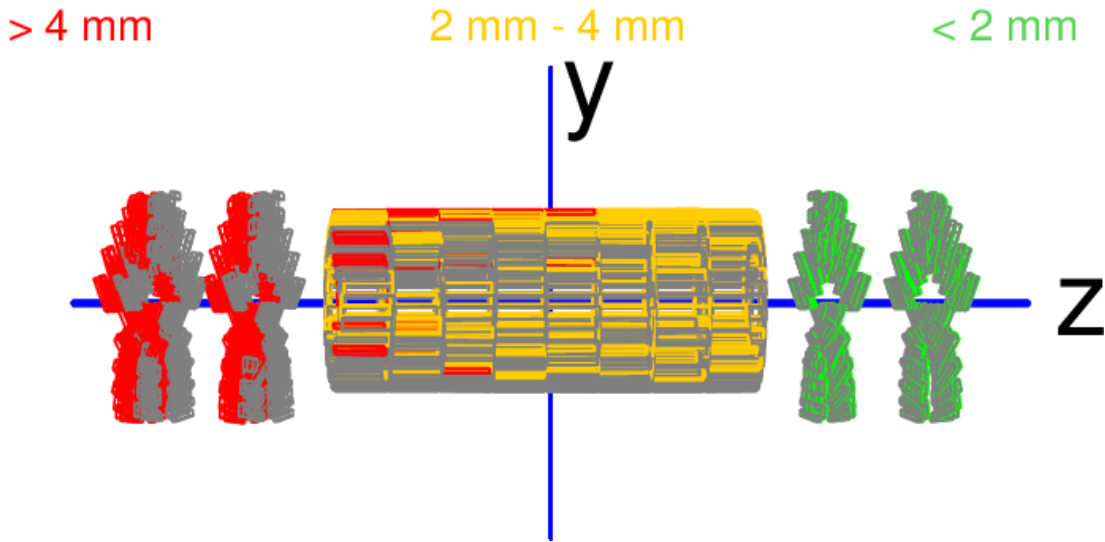


Figure 4.6: Three-dimensional geometry comparison of Run II and Run I positions in the BPIX and FPIX of the CMS tracking system. Positions are determined with the Millepede-II and HIP algorithms using cosmic ray data collected with the magnetic field of  $B = 0\text{T}$  and  $B = 3.8\text{T}$  magnetic field in the CMS solenoid and collision data with  $B = 0\text{T}$  at  $\sqrt{s} = 13\text{ TeV}$ . The positions at the end of Run I are shown in gray. The module displacements between Run I and Run II are magnified by a factor of 5 for visualization purpose. The resulting positions are shown in red, yellow, or green, depending on the displacement magnitude.

well with Run II data.

### 4.2.3 Cosmic Track Splitting Validation

To perform the cosmic track splitting validation, cosmic tracks are split into two parts at the hit closest to the center of the detector and both parts are reconstructed separately using alignment results. After that, the distributions of the differences in track parameters are prepared. The RMS values of the distributions are measures

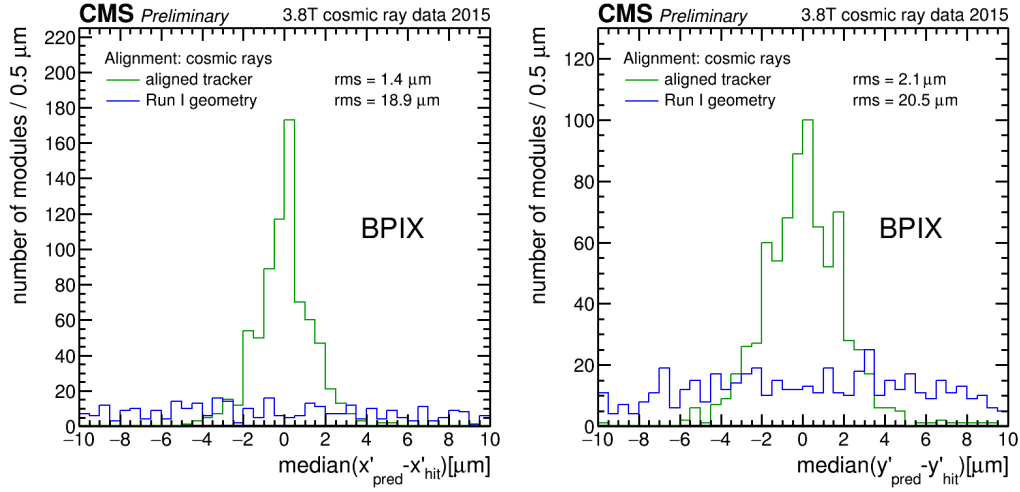


Figure 4.7: DMRs for the local  $x$ -direction (left) and for the local  $y$ -direction (right) in the BPIX of the CMS tracking system, using 2 million cosmic ray tracks collected with the magnetic field of  $B = 3.8\text{T}$ . The blue line shows the Run I geometry. The green line shows the alignment produced with the Millepede-II and HIP algorithms using cosmic ray data at  $B = 0\text{T}$  and  $B = 3.8\text{T}$ .

of the precision of the alignment constants. A deviation of a central value from zero would indicate a bias. The results of this validation for 2015 alignment are shown in Fig. 4.8.

#### 4.2.4 Primary Vertex Validation

The resolution of the reconstructed vertex position is driven by the pixel subdetectors as the closest subdetectors to the interaction point which also have the best hit resolution. The primary vertex validation is based on the study the distances between tracks and the reconstructed vertex.

Figure 4.9 compares the previous alignment to the one of a previous alignment reached during the commissioning phase with cosmic ray tracks at full magnetic field and to a detailed detector simulation with perfect alignment and calibration.

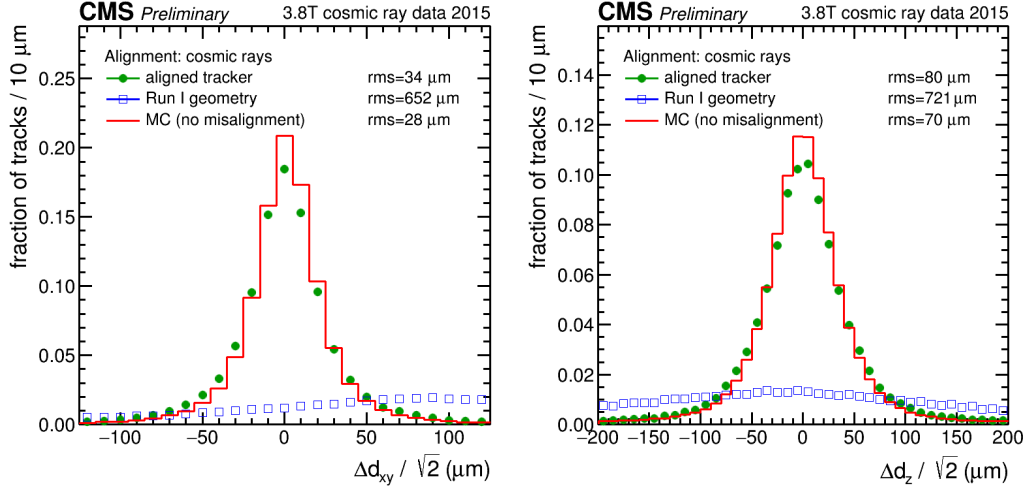


Figure 4.8: Results of the cosmic track splitting validation. The normalized differences between two parts of a cosmic track in the  $xy$  distance between the track and the origin ( $d_{xy}$ , left), and in the distance in the  $z$  direction between the track and the origin ( $d_z$ , right). Alignment is produced with the Millepede-II and HIP algorithms using cosmic ray data at the magnetic field of  $B = 0\text{T}$  and  $B = 3.8\text{T}$  of CMS solenoid. Aligned geometry is shown in green.

The structures of the green curve indicate relative movements of the pixel half-barrels.

Given the complexity of the CMS detector, any single measurement based on CMS data requires an excellent understanding of the geometry and response of all systems to particles of all types. The CMS Alignment and Calibration team coordinates hundreds of CMS physicists who are working on various aspects of this. The Chapter 4 of this dissertation presented one aspect of this work that concerns alignment of one system of CMS, the part in which the author of this dissertation played an important role.

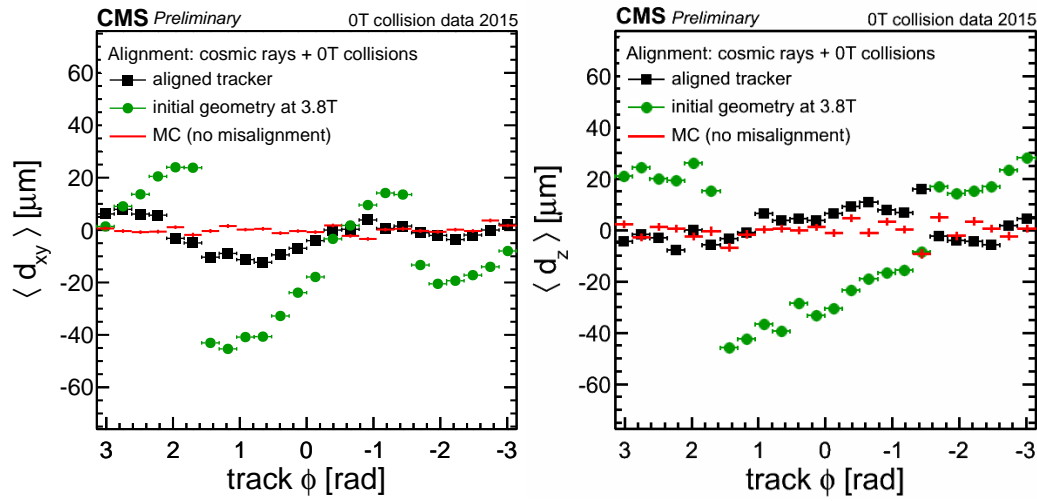


Figure 4.9: The results of the primary vertex validation. The distance of the track at its closest approach to a refit unbiased primary vertex ( $d_{xy}$ , left and  $d_z$ , right) in the transverse plane. The validation is produced with  $B = 0\text{T}$  collision data. The alignment is produced with the Millepede-II and HIP algorithms using  $B = 0\text{T}$  and  $B = 3.8\text{T}$  cosmic ray data and  $B = 0\text{T}$  collision data.

# Chapter 5

## $W\gamma$ Cross Section Measurement

The goal of the physics measurement of this dissertation is to measure the total and differential cross section of  $pp \rightarrow l\nu\gamma + X$  in bins of the photon transverse momentum  $P_T^\gamma$  using CMS data collected in 2012 at  $\sqrt{s} = 8$  TeV center-of-mass collision energy.

In the physics experiments, we measure a number of events of the specific process and determine the cross section in a certain kinematic phase space as

$$\sigma = N/L, \quad (5.1)$$

where  $N$  is the estimated number of events of the process of our interest in the given phase space, and  $L$  is the luminosity of our collider. The measurement strategy can be represented as a chain of steps that is summarized in Tab. 5.1. Chapters 5.1-5.6 describe each step in details.

The data sample we use in this analysis was recorded by the CMS experiment in 2012 in the LHC  $pp$  collisions at 8 TeV. The data collected by single electron and single muon triggers are used as the signal samples while double muon and double electron datasets are used for data-driven background estimation. Only

Table 5.1: Measurement steps. The first column is the name of the step, the second and the third columns are algebraic representations of the steps for the differential and total cross section measurements respectively.

Step	$d\sigma/dP_T$	$\sigma$
select events	$N_{sel}^j$	$N_{sel}$
subtract background	$N_{sign}^j = N_{sel}^j - N_{bkg}^j$	$N_{sign} = N_{sel} - N_{bkg}$
unfold	$N_{acc}^i = U_{ij} \cdot N_{sign}^j$	—
correct for the acceptance and efficiency	$N_{true}^i = \frac{N_{acc}^i}{(A \times \epsilon)^i}$	$N_{true} = \frac{N_{sign}}{A \times \epsilon}$
divide over luminosity and bin width	$\left(\frac{d\sigma}{dP_T}\right)^i = \frac{N_{true}^i}{L \cdot (\Delta P_T^i)^i}$	$\sigma = N_{true}/L$
estimate systematic uncertainties		

runs and luminosity sections certified by CMS are considered in the measurement, which means that good functioning of all CMS sub-detectors is required.

All simulation samples (often referred as Monte Carlo or MC samples) considered in this analysis are generated with MadGraph and reconstructed centrally by CMS simulation team. The simulated samples are reweighted to represent the distribution of the number of  $pp$  interactions per bunch crossing (pileup or PU), as measured in the data. Information regarding signal and background simulated samples used for the analysis is given in Tab. 5.2 alongside with the corresponding cross sections. The  $Z+jets$  process is often referred as Drell-Yan + jets or DY+jets.

Table 5.2: Summary of simulated background samples used in the measurement.

Process	$\sigma, \text{pb}$
$W\gamma \rightarrow l\nu\gamma$	553.92 (NLO)
$W+jets \rightarrow l\nu + jets$	36257.2 (NNLO)
$Z+jets \rightarrow ll + jets$	3503.71
$t\bar{t}+jets \rightarrow 1l+X$	99.44 (NNLO)
$t\bar{t}+jets \rightarrow 2l+X$	23.83
$t\bar{t}\gamma$	1.444
$Z\gamma \rightarrow ll\gamma$	171.62

The NLO cross section of  $W\gamma$  was calculated with the MCFM in the same phase space for which the  $W\gamma$  sample was generated. The NNLO contribution is estimated to be 19%-26% of the NLO value [61].

The cross section of  $Z\gamma$  measured by CMS is taken [17] and expanded to the phase space of the  $Z\gamma$  generated MC sample. The resulting cross section is found to be 171.62 pb.

To avoid experimentalist's bias, the whole measurement was performed in a blinded way at first. Our blinded strategy was the following:

- for  $p_T^\gamma < 45 \text{ GeV}$ : use full data; and
- for  $p_T^\gamma > 45 \text{ GeV}$ : use 5% of data.

After the whole measurement procedure was fully established, we unblinded the measurement. All plots shown in this dissertation are prepared with unblinded data.

The measurement was performed using advanced computing resources. A brief description of the software tools used and developed for the measurement is available in App. .12.

## 5.1 Event and Object Selection

### 5.1.1 Event Level Selection

In the final state of the  $W\gamma \rightarrow l\nu\gamma$  process we have a lepton, a photon, and a neutrino. Therefore, we select events with exactly one lepton (muon or electron), a photon, both originating from the primary vertex, and with significant missing transverse energy  $E_T^{miss}$ . The object selection criteria as well as criteria for the second lepton veto are described in Ch. 5.1.2.

To select events with significant  $E_T^{miss}$ , we apply a cut on the transverse mass of a  $W$  boson of  $M_T^W > 40$  GeV, where

$$M_T^W = \sqrt{(2 \cdot P_T^l \cdot E_T^{miss} \cdot (1 - \cos(\phi^l - \phi^{miss}))), \quad (5.2)}$$

where  $P_T^l$  is a lepton transverse momentum,  $\phi^l$  is an azimuthal angle of the lepton momentum, and  $\phi^{miss}$  is an azimuthal angle of the missing transverse momentum.

After that, the significant background from  $DY+jets \rightarrow ee\gamma$  in the electron channel remains. This background is caused by one of the electrons misidentified as a photon. Its contribution is the most significant around the invariant mass of the electron-photon system  $M_{e\gamma}$  is close to the mass of the  $Z$  boson as shown in the  $M_{e\gamma}$  distribution (Fig. 5.1). To reject this background, we apply  $Z$ -mass window cut: events with  $70 \text{ GeV} < M_{e\gamma} < 110 \text{ GeV}$  are rejected.

Finally, the separation  $\Delta R = \sqrt{(\Delta\phi^2 + \Delta\eta^2)}$  between the final state lepton and photon is required to be  $\Delta R(l, \gamma) > 0.7$  to avoid divergence coming from the ISR and FSR contributions and also to enhance the TGC contribution. In case if there

are more than one photon in the event passed all selection criteria including the  $\Delta R$  cut, the candidate with the hardest photon is selected (one with the highest  $P_T^\gamma$ ).

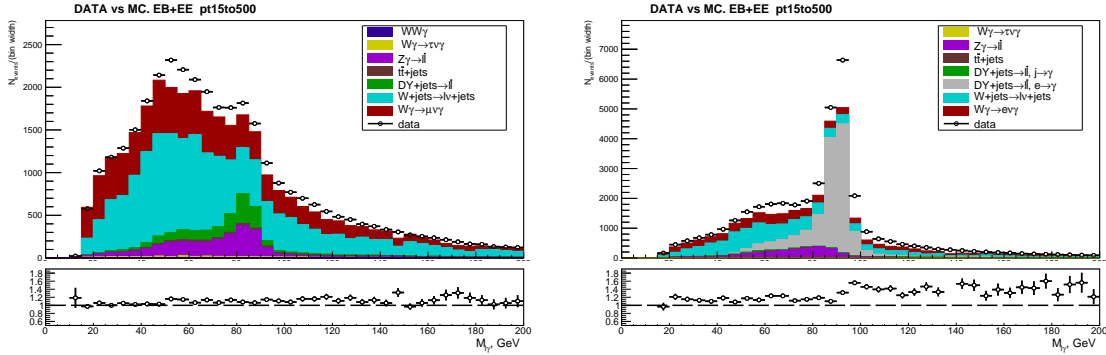


Figure 5.1: Data vs MC plots,  $M_{l\gamma}$ . Left: muon channel, right: electron channel. All selection criteria except  $M_{l\gamma}$  cut are applied on these plots.  $< P_T^\gamma > 15$  GeV. Events with  $70 \text{ GeV} < M_{l\gamma} < 110 \text{ GeV}$  are rejected in the electron channel.

### 5.1.2 Object Selection

We select events with muons and photons in the final state for the muon channel

and events with electrons and photons in the final state for the electron channel.

CMS Particle Object Group (POG) provides all CMS physics measurement groups with their recommendation for object identification (ID) criteria for any given period of data-taking. Recommendations for 2012 data include two sets of muon ID criteria: "Tight" and "Loose" and four sets of electron and photon ID criteria: "Tight", "Medium", "Loose" and "Veto".

For the muon selection, we applied the kinematics cuts of  $p_T > 25$  GeV and  $|\eta| < 2.1$  and "Tight" ID criteria. To reduce backgrounds from the process with two or more muons, like  $Z\gamma \rightarrow \mu\mu\gamma$  process, we reject all events that have the second reconstructed muon candidate with  $P_T > 10$  GeV and  $|\eta| < 2.4$ .

We consider electrons with  $p_T > 30$  GeV passing the "Tight" ID criteria and photons with  $P_T > 15$  GeV passing the modified "Medium" ID criteria. The modification of the photons ID criteria was studied in the  $W\gamma\gamma \rightarrow l\nu\gamma\gamma$  measurement [16].

In addition, electrons and photons must be within the ECal acceptance that is defined in terms of barrel (EB) and endcap (EE) sections with pseudorapidity ranges of  $|\eta| < 1.4442$  and  $1.566 < |\eta| < 2.5$ , respectively. To reject events with two or more final state electrons, events with the second reconstructed electron candidate with  $p_T > 10$  GeV and satisfying the "Veto" ID criteria are rejected.

Selection criteria are applied consistently on the data sample as well as on all MC samples. The selection efficiency may slightly differ between data and MC. The ratios data and MC efficiencies are called the scale factors. The scale factors for the selection criteria recommended by CMS POG are provided by CMS POG. For the modified photon ID criteria, the appropriate changes to the POG-recommended scale factors were applied derived by the  $W\gamma\gamma$  team [16].

### 5.1.3 Selected Events

The PU reweighting is applied on each event in each MC sample. Fig. 5.2 shows the distribution of the number of vertices for the  $Z\gamma$  selected sample in muon channel before (left) and after (right) the PU reweighting of the MC samples. The same procedure of the PU reweighting is applied for the  $W\gamma$  selected MC samples.

Our  $W+jets$ ,  $DY+jets$  and  $t\bar{t}+jets$  MC samples partially contain  $W\gamma$ ,  $Z\gamma$ , and  $t\bar{t}\gamma$  events. The overlap was removed from the  $W+jets$ ,  $DY+jets$ , and  $t\bar{t}+jets$  samples relying on their gen-level information. A good data vs MC agreement for the  $Z\gamma$  plots in Fig. 5.2 validates the procedure of the overlap removal.

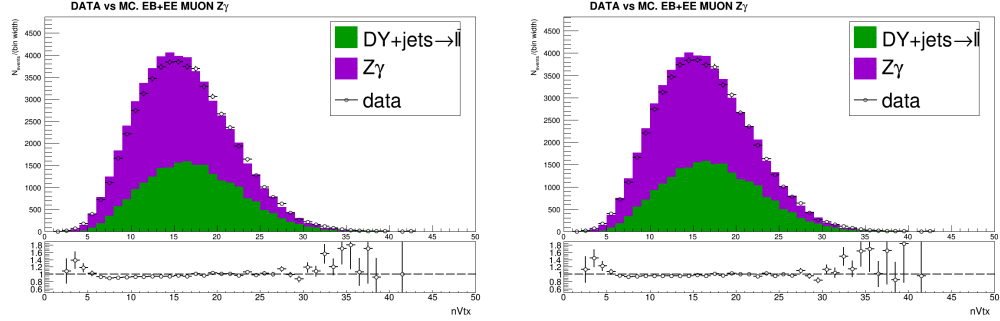


Figure 5.2: Number of vertices, data vs MC.  $Z\gamma$  selected sample, muon channel. Left: no PU reweighting applied, right: PU reweighting applied.

Distributions of  $P_T^\gamma$  of the selected events are shown in Fig. 5.3. There are large discrepancies in all the distributions and therefore the data-driven background estimates are necessary.

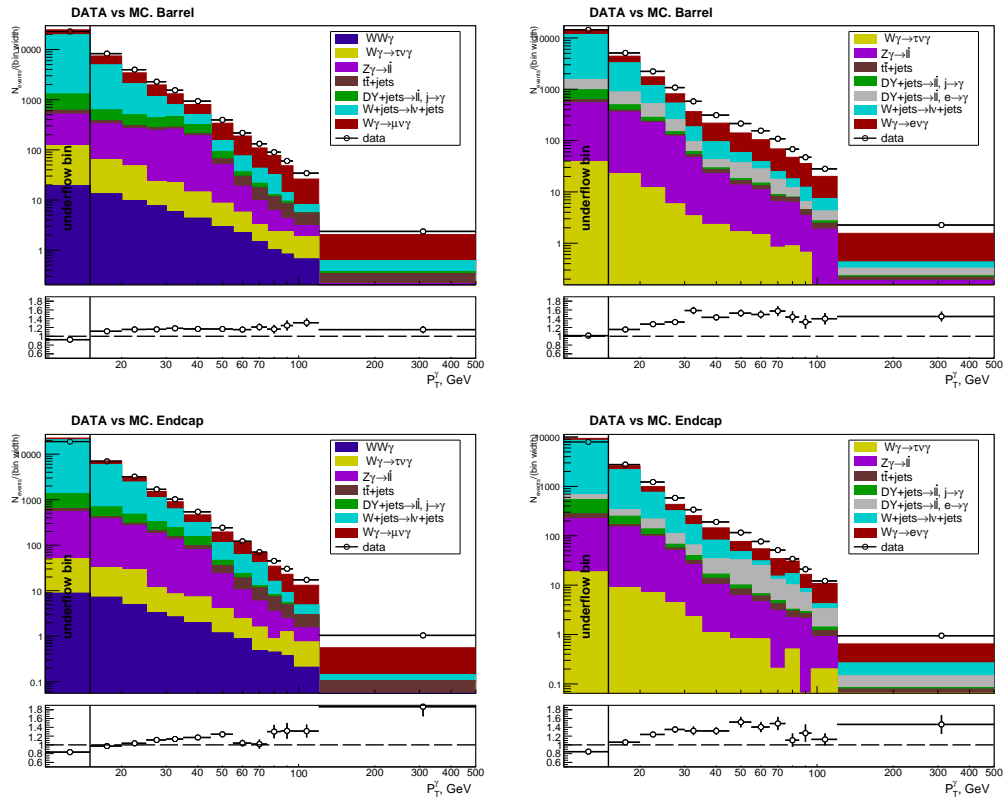


Figure 5.3: Data vs simulation plots. Left column: muon channel, right column: electron channel. Top to bottom: barrel and endcap photons.

## 5.2 Background Subtraction

In the selected sample we have our signal events as well as events coming from various backgrounds. To compute cross section, we need to subtract background and estimate how many events in each  $P_T^\gamma$  bin originate from the  $W\gamma$  process. This chapter describes the methods used for the background subtraction and provides plots and tables with the results.

### 5.2.1 Jets $\rightarrow \gamma$ Background Estimation and Subtraction

After passing through all selection criteria, the selected sample is dominated by  $W+jets$  background and this background cannot be further significantly reduced without reducing our signal sample  $W\gamma$  as well. The photon ID cut helps to reduce  $W+jets$  to a certain level but there is still a significant number of jets which are reconstructed as photons and pass all the photon ID criteria. DY+jets is another source of jets $\rightarrow \gamma$  background but this one is significantly suppressed by  $M_W^T$  cut in both channels and by the Z-mass window cut in the electron channel.

The template method is used to estimate jets $\rightarrow \gamma$  background. The method requires real- $\gamma$  template ( $T_{true}$ ) and fake- $\gamma$  template ( $T_{fake}$ ). Then the fit is performed according to:

$$F(V_{fit}) = N_{true} \cdot T_{true}(V_{fit}) + N_{fake} \cdot T_{fake}(V_{fit}), \quad (5.3)$$

where  $V_{fit}$  is a fit variable,  $N_{true}$  and  $N_{fake}$  are numbers of real and fake photons in the data sample respectively, and  $F(V_{fit})$  is a fit function.

We use charged hadron isolation  $I_{ch}^\gamma$  and a shower shape variable  $\sigma_{inj\eta}^\gamma$  as  $V_{fit}$ . To prepare templates, we use  $Z\gamma$ -selected dataset. Real- $\gamma$  templates  $T_{true}$  are taken

from the FSR events of  $Z\gamma \rightarrow \mu\mu\gamma$  while fake- $\gamma$  templates are taken from the ISR events of  $Z\gamma \rightarrow \mu\mu\gamma$ .

The FSR  $Z\gamma$  selection has looser muon-photon separation cut of  $\Delta R_{min}(\mu, \gamma) > 0.4$  (while the nominal separation cut is  $\Delta R_{min}(\mu, \gamma) > 0.7$  for both  $Z\gamma$  and  $W\gamma$  selections) and has three-particle invariant mass cut of  $M_{\gamma\mu\mu} < 101$  GeV. The FSR sample does not have enough number of events for high  $P_T^\gamma$  bins but the distribution of  $I_{ch}^\gamma$  of real photons does not depend on  $P_T^\gamma$  and, therefore, events for  $P_T^\gamma > 15$  GeV are all merged to prepare templates. Distributions of  $\sigma_{i\eta i\eta}^\gamma$  do depend on  $P_T^\gamma$ . Only events of  $P_T^\gamma > 30$  GeV are merged together to prepare templates for all  $P_T^\gamma > 30$  GeV bins. Templates for barrel and endcap photons are prepared separately.

$Z\gamma$ (ISR)-selected dataset consists of  $Z\gamma$ +(DY+jets) events. DY+jets events are needed to construct a fake photon template. Non-negligible real- $\gamma$  contribution is subtracted using  $Z\gamma$  MC predictions. ISR events were selected using nominal  $Z\gamma$  selection and  $M_{ll\gamma} > 101$  GeV,  $\Delta R_{min}(\mu, \gamma) > 1.0$  cuts.

FSR and ISR selections are illustrated in App. .1. Distributions of  $M_{ll\gamma}$  and  $M_{ll}$  for nominally selected  $Z\gamma$  dataset are shown in Fig. .11. Distributions of  $\Delta R(l, \gamma)$  for ISR and FSR  $Z\gamma$  events are shown in Fig. .12. Distributions of  $P_T^\gamma$  for ISR and FSR  $Z\gamma$  events are shown in Fig. .13. High  $P_T^\gamma$  bins have higher real- $\gamma$  contamination but even the very last bin contains enough events to prepare a template.

To extract real- $\gamma$  yield from the  $N_{true}$ , efficiency of the  $V_{fit}$  is applied on the value derived from fit based on the distribution of events which are used to prepare the real- $\gamma$  template. To extract fake- $\gamma$  yield from the  $N_{fake}$ , efficiency of the  $V_{fit}$  is applied on the value derived from fit based on the distribution of events which are used to prepare a fake- $\gamma$  template. Plots of the template fits are available in

App. .3.

Two MC closure checks are performed to validate the procedure. For the first check all MC samples that pass  $W\gamma$  selection are mixed together with appropriate weights assigned. Then fits on this sample of pseudodata is performed as on real data and the fit results are superimposed with MC samples. The results of the MC closure check are reported in App. .4 and the fit plots are shown in App. .5.

For the second MC closure check, the pseudodata sample is prepared from  $W+jets$  and  $W\gamma$  samples only. The results are reported in App. .6.

### 5.2.2 $e \rightarrow \gamma$ Background Estimation and Subtraction for the Electron Channel

For the electron channel, DY+jets is the main source of the  $e \rightarrow \gamma$  background. The Z-mass window cut of  $70 \text{ GeV} < M_{e\gamma} < 110 \text{ GeV}$  significantly suppresses this background, however, the remaining contribution is non-negligible.

The contribution of  $e \rightarrow \gamma$  is estimated separately for each  $P_T^\gamma$  bin and separately for barrel and endcap photons using the following expression:

$$N_{data-nom}^{e \rightarrow \gamma} = N_{MC-nom}^{e \rightarrow \gamma} \cdot \frac{N_{data-Zpeak}^{e \rightarrow \gamma}}{N_{MC-Zpeak}^{e \rightarrow \gamma}}, \quad (5.4)$$

where  $N_{data-nom}^{e \rightarrow \gamma}$  and  $N_{MC-nom}^{e \rightarrow \gamma}$  are the numbers of  $e \rightarrow \gamma$  events in the nominally selected of data and DY+jets MC sample respectively,  $N_{data-Zpeak}^{e \rightarrow \gamma}$  and  $N_{MC-Zpeak}^{e \rightarrow \gamma}$  are the numbers of  $e \rightarrow \gamma$  events under the Z-peak data and DY+jets MC sample respectively.

To estimate number of events under Z-peak,  $e \rightarrow \gamma$ -enriched data and DY+jets MC samples are prepared by inverting the Z-mass window cut. After that, numbers of events in DY+jets MC samples  $N_{MC-Zpeak}^{e \rightarrow \gamma}$  and  $N_{MC-nom}^{e \rightarrow \gamma}$  are estimated by

counting with appropriate weights. The number  $N_{data-Zpeak}^{e \rightarrow \gamma}$  is extracted from fitting the  $M_{e\gamma}$  in the Z-peak region (App. .7). The fits are performed separately in each  $P_T^\gamma$  bin in fine  $\eta^\gamma$  binning:

- $P_T^\gamma$  15 – 20 – 25 – 30 – 35 – 45 – 55 – 65 GeV
  - $\eta^\gamma$  binning in barrel: 0.00 – 0.10 – 0.50 – 1.00 – 1.44
  - $\eta^\gamma$  binning in endcap: 1.56 – 2.10 – 2.20 – 2.40 – 2.50
- $P_T^\gamma$  65 – 75 – 85 – 95 GeV
  - $\eta^\gamma$  binning in barrel: 0.00 – 0.50 – 1.44
  - $\eta^\gamma$  binning in endcap: 1.56 – 2.20 – 2.50
- $P_T^\gamma$ : 95 – 120 – 500 GeV
  - $\eta^\gamma$  binning in barrel: 0.00 – 1.44
  - $e\eta^\gamma$  binning in endcap: 1.56 – 2.50
- $P_T^\gamma$  10 – 15 GeV (underflow bin): MC-prediction is used, no fit performed.

The fit plots are provided in App. .7 and the tables are provided in App. .9. To prepare yields, fit results in all fine barrel  $\eta^\gamma$  bins are summed up and fit results in all fine endcap  $\eta^\gamma$  bins are summed up. The distributions of  $M_{e\gamma}$  before and after appropriate scale of the  $e \rightarrow \gamma$  of the DY+jets sample in different  $P_T^\gamma$  bins are shown in App. .10.

### 5.2.3 Other Backgrounds

In addition to the backgrounds discussed before, there are several more contributions:

- real- $\gamma$  background. Main sources of the real- $\gamma$  background are  $Z\gamma$  and  $W\gamma \rightarrow \tau\nu\gamma$ . The MC-based estimation is used to subtract these backgrounds.
- The  $e \rightarrow \gamma$  background for muon channel. Sources of these backgrounds are  $WW$  ( $W \rightarrow \mu\nu_\mu + W \rightarrow e\nu_e$ ),  $WZ$  ( $W \rightarrow \mu\nu_\mu + Z \rightarrow ee$  or  $W \rightarrow e\nu_\mu + Z \rightarrow \mu\mu$ ) and  $ZZ$  ( $Z \rightarrow \mu\mu + Z \rightarrow ee$ ). This background is neglected.
- Jets  $\rightarrow$  lepton + real- $\gamma$  ( $\gamma$ +jets and  $\gamma\gamma$ +jets events). Neglected.
- Jets  $\rightarrow$  lepton + jets  $\rightarrow \gamma$ . Neglected.

The neglected backgrounds were studied based on their MC samples in the muon channel. The total contribution of  $WW+WZ+ZZ+(\gamma\gamma+\text{jets})+(\gamma+\text{jets})+W\gamma \rightarrow \tau\nu\tau\gamma$  without  $M_T^W$  cut in the muon channel was found to be  $\tilde{2.2}\%$  of the total MC and  $\tilde{8}\%$  of  $W\gamma \rightarrow \mu\nu_\mu\gamma$ . In the samples ( $\gamma\gamma+\text{jets}$ ) and ( $\gamma+\text{jets}$ ) almost no events passed the selection criteria.  $WW$ ,  $WZ$  and  $ZZ$  contributions are shown to be negligible compared to  $W\gamma \rightarrow \tau\nu\tau\gamma$  and  $WW\gamma$  and are not shown at the plots too.

#### 5.2.4 $P_T^\gamma$ Spectra before and after the Background Subtraction

The results of the background estimation and subtraction procedure are summarized in Fig. 5.4-5.5 and in Tab. 5.3-5.6. Top and middle plots in Fig. 5.4-5.5 shows the  $P_T^\gamma$  spectrum in data superimposed with the signal MC and background estimates that includes jets  $\rightarrow \gamma$  and real- $\gamma$  backgrounds in both channels and  $e \rightarrow \gamma$  background in the electron channel. The bottom plots show data yields after full background subtraction superimposed with signal MC.

Jets  $\rightarrow \gamma$  background is estimated by two methods. The results provided by two methods differ significantly, and the difference contributes to the systematic uncertainty.

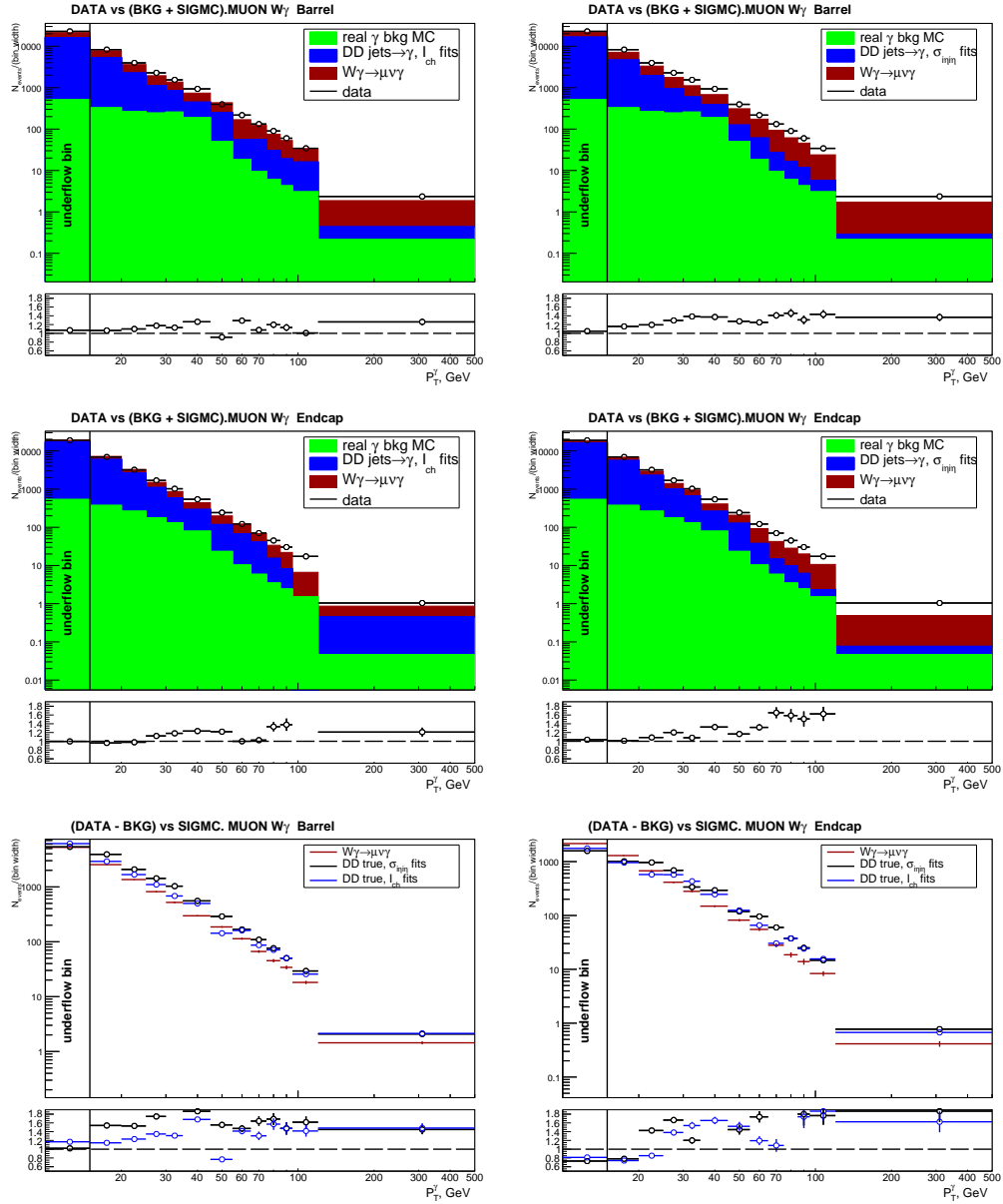


Figure 5.4: Top and middle: data vs fake- $\gamma$  background derived from the template method + real- $\gamma$  background predicted by dedicated MC samples + signal MC, with  $I_{ch}$  and  $\sigma_{inj}$  used as fit variables. Bottom: data yields after full background subtraction vs signal MC.  $I_{ch}$  vs  $\sigma_{inj}$  fit results.

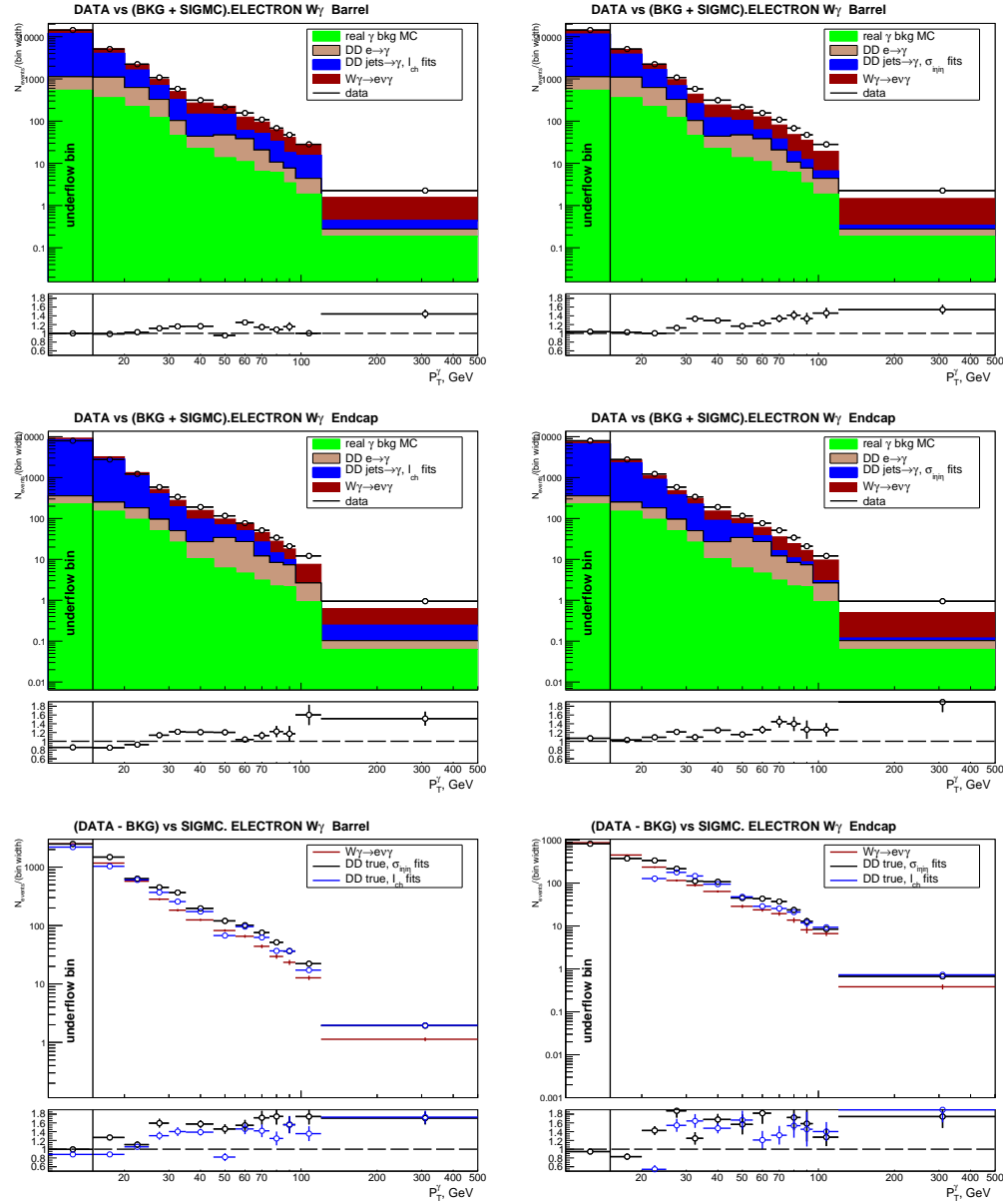


Figure 5.5: Top and middle: data vs fake- $\gamma$  background derived from the template method + real- $\gamma$  background predicted by dedicated MC samples + signal MC, with  $I_{ch}$  and  $\sigma_{i\eta}$  used as fit variables. Bottom: data yields after full background subtraction vs signal MC.  $I_{ch}$  vs  $\sigma_{i\eta}$  fit results.



Table 5.6: Data, signal and background yields.  $W\gamma$ , electron channel, endcap photons.

bin lims	jets $\rightarrow \gamma$ $I_{ch}^\gamma$	jets $\rightarrow \gamma$ $\sigma_{ij\eta i\eta}$	$e \rightarrow \gamma$	MC real- $\gamma$ bkg	SIGMC ( $W\gamma \rightarrow \nu\gamma$ )	bkg+sig $I_{ch}^\gamma$	bkg+sig $\sigma_{ij\eta i\eta}$	data
10-15	31043 $\pm$ 138	40022 $\pm$ 13	666 $\pm$ 38	1120 $\pm$ 27	4368 $\pm$ 97	37197 $\pm$ 174	46176 $\pm$ 108	39746 $\pm$ 199
15-20	9920 $\pm$ 88	12692 $\pm$ 124	509 $\pm$ 56	744 $\pm$ 21	2253 $\pm$ 68	13426 $\pm$ 127	16198 $\pm$ 154	13818 $\pm$ 118
20-25	3538 $\pm$ 56	4558 $\pm$ 63	433 $\pm$ 36	473 $\pm$ 17	1177 $\pm$ 49	5621 $\pm$ 84	6641 $\pm$ 90	6133 $\pm$ 78
25-30	1358 $\pm$ 34	1516 $\pm$ 29	229 $\pm$ 24	250 $\pm$ 12	575 $\pm$ 34	2412 $\pm$ 55	2569 $\pm$ 52	2924 $\pm$ 54
30-35	850 $\pm$ 31	694 $\pm$ 18	120 $\pm$ 16	130 $\pm$ 9	445 $\pm$ 31	1546 $\pm$ 48	1390 $\pm$ 41	1690 $\pm$ 41
35-45	613 $\pm$ 26	670 $\pm$ 16	167 $\pm$ 19	103 $\pm$ 8	638 $\pm$ 37	1522 $\pm$ 50	1578 $\pm$ 46	1905 $\pm$ 44
45-55	377 $\pm$ 30	337 $\pm$ 11	281 $\pm$ 28	61 $\pm$ 6	287 $\pm$ 24	1006 $\pm$ 49	965 $\pm$ 40	1162 $\pm$ 34
55-65	98 $\pm$ 12	228 $\pm$ 11	227 $\pm$ 28	46 $\pm$ 6	238 $\pm$ 22	608 $\pm$ 38	738 $\pm$ 38	767 $\pm$ 28
65-75	40 $\pm$ 8	139 $\pm$ 9	90 $\pm$ 18	31 $\pm$ 4	194 $\pm$ 21	354 $\pm$ 29	454 $\pm$ 29	513 $\pm$ 23
75-85	22 $\pm$ 6	57 $\pm$ 5	62 $\pm$ 15	22 $\pm$ 5	137 $\pm$ 18	243 $\pm$ 25	278 $\pm$ 25	340 $\pm$ 18
85-95	11 $\pm$ 4	25 $\pm$ 3	52 $\pm$ 19	21 $\pm$ 3	81 $\pm$ 14	166 $\pm$ 24	179 $\pm$ 24	210 $\pm$ 14
95-120	8 $\pm$ 3	-43 $\pm$ 4	43 $\pm$ 13	23 $\pm$ 5	166 $\pm$ 20	241 $\pm$ 25	190 $\pm$ 25	304 $\pm$ 17
120-500	5 $\pm$ 3	53 $\pm$ 7	15 $\pm$ 7	24 $\pm$ 4	146 $\pm$ 19	190 $\pm$ 21	237 $\pm$ 22	360 $\pm$ 19

## 5.3 Detector Resolution Unfolding

The non-zero detector resolution in  $P_T^\gamma$  causes the bin-by-bin migration. The reconstructed  $P_T^{\gamma(\text{reco})}$  may not coincide with the true  $P_T^{\gamma(\text{true})}$ , and, therefore, the event reconstructed in a  $P_T^\gamma$  bin  $i_{\text{reco}}$  may, in fact, belong to the bin  $i_{\text{true}} \neq i_{\text{reco}}$ . To recover true  $P_T^\gamma$  spectrum, we apply the procedure of the detector resolution unfolding.

Unfolding constants are derived from the signal MC sample ( $W\gamma \rightarrow \mu\nu_\mu\gamma/W\gamma \rightarrow e\nu_e\gamma$ ) where both true (gen-level) and reconstructed  $P_T^\gamma$  spectrum are known. We use the D'Agostini method [21] which unfolds the reconstructed spectrum iteratively.

Using the MC samples, we prepare the migration matrix (Fig. 5.6) which has the number of selected signal events in each  $(i_{\text{reco}}, i_{\text{gen}})$  bin. The migration matrix is then normalized in each  $i_{\text{reco}}$  bin, and we receive the response matrix  $R_{ji}$  (Fig. 5.7) which relates reconstructed and gen-level spectra as  $N_j^{\text{reco}} = R_{ji}N_i^{\text{gen}}$ .

In data, we only have  $N_j^{\text{reco}}$  which is our fully selected and background subtracted  $P_T^\gamma$  spectrum. The  $R_{ji}$  determined by signal MC is used to determine  $N_i^{\text{true}}$  in data.

After  $P_T^\gamma$  spectrum is unfolded, measurements in different  $P_T^\gamma$  bins become correlated. A correlation matrix is shown in Fig. 5.8.

To validate the detector resolution unfolding procedure, we perform the MC closure check. Gen-level and reconstructed yields are prepared using the signal MC. Then reconstructed yields are smeared by the Gaussian distribution according to the errors on the yields. The smeared yields are unfolded and compared to the gen-level yields. In addition to the D'Agostini method, we check the performance of the matrix inversion method for the unfolding which recovers the true yields as

$$N_i^{true} = (R_{ji})^{-1} N_j^{reco}.$$

The results of the MC closure check are summarized in Tab. 5.7-5.8 for the muon and electron channels respectively. The unfolded yields show reasonable agreement to the gen-level yields except the underflow bin ( $10 - 15$  GeV). The disagreement in the underflow bin may be caused by events with  $P_T^\gamma < 10$  GeV which are not available in our sample.

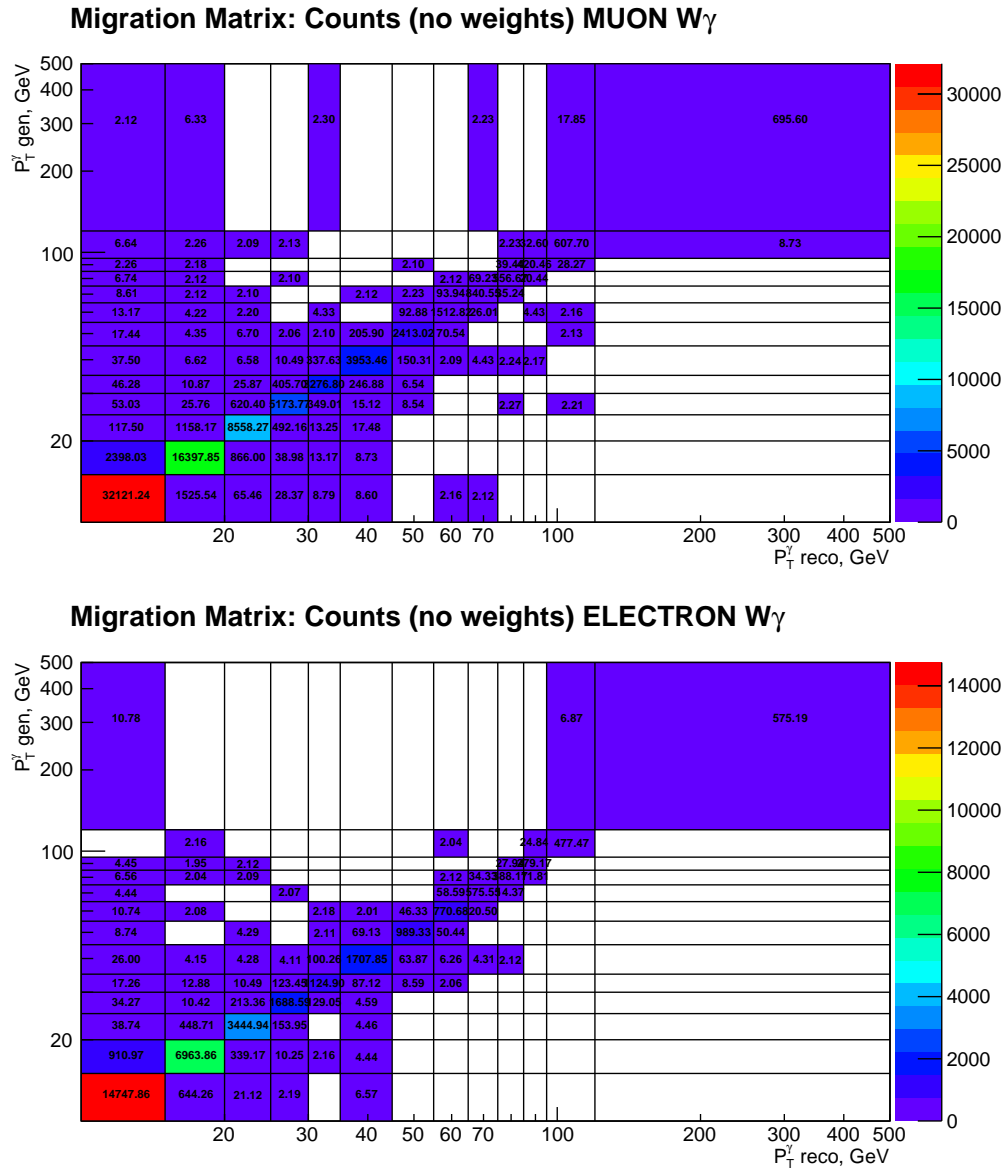


Figure 5.6: Migration matrix derived from the signal MC.

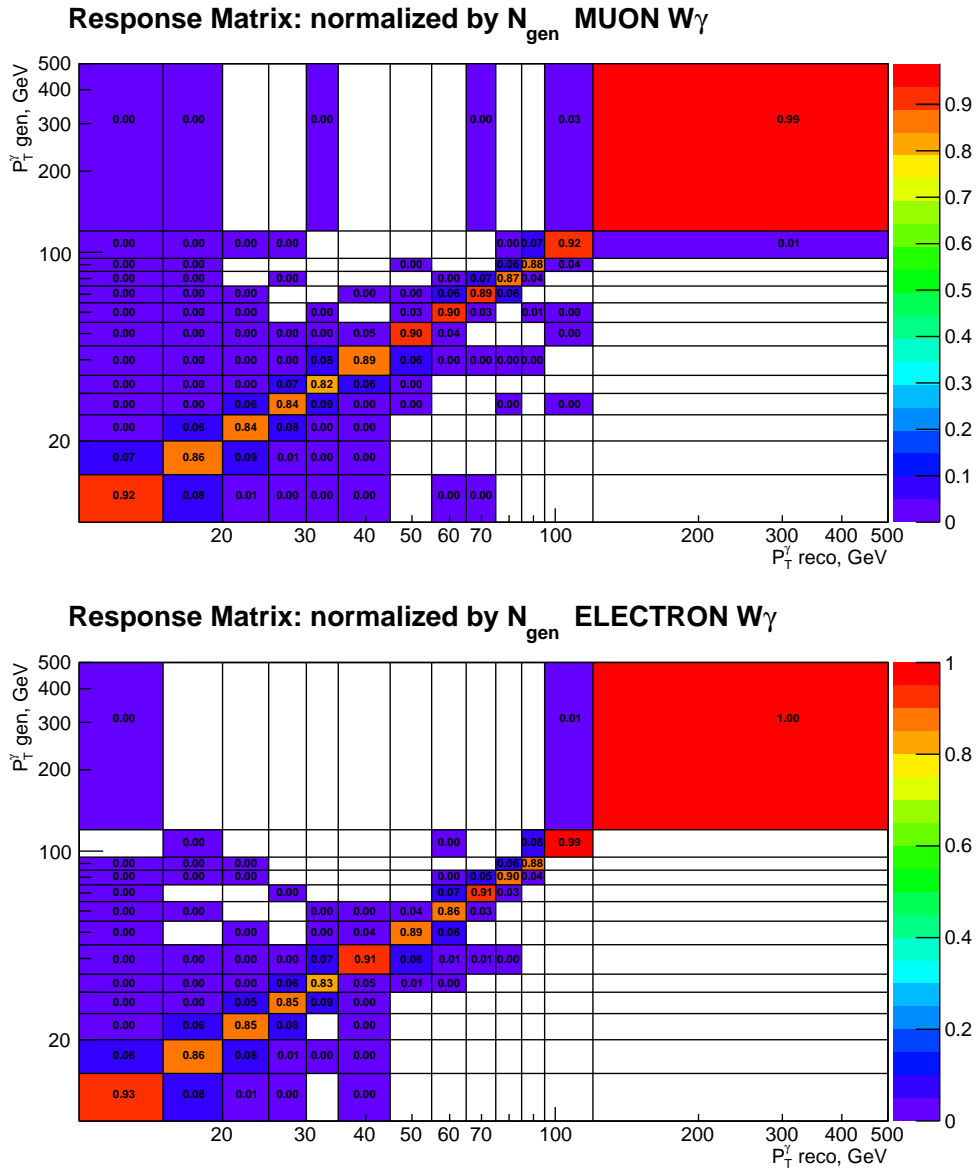


Figure 5.7: Response matrix derived from the signal MC.

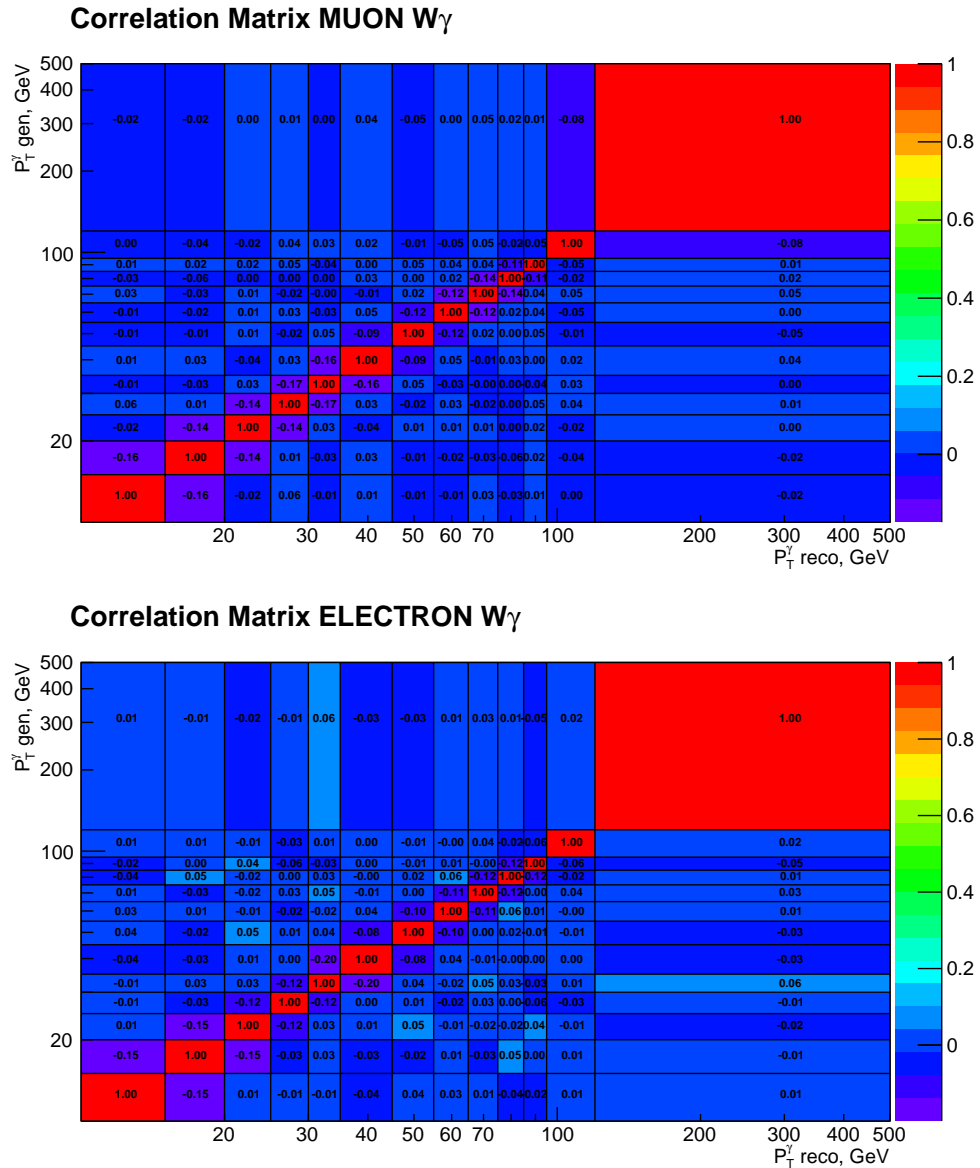


Figure 5.8: Correlation Matrices.

Table 5.7: Unfolding, MC closure test.  $W\gamma$ , muon channel.

bin	yields gen-level	yields rec	unfolded inversion	unfolded D'Agostini
limits				
10 - 15	$33888 \pm 273$	$37074 \pm 286$	$36226 \pm 206$	$36222 \pm 204$
15 - 20	$19736 \pm 207$	$19181 \pm 203$	$19612 \pm 171$	$19619 \pm 169$
20 - 25	$10364 \pm 149$	$10171 \pm 148$	$10358 \pm 122$	$10354 \pm 119$
25 - 30	$6254 \pm 116$	$6156 \pm 115$	$6233 \pm 96$	$6234 \pm 96$
30 - 35	$4026 \pm 93$	$4007 \pm 93$	$4010 \pm 81$	$4010 \pm 78$
35 - 45	$4516 \pm 99$	$4461 \pm 98$	$4502 \pm 79$	$4502 \pm 79$
45 - 55	$2731 \pm 77$	$2680 \pm 76$	$2724 \pm 57$	$2724 \pm 60$
55 - 65	$1662 \pm 60$	$1686 \pm 61$	$1655 \pm 45$	$1655 \pm 46$
65 - 75	$987 \pm 46$	$945 \pm 45$	$979 \pm 38$	$979 \pm 35$
75 - 85	$659 \pm 38$	$638 \pm 37$	$654 \pm 30$	$653 \pm 30$
85 - 95	$495 \pm 33$	$480 \pm 32$	$489 \pm 27$	$489 \pm 25$
95 - 120	$664 \pm 38$	$663 \pm 38$	$661 \pm 28$	$661 \pm 28$
120 - 500	$726 \pm 40$	$704 \pm 39$	$720 \pm 26$	$720 \pm 27$
500 - 2000	$2 \pm 2$	$2 \pm 2$	$2 \pm 1$	$2 \pm 1$

Table 5.8: Unfolding, MC closure test.  $W\gamma$ , electron channel.

bin	yields gen-level	yields rec	unfolded inversion	unfolded D'Agostini
limits				
10 - 15	$16025 \pm 185$	$16849 \pm 190$	$17117 \pm 143$	$17116 \pm 141$
15 - 20	$8246 \pm 131$	$8111 \pm 130$	$8194 \pm 109$	$8196 \pm 108$
20 - 25	$4093 \pm 92$	$4046 \pm 92$	$4083 \pm 75$	$4082 \pm 74$
25 - 30	$2080 \pm 66$	$1987 \pm 64$	$2072 \pm 55$	$2072 \pm 55$
30 - 35	$1387 \pm 54$	$1361 \pm 54$	$1378 \pm 47$	$1378 \pm 46$
35 - 45	$1925 \pm 64$	$1886 \pm 63$	$1915 \pm 51$	$1915 \pm 50$
45 - 55	$1124 \pm 49$	$1108 \pm 48$	$1116 \pm 37$	$1116 \pm 38$
55 - 65	$855 \pm 42$	$892 \pm 43$	$848 \pm 33$	$848 \pm 34$
65 - 75	$655 \pm 38$	$635 \pm 37$	$649 \pm 30$	$649 \pm 28$
75 - 85	$447 \pm 32$	$433 \pm 32$	$442 \pm 24$	$442 \pm 24$
85 - 95	$316 \pm 27$	$316 \pm 27$	$311 \pm 21$	$311 \pm 20$
95 - 120	$507 \pm 34$	$484 \pm 33$	$501 \pm 23$	$501 \pm 23$
120 - 500	$593 \pm 37$	$575 \pm 36$	$587 \pm 23$	$587 \pm 24$
500 - 2000	$4 \pm 3$	$4 \pm 3$	$4 \pm 2$	$4 \pm 2$

## 5.4 Acceptance X Efficiency

To compute the cross section in a phase space different from our selection criteria, it is necessary to apply the acceptance and efficiency corrections. They are computed in a combined manner as the bin-by-bin correction  $A \times \epsilon$  and derived from the signal MC samples.

The numerator  $num$  for the total cross section is determined as the number of selected events in the signal MC with PU weight applied. The numerator  $num_i$  for the differential cross section is determined as selected signal MC yields with PU weight applied in  $P_T^{\gamma-GEN}$  bins  $15 - 20 - 25 - 30 - 35 - 45 - 55 - 65 - 75 - 85 - 95 - 120 - 500$  GeV.

The denominator  $den$  is determined as the number of events that are within the phase space based on their gen-level kinematic values. For the differential cross section, the numbers  $den_i$  are determined separately for each  $P_T^\gamma$  bin.

The  $A \times \epsilon$  correction is determined then as  $A \times \epsilon = num/den$  for the total cross section and as  $(A \times \epsilon)_i = num_i/den_i$  for the differential cross section. The  $A \times \epsilon$  for the total cross section are

$$(21833 \pm 36)/(177606 \pm 629) = 0.1229 \pm 0.0004 \quad (5.5)$$

for the electron channel, and

$$(51771 \pm 39)/(179082 \pm 631) = 0.2891 \pm 0.0006 \quad (5.6)$$

for the muon channel. The values for the differential cross section are plotted in Fig. 5.4.

The phase space is defined in the following way:

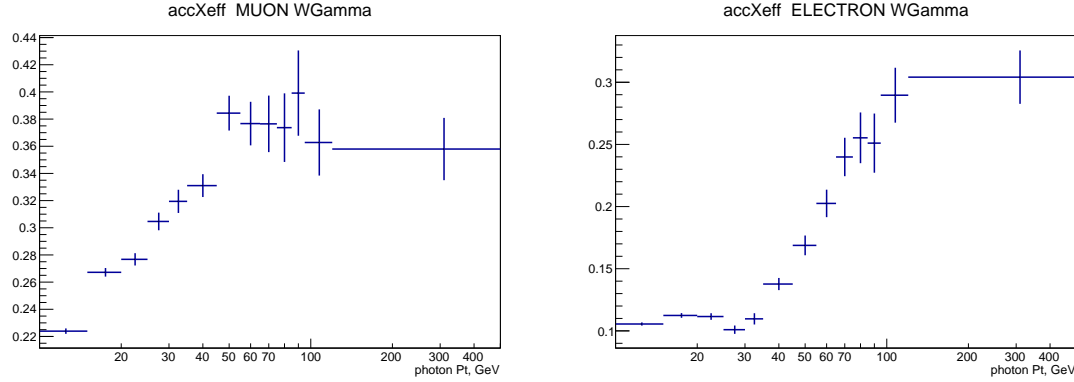


Figure 5.9:  $A \times \epsilon$  corrections. Left: muon channel, right: electron channel.

- $p_T^\gamma > 15 \text{ GeV};$
- $\Delta R(\gamma, l) > 0.7;$
- $|\eta^\gamma| < 2.5, |\eta^l| < 2.5;$
- $p_T^l > 20 \text{ GeV};$
- $I^\gamma < 5 \text{ GeV}$ , where  $I_\gamma$  is a sum of  $P_T$  of all MC generated particles particles  $p$  in the event within  $\Delta R(p, \gamma) < 0.3$ ;
- for differential cross section,  $P_T^\gamma$  binning:  $15 - 20 - 25 - 30 - 35 - 45 - 55 - 65 - 75 - 85 - 95 - 120 - 500 \text{ GeV}.$

## 5.5 Systematic Uncertainties

### 5.5.1 Uncertainties due to Jets $\rightarrow\gamma$ Data-Driven Background Estimation

The dominant systematic uncertainty is uncertainty due to jets $\rightarrow\gamma$  background estimation. The following sources contribute to the uncertainty of the jets $\rightarrow\gamma$  background estimation:

- the difference between fit results of  $I_{ch}^{\gamma}$  and  $\sigma_{i\eta i\eta}^{\gamma}$  templates;
- the uncertainty on the normalizations of  $Z\gamma$  and DY+jets MC samples when the real- $\gamma$  (fake- $\gamma$ ) portions are subtracted from the ISR (FSR) templates.
- the limited statistical power of the fake- $\gamma$  and real- $\gamma$  templates.

The systematic uncertainty due to the difference between fit results of  $I_{ch}$  and  $\sigma_{i\eta i\eta}$  templates is computed as

$$\frac{1}{2}|N_{I_{ch}} - N_{\sigma_{i\eta i\eta}}|. \quad (5.7)$$

The mean value is taken as an average between  $N_{I_{ch}}$  and  $N_{\sigma_{i\eta i\eta}}$ .

The error due to template statistics is computed by separately randomizing the real- $\gamma$  and the fake- $\gamma$  templates, we prepare 20 real- $\gamma$  and 100 fake- $\gamma$  templates by randomizing our nominal templates with the Gaussian distribution. Then we perform fits with new templates and take the standard deviation of the fit results as a error. The errors are computed separately for the real- $\gamma$  and the fake- $\gamma$  templates. The statistical error of the fake- $\gamma$  template is larger.

The results of the systematic error of  $|N_{I_{ch}} - N_{\sigma_{i\eta i\eta}}|$  and the template statistical uncertainty are summarized in the Tab. 5.9-5.12. Columns data  $I_{ch}^{\gamma}$ , data  $\sigma_{i\eta i\eta}^{\gamma}$ , MC

cl.  $I_{ch}^{\gamma}$  and MC cl.  $\sigma_{i\eta i\eta}^{\gamma}$  are the yields from the fit results of  $I_{ch}^{\gamma}$  and  $\sigma_{i\eta i\eta}^{\gamma}$  fits of data and MC mixtures. The errors include the statistical errors and the errors due to template statistics.

Table 5.9: Results of the background subtraction based on fits of different variables.  $W\gamma$ , muon channel, barrel photons.

bin lims	MC pred	data $I_{ch}^{\gamma}$	data $\sigma_{i\eta i\eta}^{\gamma}$	MC cl. $I_{ch}^{\gamma}$	MC cl. $\sigma_{i\eta i\eta}^{\gamma}$	yield average
10-15	$26250 \pm 240$	$30683 \pm 1919$	$26770 \pm 3134$	$29657 \pm 2476$	$35073 \pm 3726$	$30683 \pm 3913 \pm 1865$
15-20	$12706 \pm 164$	$14554 \pm 1070$	$19575 \pm 1771$	$10742 \pm 1079$	$14924 \pm 2123$	$14554 \pm 5021 \pm 1041$
20-25	$6793 \pm 120$	$8364 \pm 711$	$10398 \pm 4313$	$7698 \pm 626$	$9399 \pm 1741$	$8364 \pm 2033 \pm 693$
25-30	$4087 \pm 93$	$5505 \pm 685$	$7141 \pm 3437$	$4421 \pm 532$	$5023 \pm 2094$	$5505 \pm 1636 \pm 675$
30-35	$2603 \pm 74$	$3409 \pm 500$	$5152 \pm 2581$	$3422 \pm 197$	$3266 \pm 1156$	$3409 \pm 1742 \pm 490$
35-45	$2971 \pm 80$	$4990 \pm 466$	$5544 \pm 3366$	$4472 \pm 308$	$4351 \pm 1632$	$4990 \pm 554 \pm 454$
45-55	$1861 \pm 63$	$1428 \pm 410$	$2893 \pm 593$	$1799 \pm 277$	$2464 \pm 146$	$1428 \pm 1464 \pm 402$
55-65	$1135 \pm 49$	$1604 \pm 207$	$1671 \pm 501$	$1143 \pm 214$	$1475 \pm 311$	$1604 \pm 67 \pm 201$
65-75	$664 \pm 37$	$866 \pm 43$	$1090 \pm 271$	$773 \pm 193$	$680 \pm 162$	$866 \pm 223 \pm 7$
75-85	$451 \pm 31$	$710 \pm 34$	$762 \pm 88$	$621 \pm 106$	$701 \pm 143$	$710 \pm 52 \pm 0$
85-95	$340 \pm 27$	$502 \pm 139$	$502 \pm 175$	$455 \pm 62$	$443 \pm 98$	$502 \pm 0 \pm 136$
95-120	$453 \pm 31$	$641 \pm 105$	$732 \pm 31$	$714 \pm 113$	$577 \pm 83$	$641 \pm 91 \pm 98$
120-500	$546 \pm 34$	$810 \pm 214$	$792 \pm 63$	$777 \pm 105$	$678 \pm 191$	$810 \pm 18 \pm 211$

Table 5.10: Results of the background subtraction based on fits of different variables.  $W\gamma$ , muon channel, endcap photons.

bin lims	MC pred	data $I_{ch}^{\gamma}$	data $\sigma_{i\eta i\eta}^{\gamma}$	MC cl. $I_{ch}^{\gamma}$	MC cl. $\sigma_{i\eta i\eta}^{\gamma}$	yield average
10-15	$10823 \pm 154$	$8797 \pm 2242$	$7893 \pm 2947$	$16512 \pm 2900$	$-2675 \pm 1967$	$8797 \pm 903 \pm 2184$
15-20	$6474 \pm 119$	$4793 \pm 1132$	$5053 \pm 1518$	$6454 \pm 1142$	$2650 \pm 2124$	$4793 \pm 260 \pm 1101$
20-25	$3377 \pm 86$	$2877 \pm 729$	$4817 \pm 1329$	$5393 \pm 578$	$4458 \pm 1291$	$2877 \pm 1939 \pm 710$
25-30	$2068 \pm 67$	$2856 \pm 408$	$3443 \pm 1514$	$3137 \pm 356$	$3904 \pm 975$	$2856 \pm 586 \pm 394$
30-35	$1403 \pm 55$	$2160 \pm 306$	$1686 \pm 693$	$1808 \pm 401$	$1482 \pm 545$	$2160 \pm 474 \pm 295$
35-45	$1489 \pm 57$	$2465 \pm 339$	$2937 \pm 1009$	$2385 \pm 279$	$2185 \pm 935$	$2465 \pm 471 \pm 329$
45-55	$818 \pm 42$	$1246 \pm 243$	$1184 \pm 595$	$894 \pm 176$	$1139 \pm 226$	$1246 \pm 61 \pm 237$
55-65	$550 \pm 34$	$657 \pm 208$	$957 \pm 375$	$572 \pm 219$	$320 \pm 260$	$657 \pm 299 \pm 204$
65-75	$280 \pm 24$	$304 \pm 169$	$599 \pm 206$	$471 \pm 80$	$452 \pm 141$	$304 \pm 295 \pm 166$
75-85	$186 \pm 20$	$375 \pm 162$	$374 \pm 91$	$244 \pm 69$	$195 \pm 66$	$375 \pm 1 \pm 161$
85-95	$139 \pm 17$	$242 \pm 60$	$250 \pm 28$	$318 \pm 19$	$199 \pm 30$	$242 \pm 8 \pm 57$
95-120	$208 \pm 21$	$390 \pm 55$	$369 \pm 195$	$348 \pm 41$	$168 \pm 54$	$390 \pm 21 \pm 51$
120-500	$157 \pm 18$	$255 \pm 88$	$294 \pm 17$	$257 \pm 53$	$181 \pm 30$	$255 \pm 38 \pm 85$

The uncertainty on the  $Z\gamma$  MC normalization for jets $\rightarrow\gamma$  background estimation is determined by performing the fits with the different  $Z\gamma$  normalizations and propagating the spread of the results as the systematic error. The uncertainty on the  $Z\gamma$  normalization is set to be 4.6% as quoted by  $Z\gamma$  8 TeV measurement [17].

Table 5.11: Results of the background subtraction based on fits of different variables.  $W\gamma$ , electron channel, barrel photons.

bin lims	MC pred	data $I_{ch}^{\gamma}$	data $\sigma_{inj}^{\gamma}$	MC cl. $I_{ch}^{\gamma}$	MC cl. $\sigma_{inj}^{\gamma}$	yield average
10-15	$12480 \pm 163$	$10994 \pm 1331$	$12425 \pm 2000$	$10640 \pm 1500$	$14995 \pm 2225$	$10994 \pm 1430 \pm 1277$
15-20	$5857 \pm 110$	$5160 \pm 668$	$7421 \pm 1173$	$4124 \pm 602$	$5721 \pm 1927$	$5160 \pm 2261 \pm 613$
20-25	$2868 \pm 77$	$3022 \pm 384$	$3168 \pm 2937$	$3390 \pm 258$	$3699 \pm 1261$	$3022 \pm 145 \pm 338$
25-30	$1411 \pm 54$	$1846 \pm 293$	$2250 \pm 1984$	$1365 \pm 152$	$1339 \pm 1167$	$1846 \pm 404 \pm 273$
30-35	$915 \pm 43$	$1283 \pm 193$	$1831 \pm 971$	$877 \pm 111$	$891 \pm 278$	$1283 \pm 547 \pm 180$
35-45	$1247 \pm 51$	$1732 \pm 190$	$1965 \pm 882$	$1359 \pm 111$	$1330 \pm 277$	$1732 \pm 232 \pm 178$
45-55	$820 \pm 41$	$673 \pm 207$	$1199 \pm 485$	$698 \pm 118$	$933 \pm 65$	$673 \pm 526 \pm 196$
55-65	$654 \pm 37$	$956 \pm 302$	$1010 \pm 157$	$566 \pm 95$	$666 \pm 152$	$956 \pm 53 \pm 296$
65-75	$440 \pm 30$	$625 \pm 252$	$756 \pm 47$	$357 \pm 99$	$458 \pm 123$	$625 \pm 131 \pm 248$
75-85	$295 \pm 25$	$367 \pm 137$	$516 \pm 134$	$339 \pm 45$	$285 \pm 84$	$367 \pm 148 \pm 132$
85-95	$234 \pm 22$	$364 \pm 29$	$366 \pm 33$	$315 \pm 63$	$283 \pm 83$	$364 \pm 1 \pm 2$
95-120	$318 \pm 26$	$430 \pm 88$	$555 \pm 66$	$397 \pm 77$	$400 \pm 135$	$430 \pm 124 \pm 78$
120-500	$429 \pm 30$	$743 \pm 234$	$734 \pm 40$	$568 \pm 54$	$537 \pm 236$	$743 \pm 9 \pm 231$

Table 5.12: Results of the background subtraction based on fits of different variables.  $W\gamma$ , electron channel, endcap photons.

bin lims	MC pred	data $I_{ch}^{\gamma}$	data $\sigma_{inj}^{\gamma}$	MC cl. $I_{ch}^{\gamma}$	MC cl. $\sigma_{inj}^{\gamma}$	yield average
10-15	$4368 \pm 96$	$-1785 \pm 122$	$4129 \pm 1180$	$2286 \pm 1356$	$-1502 \pm 1196$	$-1785 \pm 5915 \pm 108$
15-20	$2253 \pm 68$	$-241 \pm 537$	$1869 \pm 762$	$1541 \pm 483$	$352 \pm 759$	$-241 \pm 2110 \pm 506$
20-25	$1177 \pm 49$	$637 \pm 298$	$1679 \pm 534$	$1308 \pm 192$	$1414 \pm 481$	$637 \pm 1042 \pm 277$
25-30	$574 \pm 34$	$887 \pm 147$	$1078 \pm 646$	$674 \pm 117$	$1125 \pm 370$	$887 \pm 190 \pm 131$
30-35	$445 \pm 31$	$731 \pm 107$	$555 \pm 249$	$451 \pm 119$	$355 \pm 155$	$731 \pm 176 \pm 96$
35-45	$638 \pm 37$	$943 \pm 116$	$1071 \pm 326$	$773 \pm 76$	$789 \pm 189$	$943 \pm 127 \pm 104$
45-55	$287 \pm 24$	$478 \pm 106$	$449 \pm 449$	$307 \pm 67$	$347 \pm 78$	$478 \pm 28 \pm 95$
55-65	$237 \pm 22$	$287 \pm 155$	$433 \pm 44$	$225 \pm 51$	$220 \pm 114$	$287 \pm 145 \pm 150$
65-75	$194 \pm 21$	$255 \pm 73$	$372 \pm 38$	$154 \pm 45$	$37 \pm 87$	$255 \pm 116 \pm 67$
75-85	$137 \pm 18$	$210 \pm 47$	$236 \pm 28$	$201 \pm 59$	$155 \pm 73$	$210 \pm 25 \pm 40$
85-95	$81 \pm 14$	$118 \pm 47$	$128 \pm 30$	$146 \pm 39$	$44 \pm 40$	$118 \pm 10 \pm 40$
95-120	$166 \pm 20$	$233 \pm 51$	$211 \pm 21$	$224 \pm 21$	$192 \pm 49$	$233 \pm 21 \pm 46$
120-500	$145 \pm 18$	$276 \pm 21$	$254 \pm 24$	$227 \pm 31$	$194 \pm 46$	$276 \pm 22 \pm 3$

### 5.5.2 Other sources of the systematic uncertainties

The next significant uncertainty after the uncertainty due to jets $\rightarrow\gamma$  background estimation in the electron channel is the uncertainty due to  $e\rightarrow\gamma$  background estimation. This uncertainty is comprised of a fit bias and a statistical power of the MC samples used for this background estimation.

The uncertainty due to fit bias is taken into account by fitting Z-peak before and after  $M_T^W$  cut is applied. Other selection cuts are applied except Z-mass window

cut. The fits plots of the datasets before and after  $M_W^T$  cut applied are shown in App. .8 and .7 respectively.

Another source of uncertainty comes from the limited statistics of all MC samples involved in the  $e \rightarrow \gamma$  background estimation. The uncertainty is propagated through the unfolding,  $A \times \epsilon$  correction, is divided over the luminosity and the bin width (for the differential cross section). Values of  $e \rightarrow \gamma$  uncertainties from both sources are summarized in Tab. 5.17.

For the real- $\gamma$  background subtraction, the statistical uncertainties of  $Z\gamma$  and  $W\gamma \rightarrow \tau\nu\gamma$  samples and their normalization uncertainties are taken into account. The normalization uncertainty applied for the  $Z\gamma$  sample is 4.6% and for the  $W\gamma \rightarrow \tau\nu\gamma$  is 20%. The  $Z\gamma$  normalization uncertainty is dominant out of the four sources to the real- $\gamma$  background subtraction.

For differential cross section, the statistical uncertainty on the signal MC sample is taken into account for the unfolding uncertainty. It is done with the randomization of the migration matrix. The procedure is the following:

- randomize migration matrix 100 times according with the signal MC statistical uncertainties in each  $[P_T^{gen}, P_T^{reco}]$  bin;
- the unfolding is applied for each migration matrix;
- the standard deviation out of 100 unfolding outputs is taken as a error;
- the error is propagated through the  $A \times \epsilon$  correction and is divided over the luminosity and the bin width.

For the uncertainty due to the  $A \times \epsilon$  correction, the signal MC statistical power

is also taken into account. To estimate this uncertainty, we take the value of

$$\Delta N_{true}^i = N_{acc}^i \cdot \frac{\Delta(A \times \epsilon)^i}{((A \times \epsilon)^i)^2}, \quad (5.8)$$

where  $N_{acc}$  is an yield for given bin after unfolding but before  $A \times \epsilon$  correction. Then the uncertainty is divided over the luminosity and the bin width (for the differential cross section).

Another source of the systematic uncertainty is the uncertainty of  $E_T^{miss}$  mis-modeling in the MC. To estimate this uncertainty, we:

- vary the  $P_T$  of the photons, electrons (for the electron channel) and jets in the event by their uncertainties as prescribed by POG;
- sum up all the listed contributions as the Lorentz vectors and propagate their variations to the variation of  $E_T^{miss}$ ;
- recalculate  $M_T^W$ ;
- recompute  $A \times \epsilon$  and unfolding constants with the new  $M_T^W$  values;
- recompute the cross section values;
- take the spread in the cross section between the lower, upper and nominal  $M_T^W$  values as a systematic error.

The contribution from the uncertainties of the efficiency scale factors are also estimated. The scale factors are varied by  $\pm 1\sigma$ , then the  $A \times \epsilon$  and unfolding constants are recomputed and new values of the cross section are found. The spread in the cross section between the  $+1\sigma$ ,  $-1\sigma$  and the nominal scale factor values is taken as a systematic uncertainty.

The systematic error due to pileup reweighting is estimated by varying the pileup cross section by  $\pm 5\%$ . The luminosity uncertainty is 2.6%.

### 5.5.3 Results

The relative systematic uncertainties are summarized in Tab. 5.13 and Tab. 5.14 for the muon and electron channels respectively. When systematic uncertainties are propagated through unfolding, a correlation matrix appears for each such uncertainty. Correlation matrices for different systematic uncertainties are plotted in App. .11.

Table 5.13: Relative errors [%].  $W\gamma$ , muon channel. The details of the “syst other” column are provided in Tab. 5.15.

bin lims	err stat	syst $ N_{I^{ch}} - N_{\sigma i \eta i \eta} $	$Z\gamma$ MC norm	templ stat	SFs err	syst lumi	syst other	syst total
total	1	10	24	4	2	3	4	27
15-20	2	31	12	10	3	3	6	35
20-25	2	29	13	11	1	3	6	34
25-30	2	24	13	11	1	3	5	30
30-35	3	40	15	13	2	3	7	45
35-45	2	11	12	8	2	3	6	19
45-55	4	62	19	20	2	3	8	68
55-65	3	15	12	14	1	3	7	24
65-75	6	36	19	17	1	3	10	44
75-85	4	6	11	16	1	3	10	21
85-95	5	2	9	23	1	3	13	25
95-120	5	10	8	12	1	3	9	18
120-500	3	4	11	21	2	3	9	24

Table 5.14: Relative errors [%].  $W\gamma$ , electron channel. The details of the “syst other” and “ $e \rightarrow \gamma$ ” column are provided in Tab. 5.16 and 5.17 respectively.

bin lims	err stat	syst $ N_{I\gamma h} - N_{\pi\eta\eta\eta} $	$Z\gamma$ MC norm	templ stat	SFs err	syst lumi	$e \rightarrow \gamma$	syst other	syst total
total	2	15	35	5	19	3	4	5	44
15-20	8	80	27	19	17	3	18	11	90
20-25	7	38	20	14	12	3	11	10	48
25-30	5	25	16	12	14	3	8	8	36
30-35	5	35	14	12	14	3	3	8	42
35-45	3	14	13	8	18	3	2	7	28
45-55	8	53	20	22	36	3	7	11	71
55-65	7	17	12	30	44	3	5	10	58
65-75	7	23	15	32	44	3	4	11	61
75-85	8	32	17	27	44	3	6	13	64
85-95	9	9	7	9	40	3	8	14	44
95-120	7	19	9	14	44	3	5	11	51
120-500	4	12	6	24	39	3	1	9	48

Table 5.15: Relative systematic uncertainties [%] of smaller contributions.  $W\gamma$ , muon channel.

bin lims	syst other	real- $\gamma$ bkg	$A \times \epsilon$ MC stat	$M_T^W$ cut	PU weight	unf MC stat
total	4	1	0	1	4	1
15-20	6	2	1	1	4	2
20-25	6	3	2	2	4	3
25-30	5	3	2	2	2	2
30-35	7	4	3	1	4	3
35-45	6	3	3	2	3	2
45-55	8	3	3	1	4	5
55-65	7	2	4	2	4	3
65-75	10	2	6	3	5	6
75-85	10	1	7	3	3	5
85-95	13	2	8	4	6	7
95-120	9	2	7	2	2	6
120-500	9	1	6	1	4	4

Table 5.16: Relative systematic uncertainties [%] of smaller contributions.  $W\gamma$ , electron channel.

bin lims	syst other	real- $\gamma$ bkg	$A \times \epsilon$ MC stat	$M_T^W$ cut	PU weight	unf MC stat
total	5	2	0	1	4	2
15-20	11	6	2	1	4	8
20-25	10	5	2	1	4	7
25-30	8	3	3	1	3	6
30-35	8	2	4	1	3	6
35-45	7	1	4	1	4	4
45-55	11	2	5	3	4	9
55-65	10	2	5	3	5	7
65-75	11	1	6	1	4	8
75-85	13	2	8	2	3	9
85-95	14	2	9	2	2	9
95-120	11	1	8	1	4	7
120-500	9	1	7	2	3	4

Table 5.17: Relative systematic uncertainties [%] of  $e \rightarrow \gamma$  background estimation.  $W\gamma$ , electron channel.

bin lims	$e \rightarrow \gamma$	$e \rightarrow \gamma$ y/n $M_T^W$ cut	$e \rightarrow \gamma$ samp. stat
total	4	4	1
15-20	18	17	4
20-25	11	10	4
25-30	8	7	3
30-35	3	1	2
35-45	2	1	1
45-55	7	4	5
55-65	5	3	4
65-75	4	1	4
75-85	6	4	4
85-95	8	5	6
95-120	5	3	4
120-500	1	0	1

## 5.6 Cross Section

The cross section is computed as described in the beginning of Ch. 5. For comparison purposes, in addition to the measured cross section, we also estimate the cross section based on the signal MC sample which is referred as the MC-based cross section.

The cross section of the whole simulated sample was computed with MCFM in NLO and is for the dedicated signal MC sample  $\sigma_1 = 553.92 \text{ pb}$ . The MC sample was generated with MadGraph, and the cross section in our selected phase space was computed as

$$\sigma_2 = \sigma_1 \cdot N_2 / N_1,$$

where  $N_2$  and  $N_1$  are numbers of events falling into selected phase space and generated in the whole MC sample respectively. For the differential cross section,  $N_2$  is number of events falling into specific  $P_T^\gamma$  bin and to compute

$$\frac{d\sigma}{dP_T^\gamma},$$

we divide over the bin width.

Tables 5.18-5.19 and Fig. 5.10 summarize the results. The measured cross section agrees with the MC-based cross section within the estimated errors. The measurement is systematically-dominated.

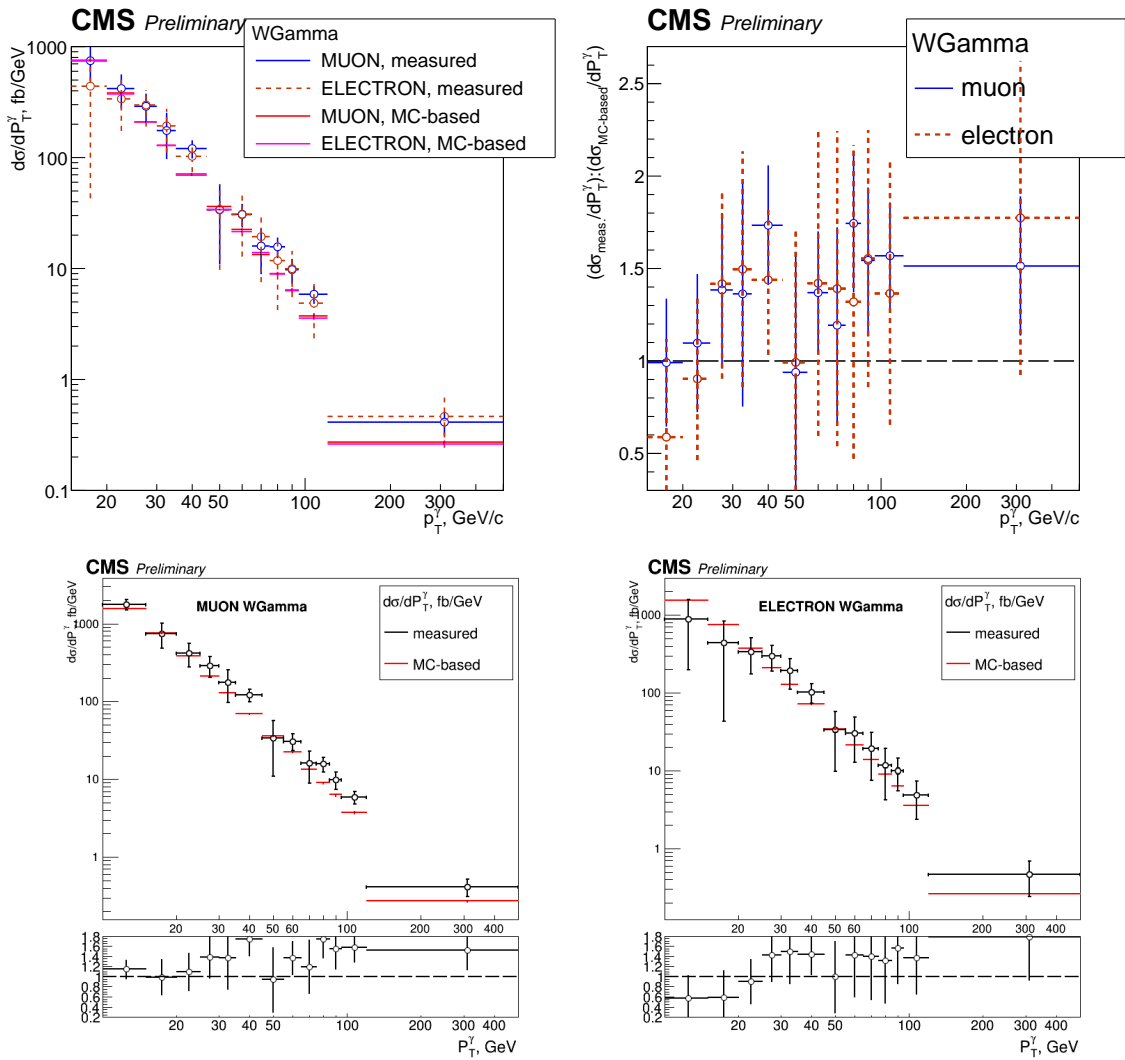
For additional validation of the measurement procedure, we estimate the cross section of  $Z\gamma$  and compare the result with the published CMS result for  $Z\gamma$  at 8 TeV. The summary of this  $Z\gamma$  check is available in App. .13.

Table 5.18: Cross section and errors.  $W\gamma$ , muon channel.

bin lims	$d\sigma/dP_T$ MC based	$d\sigma/dP_T$ meas.
total	9139	$10949 \pm 91 \pm 2959$
15-20	754	$747 \pm 17 \pm 260$
20-25	382	$419 \pm 10 \pm 142$
25-30	210	$290 \pm 6 \pm 87$
30-35	129	$175 \pm 5 \pm 78$
35-45	70	$121 \pm 2 \pm 22$
45-55	36	$34 \pm 1 \pm 23$
55-65	23	$31 \pm 1 \pm 7$
65-75	13	$16 \pm 1 \pm 7$
75-85	9	$16 \pm 1 \pm 3$
85-95	6.3	$9.8 \pm 0.5 \pm 2.4$
95-120	3.7	$5.9 \pm 0.3 \pm 1.0$
120-500	0.27	$0.41 \pm 0.01 \pm 0.10$

Table 5.19: Cross section and errors.  $W\gamma$ , electron channel.

bin lims	$d\sigma/dP_T$ MC based	$d\sigma/dP_T$ meas.
total	9064	$9146 \pm 185 \pm 3981$
15-20	749	$440 \pm 35 \pm 396$
20-25	375	$338 \pm 23 \pm 163$
25-30	210	$298 \pm 16 \pm 107$
30-35	129	$193 \pm 9 \pm 82$
35-45	71	$103 \pm 3 \pm 29$
45-55	34	$34 \pm 3 \pm 24$
55-65	22	$31 \pm 2 \pm 18$
65-75	14	$19 \pm 1 \pm 12$
75-85	9	$12 \pm 1 \pm 8$
85-95	6.4	$10.0 \pm 0.9 \pm 4.3$
95-120	3.6	$4.9 \pm 0.4 \pm 2.5$
120-500	0.26	$0.46 \pm 0.02 \pm 0.22$

Figure 5.10:  $W\gamma$  differential cross section.

## .1 APPENDIX: $Z\gamma$ FSR and ISR Plots

Data sample selected in  $Z\gamma \rightarrow \mu\mu\gamma$  conditions where photon selection is the same as for  $W\gamma$  selection is used to prepare real- $\gamma$  and fake- $\gamma$  templates for the jets $\rightarrow\gamma$  background estimation. The distributions of three-particle invariant mass  $M_{\mu\gamma\gamma}$ , of the invariant mass of the dimuon system  $M_{\mu\mu}$  (Fig. .11), and of the separation between the muon and the photon  $\Delta R(\mu, \gamma)$  (Fig. .12) are used to split the dataset into the FSR sample which is dominated by real- $\gamma$  events and the ISR sample which is a mixture of real- $\gamma$  and fake- $\gamma$  events. The FSR sample is used to prepare real- $\gamma$  templates, and the fake- $\gamma$  contribution into the region is subtracted based on DY+jets MC predictions. The ISR sample is used to prepare fake- $\gamma$  templates, and the real- $\gamma$  contribution into the region is subtracted based on  $Z\gamma$  MC predictions. The number of real- $\gamma$  and fake- $\gamma$  events in different  $P_T^\gamma$  bins is shown in Fig. .13. Various  $I_{ch}^\gamma$  and  $\sigma_{i\eta i\eta}^\gamma$  templates are shown in Fig. .14-.19.

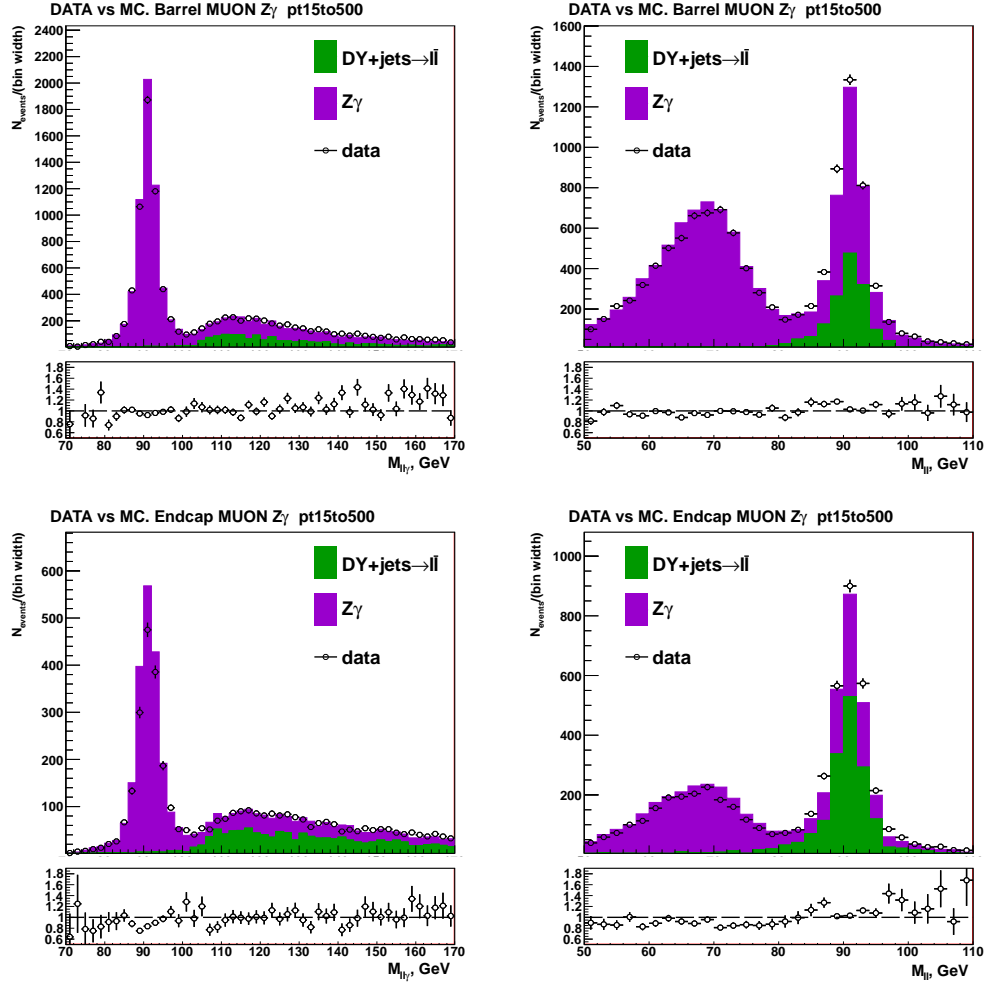


Figure .11:  $Z\gamma$ -selected events, data vs MC. Left:  $M_{ll\gamma}$ , right:  $M_{ll}$ . Top: barrel photons, bottom: endcap. Peak highly dominated by real- $\gamma$  corresponds to FSR events. FSR selection used:  $81 \text{ GeV} < M_{ll\gamma} < 101 \text{ GeV}$ ,  $\Delta R(l_{1,2}, \gamma) > 0.4$ ,  $\Delta R(l, \gamma)_{min} < 1.0$ ,  $M_{ll} < 80 \text{ GeV}$ . ISR selection used:  $80 \text{ GeV} < M_{ll} < 100 \text{ GeV}$ ,  $\Delta R(l_{1,2}, \gamma) > 1.0$ .

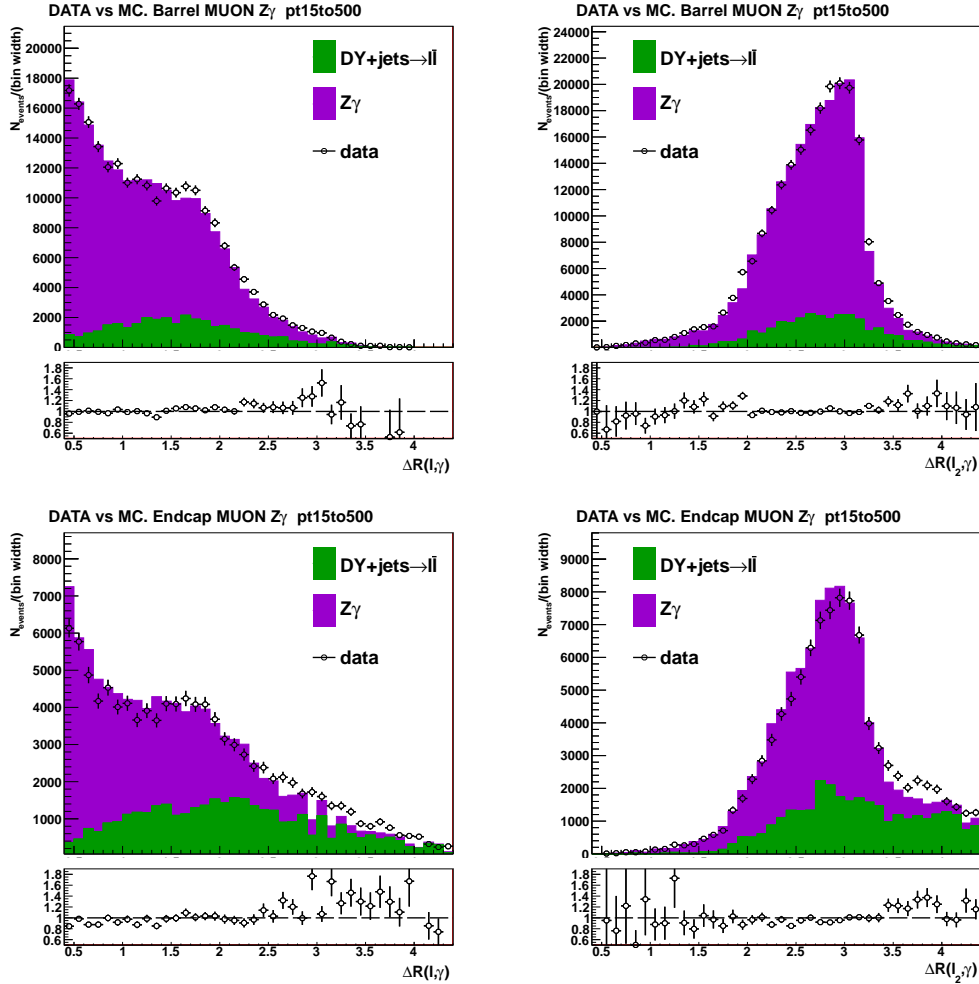


Figure .12:  $Z\gamma$ -selected FSR (top) and ISR (bottom) events, data vs MC. FSR selection used:  $81 \text{ GeV} < M_{ll\gamma} < 101 \text{ GeV}$ ,  $\Delta R(l_{1,2}, \gamma) > 0.4$ ,  $\Delta R(l, \gamma)_{\min} < 1.0$ ,  $M_{ll} < 80 \text{ GeV}$ . ISR selection used:  $80 \text{ GeV} < M_{ll} < 100 \text{ GeV}$ ,  $\Delta R(l_{1,2}, \gamma) > 1.0$ .

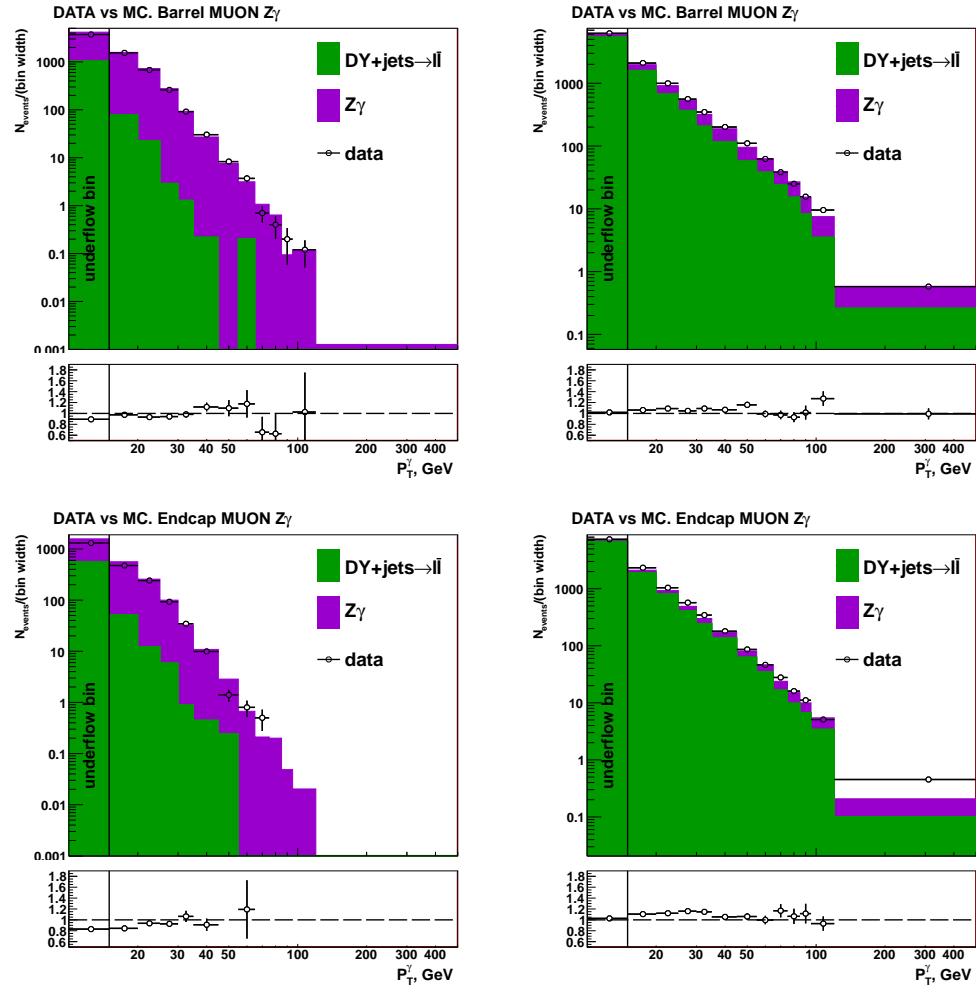


Figure .13:  $Z\gamma$ -selected FSR (left) and ISR (right) events, data vs MC. FSR selection used:  $81 \text{ GeV} < M_{ll\gamma} < 101 \text{ GeV}$ ,  $\Delta R(l_{1,2}, \gamma) > 0.4$ ,  $\Delta R(l, \gamma)_{min} < 1.0$ ,  $M_{ll} < 80 \text{ GeV}$ . ISR selection used:  $80 \text{ GeV} < M_{ll} < 100 \text{ GeV}$ ,  $\Delta R(l_{1,2}, \gamma) > 1.0$ .

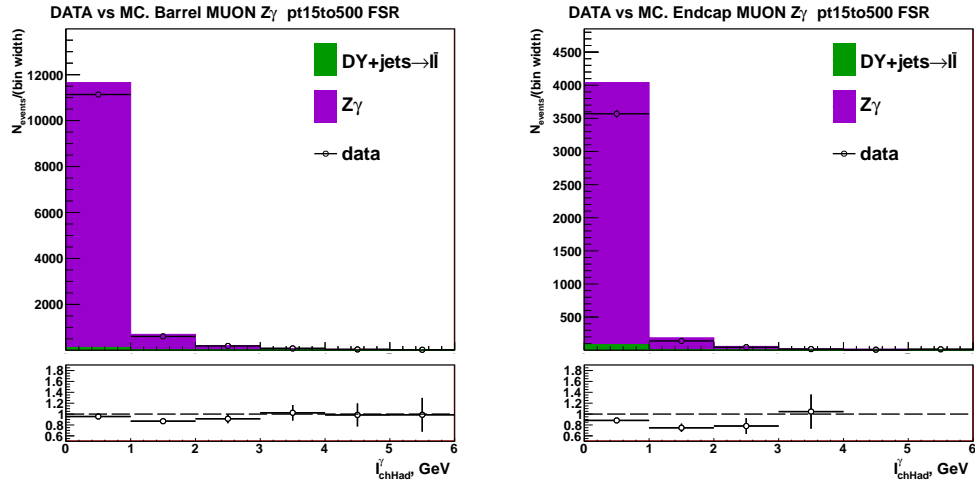


Figure .14:  $Z\gamma$ -selected FSR events, data vs MC.  $P_T^\gamma > 10$  GeV. Distributions of  $I_{chHad}^\gamma$  used for preparing real- $\gamma$  templates. Fake- $\gamma$  contribution to FSR region is subtracted based on DY+jets MC prediction to prepare real- $\gamma$  templates.

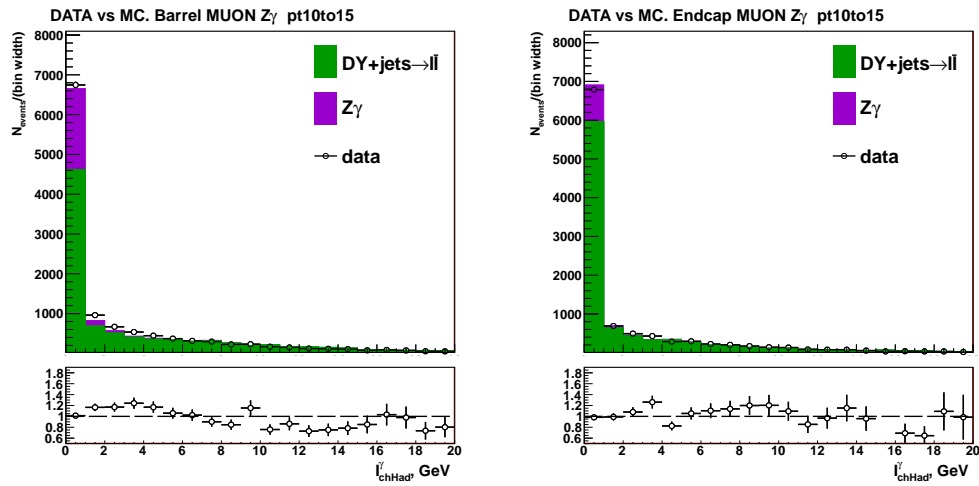


Figure .15:  $Z\gamma$ -selected ISR events, data vs MC.  $10 \text{ GeV} < P_T^\gamma < 15 \text{ GeV}$ . Distributions of  $I_{chHad}^\gamma$  used for preparing fake- $\gamma$  templates. Real- $\gamma$  contribution to ISR region is subtracted based on  $Z\gamma$  signal MC prediction to prepare fake- $\gamma$  templates.

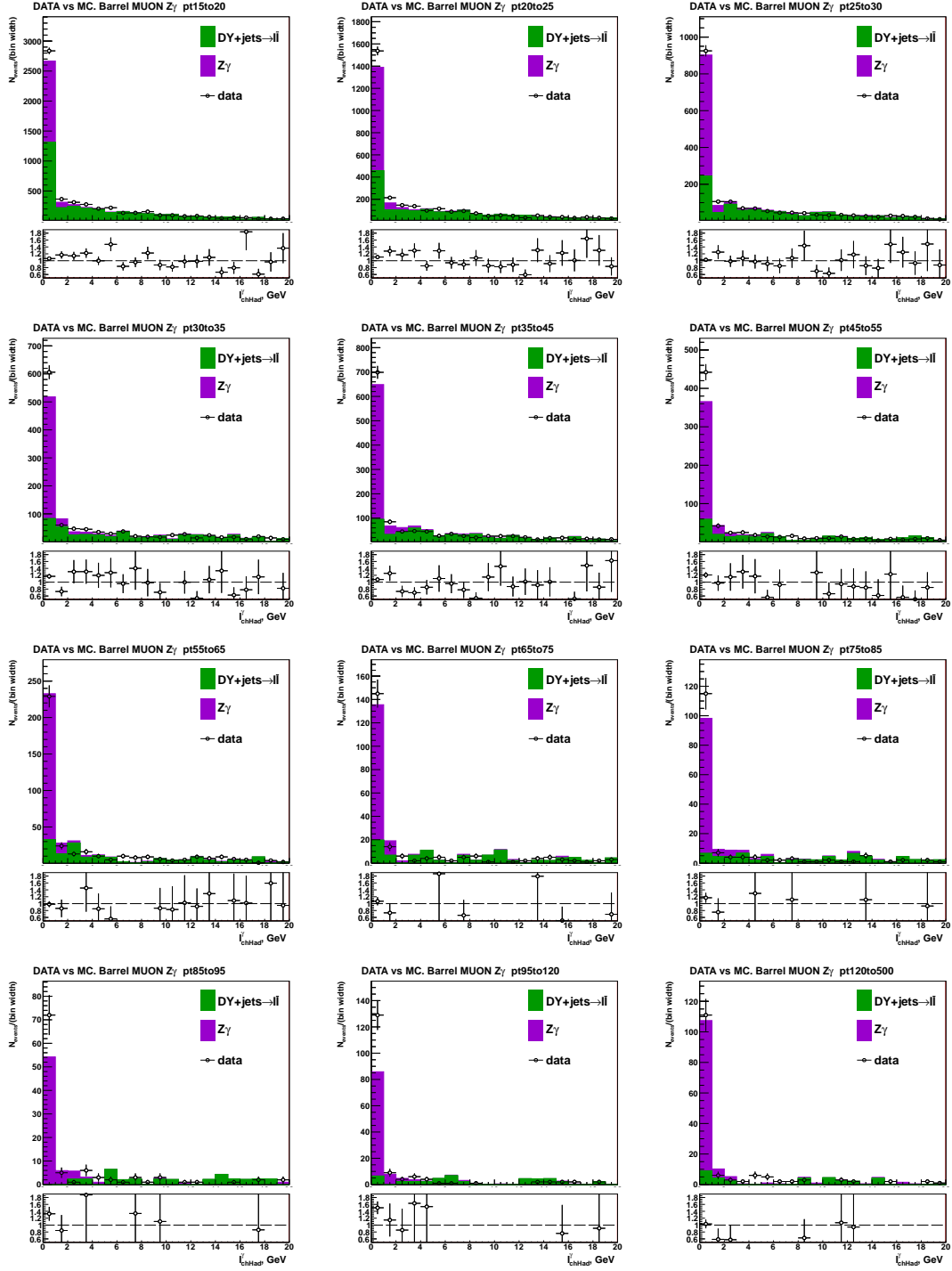


Figure .16:  $Z\gamma$ -selected ISR events, data vs MC.  $15 \text{ GeV} < P_T^\gamma < 500 \text{ GeV}$ , Barrel photons. Distributions of  $I_{chHad}^\gamma$  used for preparing fake- $\gamma$  templates. Real- $\gamma$  contribution to ISR region is subtracted based on  $Z\gamma$  signal MC prediction to prepare fake- $\gamma$  templates.

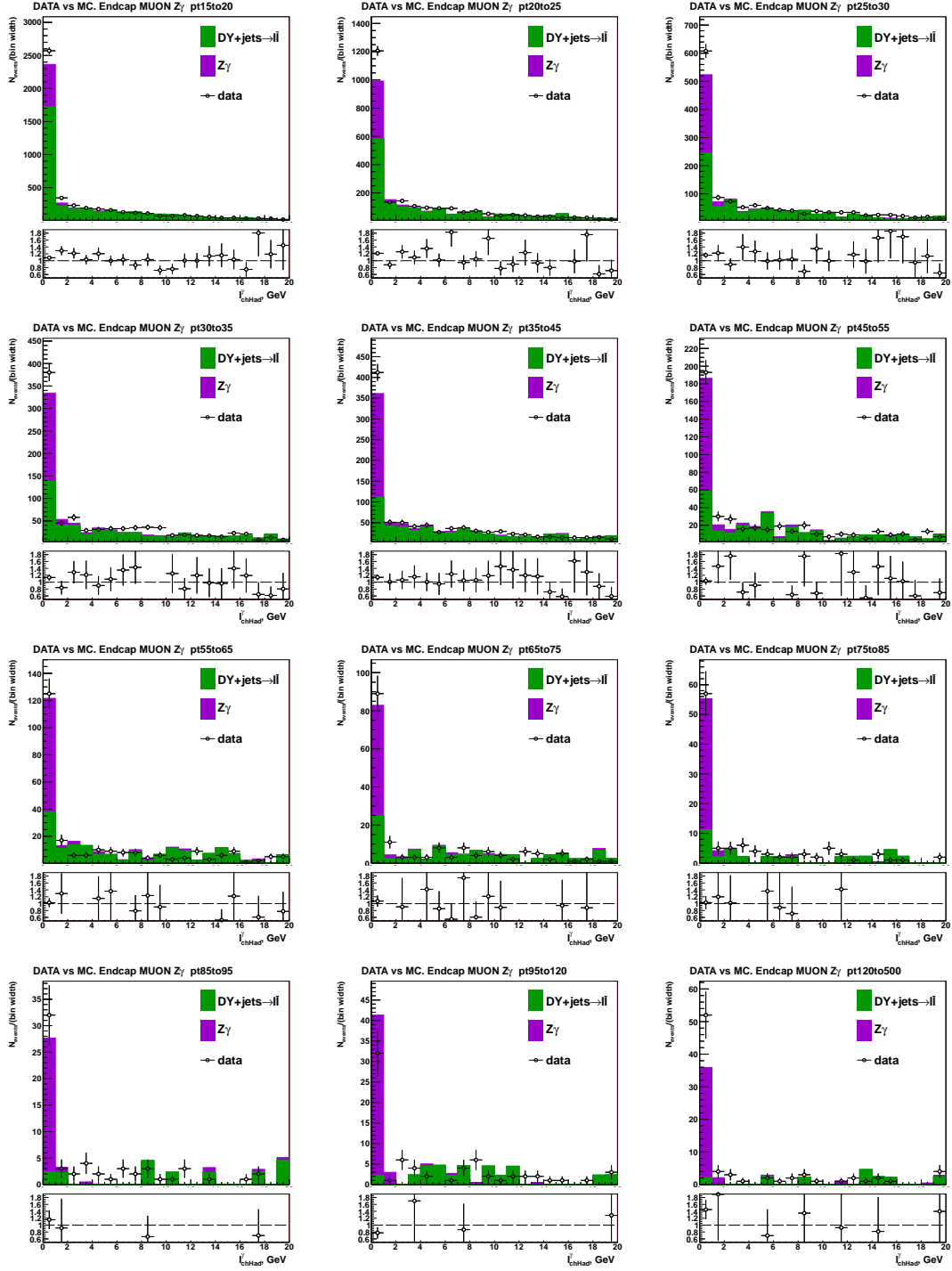


Figure .17:  $Z\gamma$ -selected ISR events, data vs MC.  $15 \text{ GeV} < P_T^\gamma < 500 \text{ GeV}$ , Endcap photons. Distributions of  $I_{chHad}^\gamma$  used for preparing fake- $\gamma$  templates. Real- $\gamma$  contribution to ISR region is subtracted based on  $Z\gamma$  signal MC prediction to prepare fake- $\gamma$  templates.

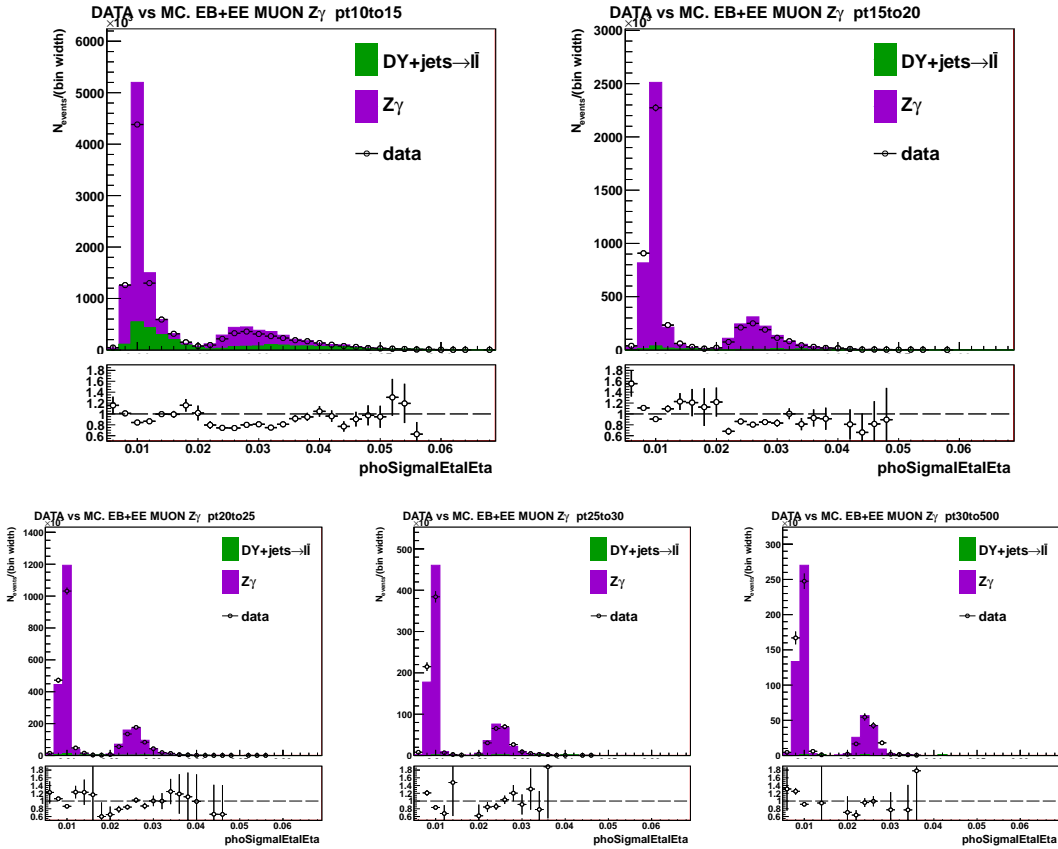


Figure .18:  $Z\gamma$ -selected FSR events, data vs MC. Distributions of  $\sigma_{i\eta i\eta}$  are used for preparing real- $\gamma$  templates. Fake- $\gamma$  contribution to FSR region is subtracted based on  $\text{DY+jets}$  MC prediction to prepare real- $\gamma$  templates. The templates are prepared separately for barrel and endcap photons.

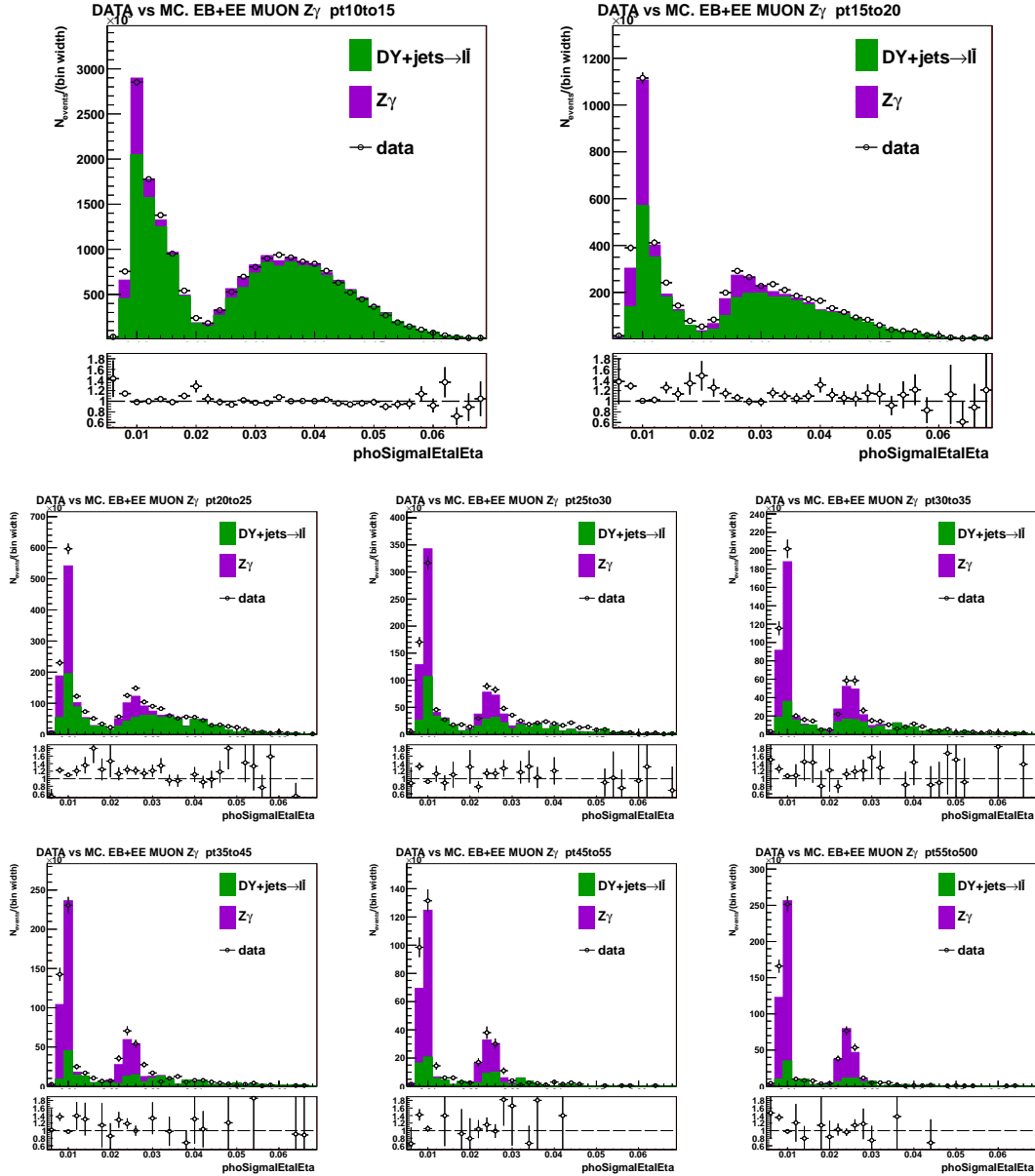


Figure .19:  $Z\gamma$ -selected ISR events, data vs MC. Distributions of  $\sigma_{i\eta i\eta}$  are used for preparing real- $\gamma$  templates. Fake- $\gamma$  contribution to ISR region is subtracted based on DY+jets MC prediction to prepare real- $\gamma$  templates. The templates are prepared separately for barrel and endcap photons.

## .2 APPENDIX: Studies of $E_T^{miss}$ Dependence of Templates

Figure .20 shows the  $I_{ch}^{\gamma}$  and  $\sigma_{i\eta i\eta}^{\gamma}$  fake- $\gamma$  templates. Black histograms represent nominal  $Z\gamma$  ISR selection while red histograms have additional cuts of  $E_T^{miss} > 10$  GeV and  $\Delta\phi(E_T^{miss}, \gamma) < 0.5$ . These histograms do not show template dependence of  $E_T^{miss}$ . Fig. .21-.24 show  $I_{ch}^{\gamma}$  and  $\sigma_{i\eta i\eta}^{\gamma}$  distributions of  $W\gamma$  and  $W+\text{jets}$  MC with different  $M_T^W$  cuts.

The  $\sigma_{i\eta i\eta}^{\gamma}$  distributions of  $W+\text{jets}$  for different  $M_T^W$  cuts are different which indicates  $\sigma_{i\eta i\eta}^{\gamma}$  fake template dependence of  $M_T^W$ . We use  $Z\gamma$ -selected sample to prepare fake- $\gamma$  and real- $\gamma$   $\sigma_{i\eta i\eta}^{\gamma}$  templates, and we cannot apply the same  $M_T^W$  cut on the sample as we apply in  $W\gamma$  selection. That causes a systematic uncertainty due to mismodeling of the  $\sigma_{i\eta i\eta}^{\gamma}$  shape. This uncertainty is covered of by comparison between fit results of  $\sigma_{i\eta i\eta}^{\gamma}$  and  $I_{ch}^{\gamma}$  templates.

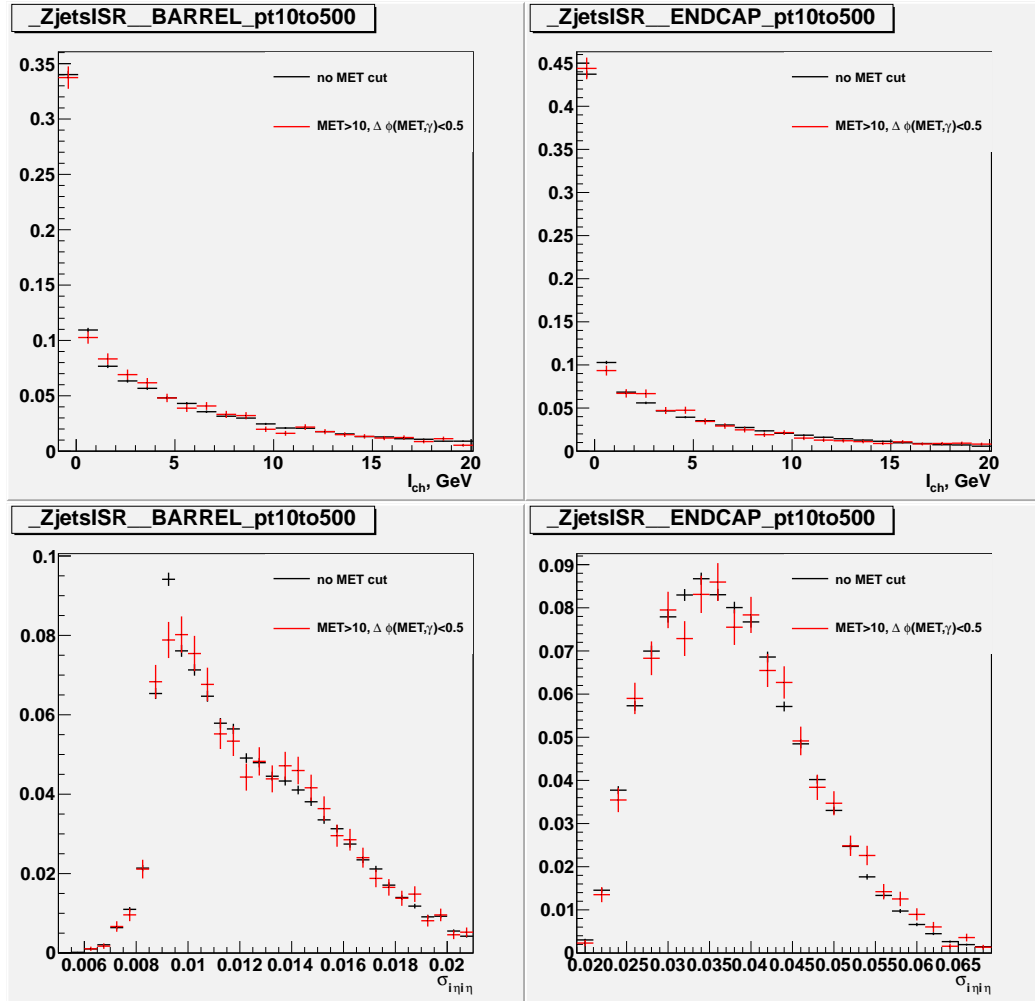


Figure .20:  $Z\gamma$  ISR-selected data (includes DY+jets and  $Z\gamma$  events),  $I_{ch}^\gamma$  (top) and  $\sigma_{i\eta i\eta}^\gamma$  (bottom) fake- $\gamma$  templates with and without  $E_T^{miss}$  cut.

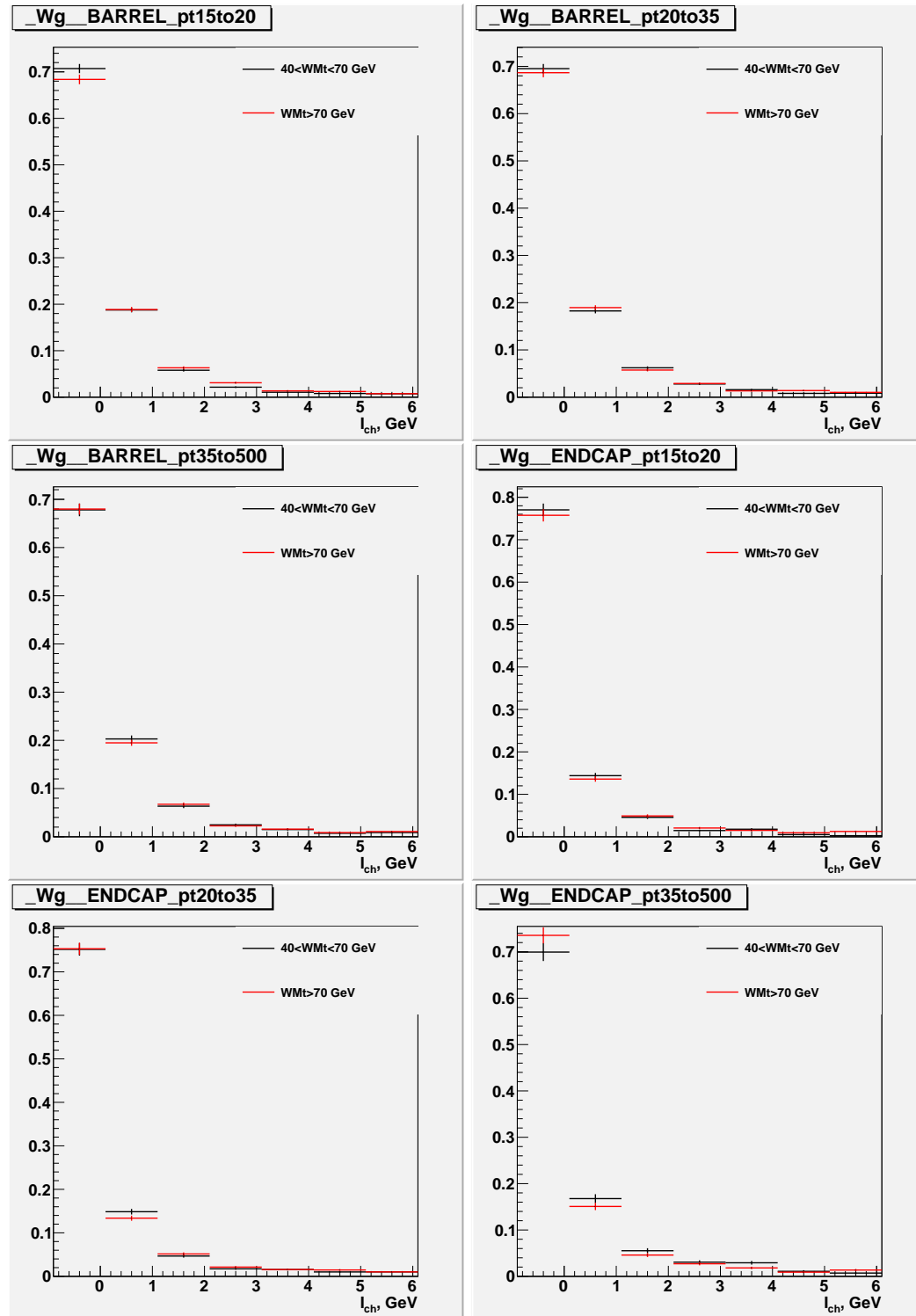
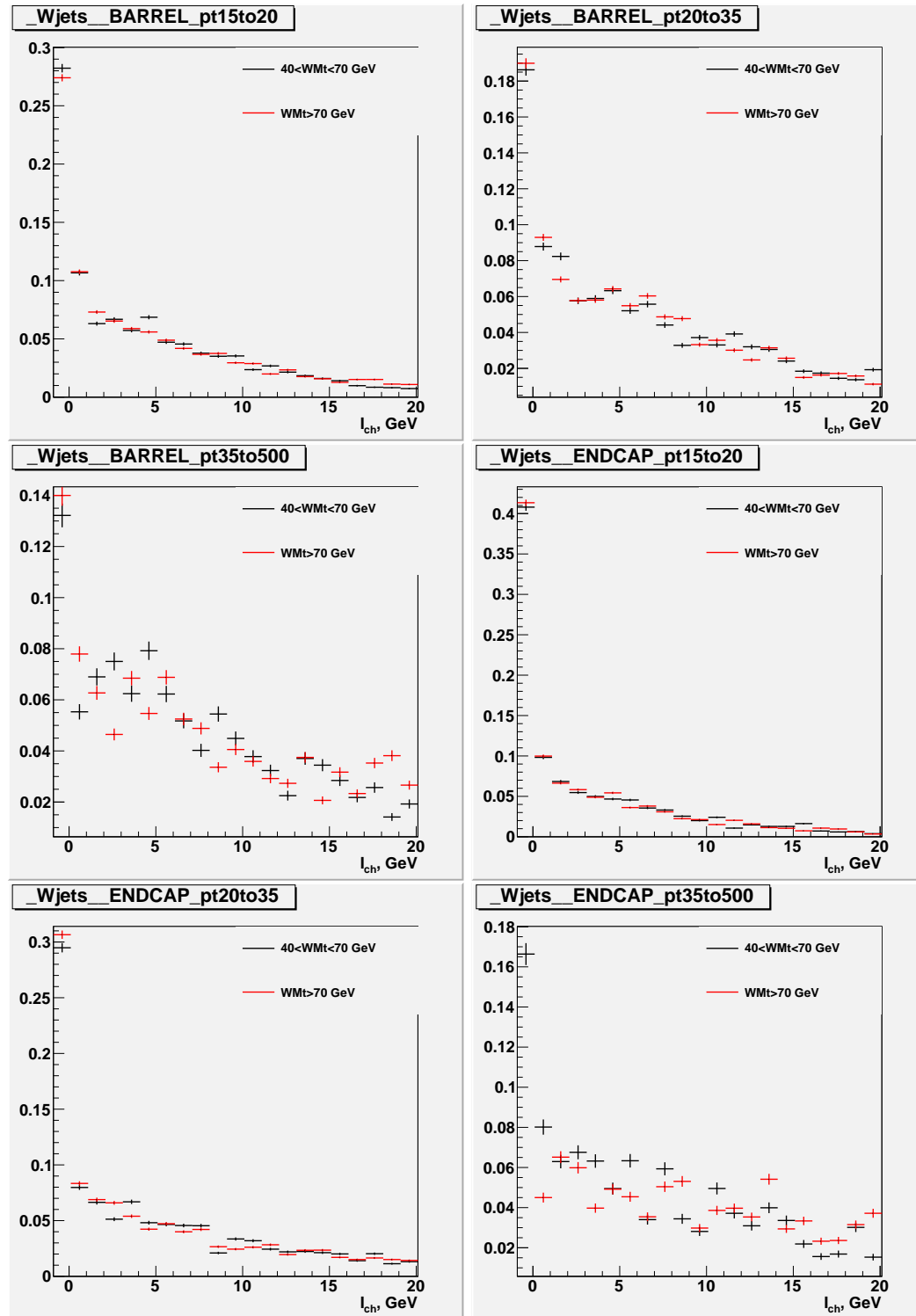


Figure .21:  $W\gamma, I_{ch}^\gamma$  templates.

Figure .22:  $W+jets, I_{ch}^{\gamma}$  templates

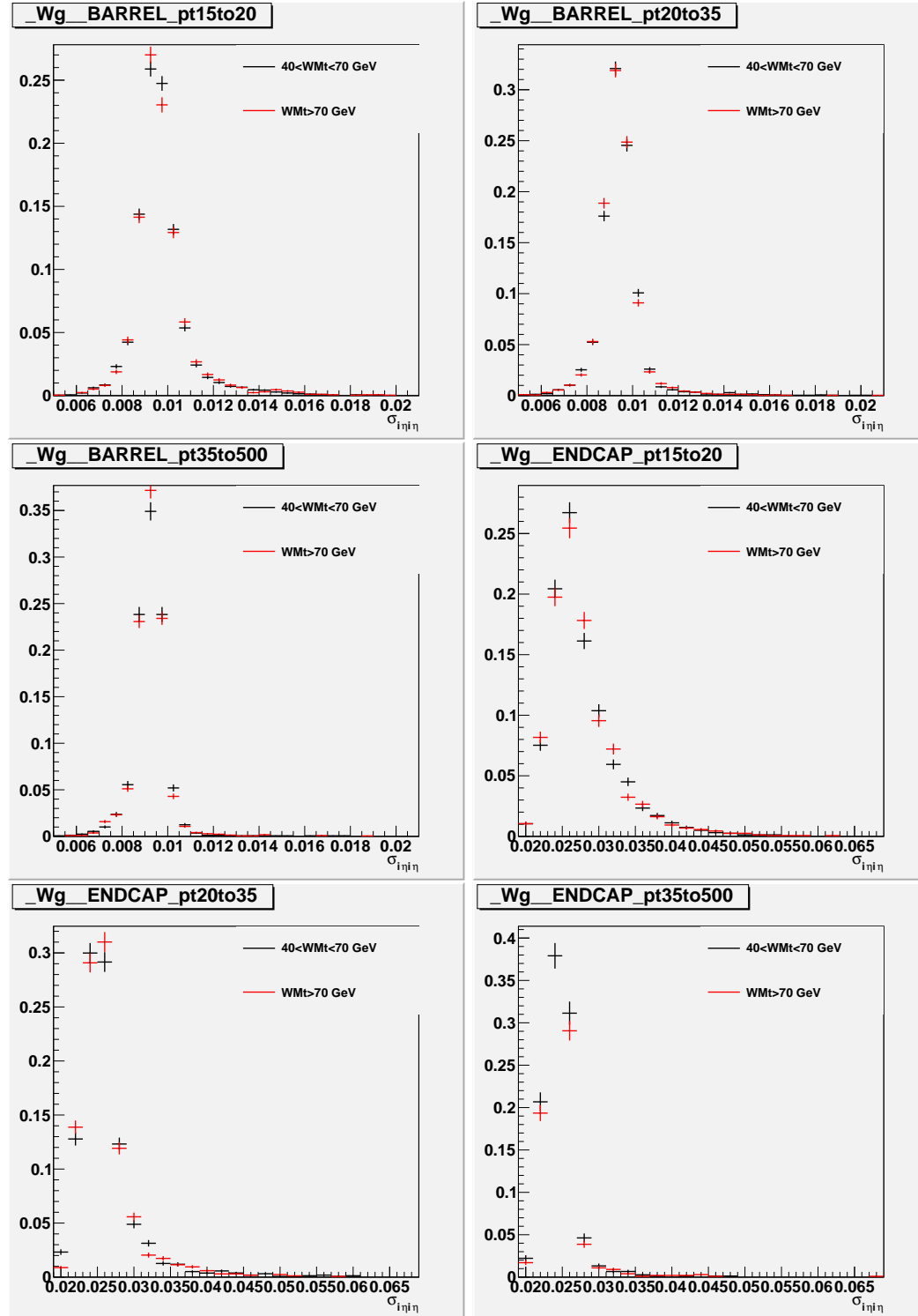
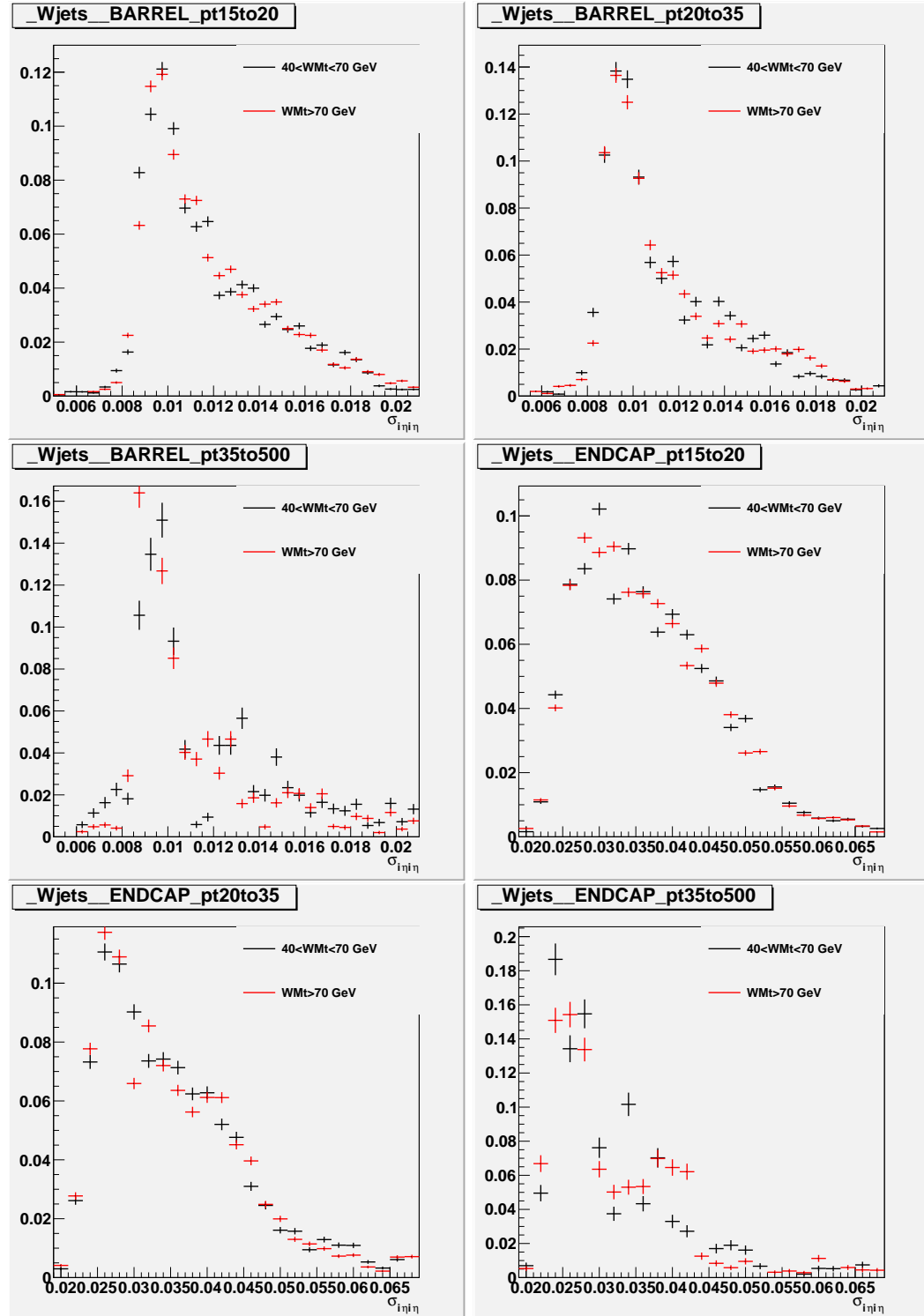


Figure .23:  $W\gamma, \sigma_{i\eta i\eta}^\gamma$  templates

Figure .24:  $W+jets$ ,  $\sigma_{i\eta i\eta}$  templates

### .3 APPENDIX: Template Fit Plots, $W\gamma$ , Data

This appendix contains fit results for jets $\rightarrow\gamma$  background estimation. On any plot, black histogram is data, green is a real- $\gamma$  template, blue is a fake- $\gamma$  template, and red is the fit function. These fits are part of the procedure of jets $\rightarrow\gamma$  background estimation which is described in Ch. 5.2.1.

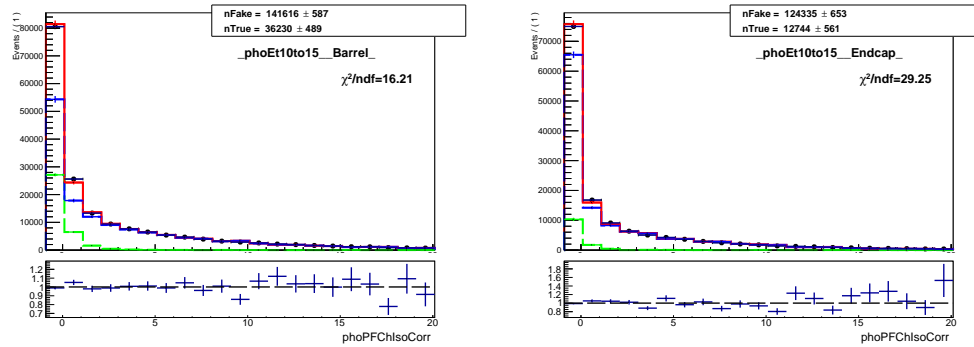


Figure .25: Fits of  $I_{ch}^{\gamma}$  templates,  $W\gamma$ , muon channel, underflow bin (10 – 15 GeV).

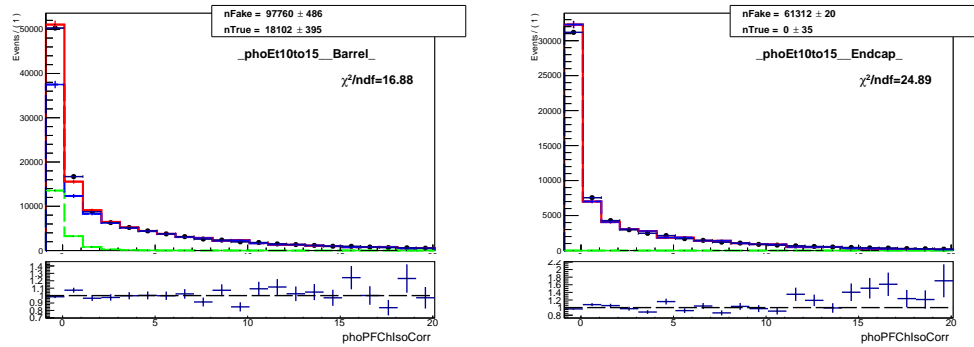


Figure .26: Fits of  $I_{ch}^{\gamma}$  templates,  $W\gamma$ , electron channel, underflow bin (10 – 15 GeV).

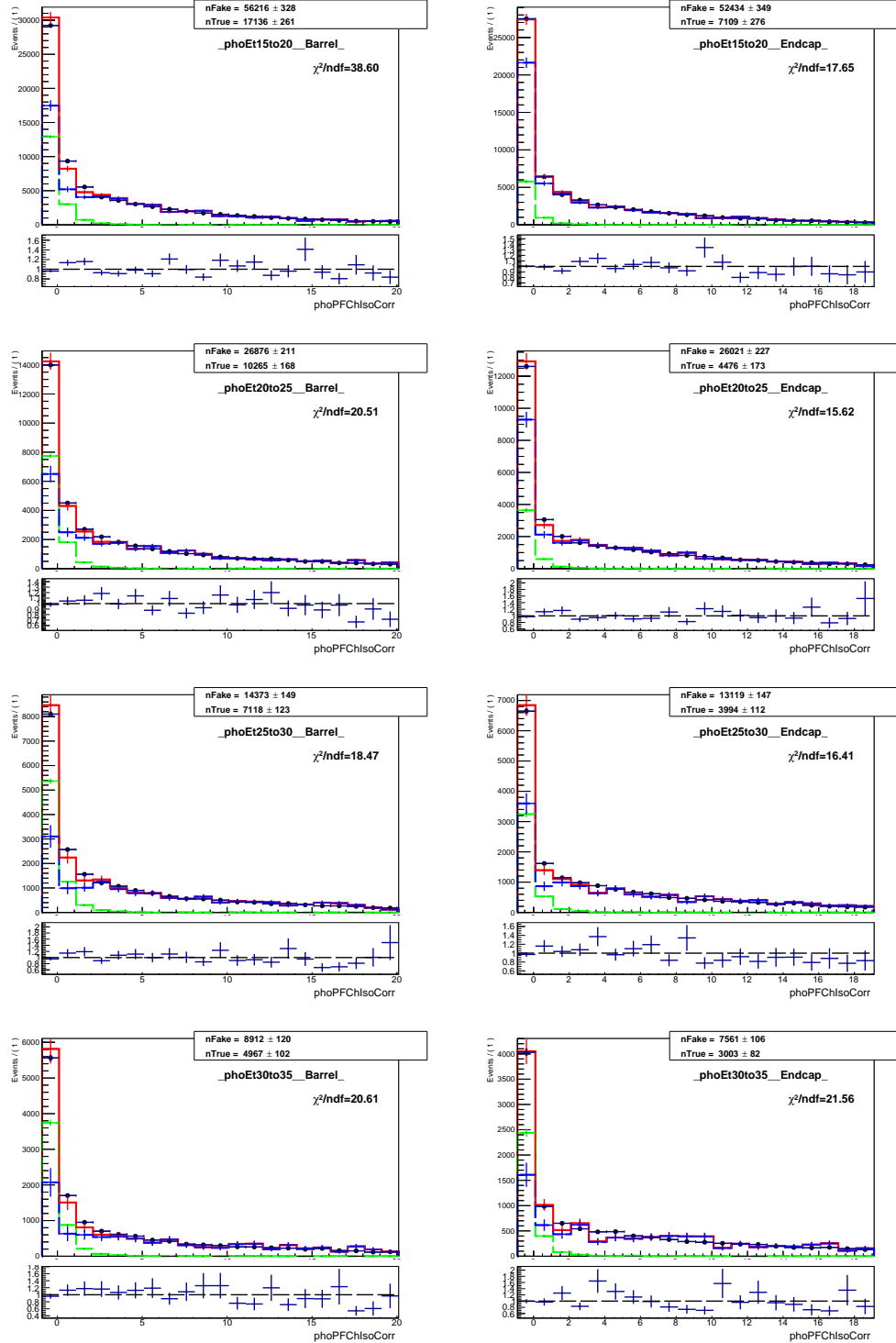


Figure .27: Fits of  $I_{ch}^{\gamma}$  templates,  $W\gamma$ , muon channel.

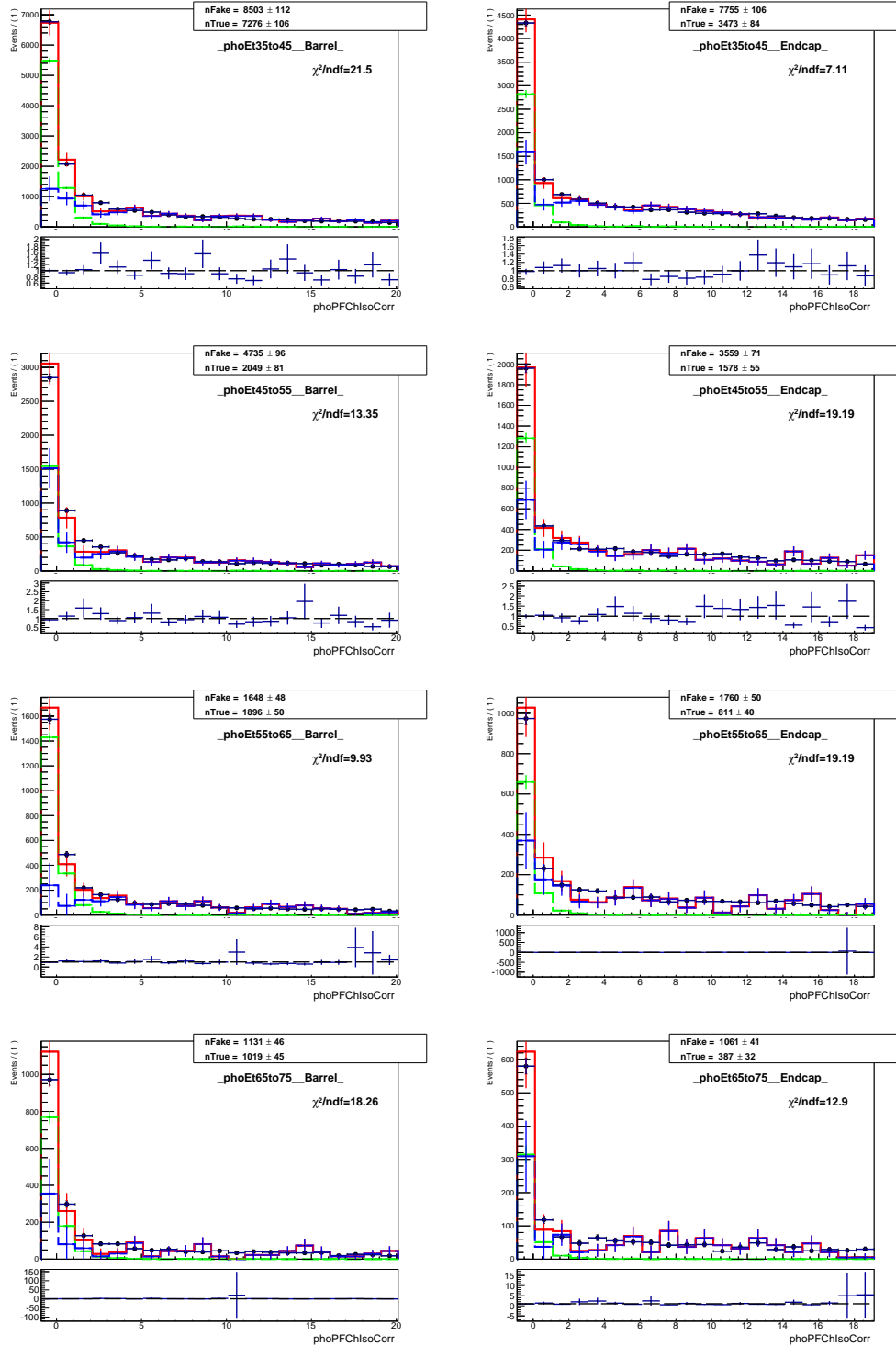


Figure .28: Fits of  $I_{ch}^{\gamma}$  templates,  $W\gamma$ , muon channel.

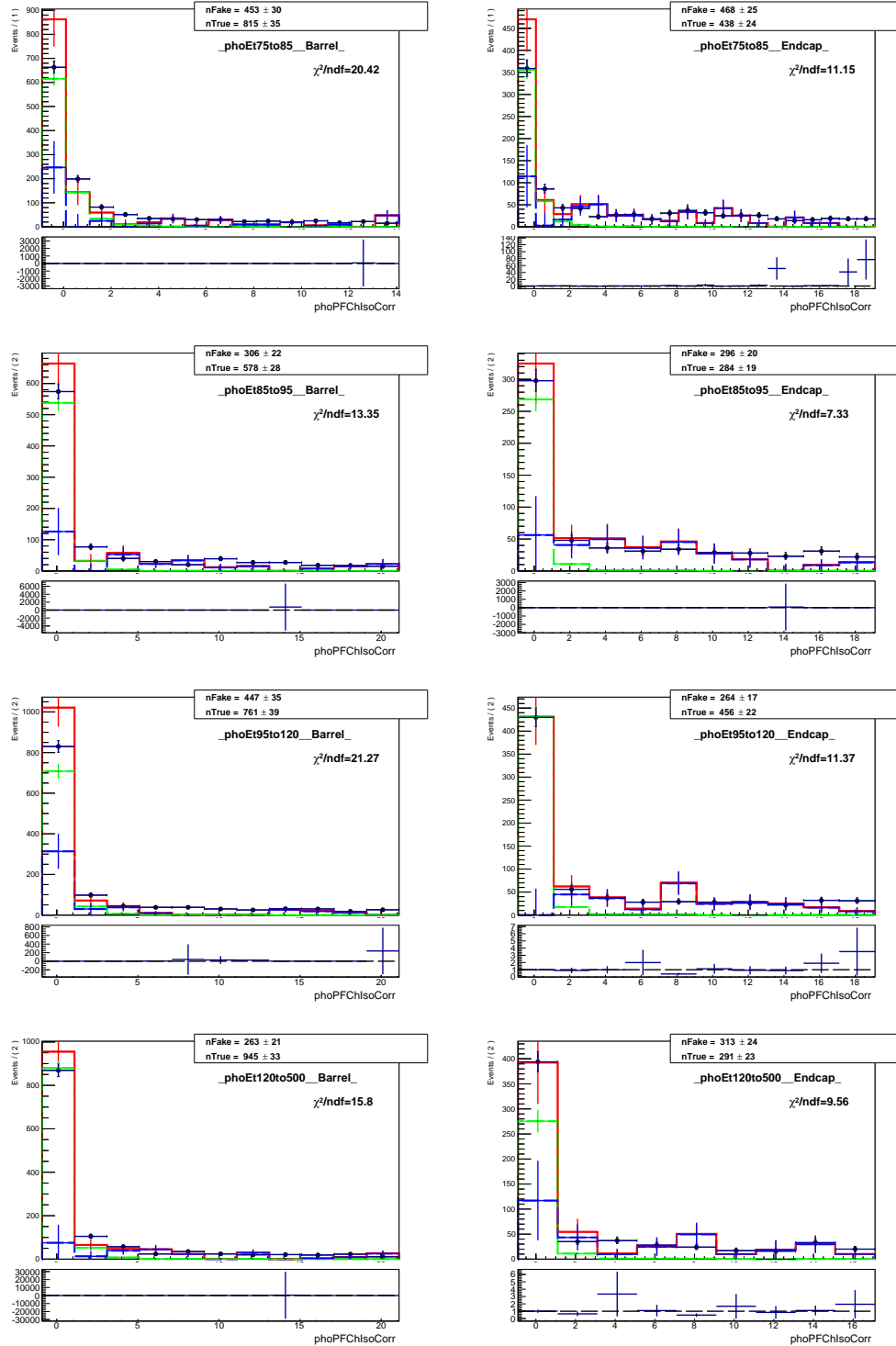


Figure .29: Fits of  $I_{ch}^{\gamma}$  templates,  $W\gamma$ , muon channel.

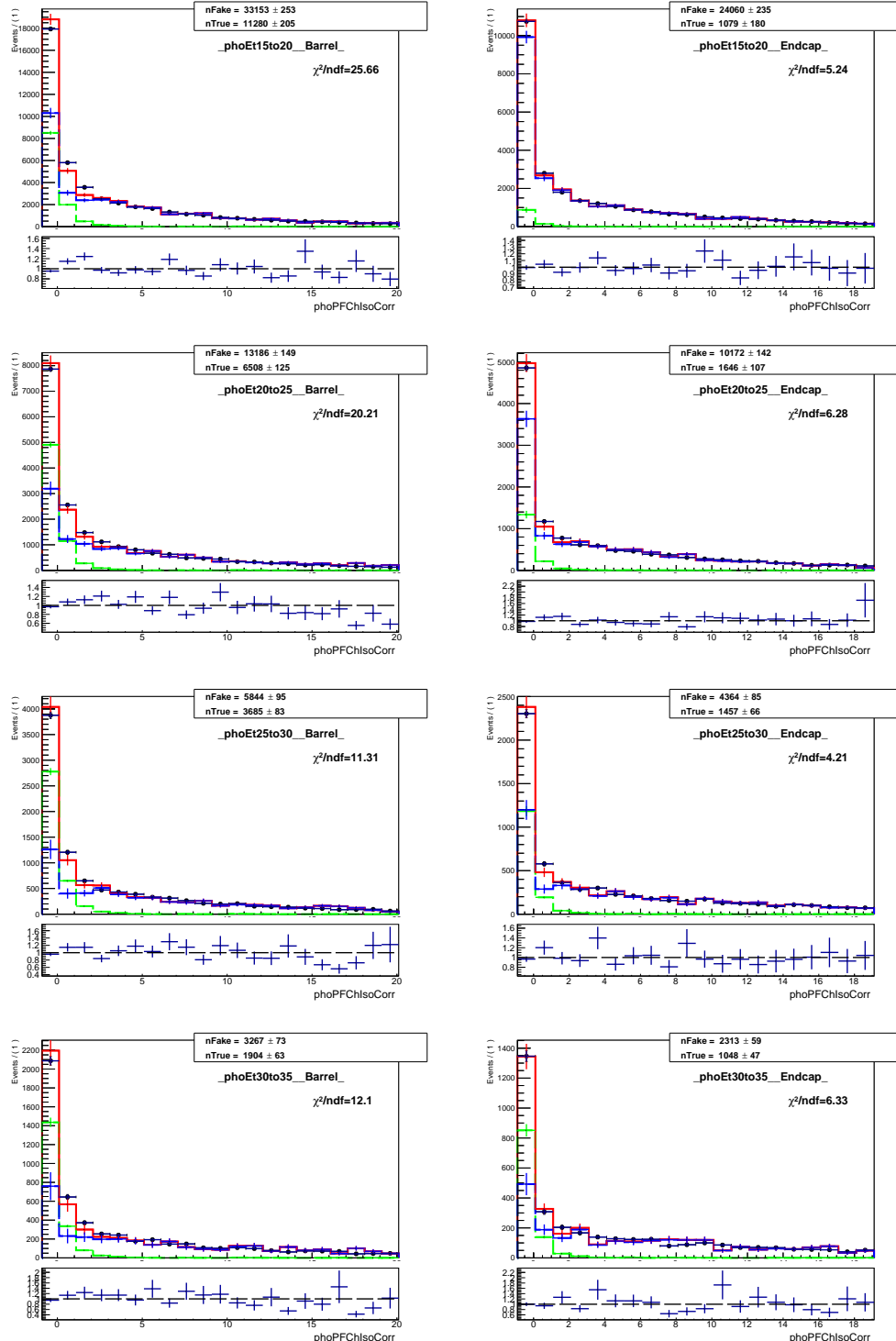


Figure .30: Fits of  $I_{ch}^{\gamma}$  templates,  $W\gamma$ , electron channel.

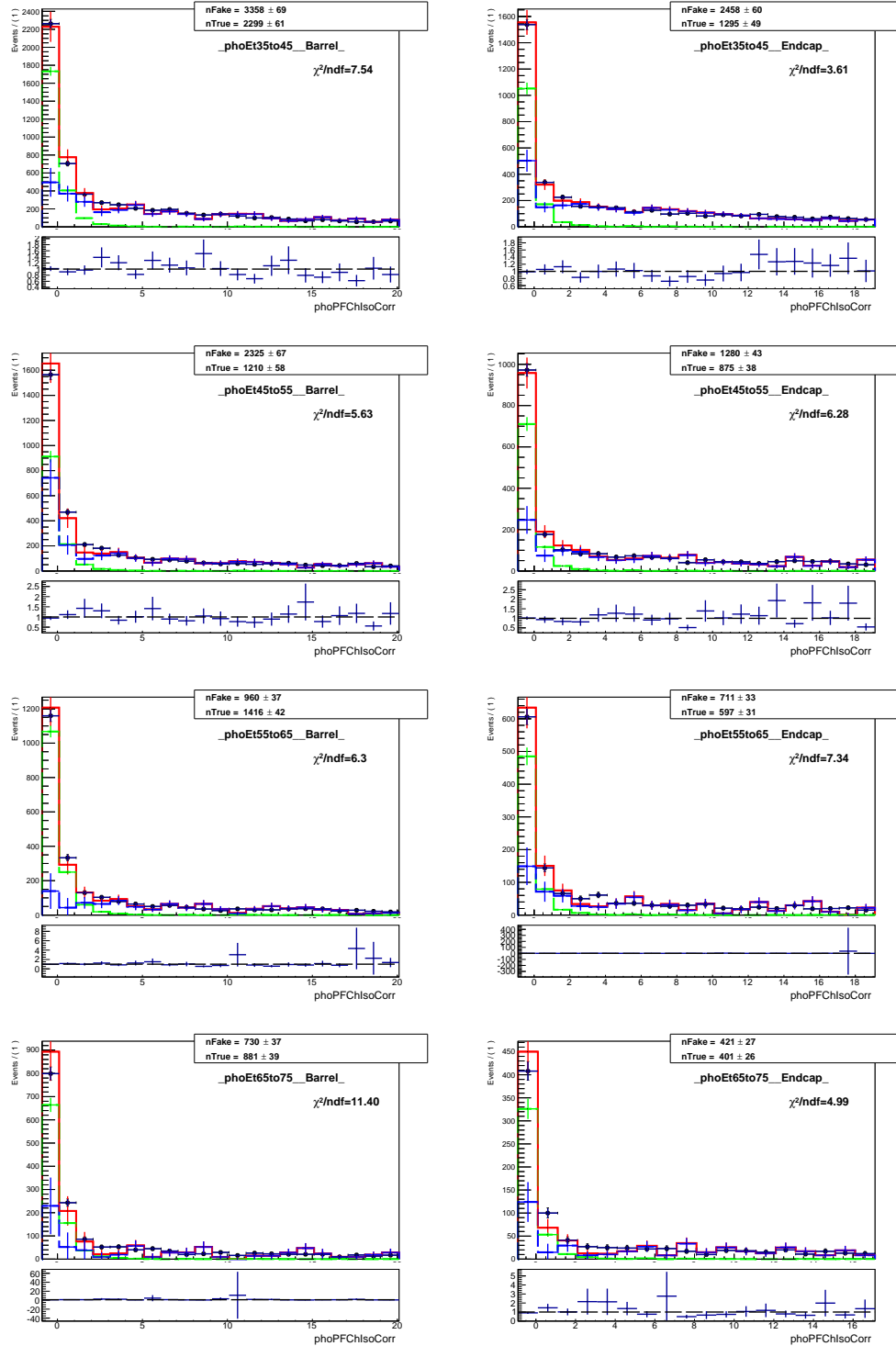


Figure .31: Fits of  $I_{ch}^{\gamma}$  templates,  $W\gamma$ , electron channel.

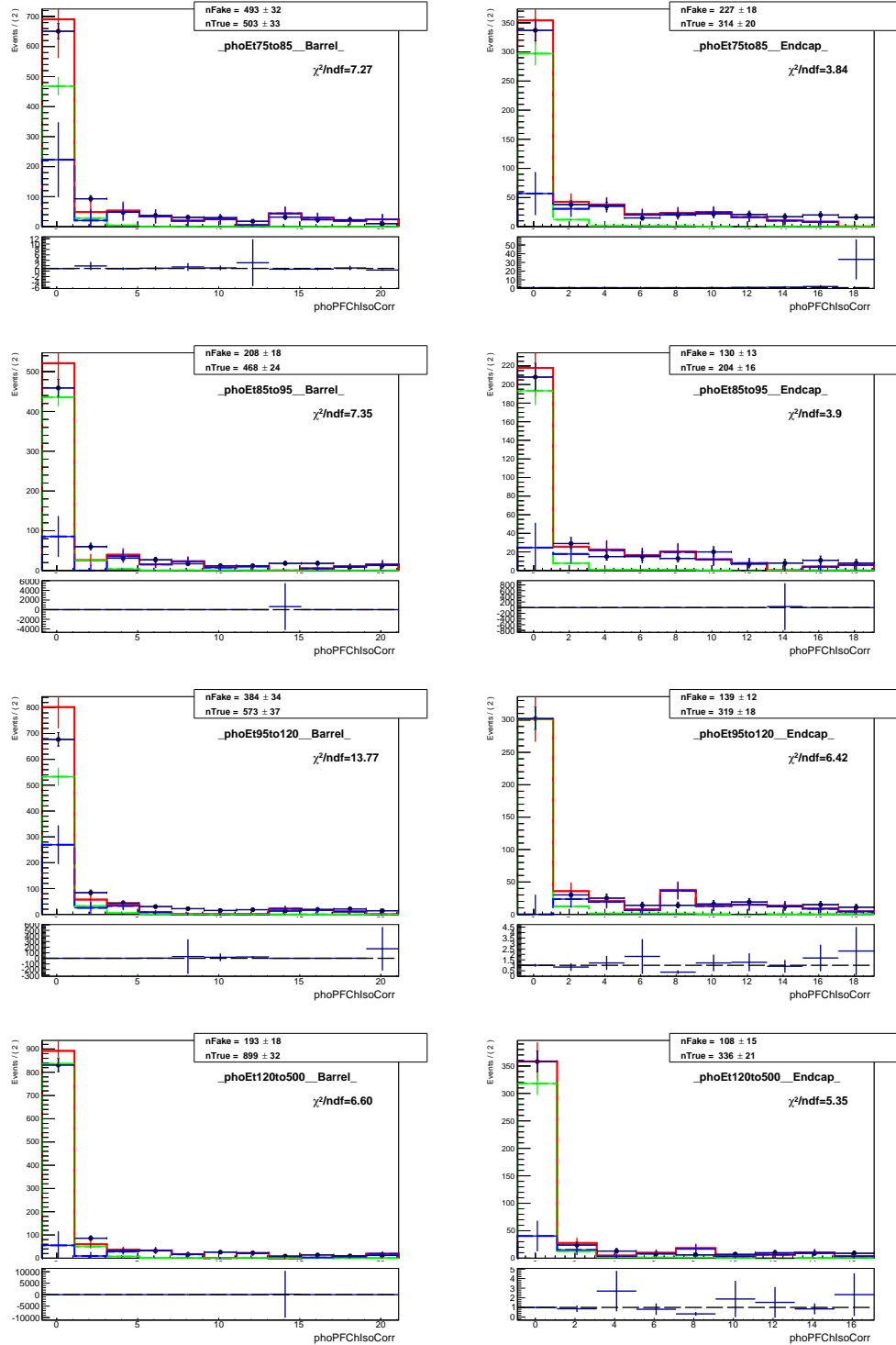


Figure .32: Fits of  $I_{ch}^{\gamma}$  templates,  $W\gamma$ , electron channel.

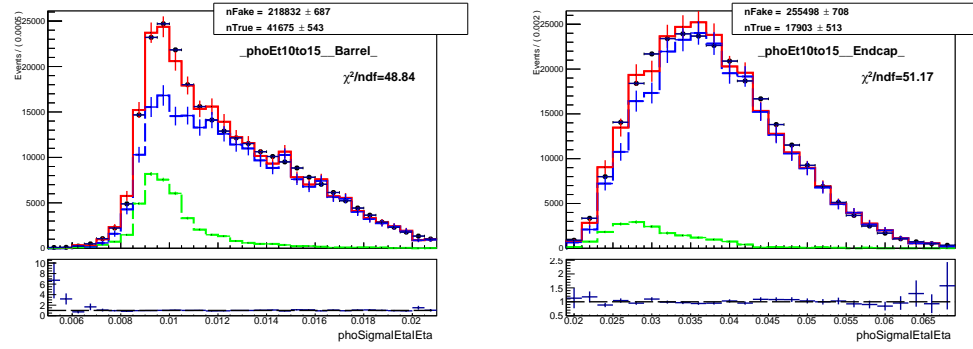


Figure .33: Fits of  $\sigma_{i\eta i\eta}$  templates,  $W\gamma$ , muon channel, underflow bin ( $10 - 15$  GeV).

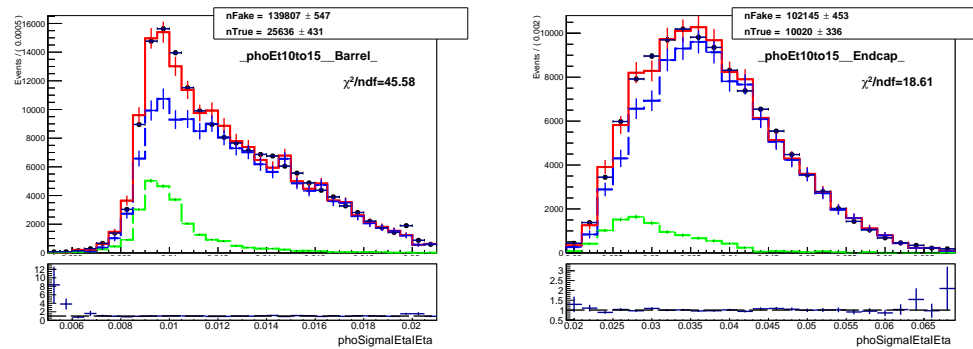


Figure .34: Fits of  $\sigma_{i\eta i\eta}$  templates,  $W\gamma$ , electron channel, underflow bin ( $10 - 15$  GeV).

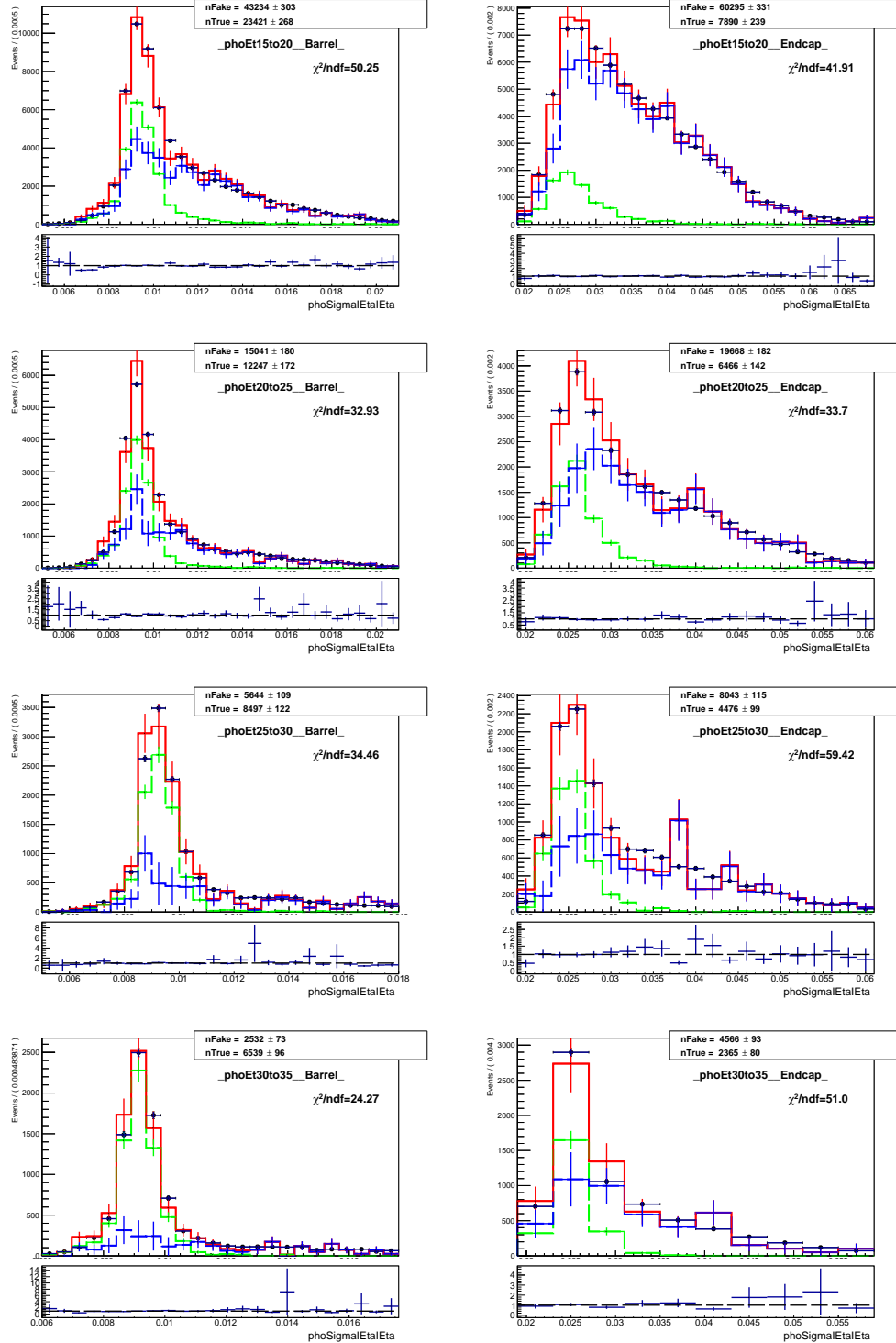


Figure .35: Fits of  $\sigma_{i\eta i\eta}$  templates,  $W\gamma$ , muon channel.

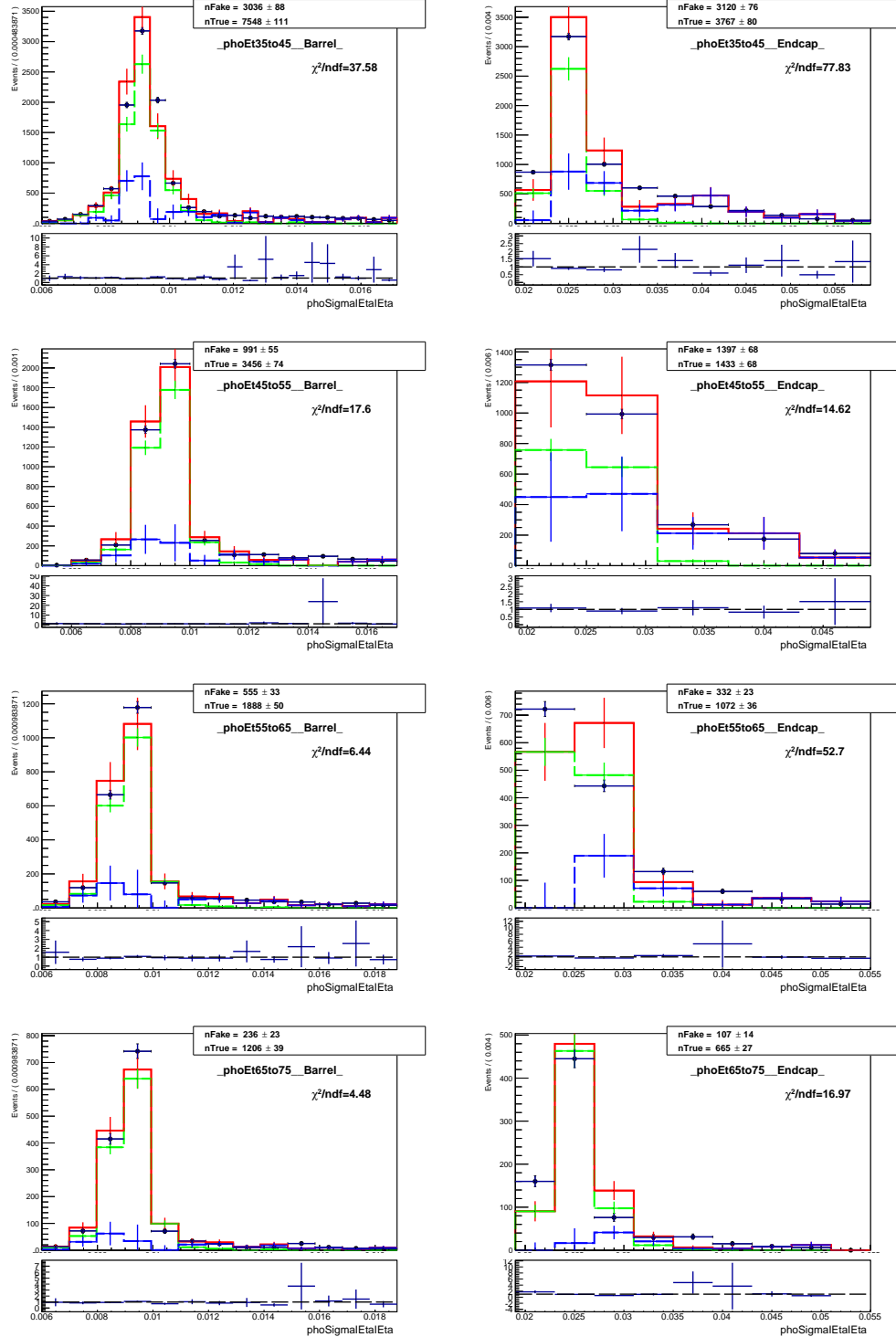


Figure .36: Fits of  $\sigma_{i\eta i\eta}$  templates,  $W\gamma$ , muon channel.

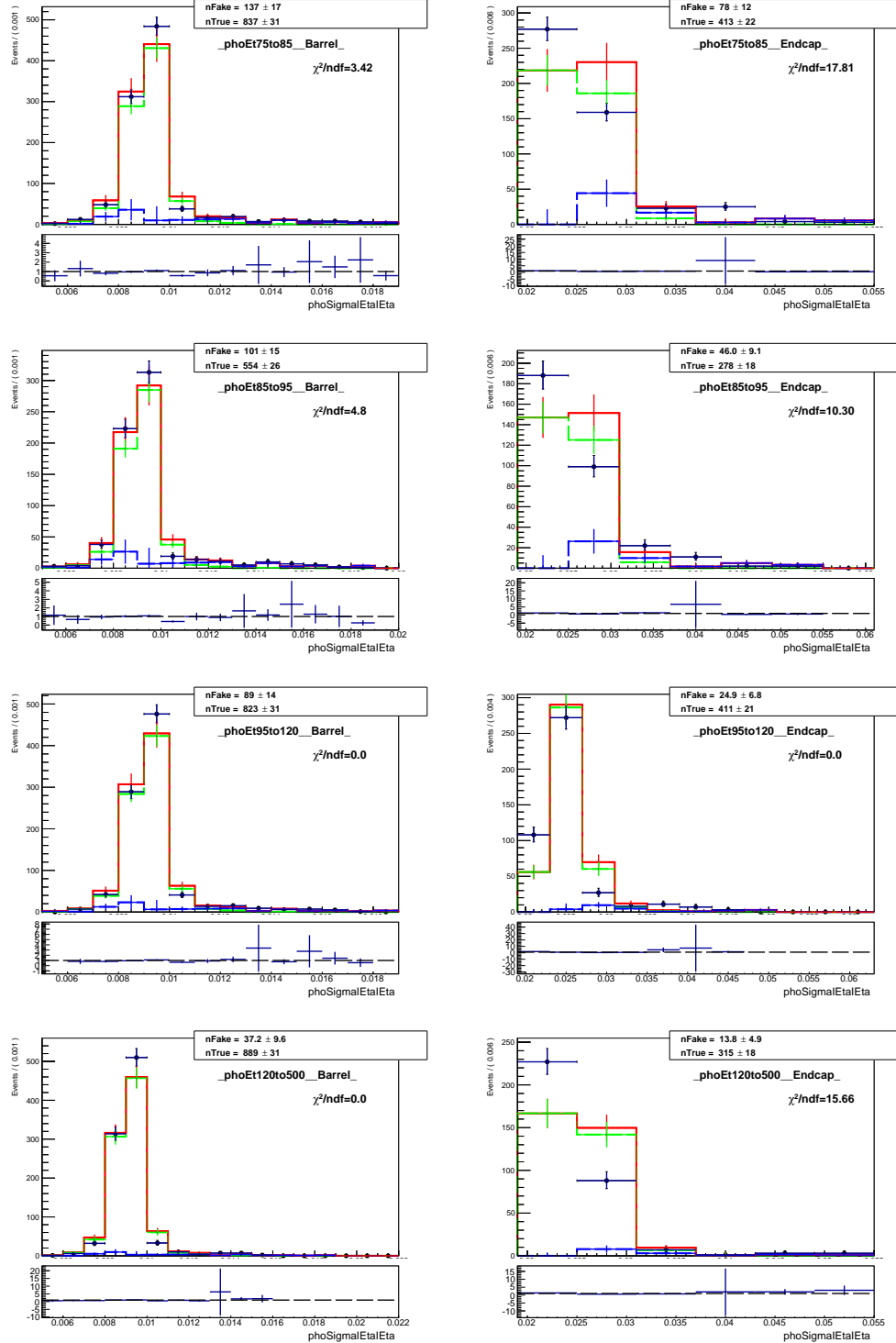
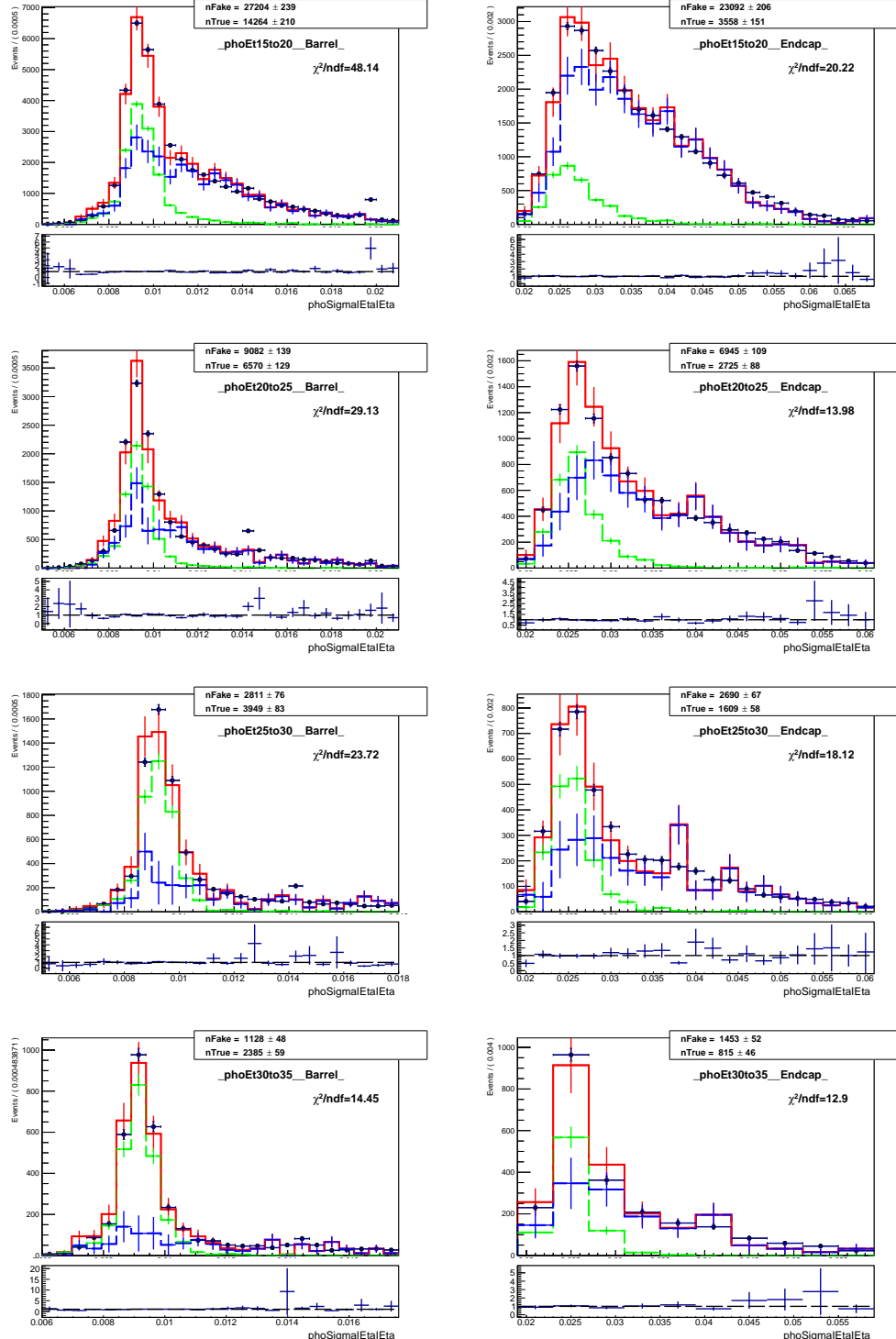


Figure .37: Fits of  $\sigma_{i\eta i\eta}$  templates,  $W\gamma$ , muon channel.

Figure .38: Fits of  $\sigma_{ijij}$  templates,  $W\gamma$ , electron channel.

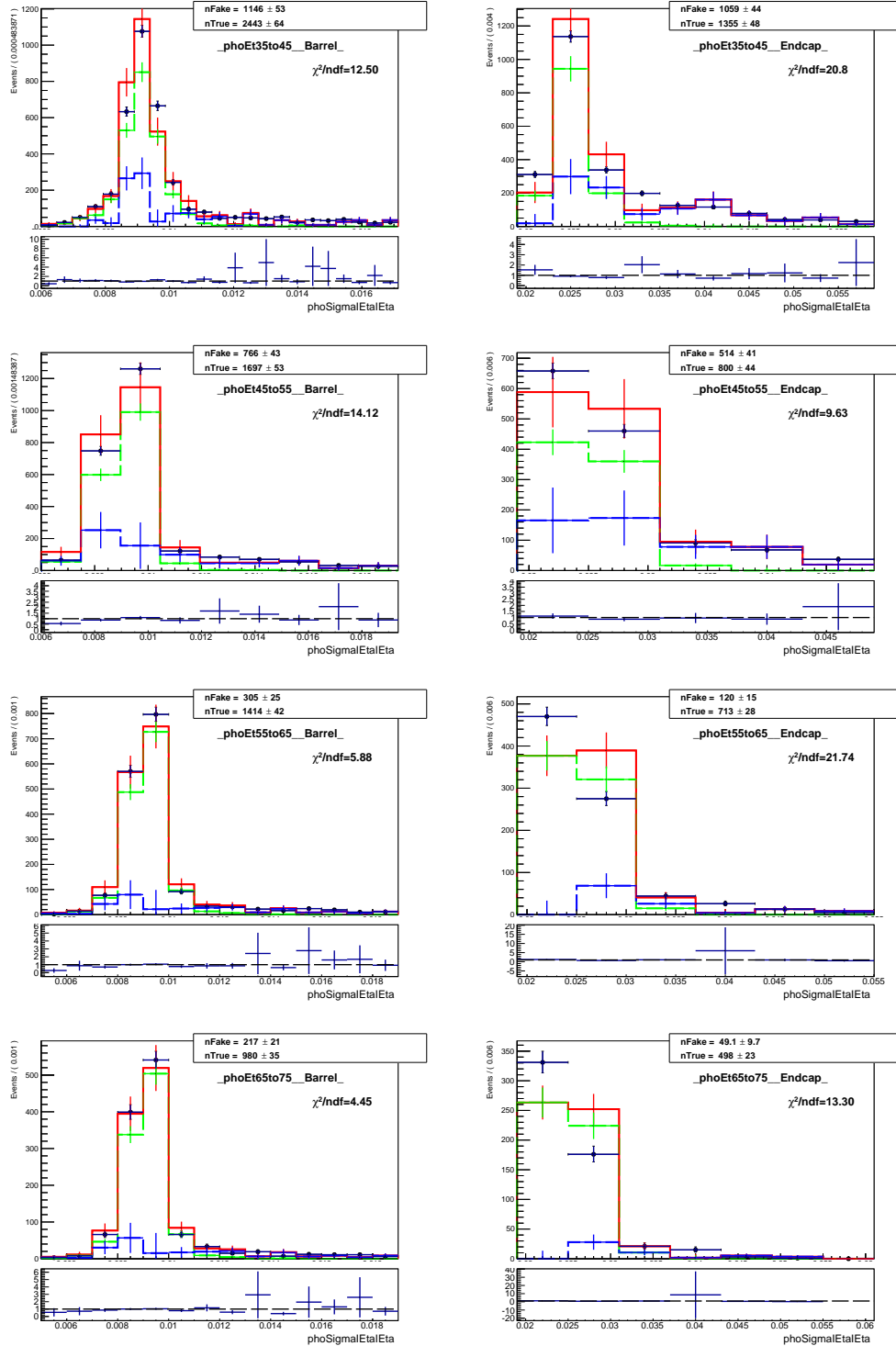


Figure .39: Fits of  $\sigma_{i\eta i\eta}$  templates,  $W\gamma$ , electron channel.

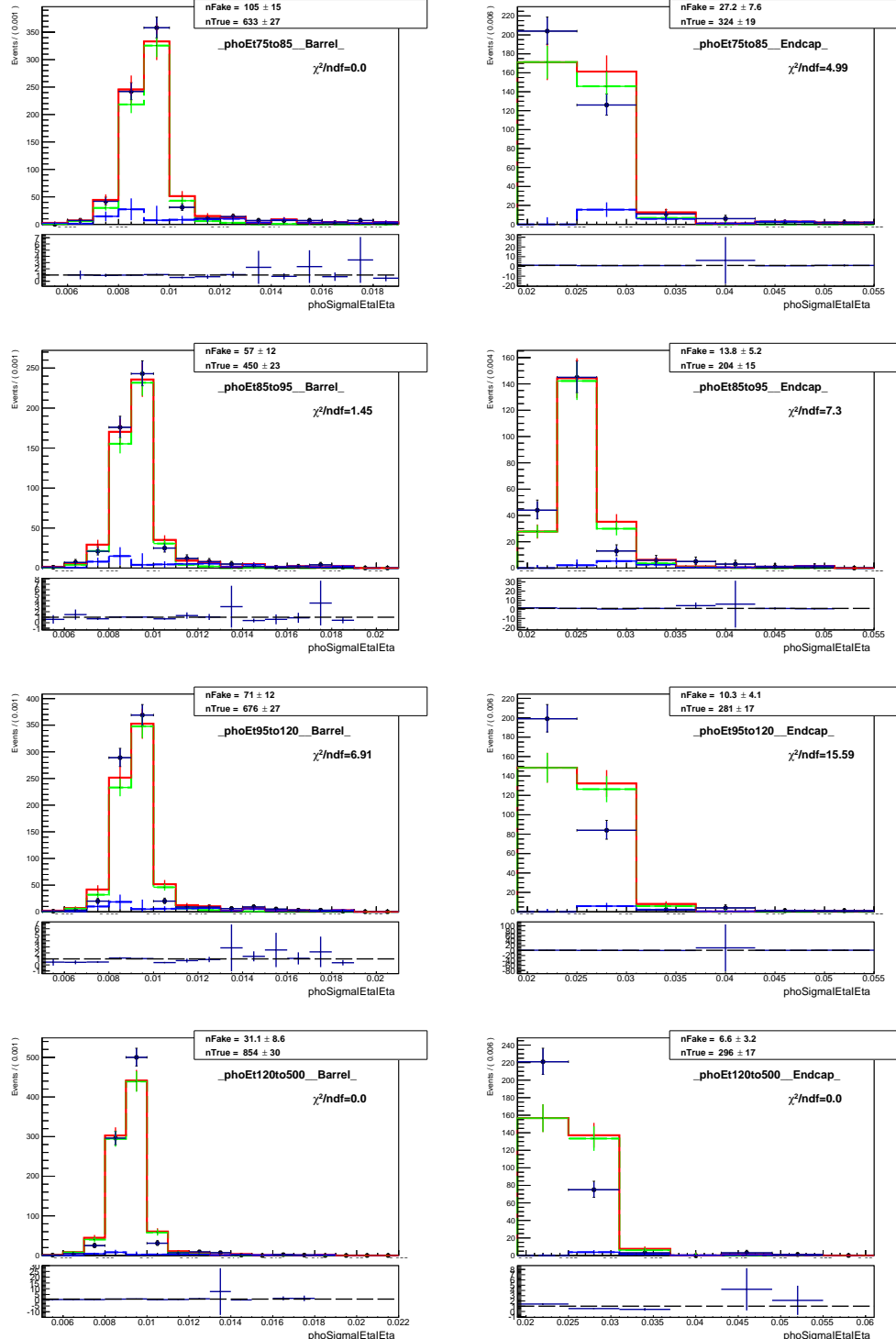


Figure .40: Fits of  $\sigma_{ijij}$  templates,  $W\gamma$ , electron channel.

## .4 APPENDIX: MC Closure Check

To perform the MC closure check, the pseudodata samples are prepared to mimic each of the data samples needed for the fit. This includes:

- $W\gamma$ -selected samples to be used for fit (full analysis selection without  $I_{ch}$  or  $\sigma_{i\eta i\eta}$  cuts), those samples are prepared separately for the muon and electron channels;
- $W\gamma$  in full selection to be plotted into the [data vs bkg+signal] plots, separately for the two channels;
- $Z\gamma \rightarrow \mu\mu\gamma$  FSR selected sample for the real- $\gamma$  templates;
- $Z\gamma \rightarrow \mu\mu\gamma + (\text{DY+jets})$  ISR selected sample for the fake- $\gamma$  templates.

To prepare the pseudodata  $W\gamma$ -selected samples, the  $W\gamma$ ,  $W+\text{jets}$ ,  $Z\gamma$ ,  $\text{DY}+\text{jets}$ ,  $t\bar{t}\gamma$ ,  $t\bar{t}+\text{jets}$ , and  $WW\gamma$  MC samples are merged with the  $W\gamma$  selection applied. To prepare the pseudodata  $Z\gamma$ -selected samples, the  $Z\gamma$  and  $\text{DY}+\text{jets}$  MC samples are merged with the appropriate  $Z\gamma$  selections applied. Luminosity normalizations, PU and scale factor weights are applied on all MC samples. Then the pseudodata are treated as if they were data to perform the fits, prepare the plots and subtract the background. All the MC samples used in the nominal  $W\gamma$  measurement are used for this MC closure check the same way.

Figures .41-.44 show the selection and background estimation results in data (left column) and pseudodata (right column). Top plots are data and pseudodata superimposed with MC. Because the pseudodata was prepared as MC samples merged together, there is an exact match in right-top plots by construction. Middle and bottom plots are results of the background estimation in data and pseudodata.

Plots show data (pseudodata) vs background estimates and signal MC where jets $\rightarrow \gamma$  background is estimated from fits of  $I_{ch}^{\gamma}$  (middle) and  $\sigma_{i\eta i\eta}^{\gamma}$  (bottom) templates. Plots of fits themselves on the pseudodata are available in App. .5.

The agreement in pseudodata vs background plus signal plots is significantly better than in data plots. Thus, the poor agreement in data can be partially explained by wrong normalizations of the signal MC and other real- $\gamma$  MC samples. The disagreement between  $I_{ch}^{\gamma}$  and  $\sigma_{i\eta i\eta}^{\gamma}$  fit results in pseudodata is smaller than in data however is still significant in many  $P_T^{\gamma}$  bins which indicates systematic bias of the fit procedure.

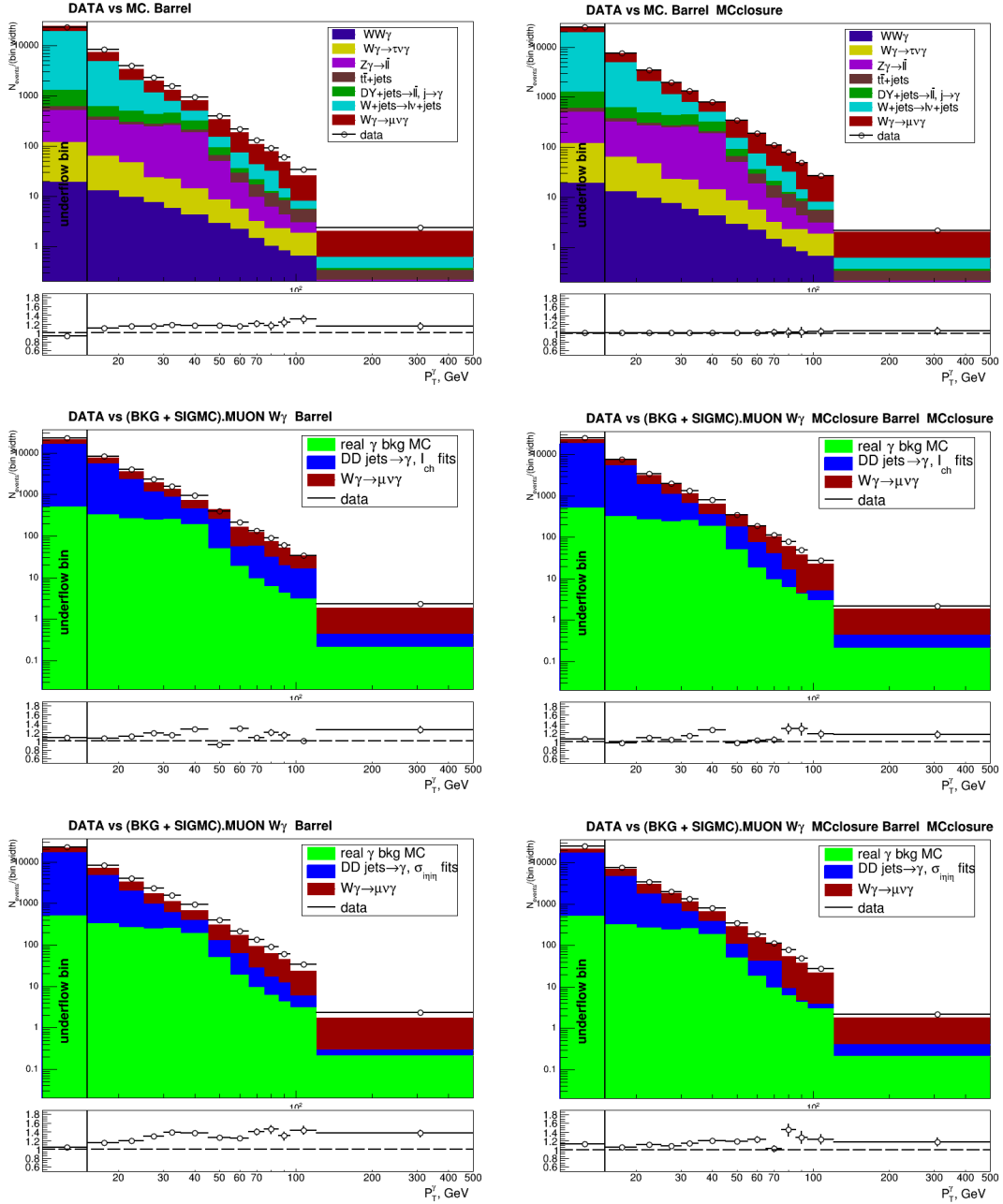


Figure .41: Top: data (left) and pseudodata (right) vs MC. Middle and bottom: data (left) and pseudodata (right) vs background estimates and signal MC in bins of  $P_T^{\gamma}$ . Jets  $\rightarrow \gamma$  background estimated from fits of  $I_{ch}^{\gamma}$  (top) and  $\sigma_{inj\eta}^{\gamma}$  (bottom). Muon channel. Barrel photons.

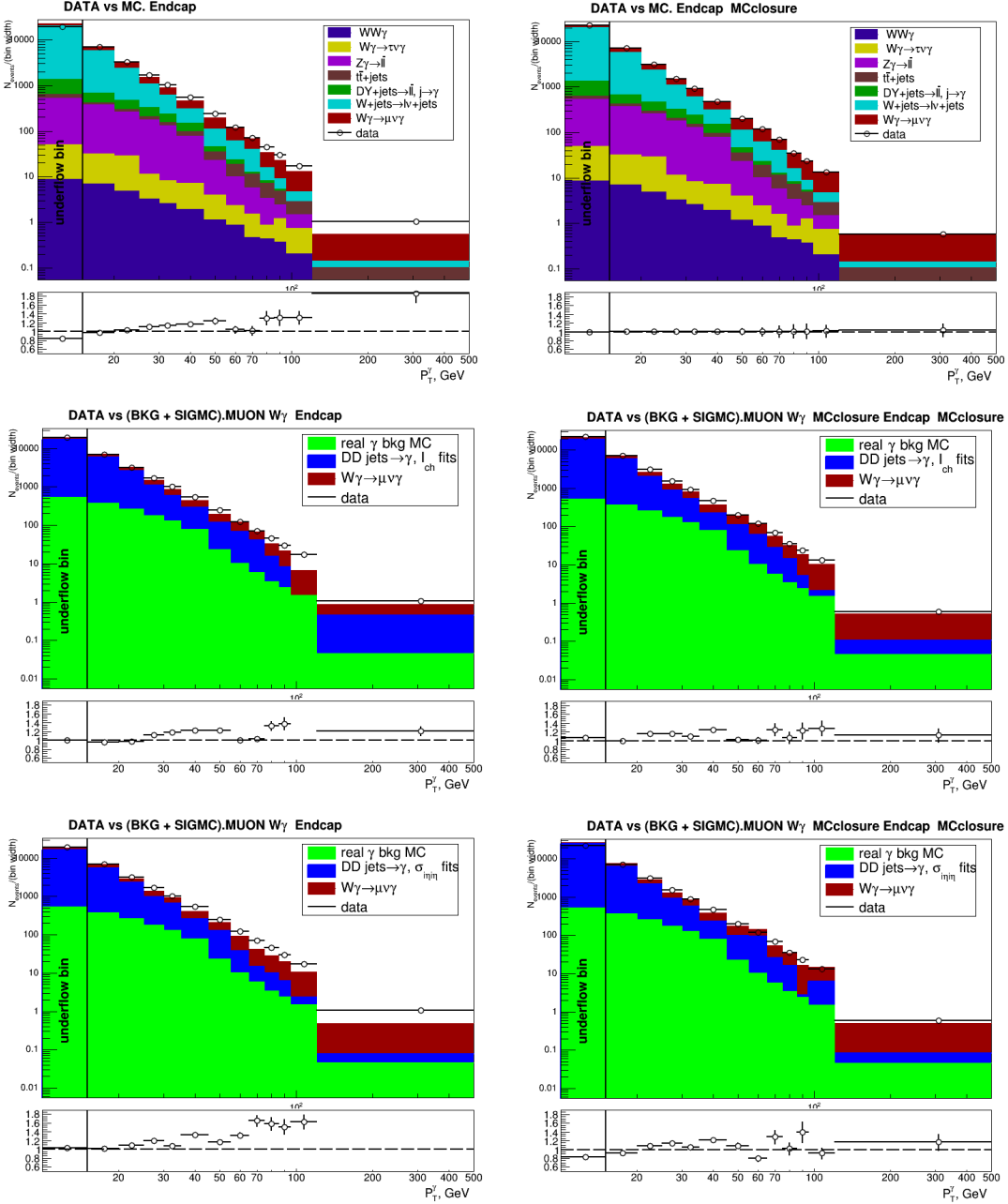


Figure .42: Top: data (left) and pseudodata (right) vs MC. Middle and bottom: data (left) and pseudodata (right) vs background estimates and signal MC in bins of  $P_T^\gamma$ . Jets $\rightarrow\gamma$  background estimated from fits of  $I_{ch}^\gamma$  (middle) and  $\sigma_{ij\eta}^\gamma$  (bottom). Muon channel. Endcap photons.

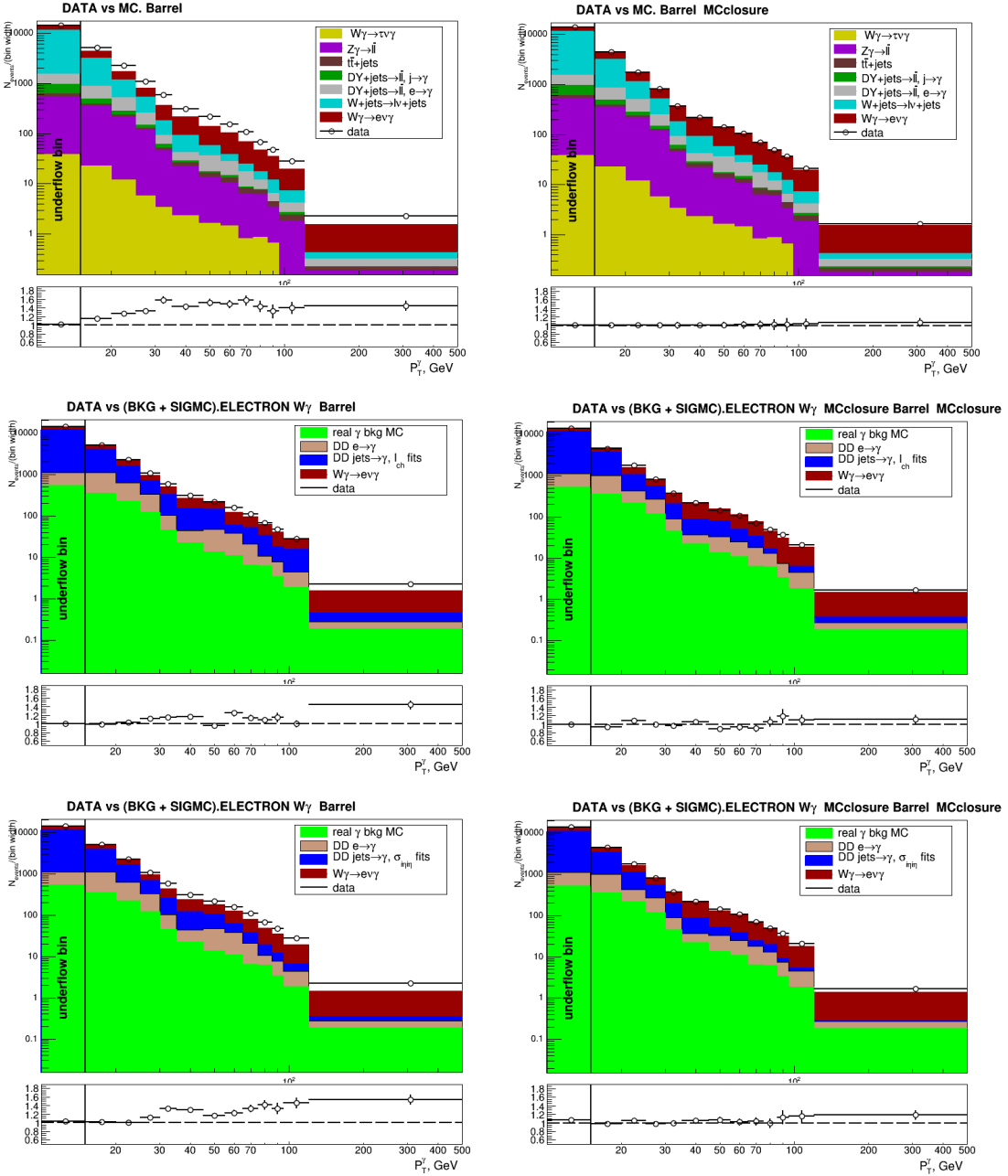


Figure .43: Top: data (left) and pseudodata (right) vs MC. Middle and bottom: data (left) and pseudodata (right) vs background estimates and signal MC in bins of  $P_T^\gamma$ . Jets  $\rightarrow \gamma$  background estimated from fits of  $I_{ch}^\gamma$  (middle) and  $\sigma_{ij\eta i\eta}^\gamma$  (bottom). Electron channel. Barrel photons.

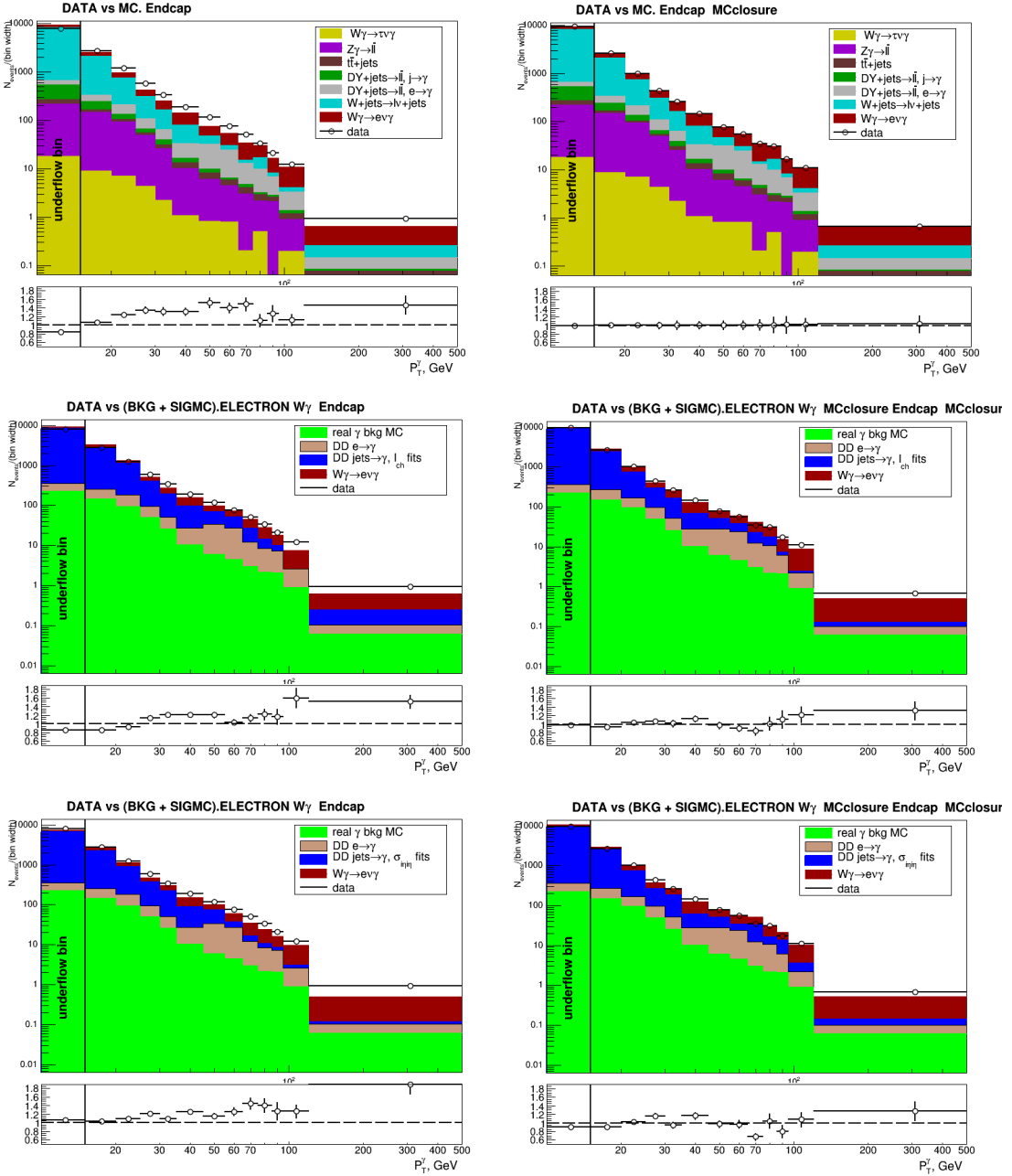


Figure .44: Top: data (left) and pseudodata (right) vs MC. Middle and bottom: data (left) and pseudodata (right) vs background estimates and signal MC in bins of  $P_T^\gamma$ . Jets  $\rightarrow \gamma$  background estimated from fits of  $I_{ch}^\gamma$  (middle) and  $\sigma_{ij\eta i\eta}^\gamma$  (bottom). Electron channel. Endcap photons.

## 5 APPENDIX: Template Fit Plots, $W\gamma$ , MC closure

This appendix contains fit results for jets $\rightarrow\gamma$  background estimation performed on pseudodata. The pseudodata were prepared as MC samples appropriately weighted and mixed together. On each of the plots, black histogram is the pseudodata, green is a real- $\gamma$  template, blue is a fake- $\gamma$  template, and red is the fit function. Cyan is a histogram of  $W$ +jets MC sample in a given channel. The fits on pseudodata is performed for MC the closure check.

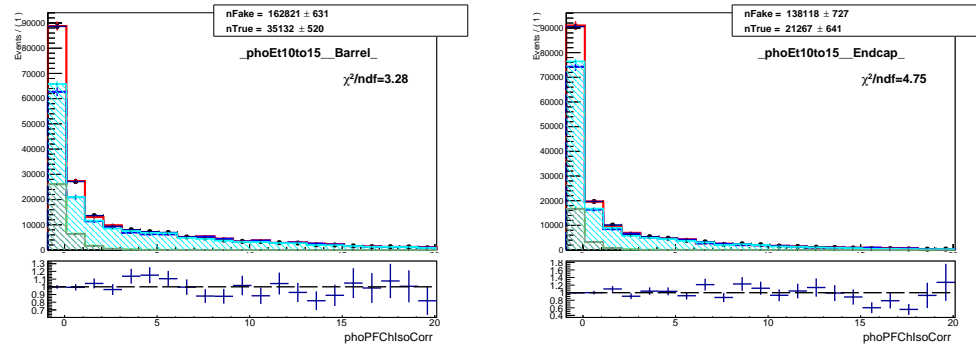


Figure .45: Fits of  $I_{ch}^{\gamma}$  templates, pseudodata (MC mixtures),  $W\gamma$ , muon channel, underflow bin (10 – 15 GeV).

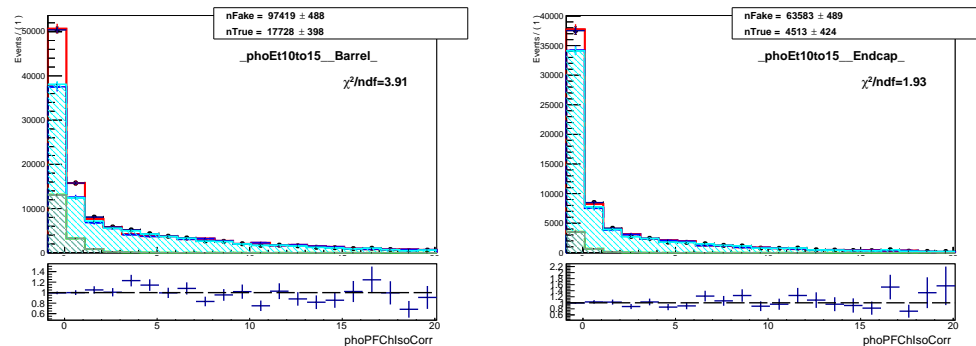


Figure .46: Fits of  $I_{ch}^{\gamma}$  templates, pseudodata (MC mixtures),  $W\gamma$ , electron channel, underflow bin (10 – 15 GeV).

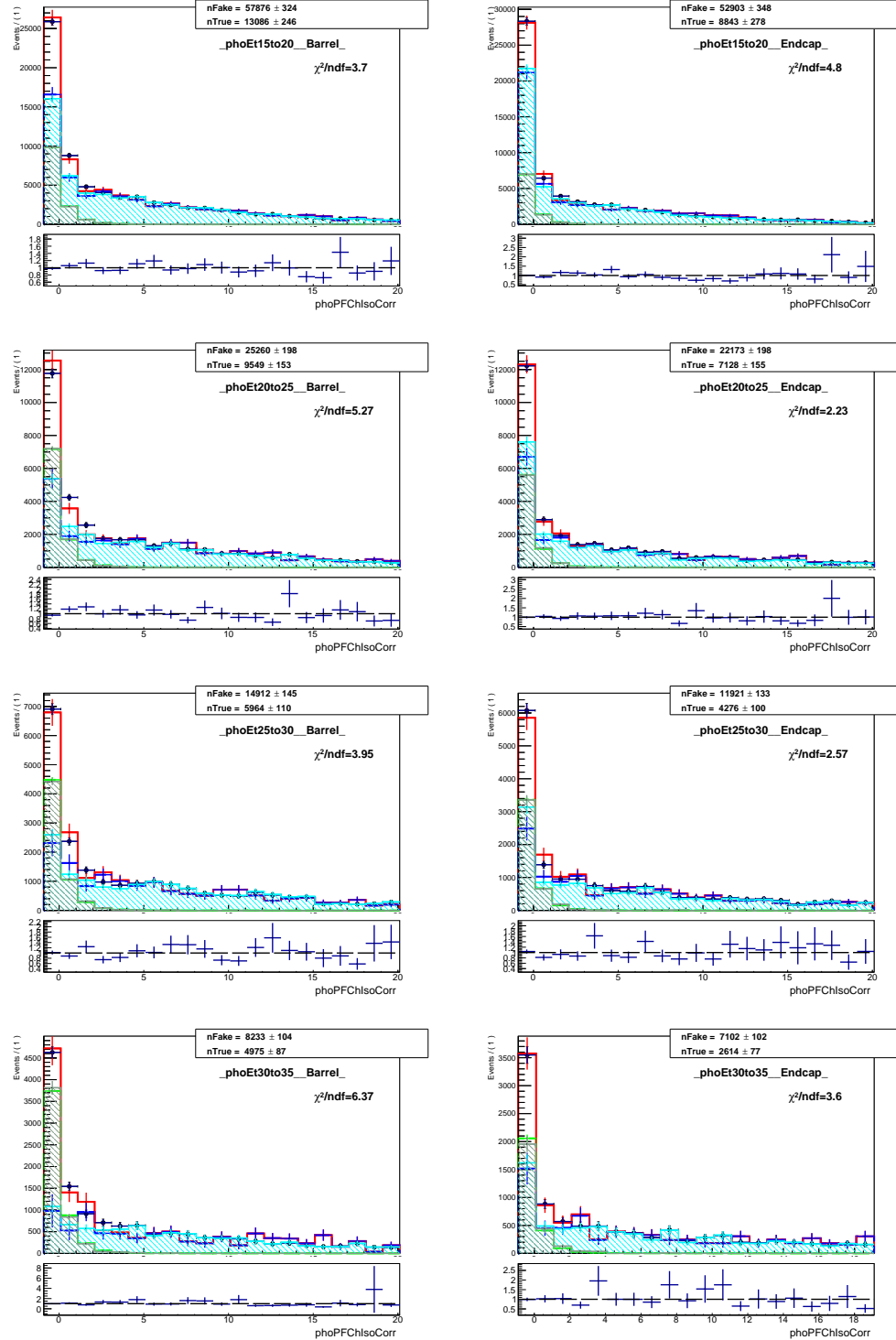


Figure .47: Fits of  $L_{ch}^\gamma$  templates, pseudodata (MC mixtures),  $W\gamma$ , muon channel.

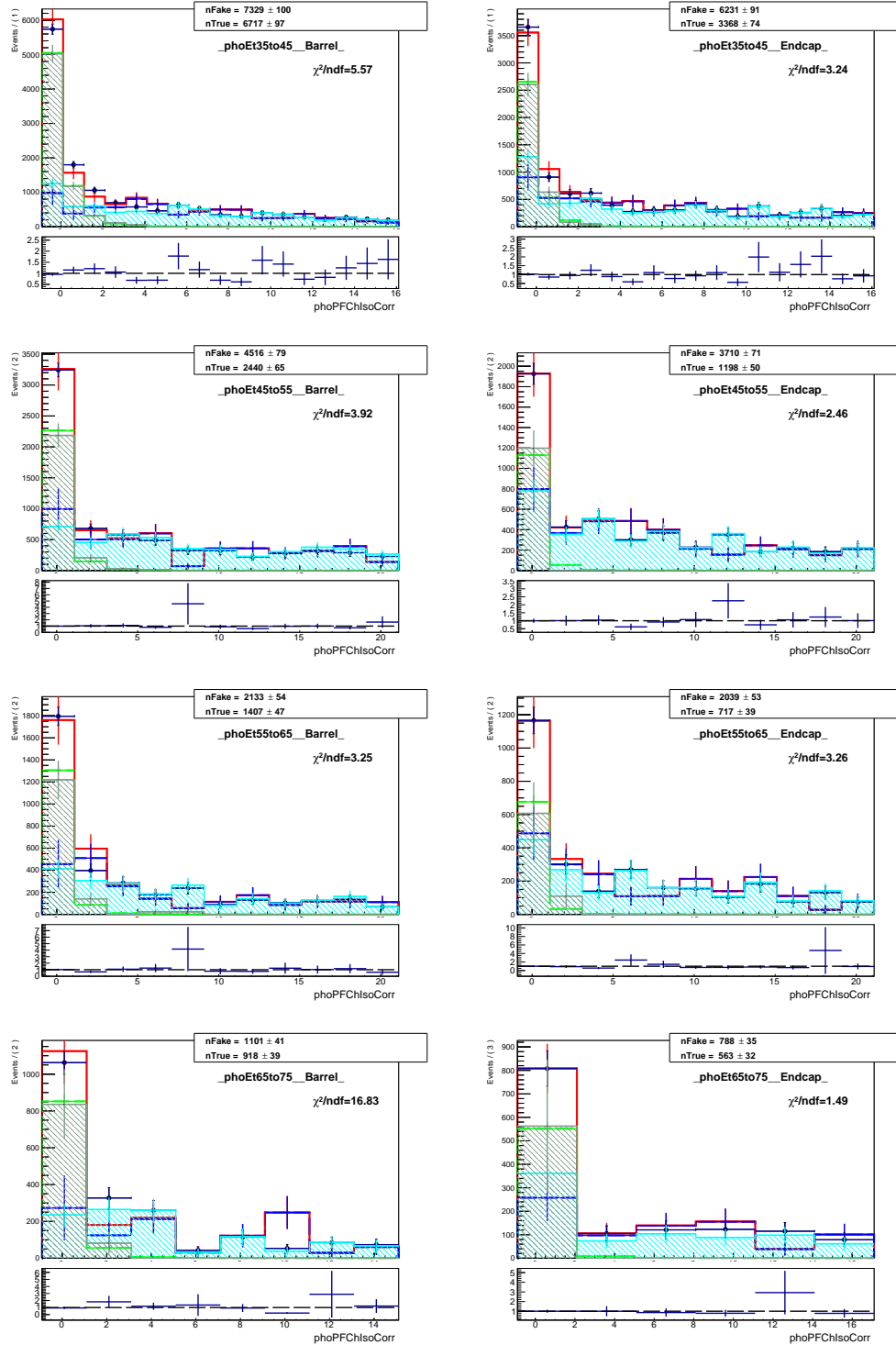


Figure .48: Fits of  $L_{ch}^\gamma$  templates, pseudodata (MC mixtures),  $W\gamma$ , muon channel.

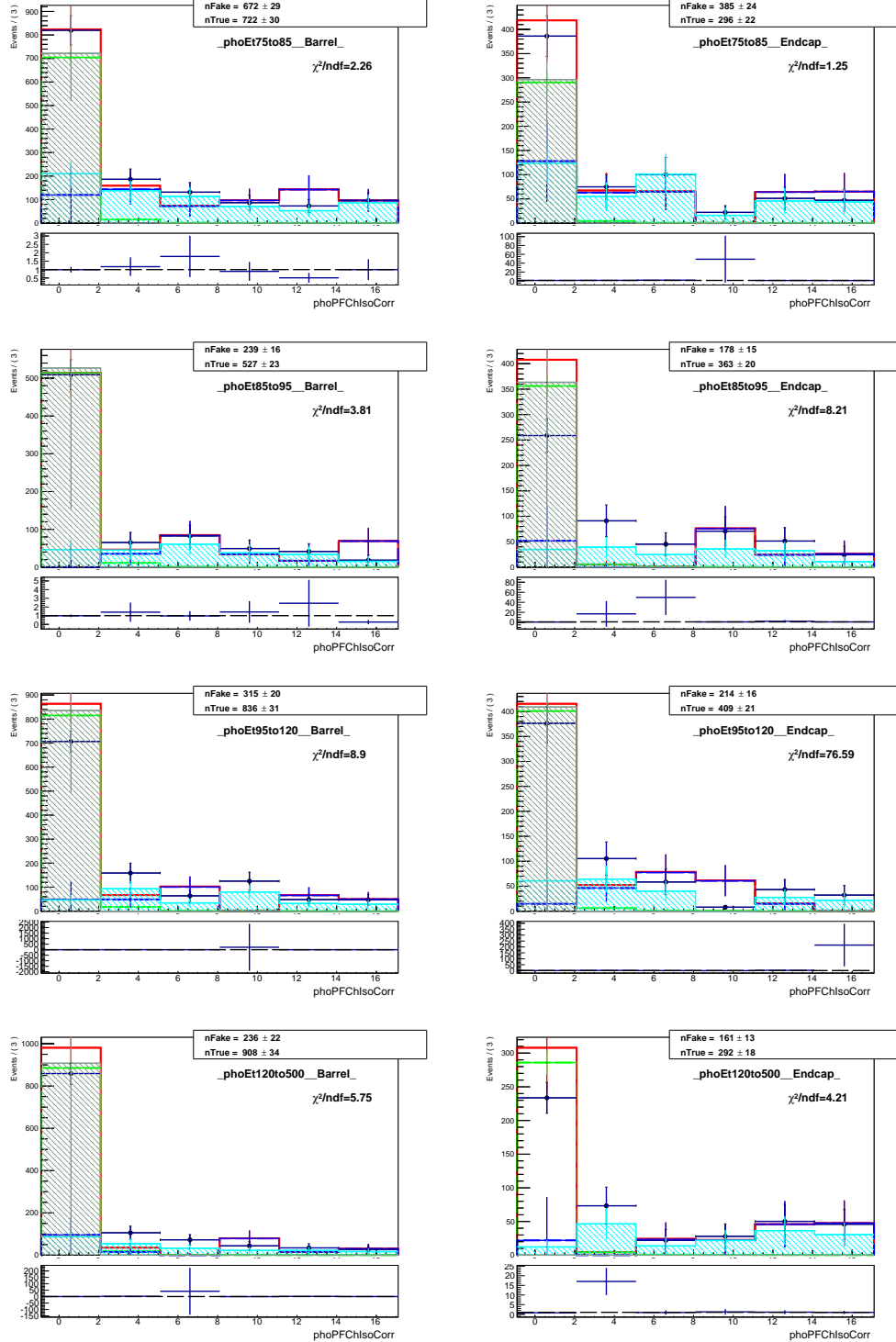


Figure .49: Fits of  $L_{ch}^\gamma$  templates, pseudodata (MC mixtures),  $W\gamma$ , muon channel.

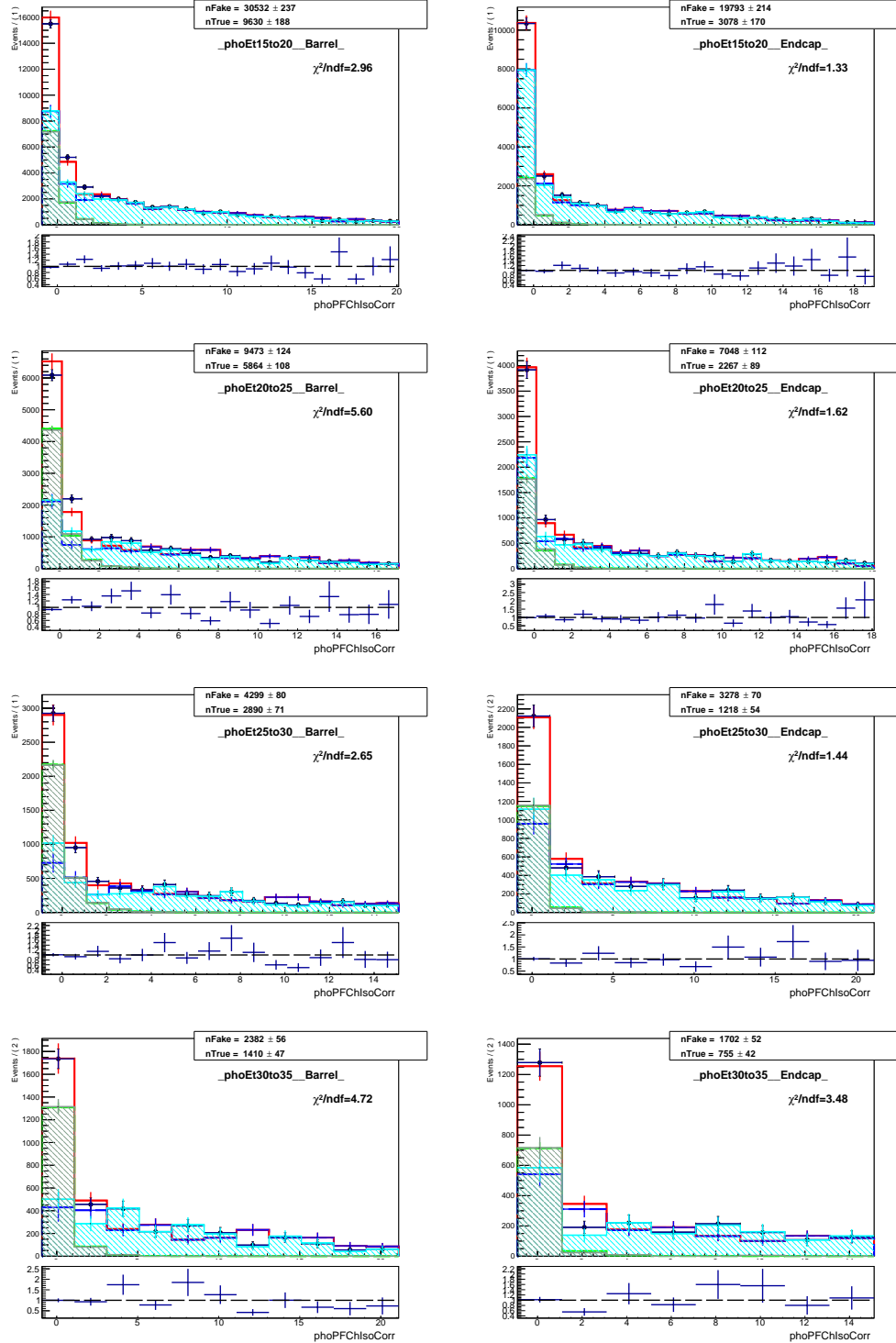


Figure .50: Fits of  $I_{ch}^{\gamma}$  templates, pseudodata (MC mixtures),  $W\gamma$ , electron channel.

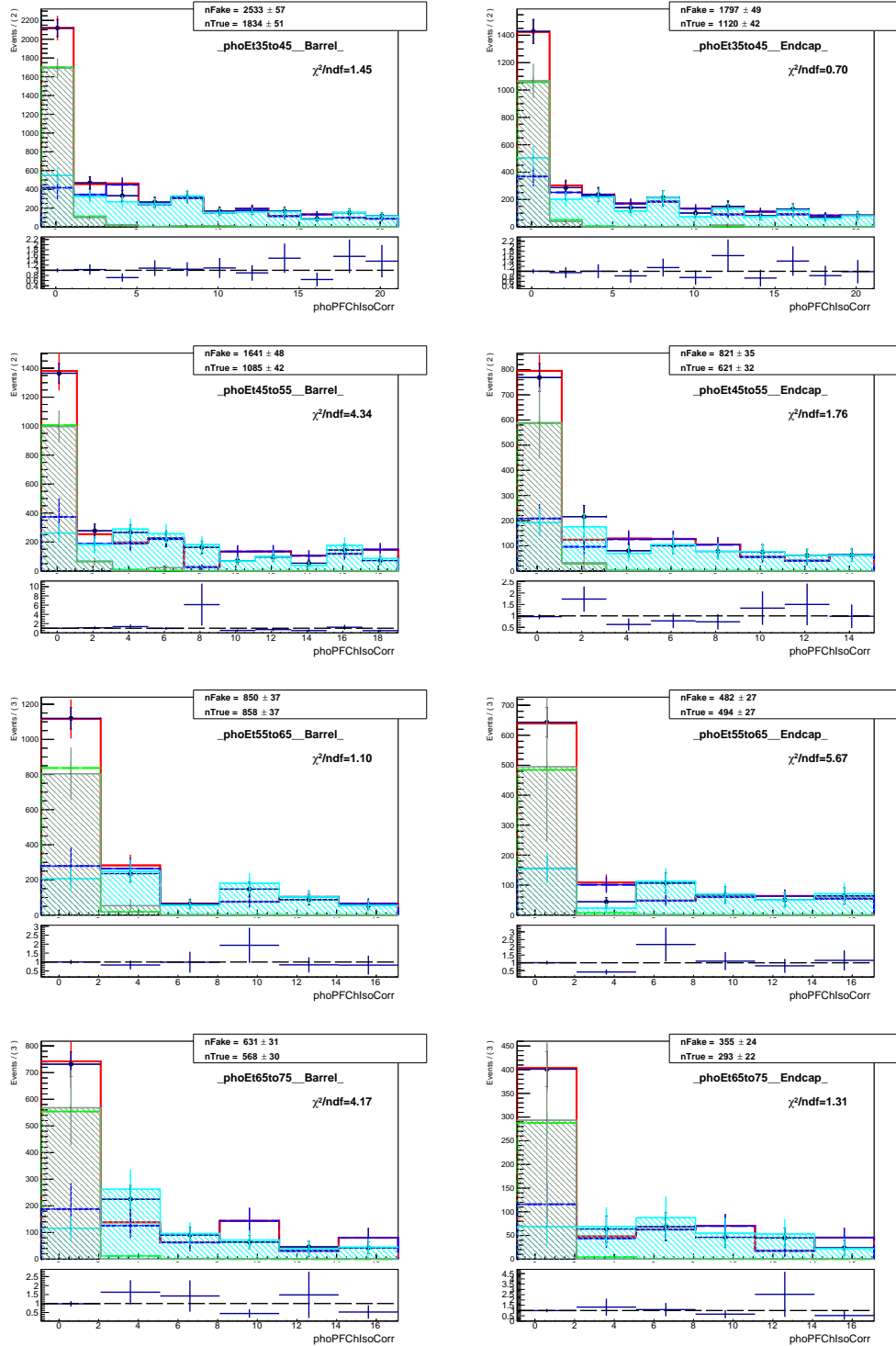


Figure .51: Fits of  $I_{ch}^{\gamma}$  templates, pseudodata (MC mixtures),  $W\gamma$ , electron channel.

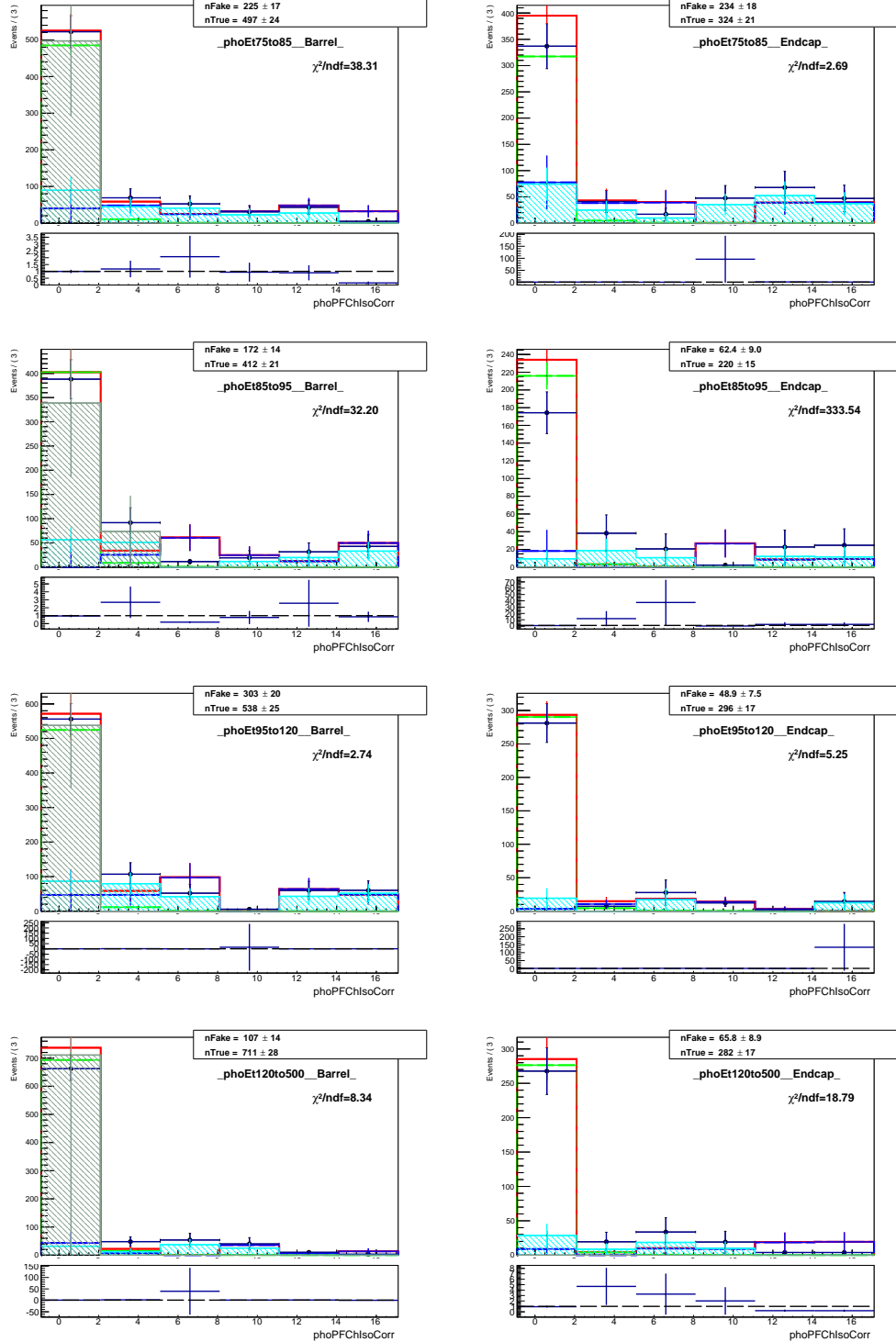


Figure .52: Fits of  $I_{ch}^{\gamma}$  templates, pseudodata (MC mixtures),  $W\gamma$ , electron channel.

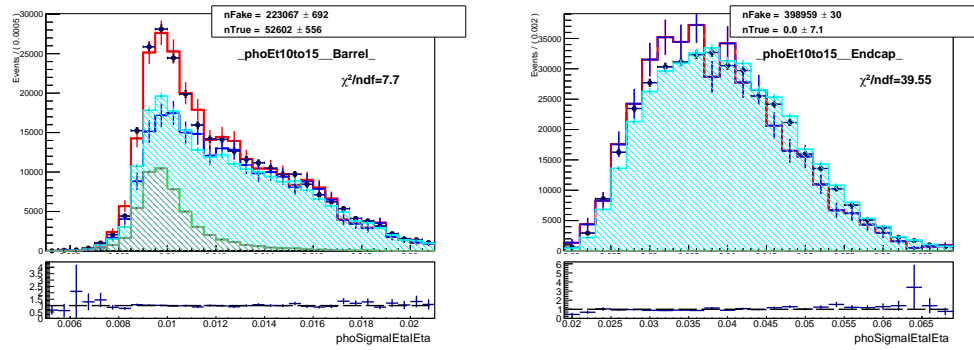


Figure .53: Fits of  $\sigma_{i\eta i\eta}$  templates, pseudodata (MC mixtures),  $W\gamma$ , muon channel, underflow bin (10 – 15 GeV).

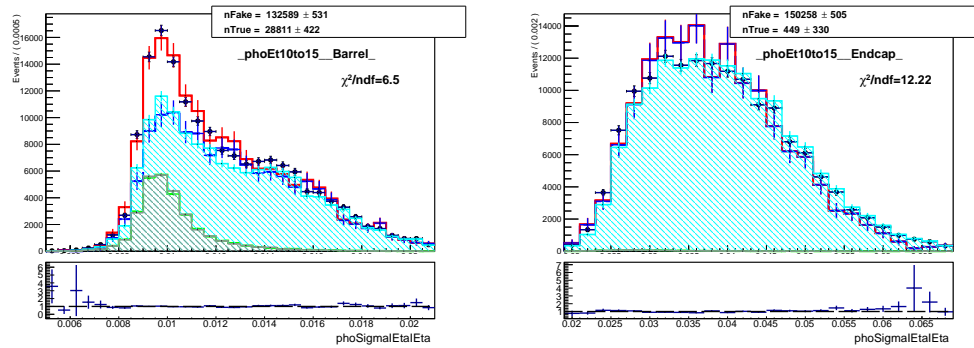


Figure .54: Fits of  $\sigma_{i\eta i\eta}$  templates, pseudodata (MC mixtures),  $W\gamma$ , electron channel, underflow bin (10 – 15 GeV).

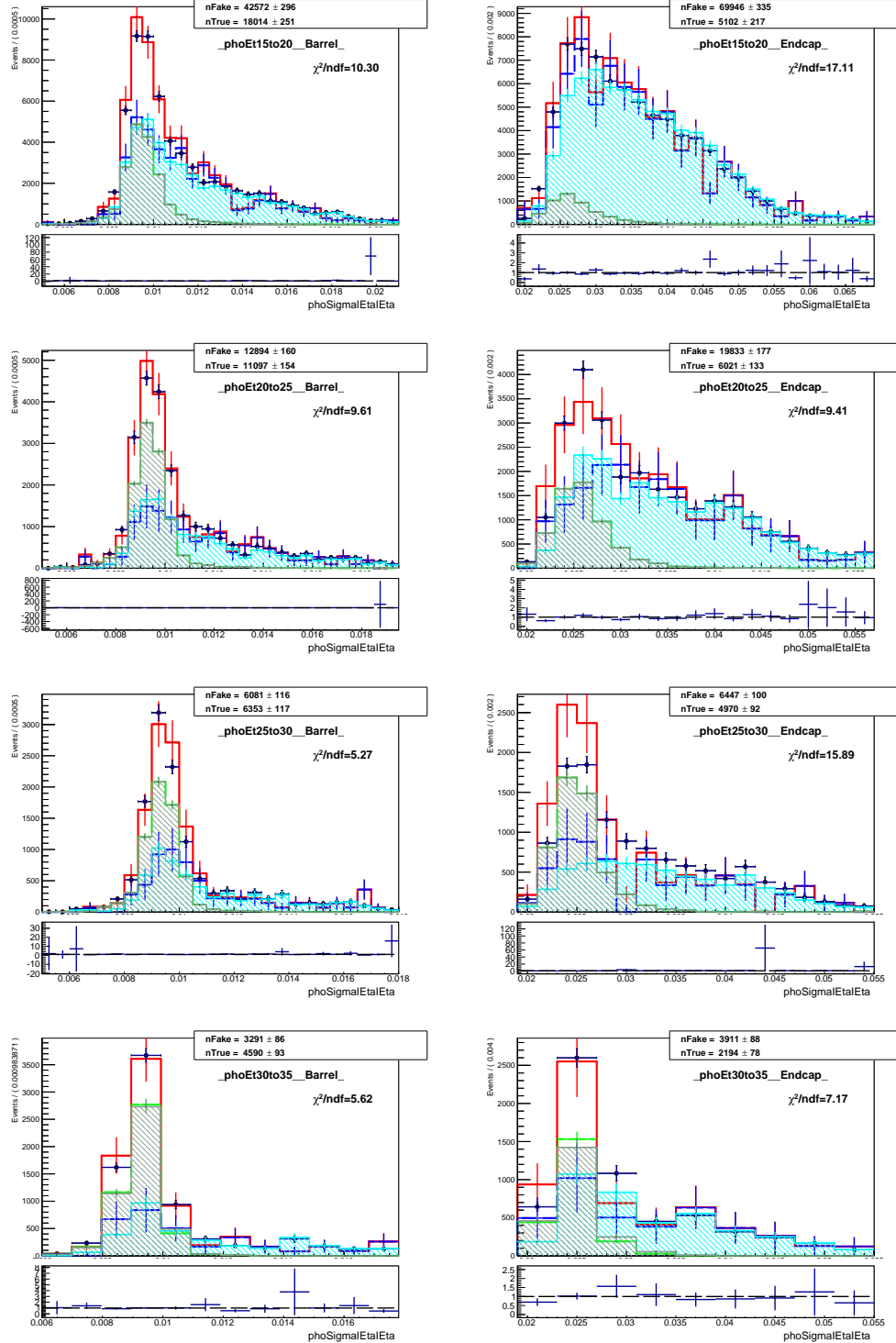


Figure .55: Fits of  $\sigma_{ijij}$  templates, pseudodata (MC mixtures),  $W\gamma$ , muon channel.

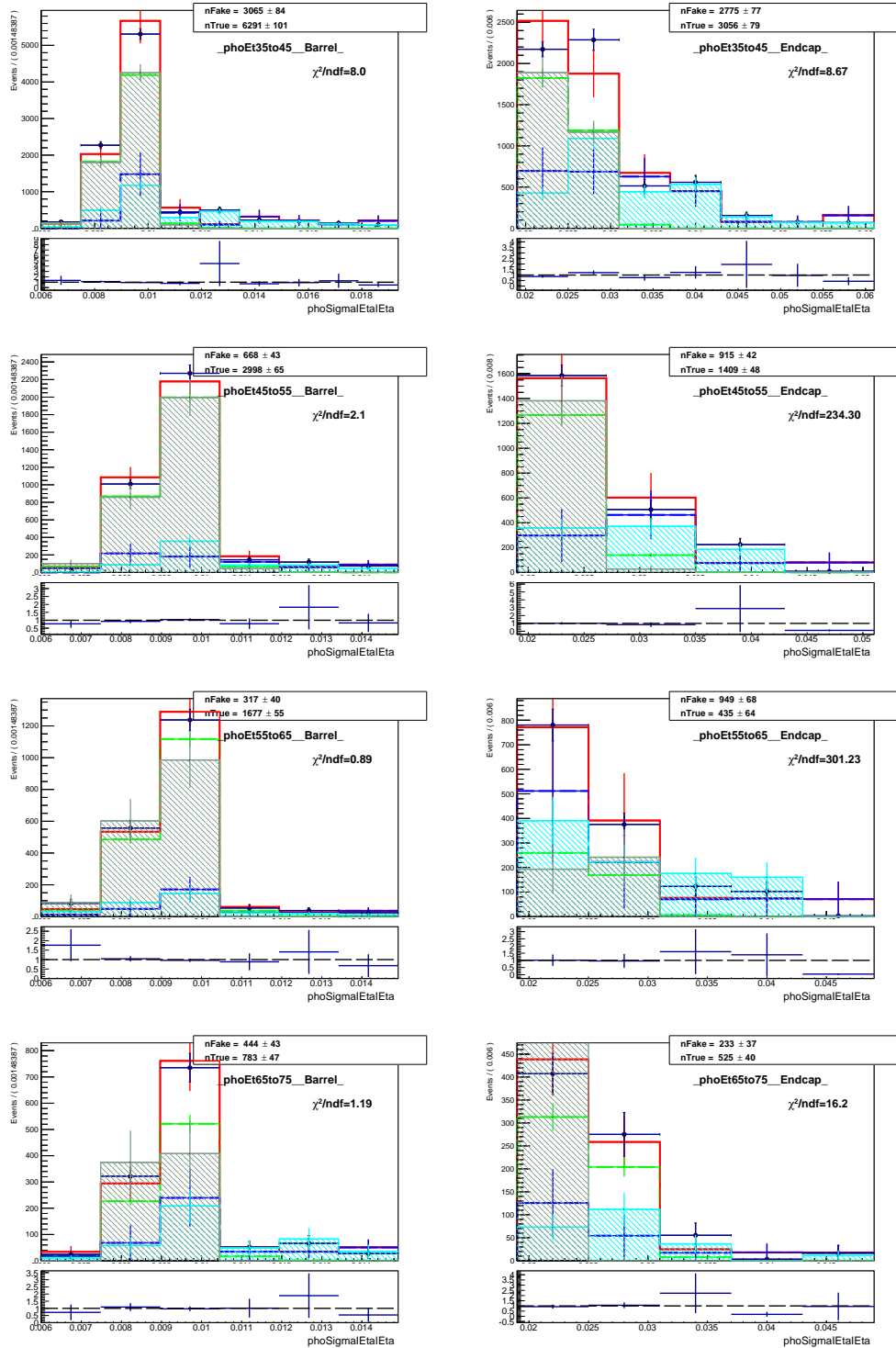


Figure .56: Fits of  $\sigma_{ijij}$  templates, pseudodata (MC mixtures),  $W\gamma$ , muon channel.

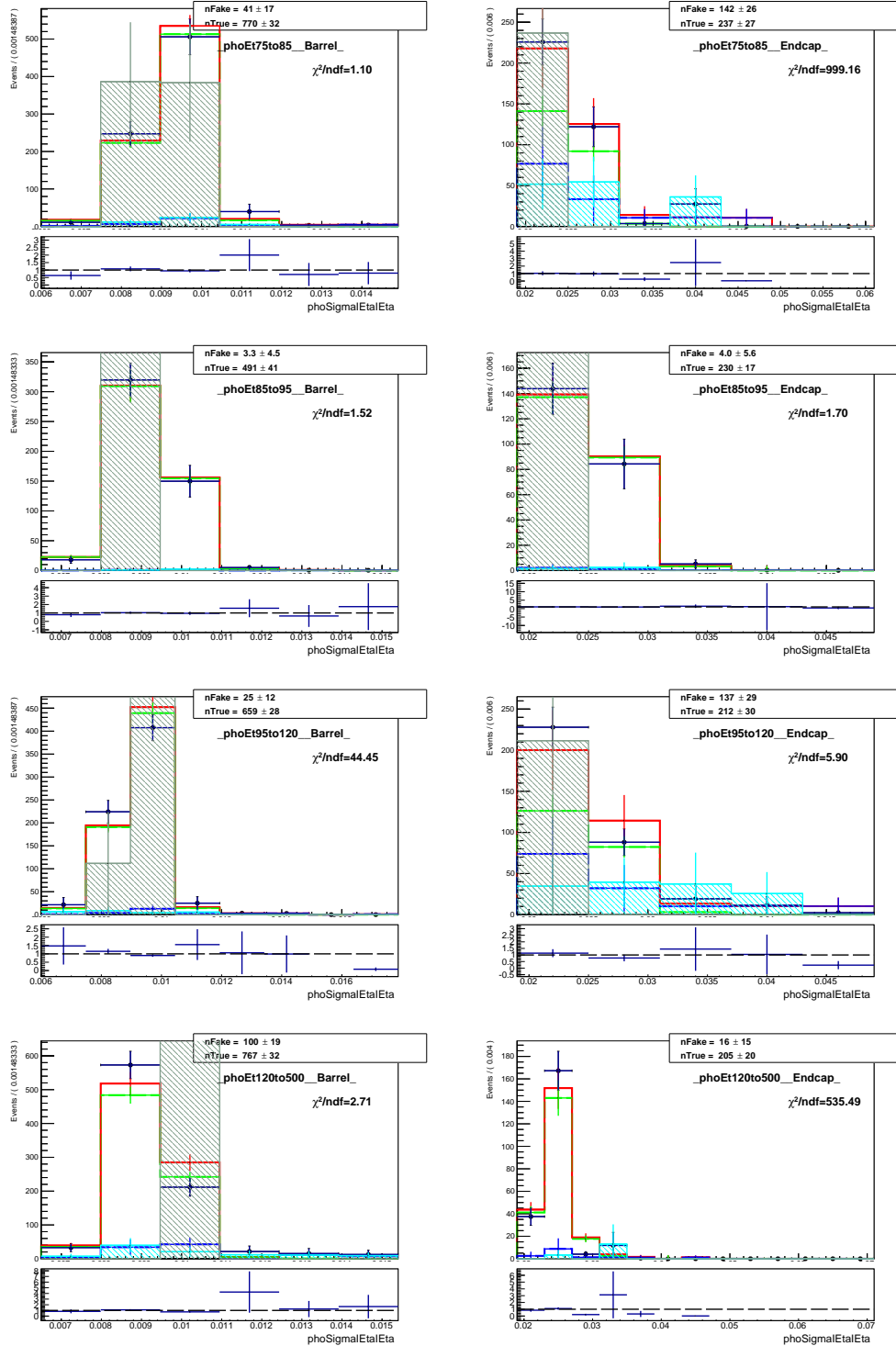


Figure .57: Fits of  $\sigma_{ijij\eta}$  templates, pseudodata (MC mixtures),  $W\gamma$ , muon channel.

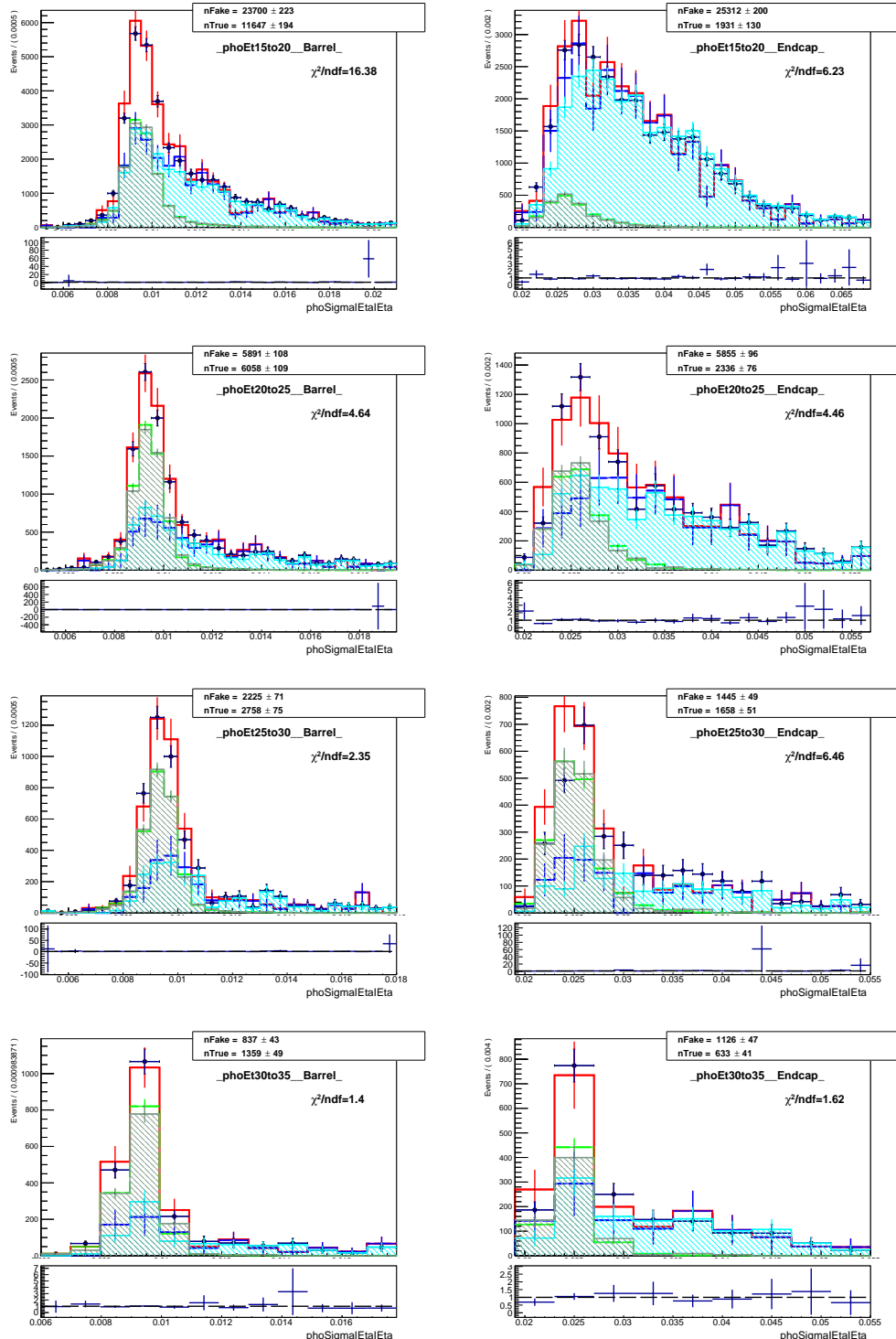


Figure .58: Fits of  $\sigma_{i\eta i\eta}$  templates, pseudodata (MC mixtures),  $W\gamma$ , electron channel.

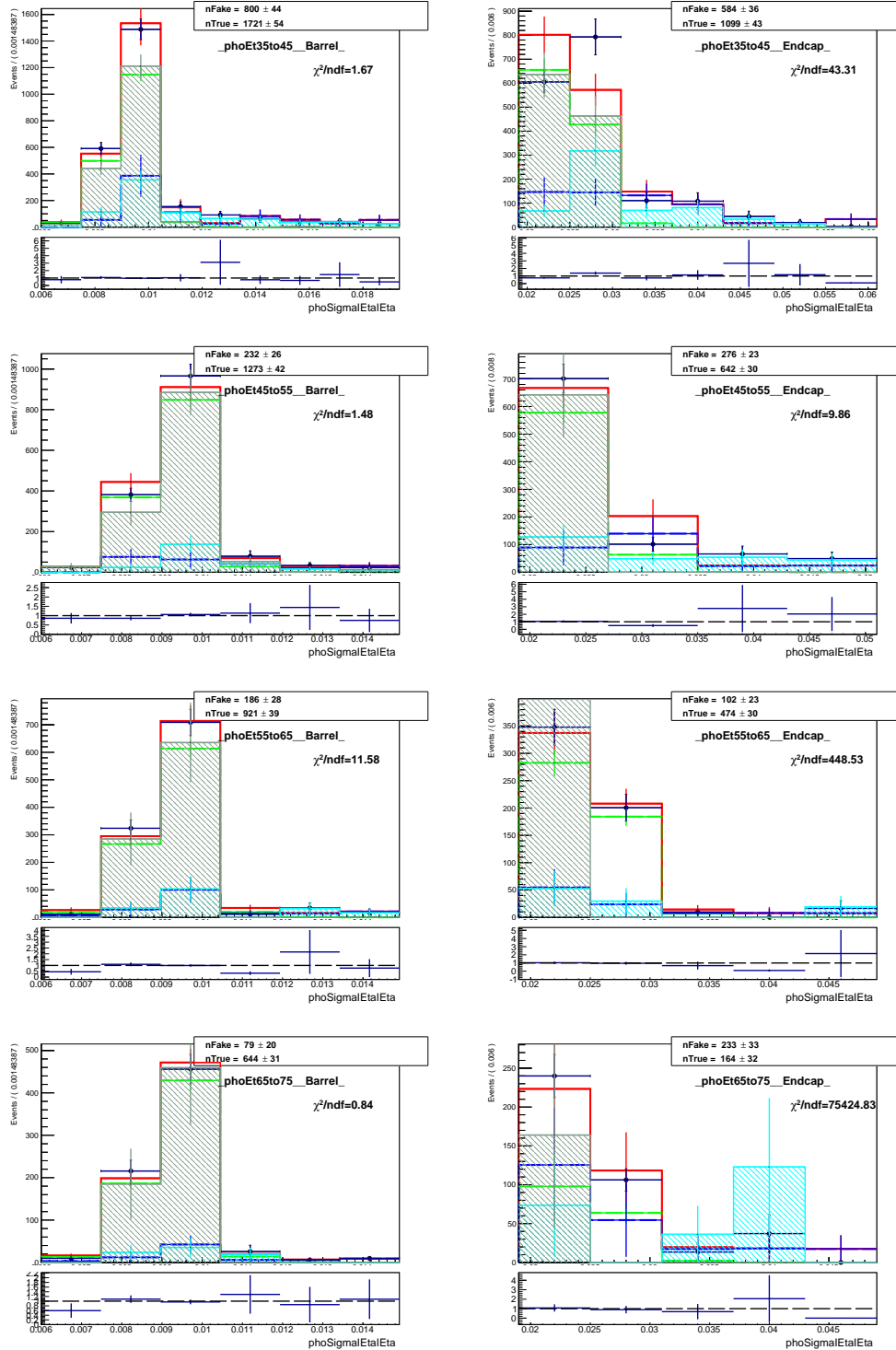


Figure .59: Fits of  $\sigma_{ii\eta_i\eta_j}$  templates, pseudodata (MC mixtures),  $W\gamma$ , electron channel.

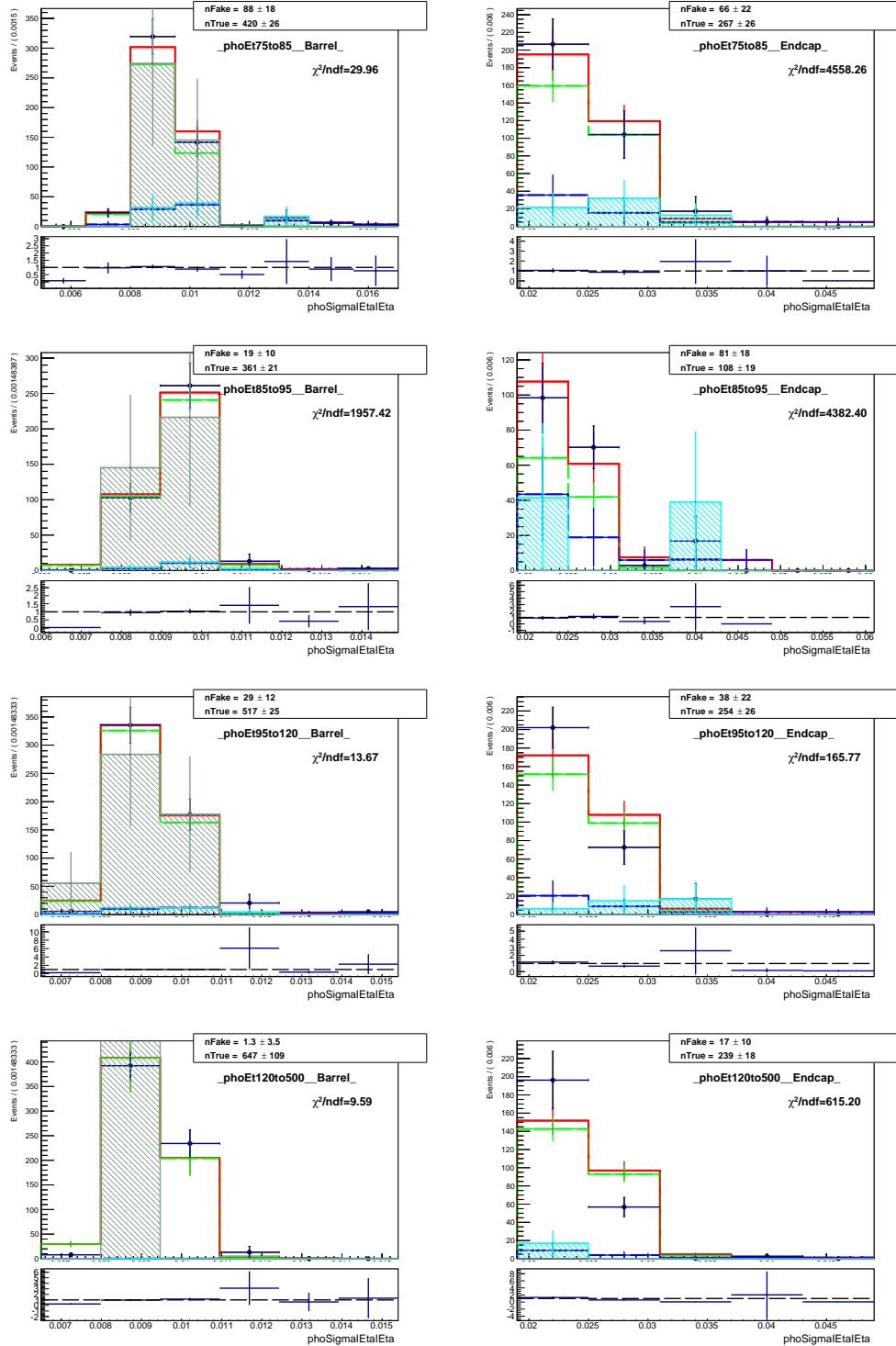


Figure .6o: Fits of  $\sigma_{ii\eta_i\eta_j}$  templates, pseudodata (MC mixtures),  $W\gamma$ , electron channel.

## .6 APPENDIX: Template Fit Plots, MC Closure

### $W+\text{jets}$ and $W\gamma$ Only

Fit results of jets $\rightarrow\gamma$  background estimation on pseudodata prepared as  $W+\text{jets}$  and  $W\gamma$  samples appropriately weighted and mixed together. On all the plots, the black histogram is the pseudodata, green is a real- $\gamma$  template, blue is a fake- $\gamma$  template, and red is a fit function. Cyan is a histogram of  $W+\text{jets}$  MC sample in a given channel.

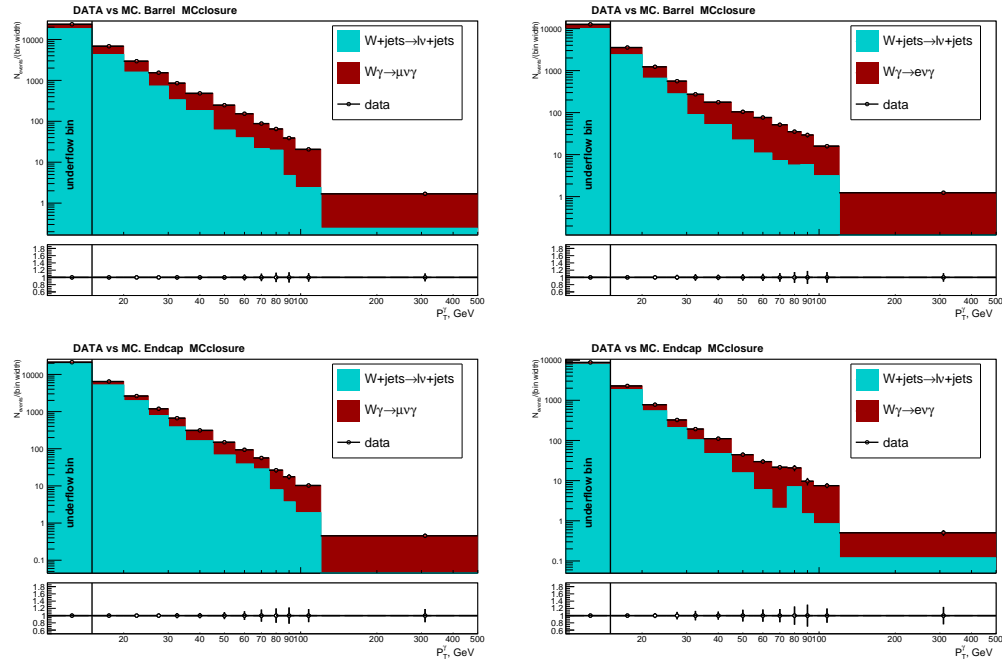


Figure .61: Pseudodata vs MC plots, MC closure  $W+\text{jets}$  and  $W\gamma$ . Left column - muon channel, right column - electron channel. Top to bottom: barrel and endcap photons.

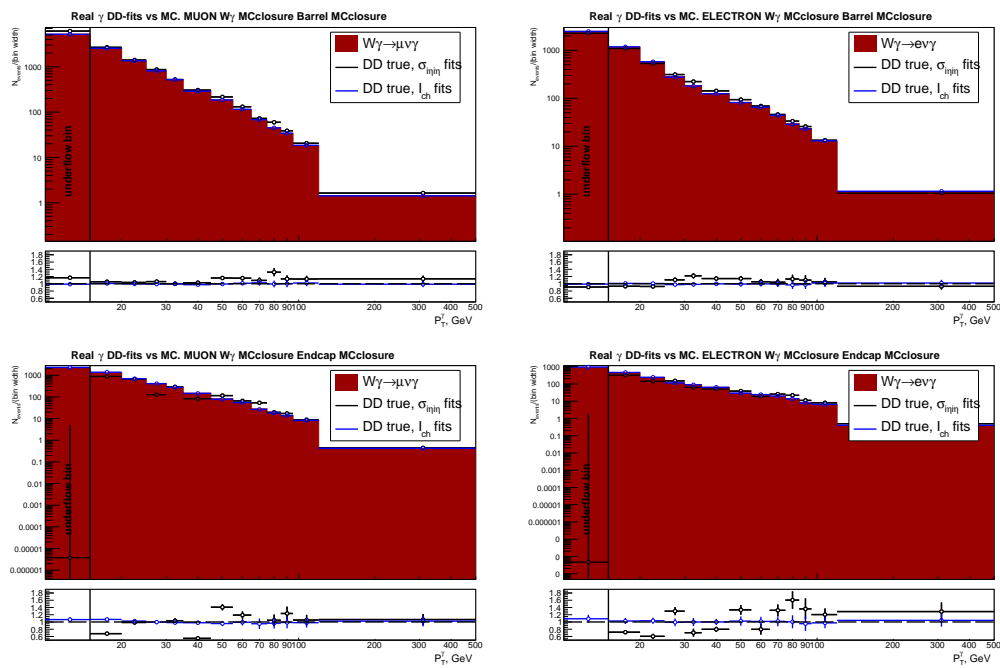


Figure .62: Real- $\gamma$  yields derived from fits of pseudodata superimposed with  $W\gamma$  MC. Left column - muon channel, right column - electron channel. Top to bottom: barrel and endcap photons.

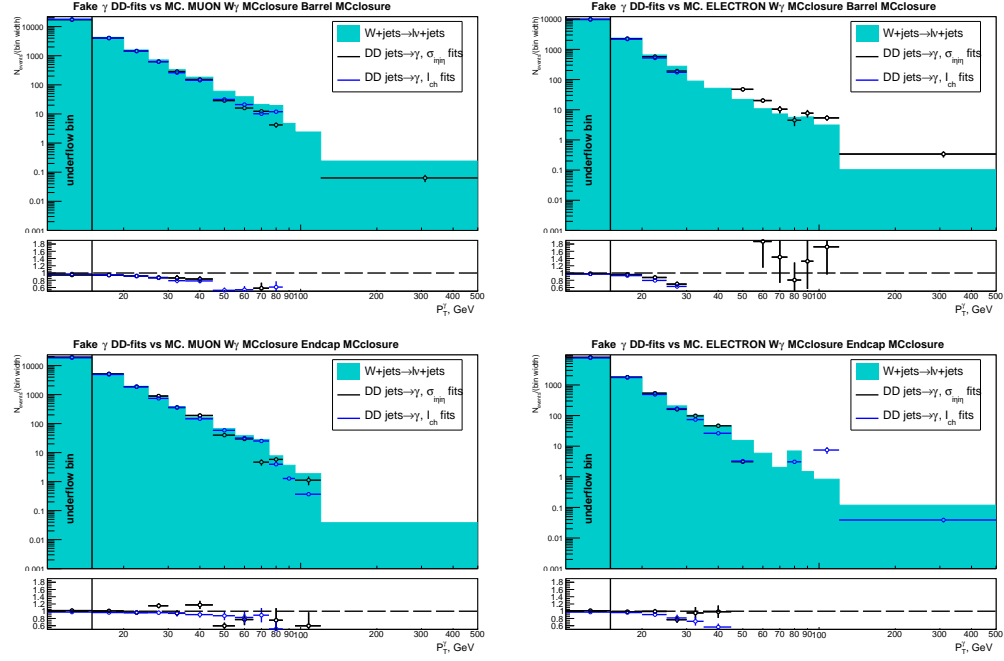


Figure .63:  $W+jets$  yields derived from fits of pseudodata superimposed with  $W+jets$  MC. Left column - muon channel, right column - electron. Top to bottom: barrel and endcap photons.

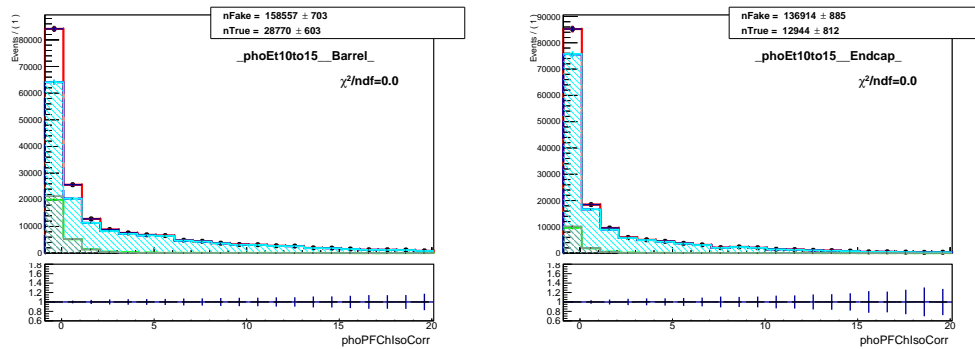


Figure .64: Fits of  $I_{ch}^{\gamma}$  templates, MC closure  $W+jets$  and  $W\gamma$ , muon channel, underflow bin.

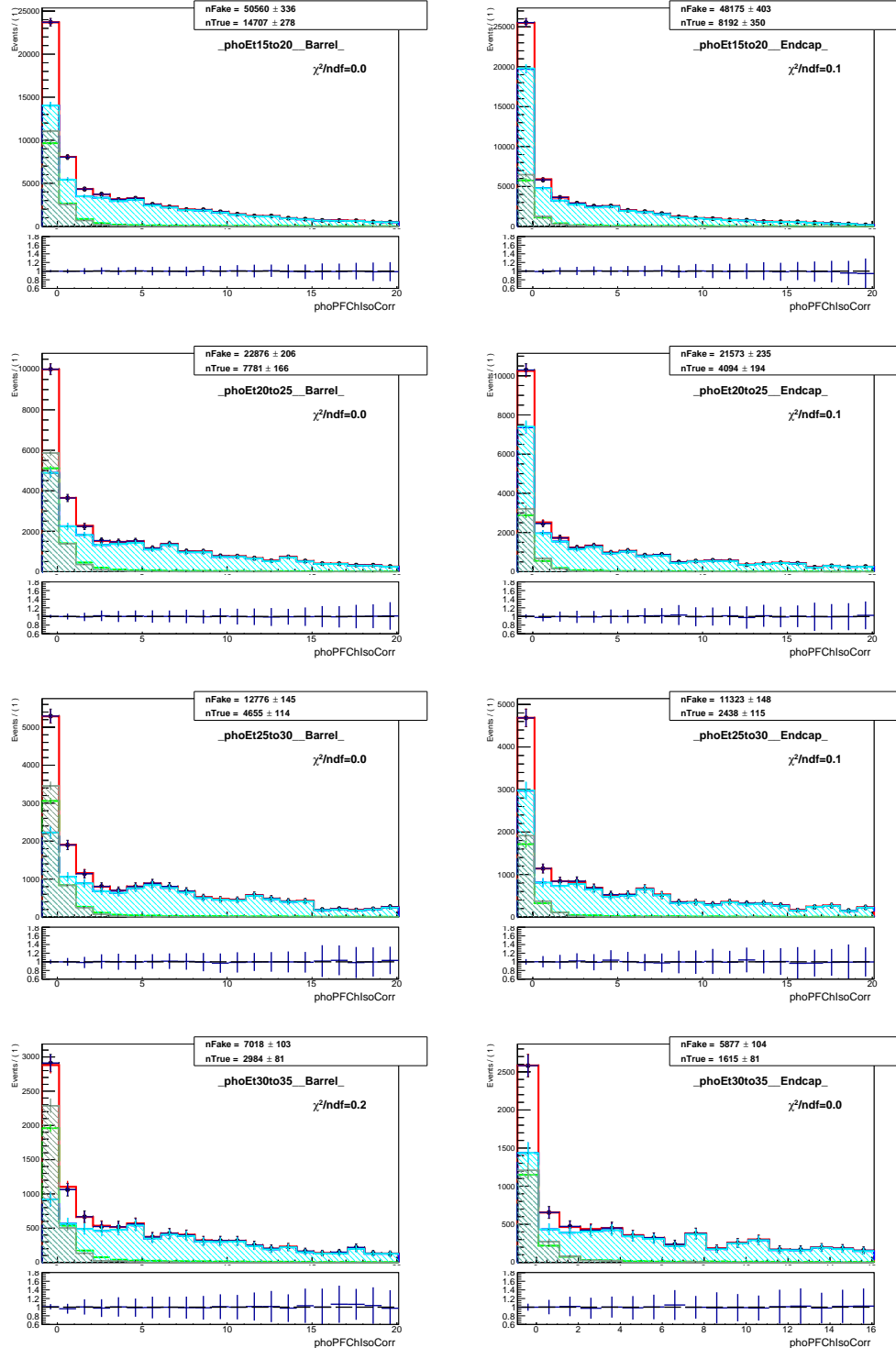


Figure .65: Fits of  $I_{ch}^{\gamma}$  templates, MC closure  $W+jets$  and  $W\gamma$ , muon channel.

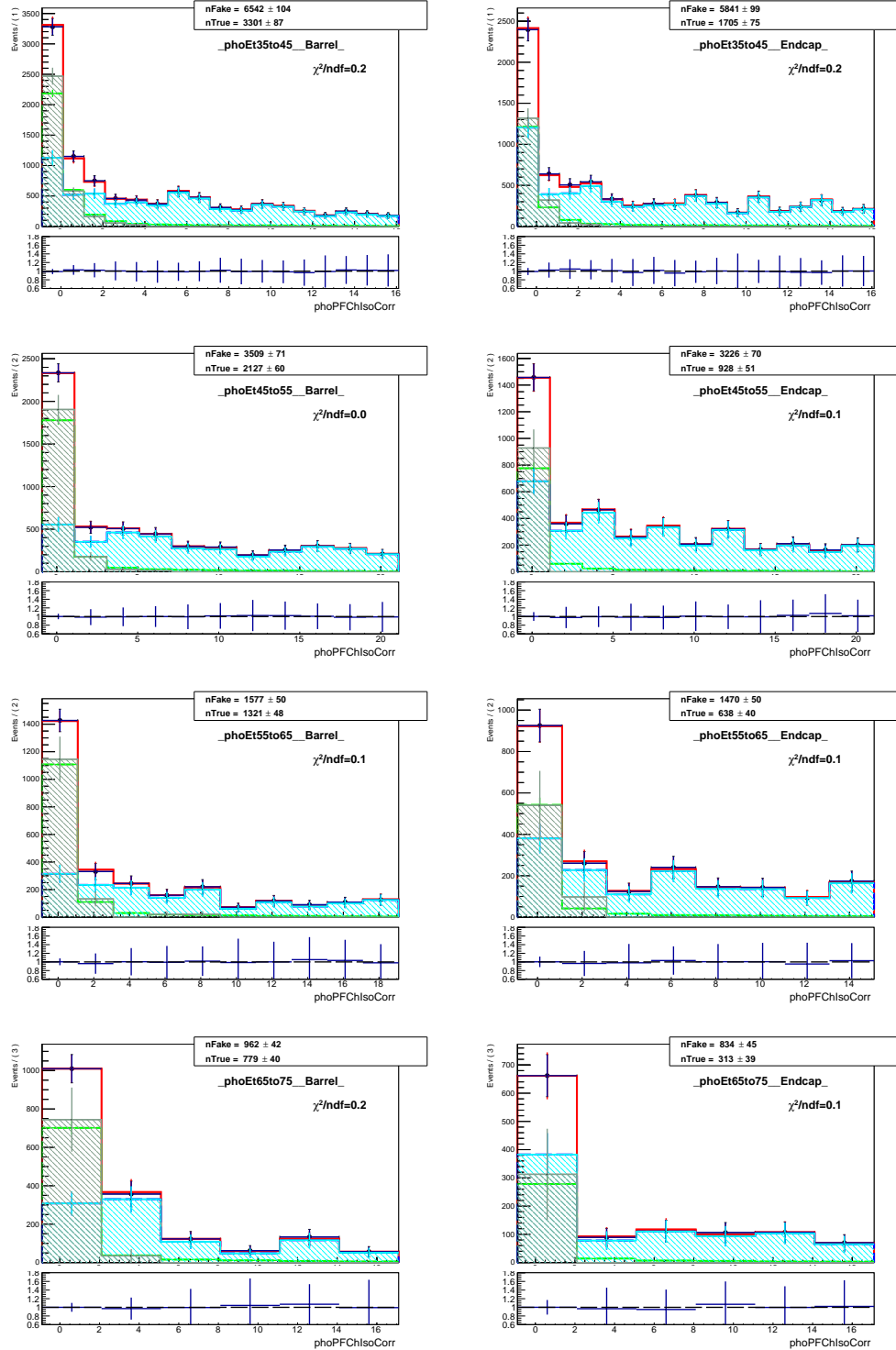


Figure .66: Fits of  $I_{ch}^{\gamma}$  templates, MC closure  $W+jets$  and  $W\gamma$ , muon channel.

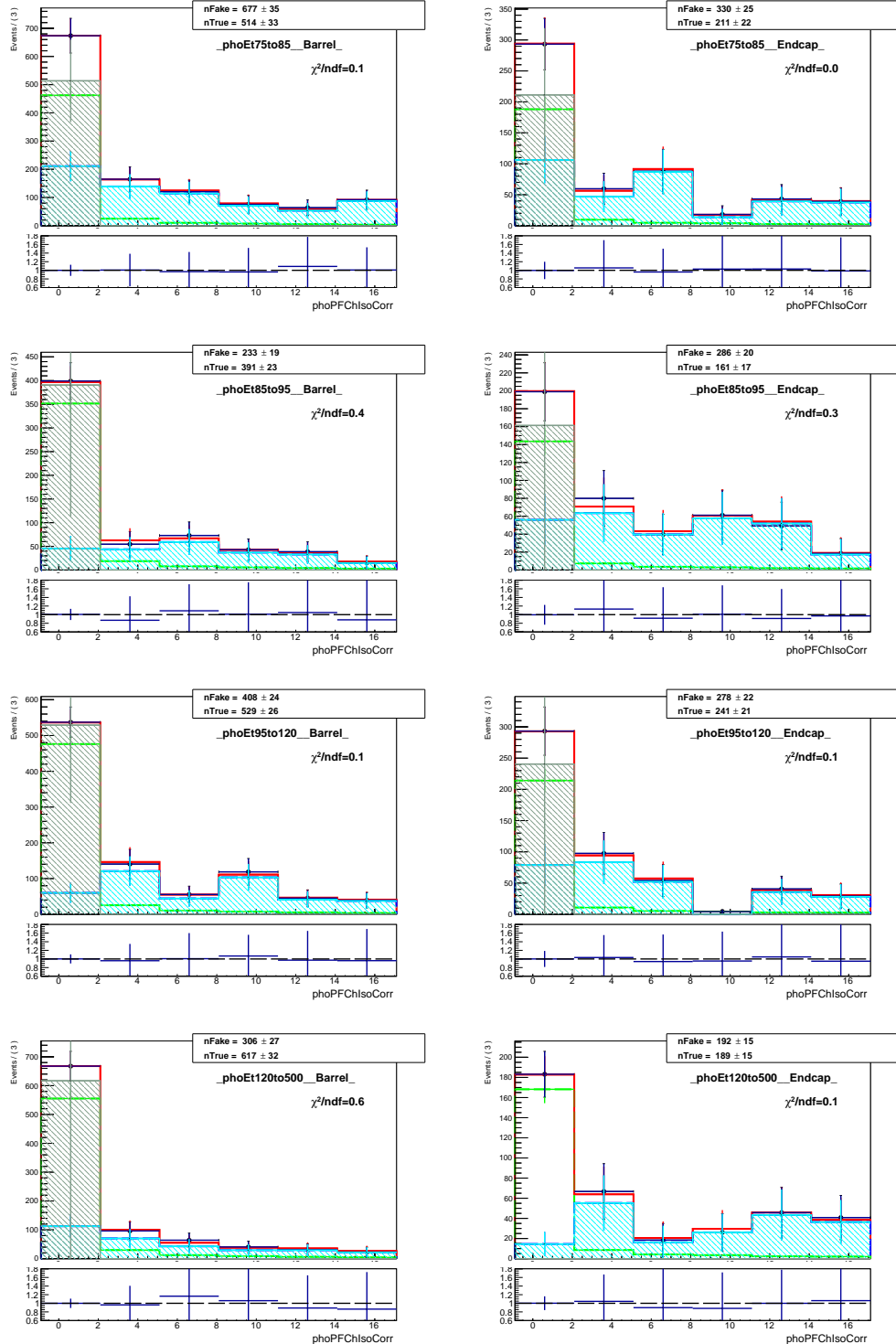


Figure .67: Fits of  $I_{ch}^{\gamma}$  templates, MC closure  $W+jets$  and  $W\gamma$ , muon channel.

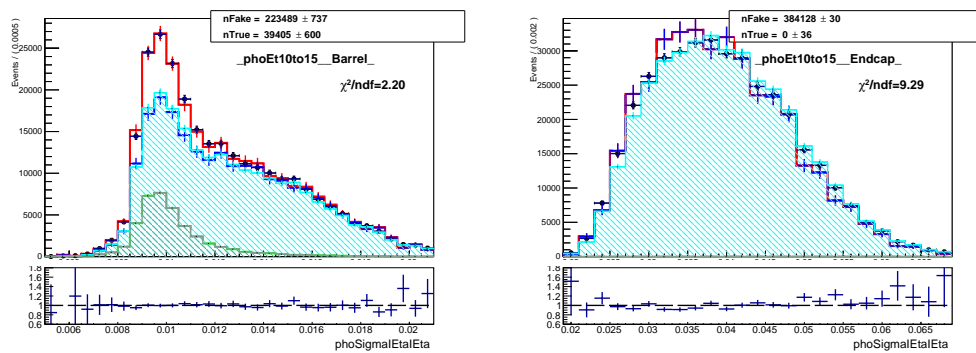


Figure .68: Fits of  $\sigma_{i\eta i\eta}$  templates, MC closure  $W+\text{jets}$  and  $W\gamma$ , muon channel, underflow bin.

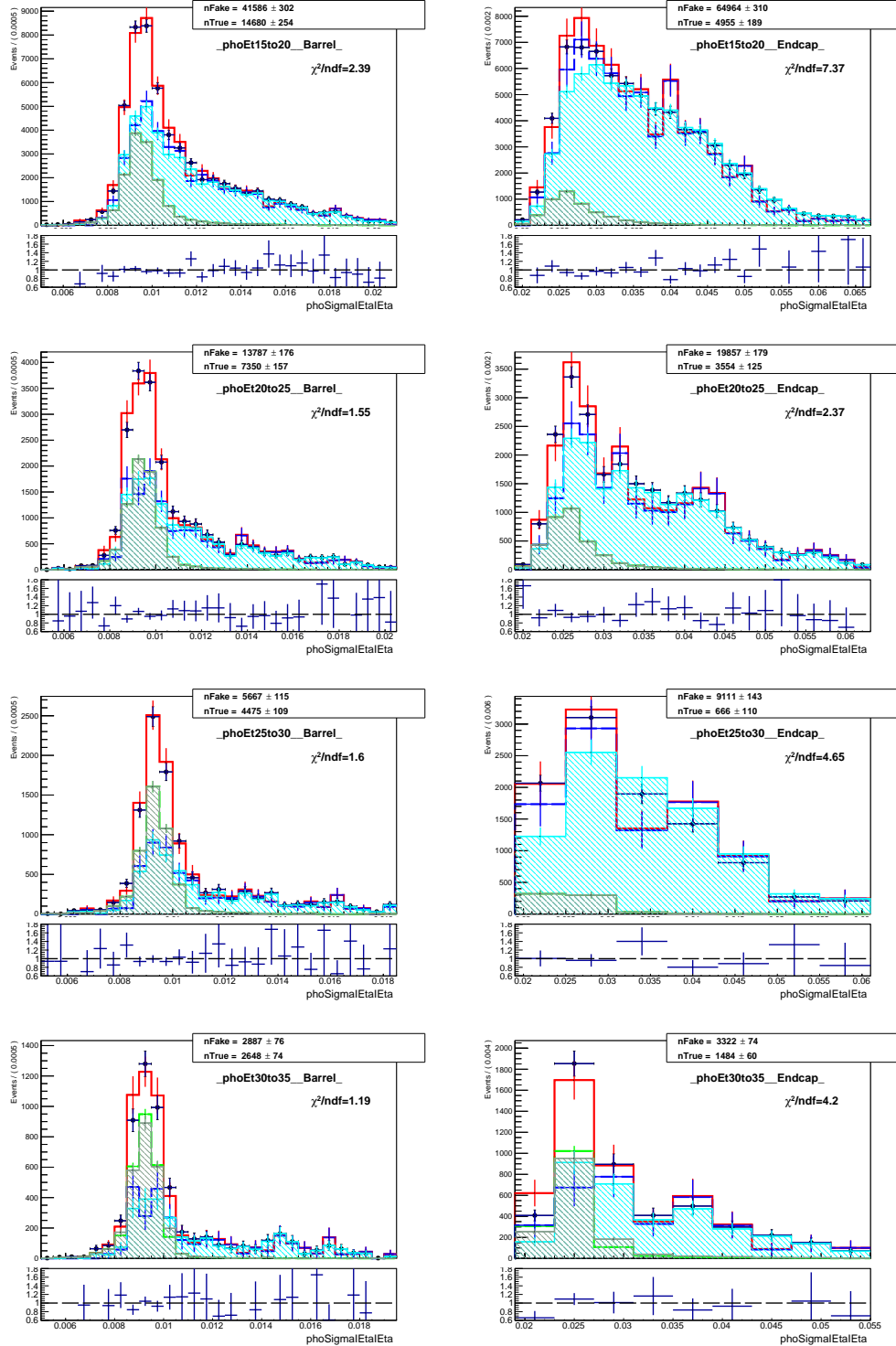


Figure .69: Fits of  $\sigma_{i\eta i\eta}$  templates, MC closure  $W+jets$  and  $W\gamma$ , muon channel.

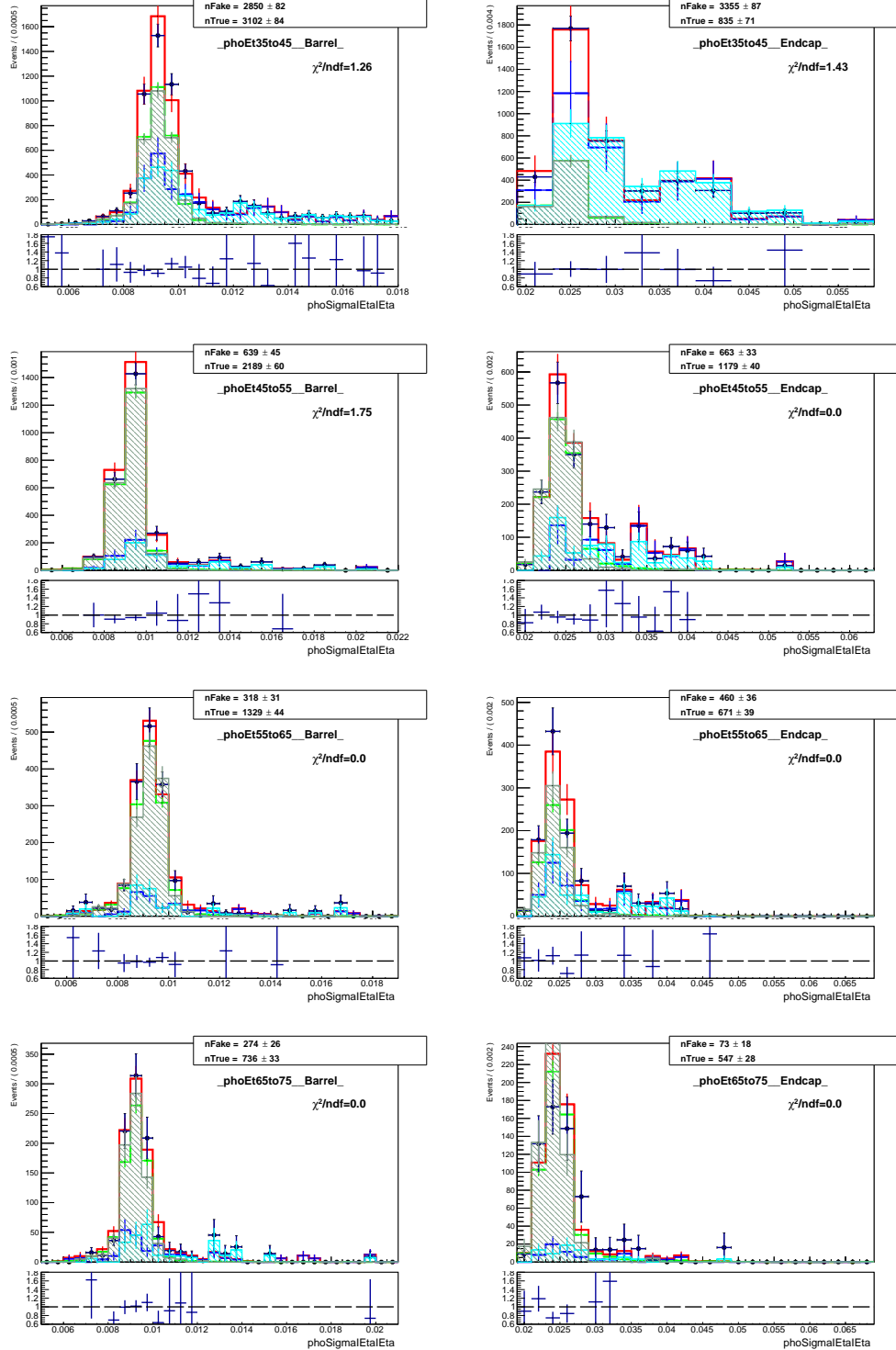


Figure .70: Fits of  $\sigma_{i\eta i\eta}$  templates, MC closure  $W+jets$  and  $W\gamma$ , muon channel.

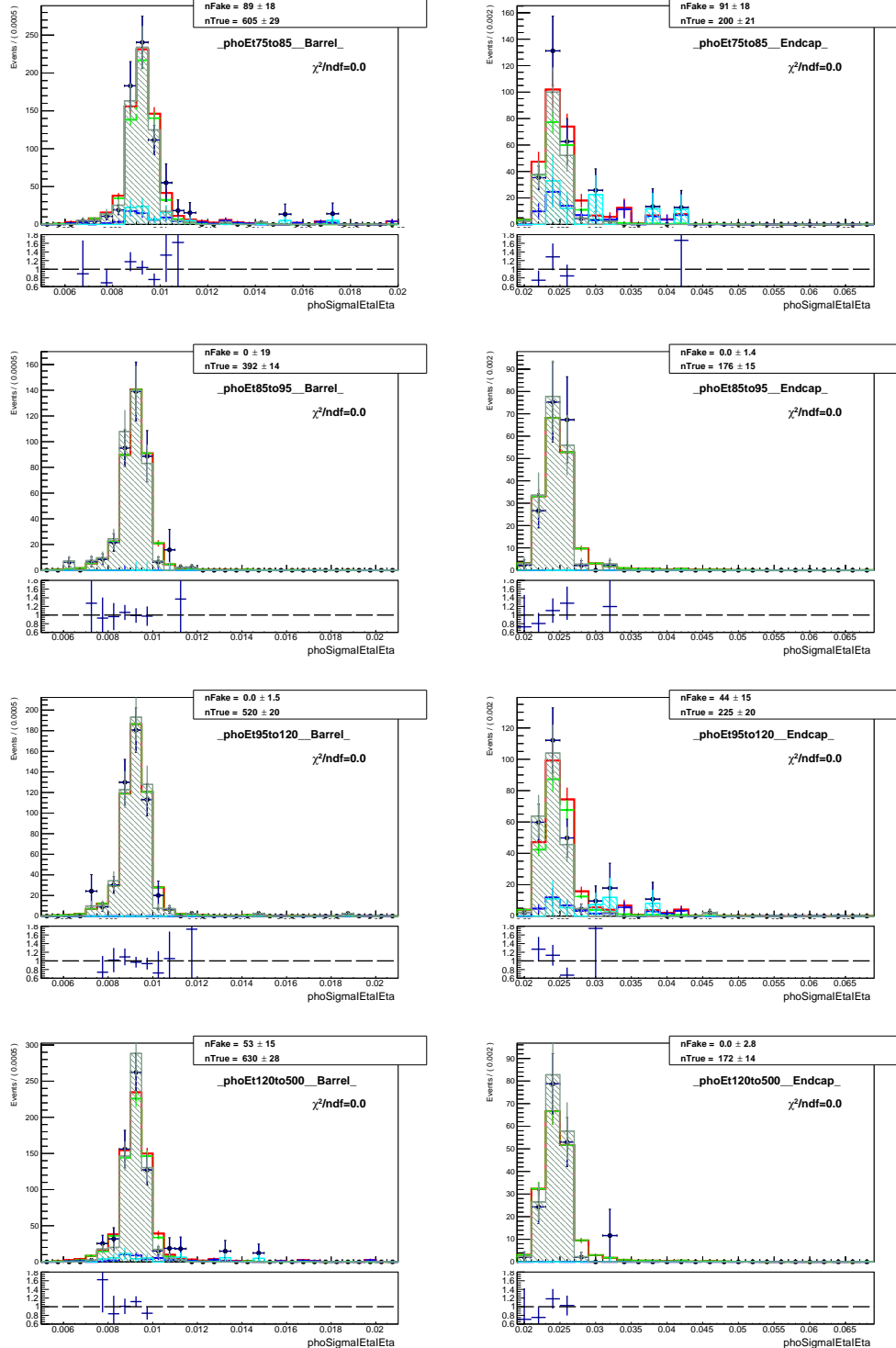


Figure .71: Fits of  $\sigma_{i\eta i\eta}$  templates, MC closure  $W+jets$  and  $W\gamma$ , muon channel.

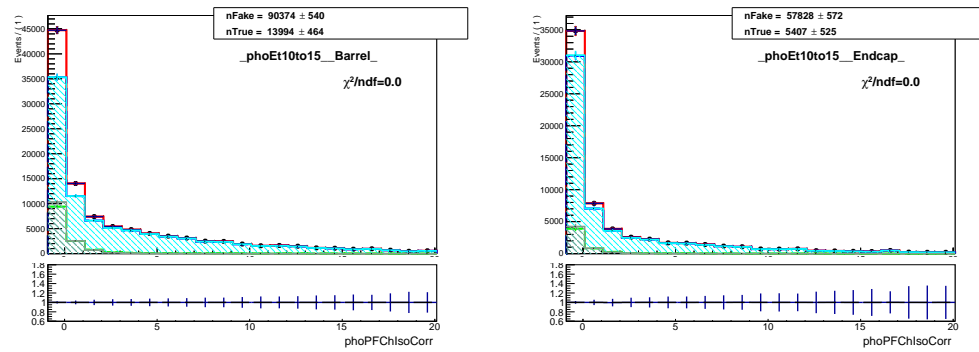


Figure .72: Fits of  $I_{ch}^{\gamma}$  templates, MC closure  $W+\text{jets}$  and  $W\gamma$ , electron channel, underflow bin.

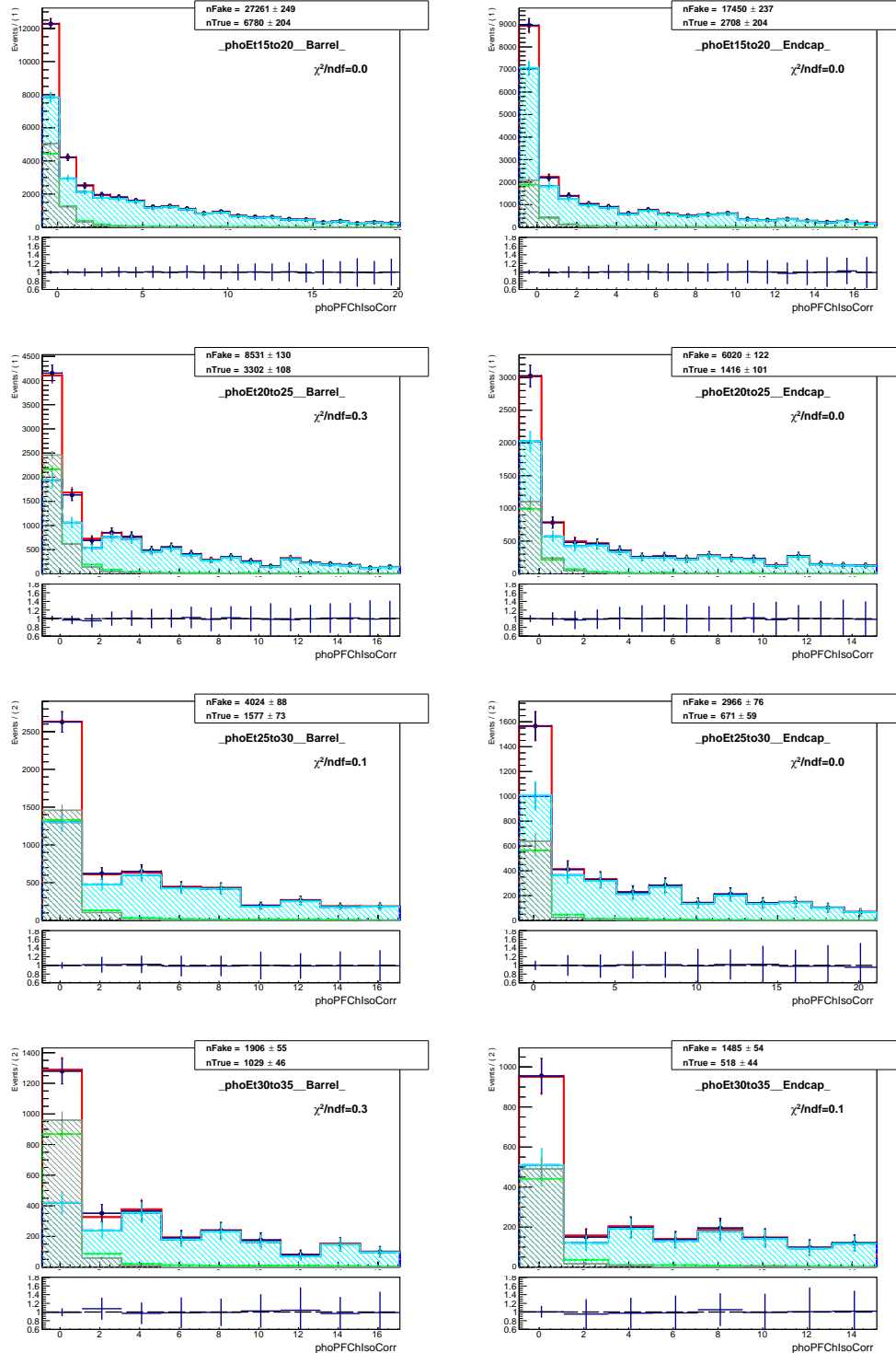


Figure .73: Fits of  $I_{ch}^{\gamma}$  templates, MC closure  $W+jets$  and  $W\gamma$ , electron channel.

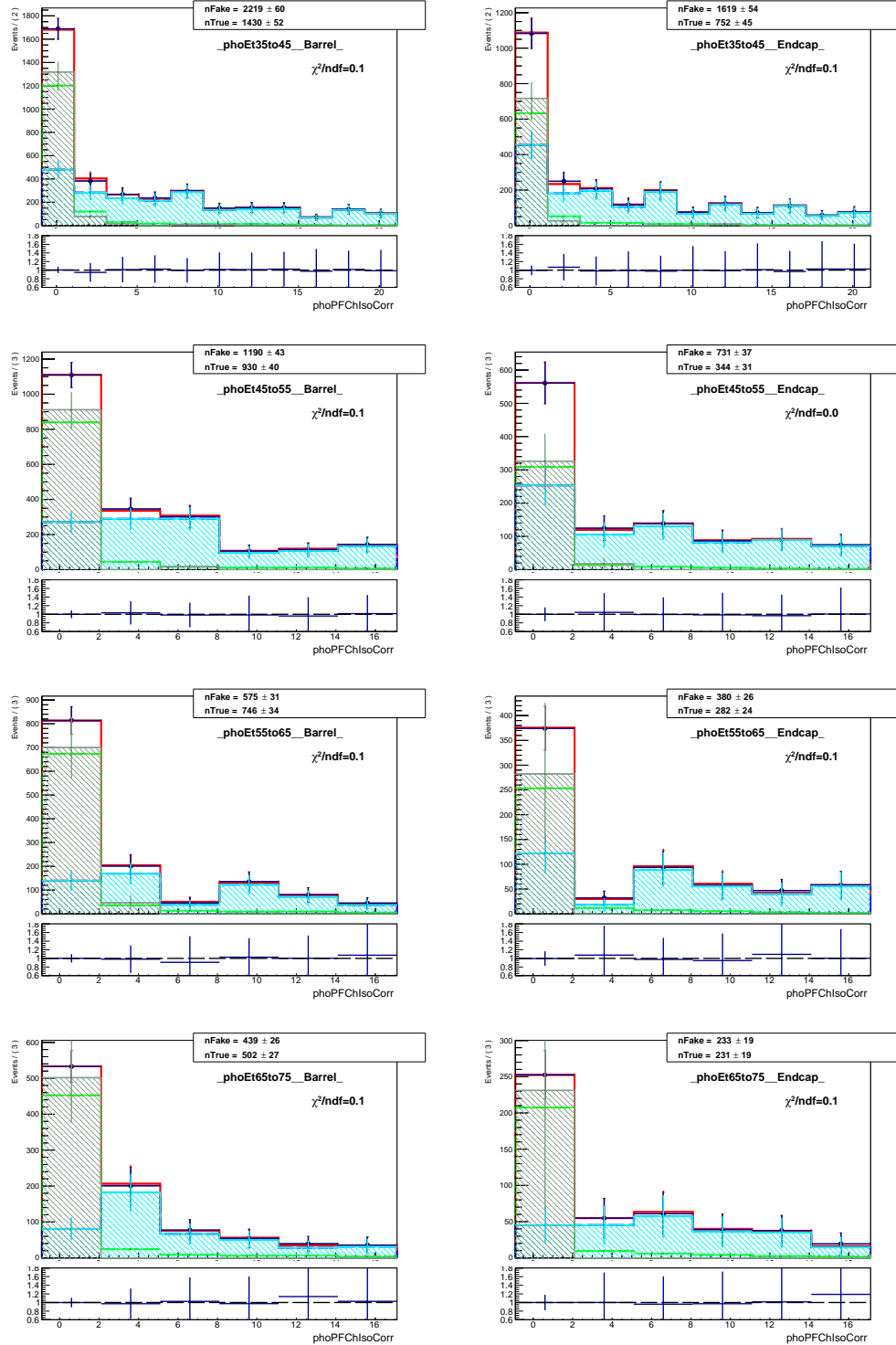


Figure .74: Fits of  $I_{ch}^{\gamma}$  templates, MC closure  $W+jets$  and  $W\gamma$ , electron channel.

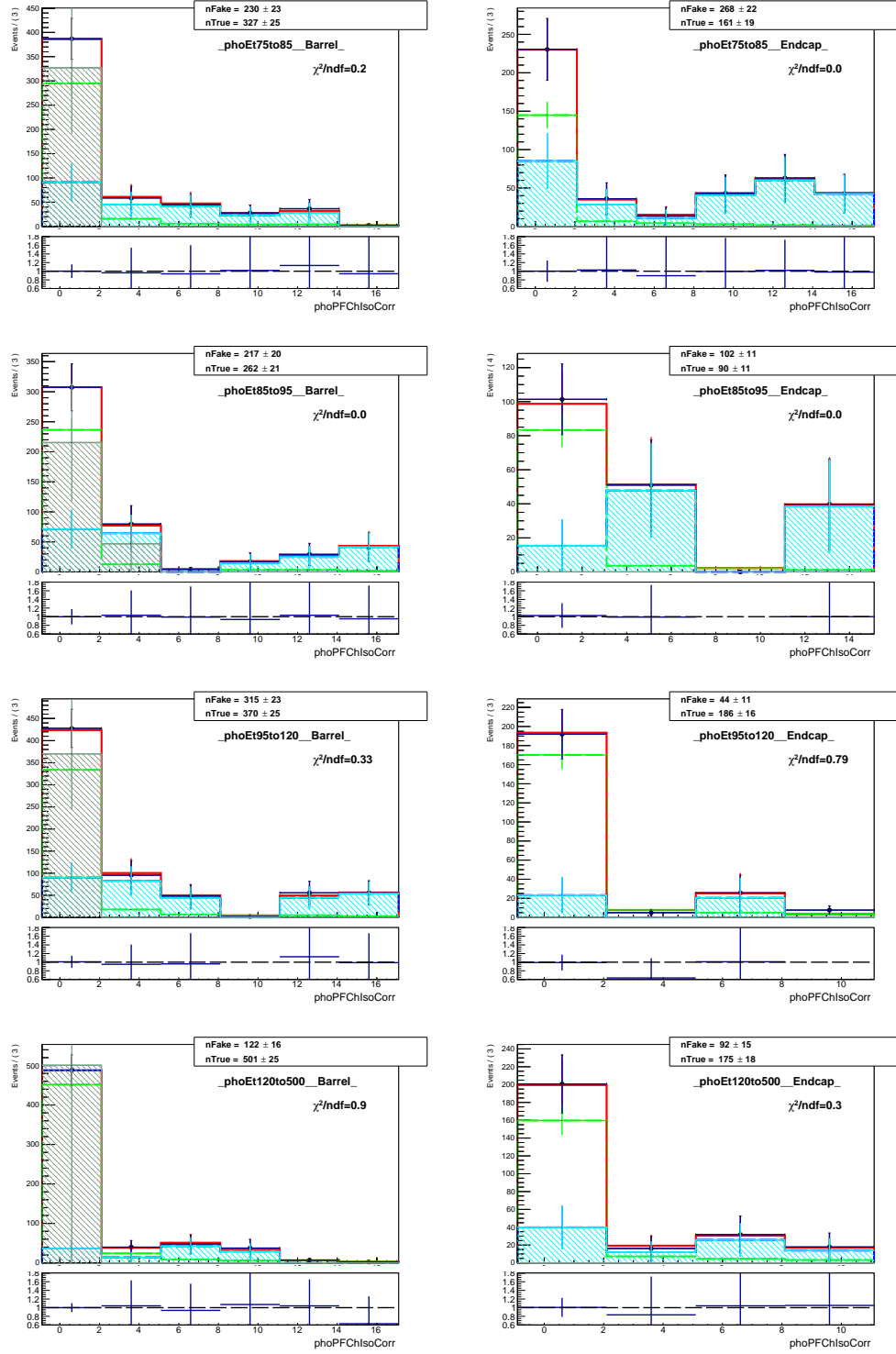


Figure .75: Fits of  $I_{ch}^{\gamma}$  templates, MC closure  $W+jets$  and  $W\gamma$ , electron channel.

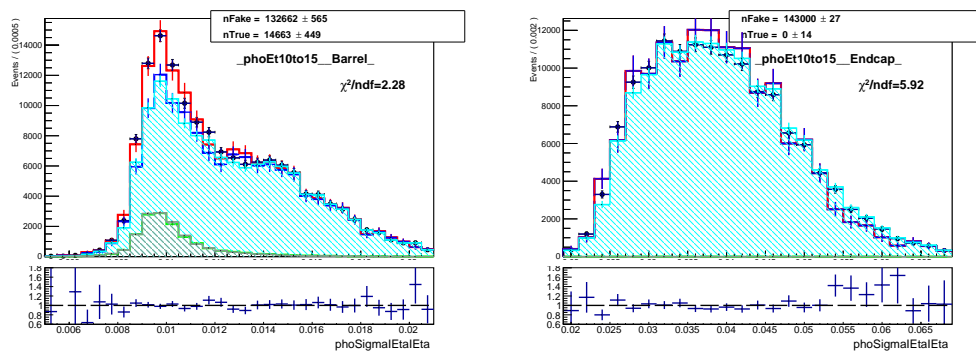


Figure .76: Fits of  $\sigma_{i\eta i\eta}$  templates, MC closure  $W+jets$  and  $W\gamma$ , electron channel, underflow bin.

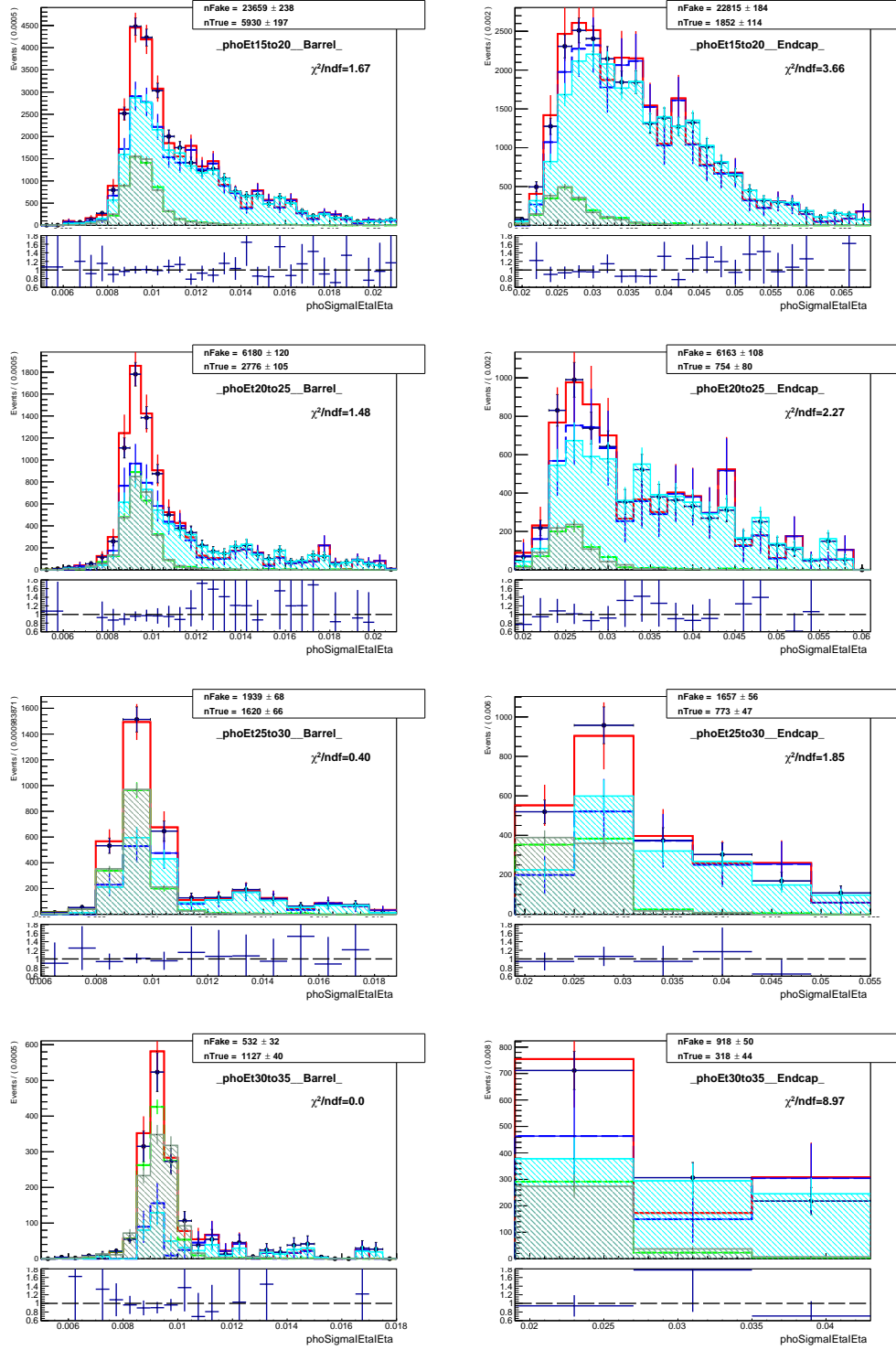


Figure .77: Fits of  $\sigma_{\eta\eta\eta\eta}$  templates, MC closure  $W+jets$  and  $W\gamma$ , electron channel.

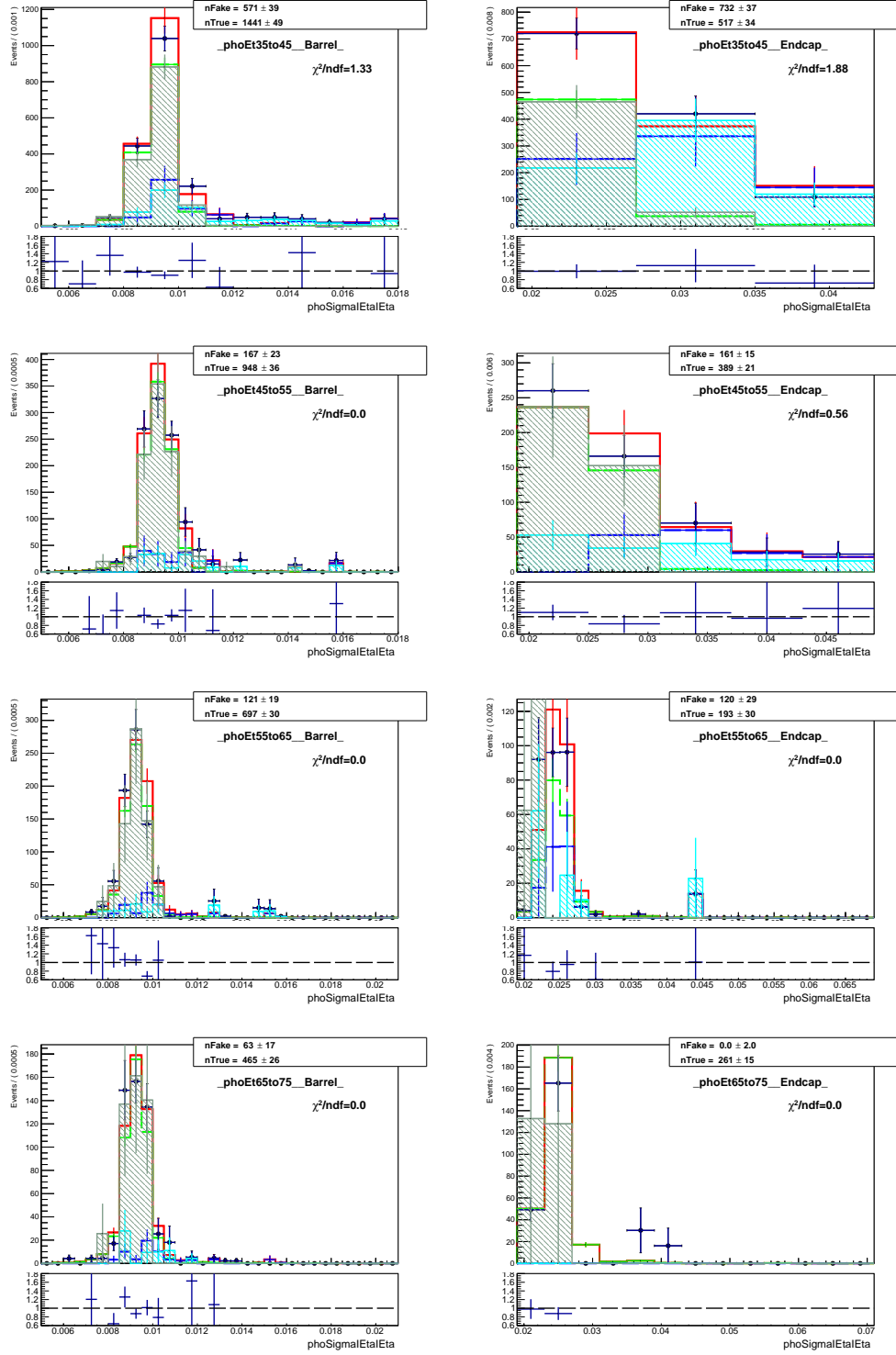


Figure .78: Fits of  $\sigma_{i\eta i\eta}$  templates, MC closure  $W+\text{jets}$  and  $W\gamma$ , electron channel.

## .7 APPENDIX: Fit Plots of $M_{e\gamma}$

Fit results of electron-photon invariant mass  $M_{e\gamma}$  for the  $e \rightarrow \gamma$  data-driven estimation in the electron channel. The procedure of the background estimation is described in Ch. 5.2.2.

The number of  $e\gamma$  events in data under the Z-peak  $N_{MC-Zpeak}^{e\rightarrow\gamma}$  is extracted from the fit of the model:

$$F_{fit} = N_{sig} \cdot (RooNDKeysPdf \times Gaussian) + N_{bkg} \cdot (RooCMSShapePdf). \quad (9)$$

The function *RooNDKeysPdf* is part of the RooFit package [53] and the *RooCMSShapePdf* was developed specifically for CMS [52].

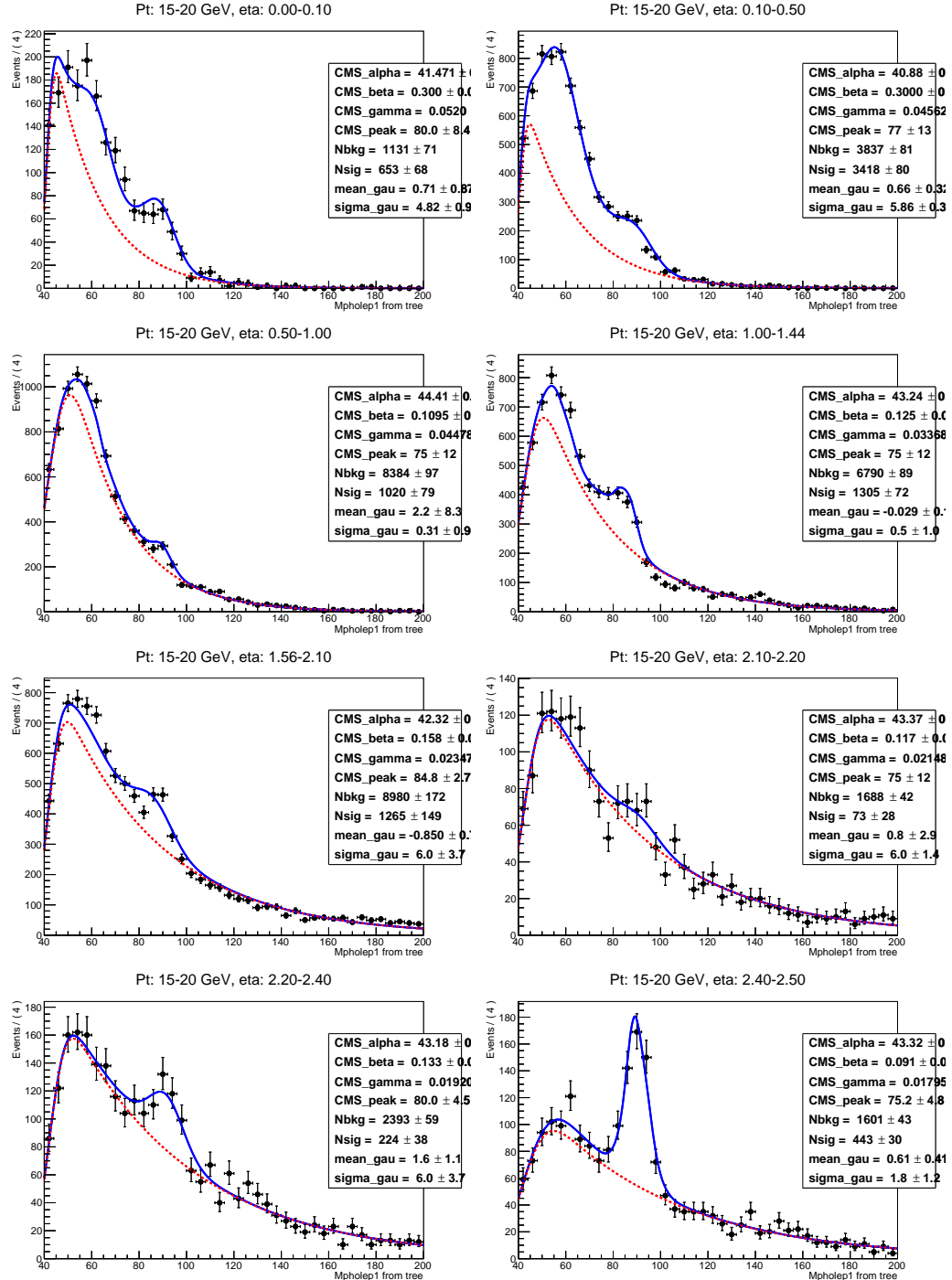


Figure .80:  $M_{e\gamma}$  fits,  $W\gamma$ , electron channel,  $15-20 \text{ GeV}$ , 8  $\eta^\gamma$  bins.

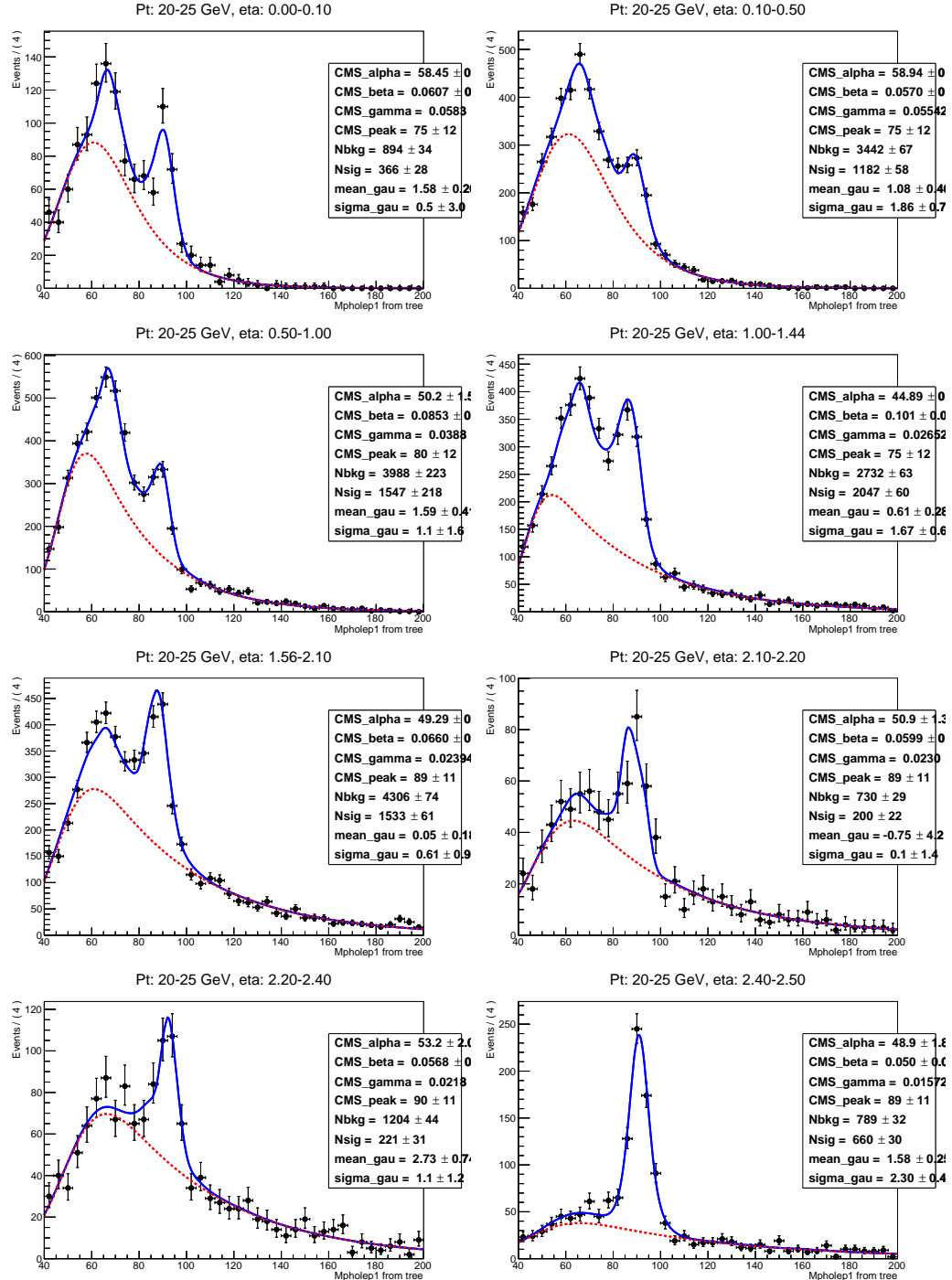


Figure .81:  $M_{e\gamma}$  fits,  $W\gamma$ , electron channel, 20-25 GeV, 8  $\eta^{\gamma}$  bins.

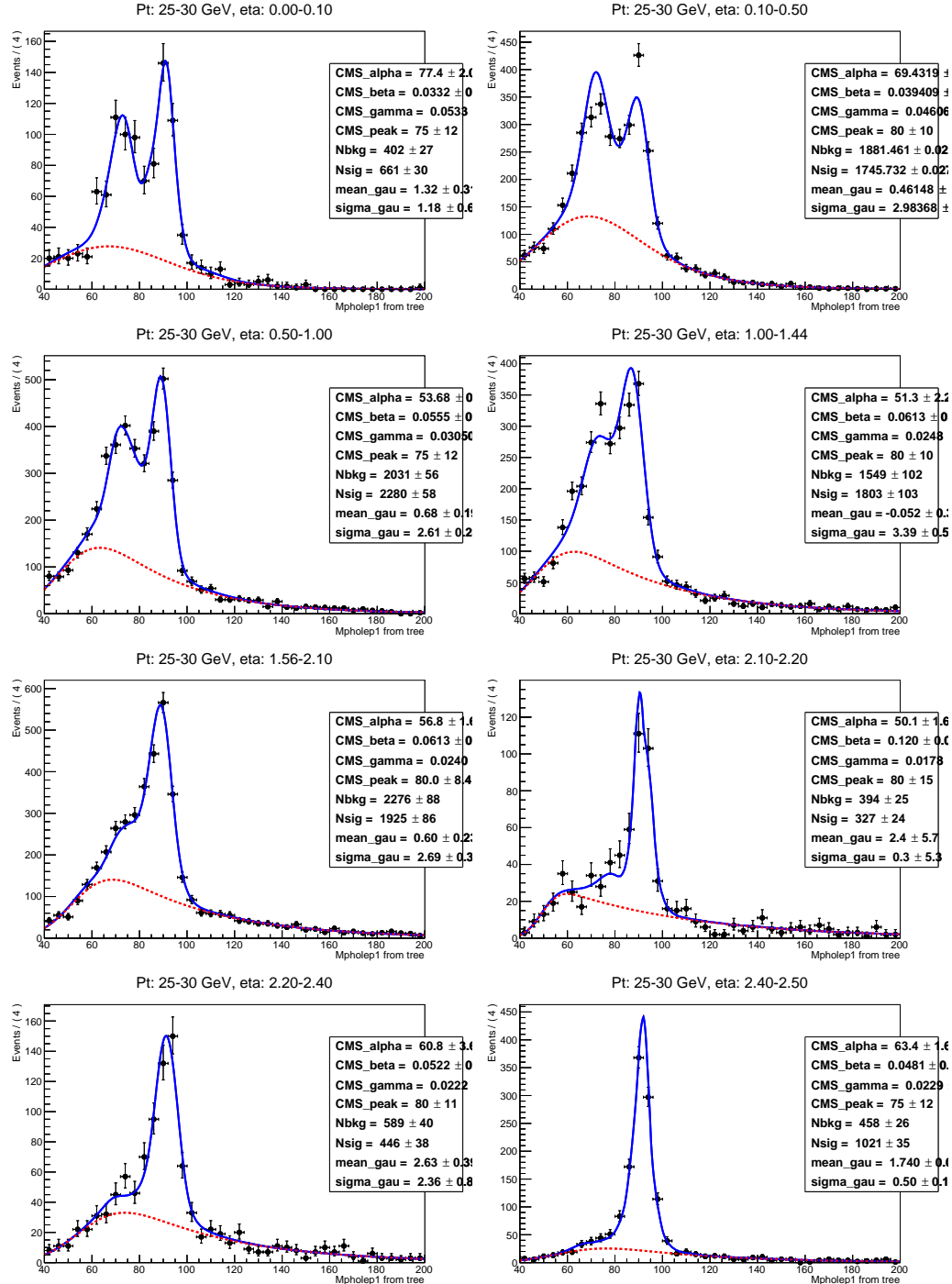


Figure .82:  $M_{e\gamma}$  fits,  $W\gamma$ , electron channel, 25-30 GeV, 8  $\eta^\gamma$  bins.

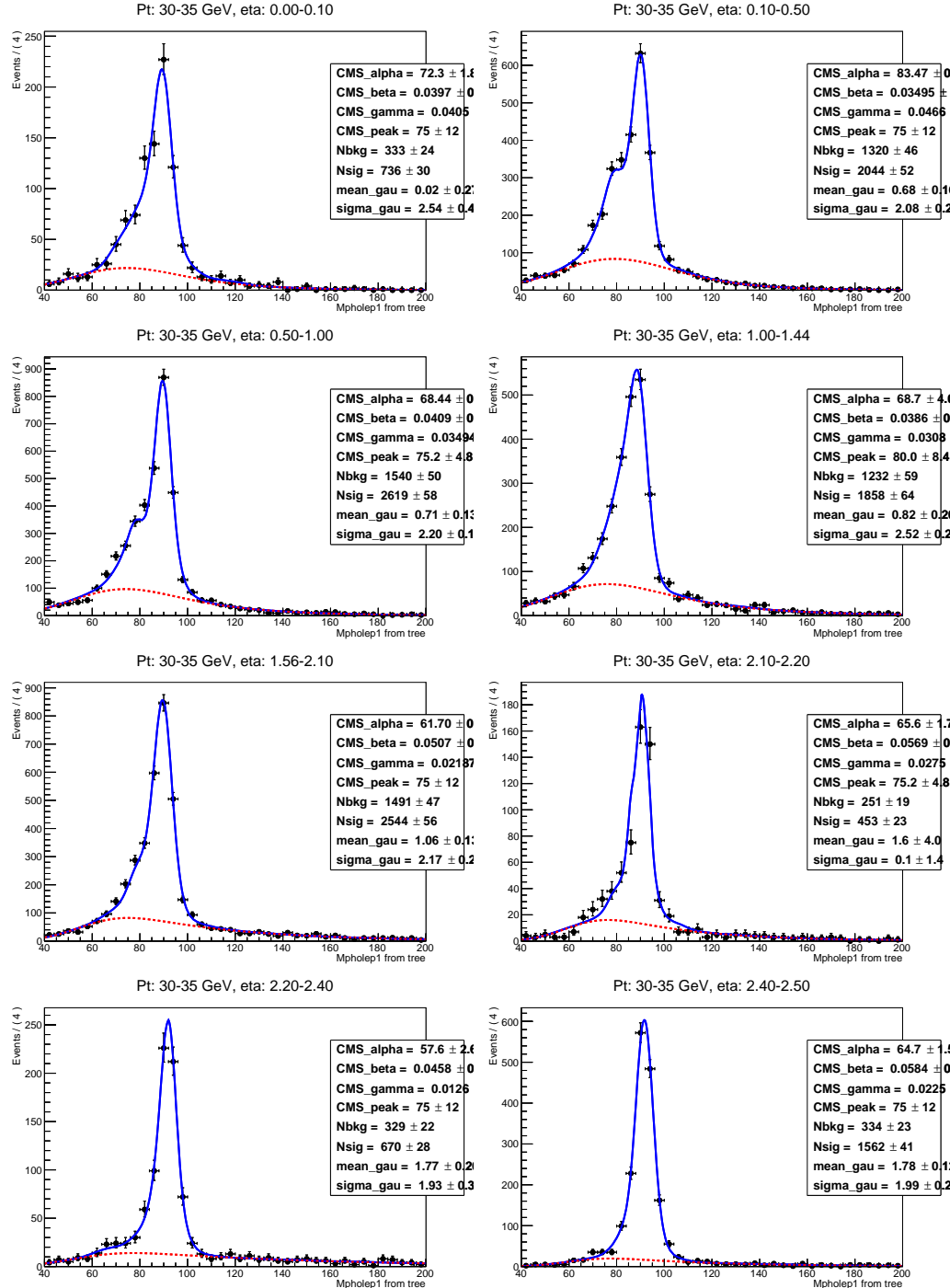


Figure .83:  $M_{e\gamma}$  fits,  $W\gamma$ , electron channel, 30-35 GeV, 8  $\eta^\gamma$  bins.

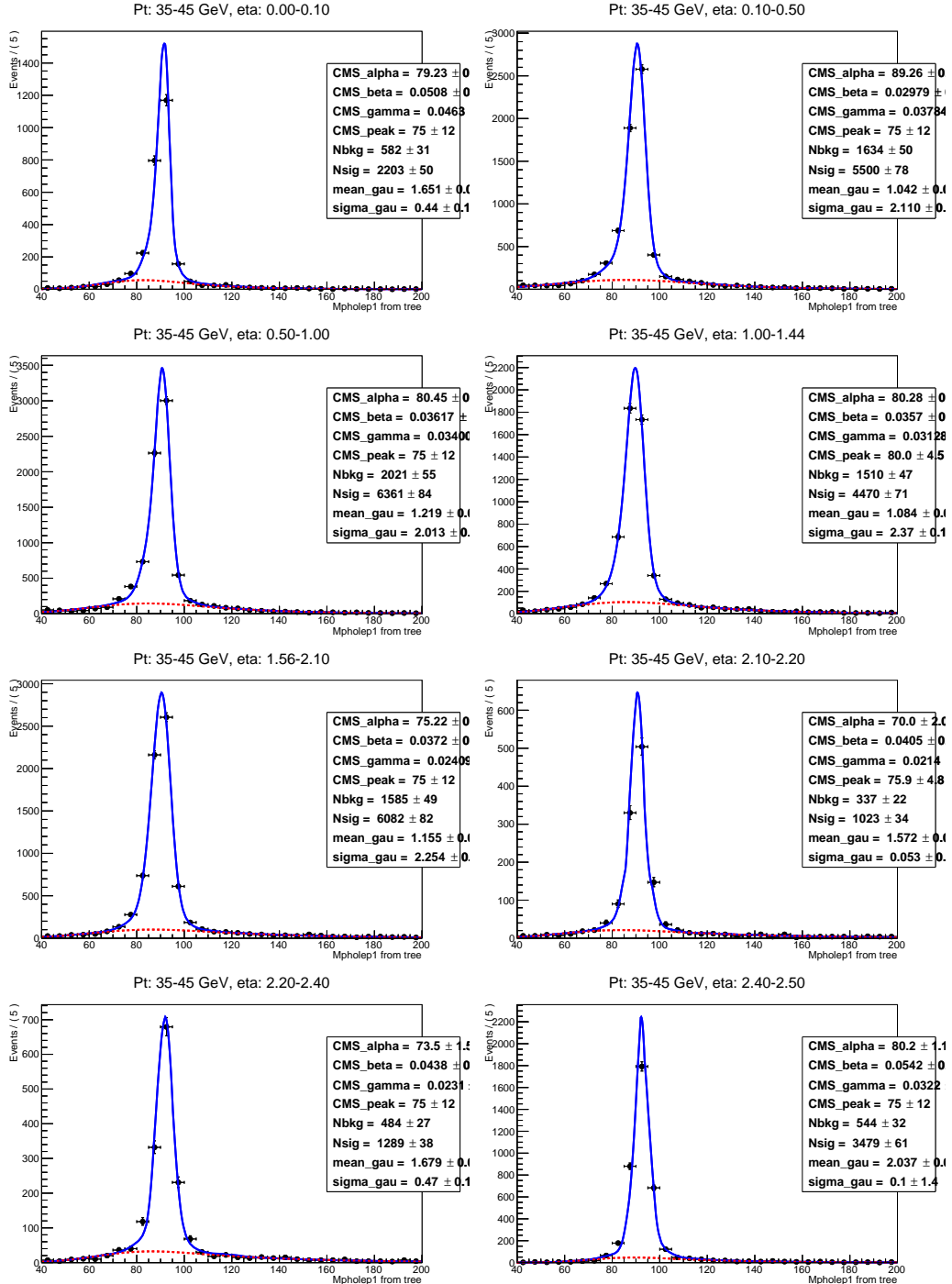


Figure .84:  $M_{e\gamma}$  fits,  $W\gamma$ , electron channel, 35-45 GeV, 8  $\eta^\gamma$  bins.

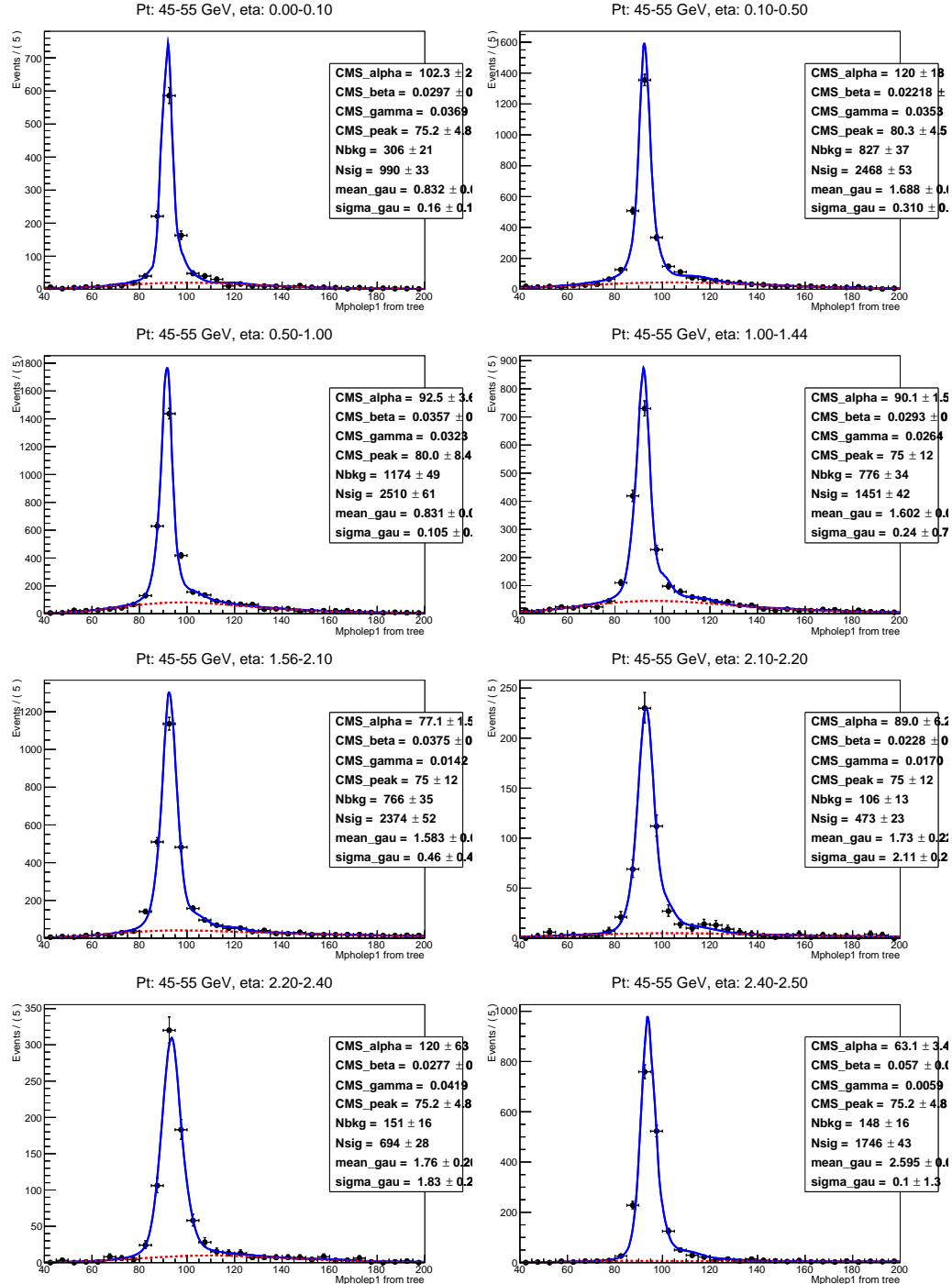


Figure .85:  $M_{e\gamma}$  fits,  $W\gamma$ , electron channel, 45-55 GeV, 8  $\eta^\gamma$  bins.

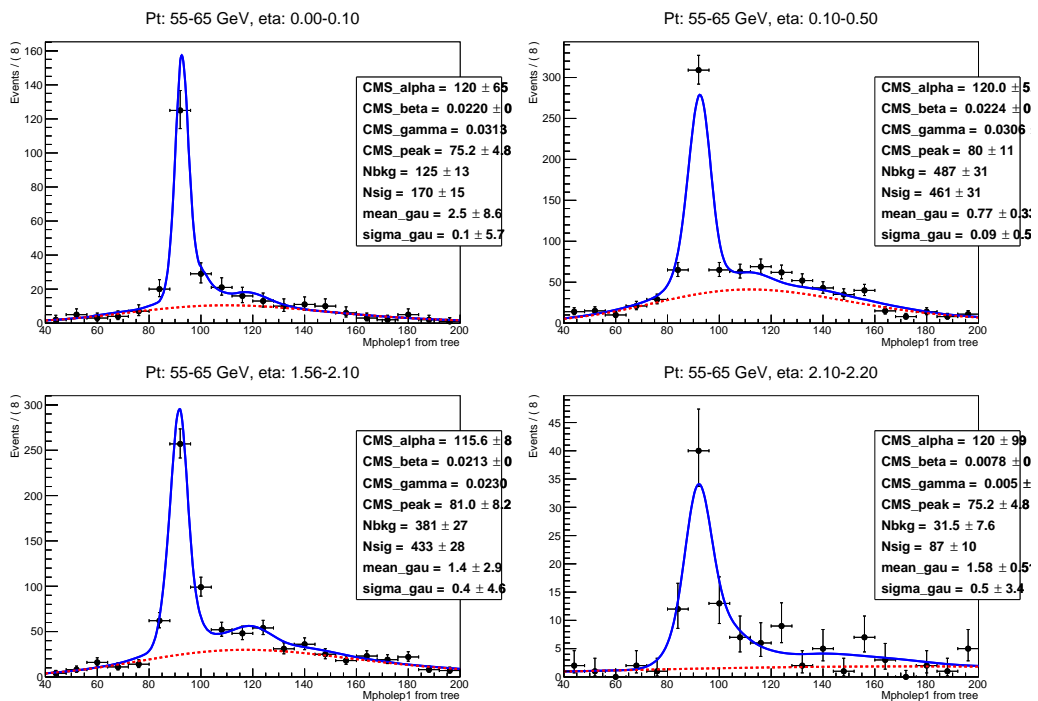


Figure .86:  $M_{e\gamma}$  fits,  $W\gamma$ , electron channel, 55-65 GeV, 4  $\eta^\gamma$  bins.

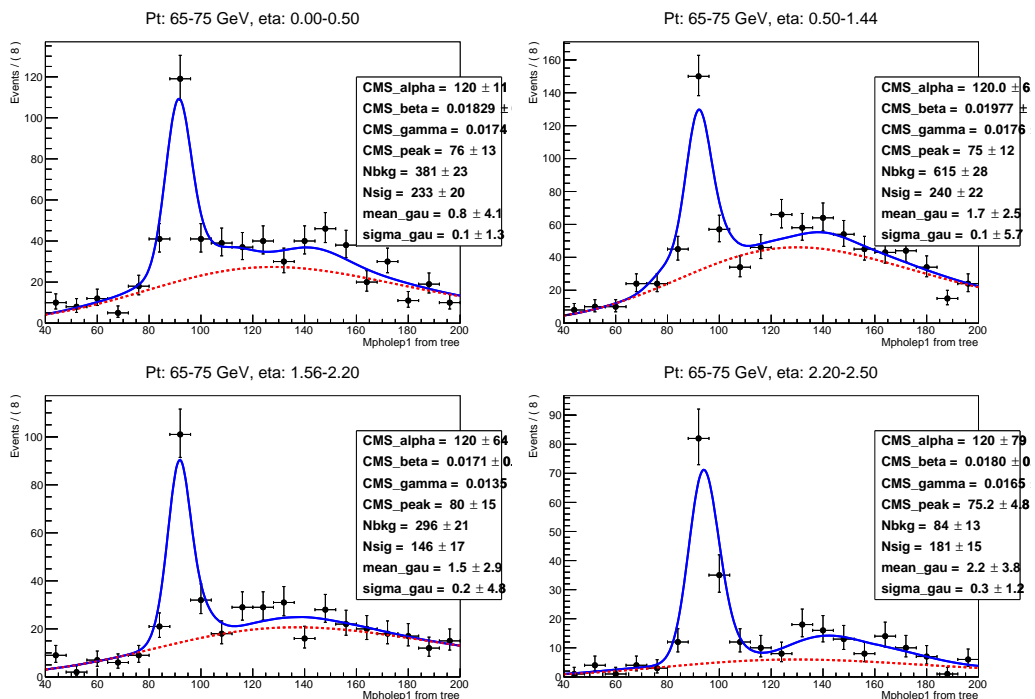


Figure .87:  $M_{e\gamma}$  fits,  $W\gamma$ , electron channel, 65-75 GeV, 4  $\eta^\gamma$  bins.

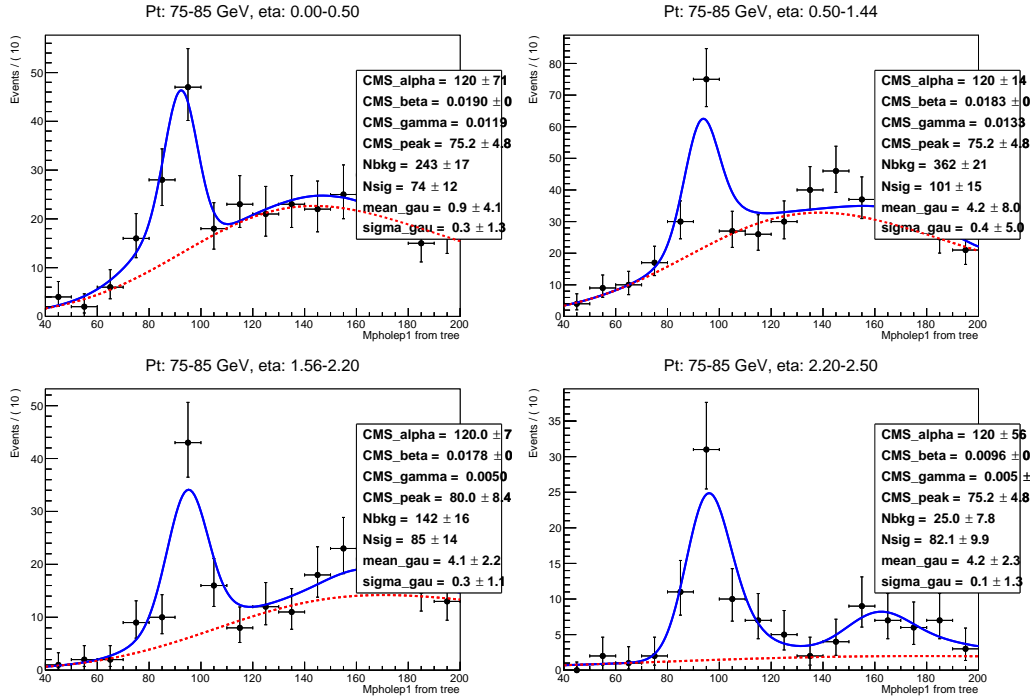


Figure .88:  $M_{e\gamma}$  fits,  $W\gamma$ , electron channel,  $75-85 \text{ GeV}$ , 4  $\eta^\gamma$  bins.

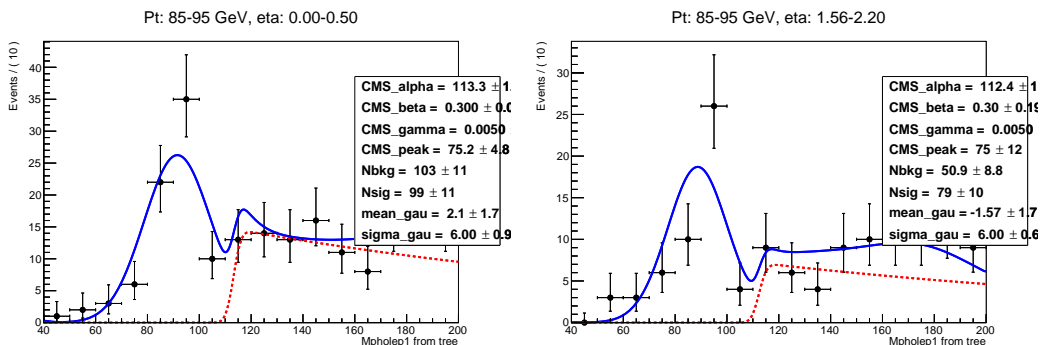


Figure .89:  $M_{e\gamma}$  fits,  $W\gamma$ , electron channel,  $85-95 \text{ GeV}$ , 2  $\eta^\gamma$  bins.

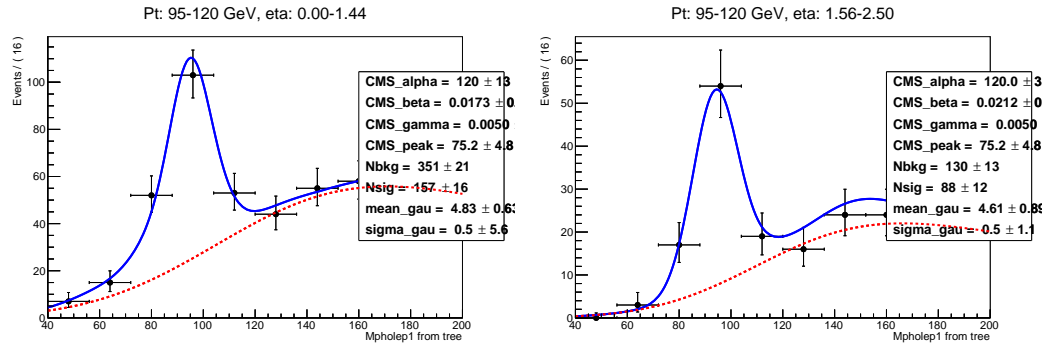


Figure .90:  $M_{e\gamma}$  fits,  $W\gamma$ , electron channel, 95-120 GeV, 2  $\eta^\gamma$  bins.

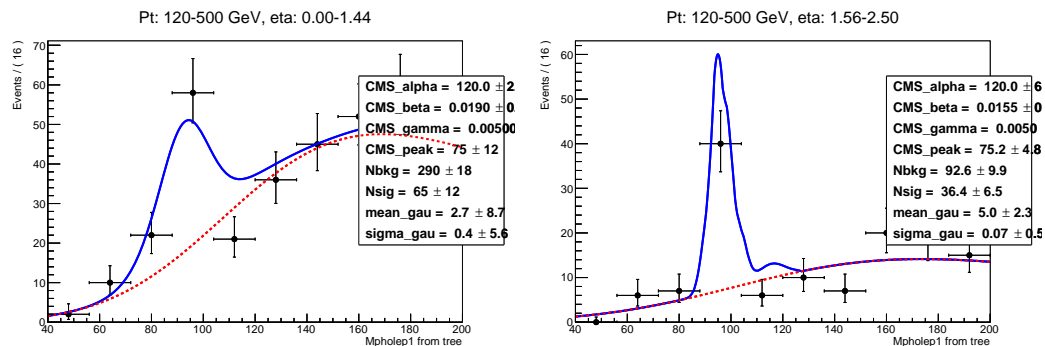


Figure .91:  $M_{e\gamma}$  fits,  $W\gamma$ , electron channel, 120-500 GeV, 2  $\eta^\gamma$  bins.

## .8 APPENDIX: Fit Plots of $M_{e\gamma}$ without $M_T^W$ cut

Fit results of electron-photon invariant mass  $M_{e\gamma}$  without  $M_T^W$  cut applied for the estimation of the systematic uncertainty for the procedure of the  $e \rightarrow \gamma$  background estimation in the electron channel. The procedure of the background estimation is described in Ch. 5.2.2, the procedure of the estimation of the systematic uncertainty is described in Ch. 5.5.2.

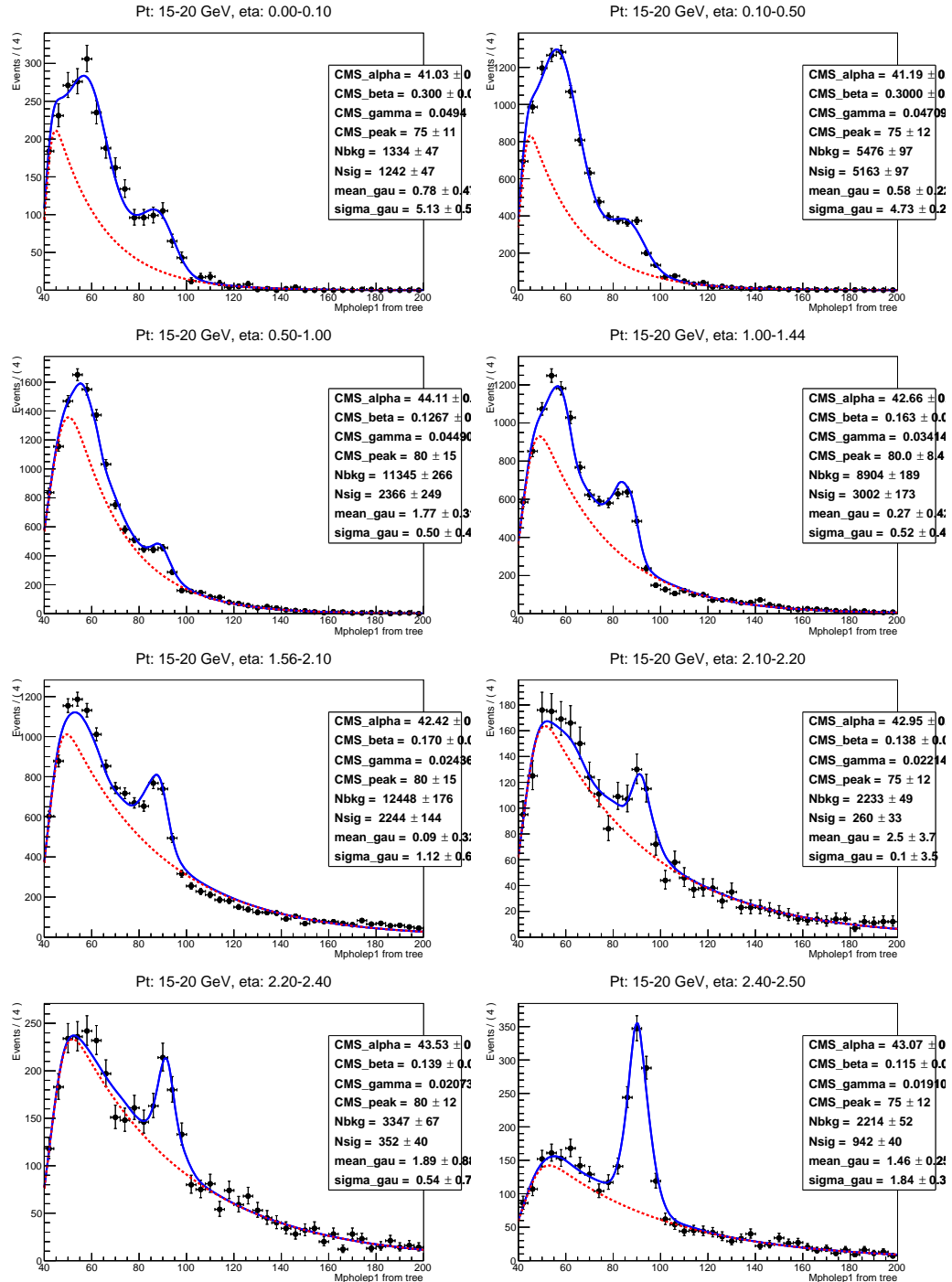


Figure .92:  $M_{e\gamma}$  fits,  $W\gamma$ , electron channel, underflow bin (15-20 GeV), 8  $\eta\gamma$  bins.

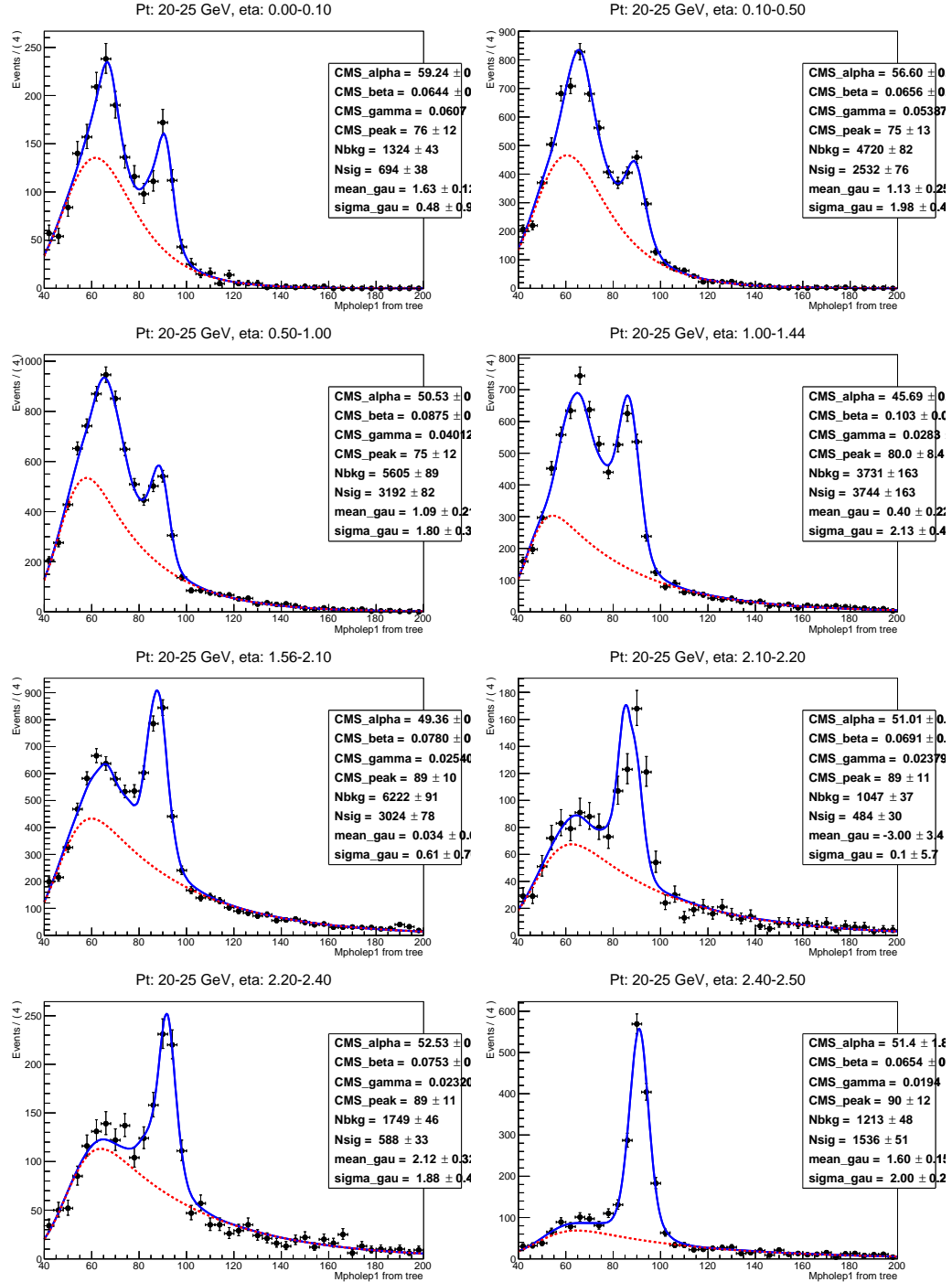


Figure .93:  $M_{e\gamma}$  fits,  $W\gamma$ , electron channel, underflow bin (20-25 GeV), 8  $\eta^\gamma$  bins.

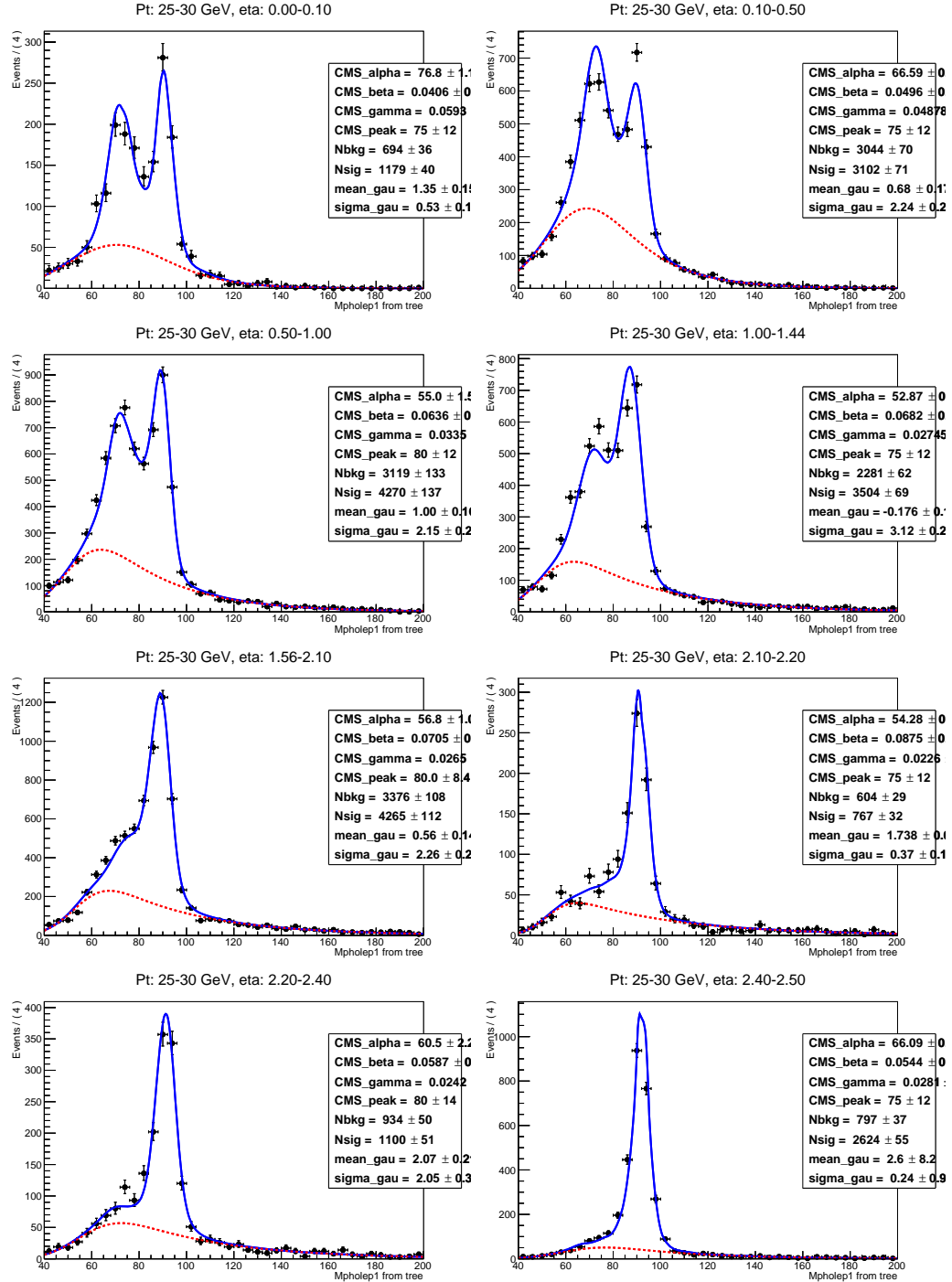


Figure .94:  $M_{e\gamma}$  fits,  $W\gamma$ , electron channel, underflow bin (25-30 GeV), 8  $\eta\gamma$  bins.

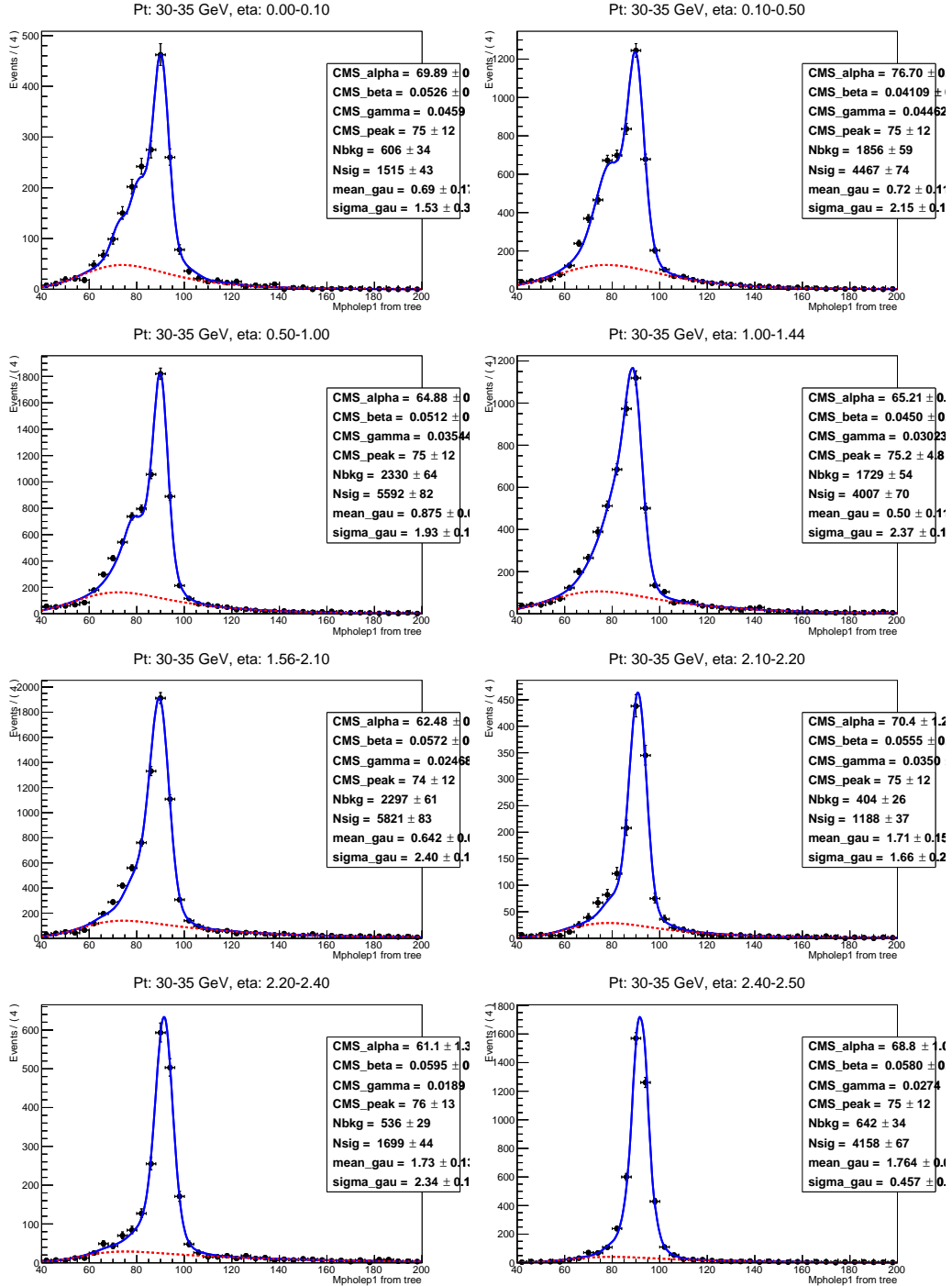


Figure .95:  $M_{e\gamma}$  fits,  $W\gamma$ , electron channel, underflow bin (30-35 GeV), 8  $\eta\gamma$  bins.

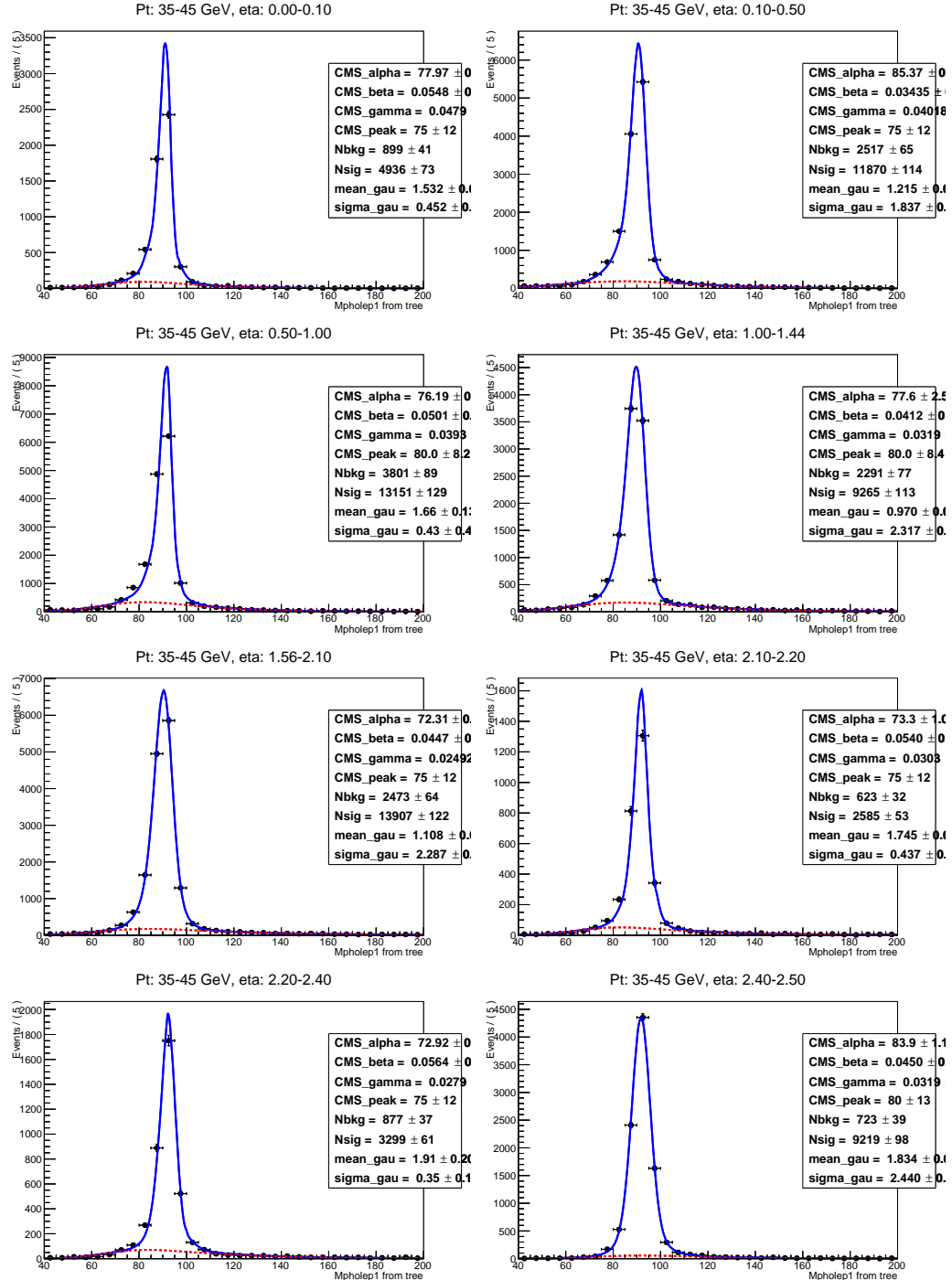


Figure .96:  $M_{e\gamma}$  fits,  $W\gamma$ , electron channel, underflow bin (35-45 GeV), 8  $\eta\gamma$  bins.

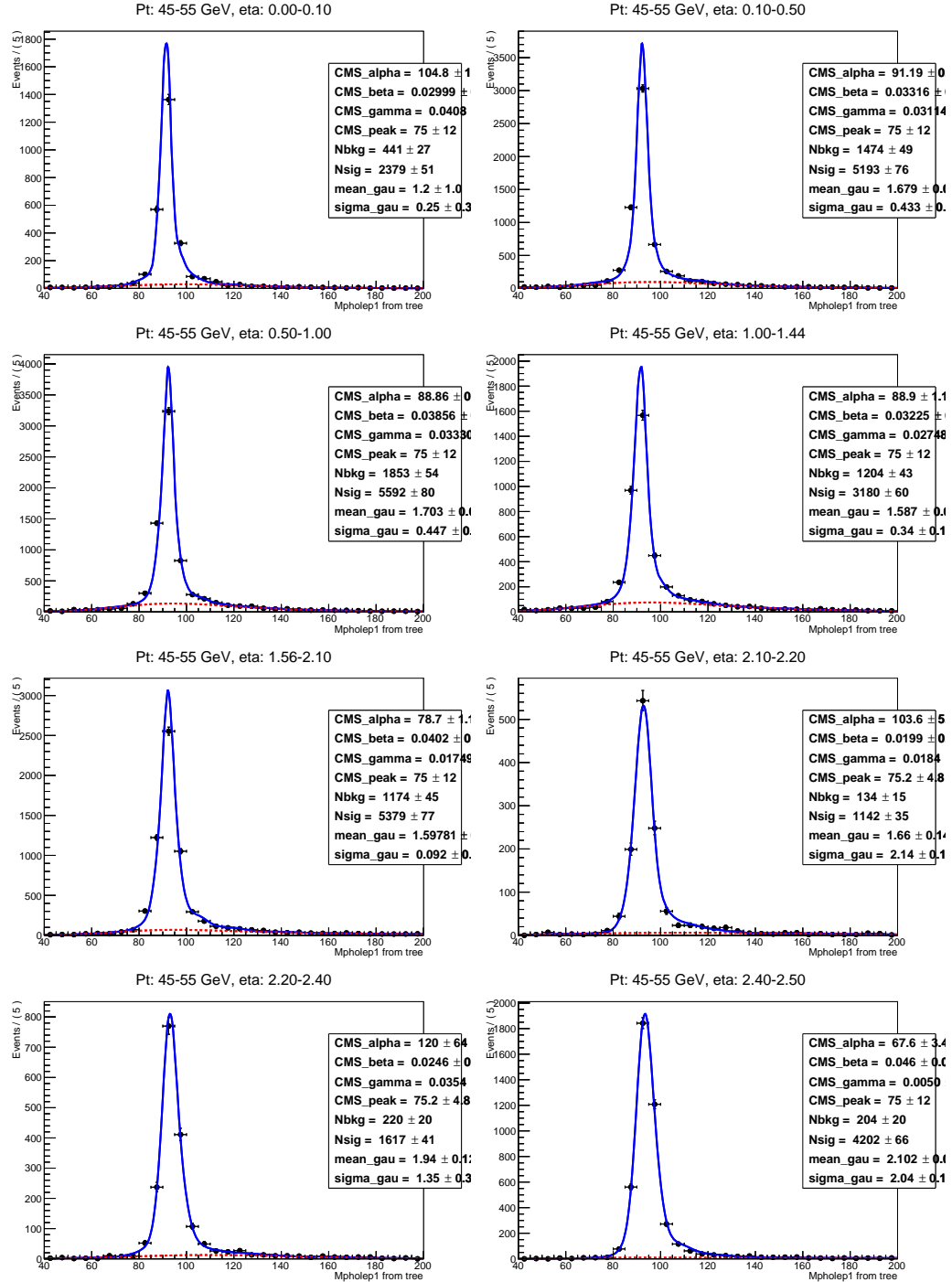


Figure .97:  $M_{e\gamma}$  fits,  $W\gamma$ , electron channel, underflow bin (45-55 GeV), 8  $\eta\gamma$  bins.

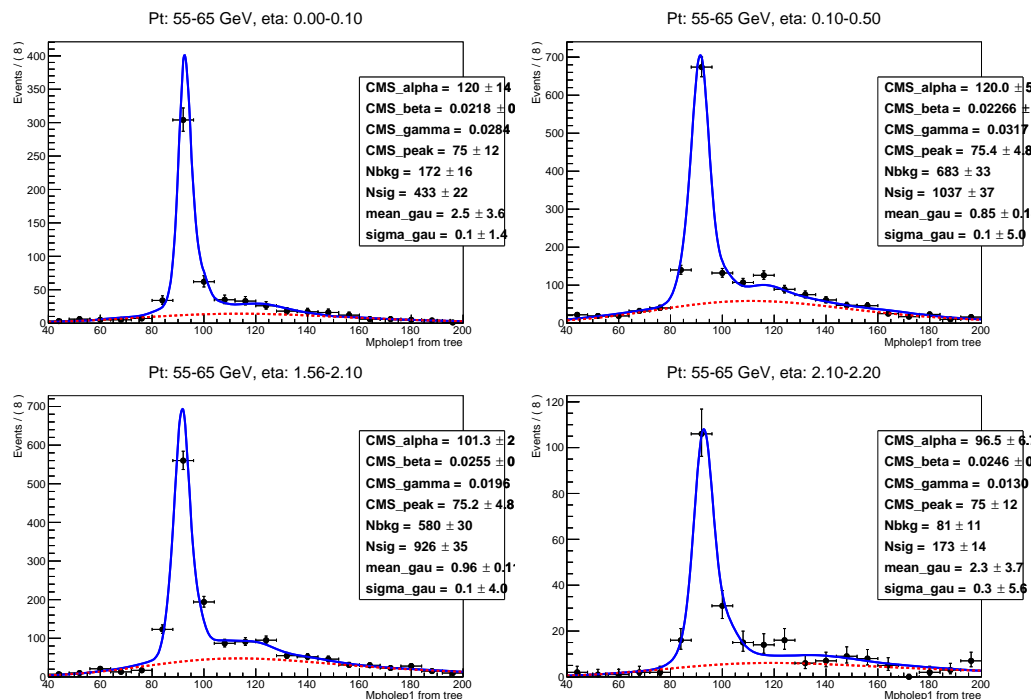


Figure .98:  $M_{e\gamma}$  fits,  $W\gamma$ , electron channel, underflow bin (55-65 GeV), 4  $\eta^\gamma$  bins.

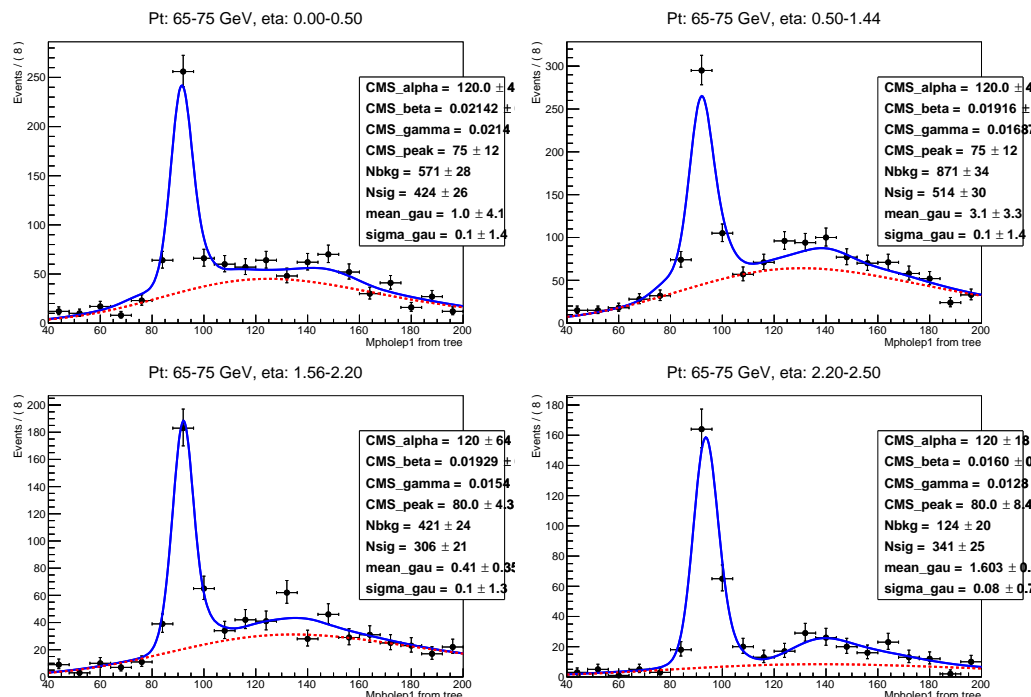


Figure .99:  $M_{e\gamma}$  fits,  $W\gamma$ , electron channel, underflow bin (65-75 GeV), 4  $\eta^\gamma$  bins.

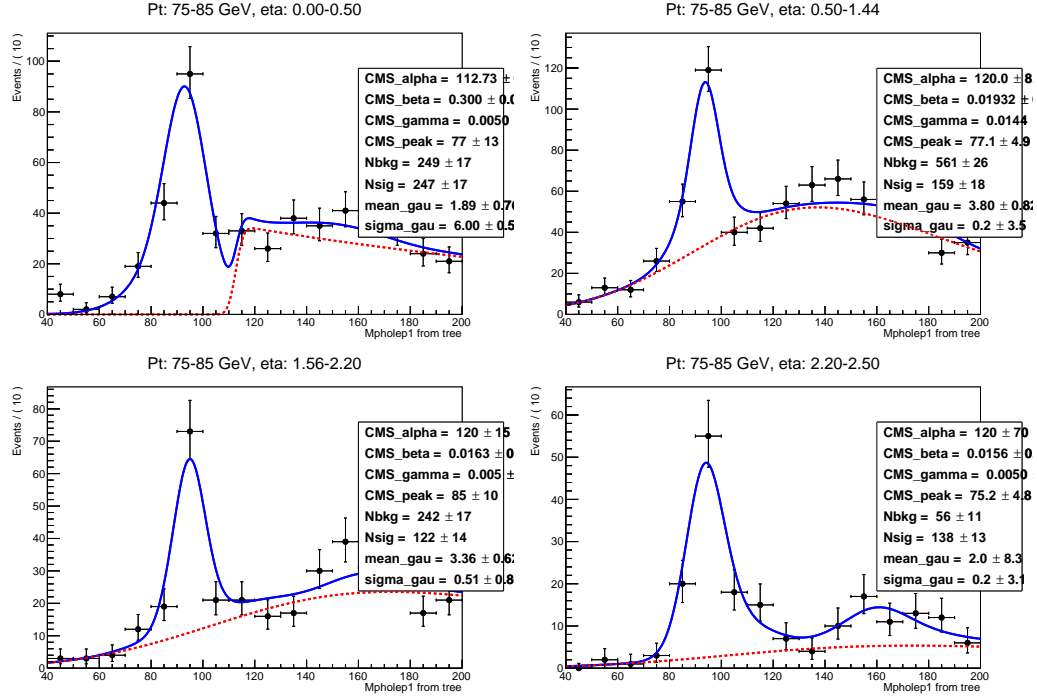


Figure .100:  $M_{e\gamma}$  fits,  $W\gamma$ , electron channel, underflow bin (75-85 GeV), 4  $\eta^\gamma$  bins.

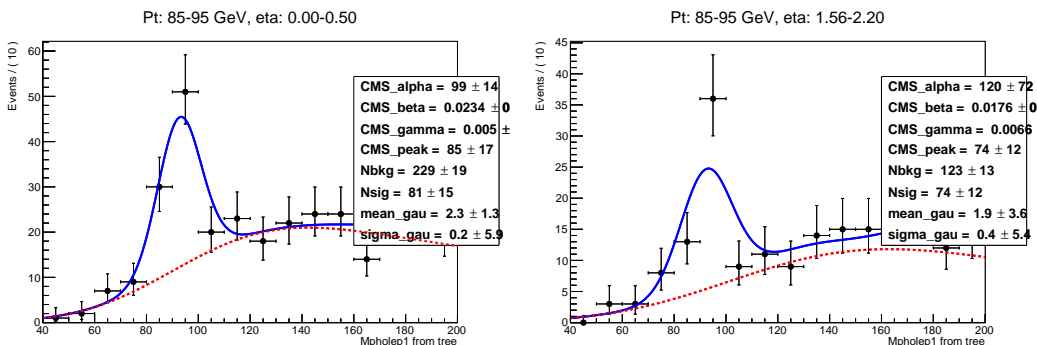


Figure .101:  $M_{e\gamma}$  fits,  $W\gamma$ , electron channel, underflow bin (85-95 GeV), 2  $\eta^\gamma$  bins.

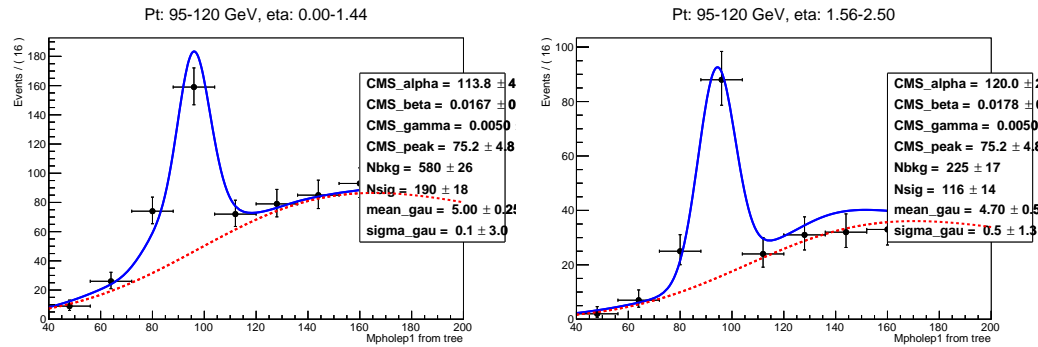


Figure .102:  $M_{e\gamma}$  fits,  $W\gamma$ , electron channel, underflow bin (95-120 GeV), 2  $\eta^\gamma$  bins.

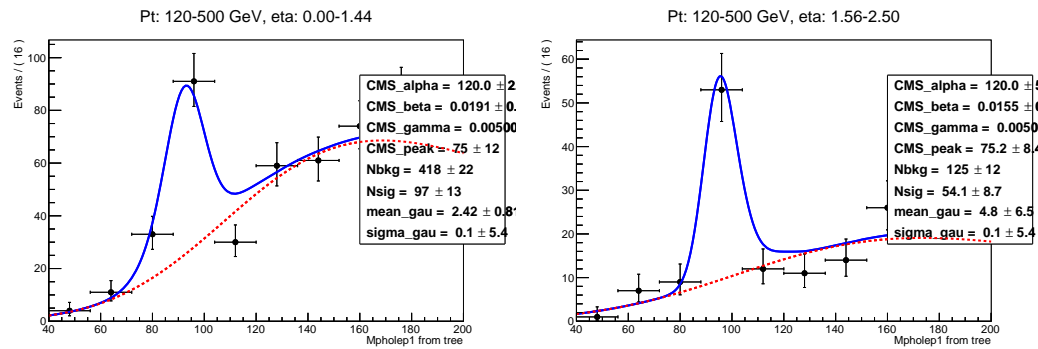


Figure .103:  $M_{e\gamma}$  fits,  $W\gamma$ , electron channel, underflow bin (120-500 GeV), 2  $\eta^\gamma$  bins.

## .9 APPENDIX: Tables for $e \rightarrow \gamma$ Background

### Estimation

This appendix presents results of  $e \rightarrow \gamma$  background estimation. Tab. .20-.21 show results of  $e \rightarrow \gamma$  background estimation when fits are performed on data with all selection criteria applied except Z-mass window cut. These results are used for the background subtraction. Tables .22-.23 show results of  $e \rightarrow \gamma$  background estimation when fits are performed on data without  $M_T^W$  cut. These results are used for the estimation of the systematic uncertainties.

In each table, the first column is a  $P_T^\gamma$  bin, the second column is yields of weighted DY+jets MC in conditions of full nominal selection, the third column is yields of  $e \rightarrow \gamma$ -enriched dataset with or without  $M_T^W$  cut. These yields are extracted from fit. The fourth column is yields of weighted DY+jets MC in conditions of  $e \rightarrow \gamma$ -enriched selection with or without  $M_T^W$  cut, consistently with the dataset. The fifth column is the scale which is computed as the yield in the third column divided over the yield in the fourth column. The sixth column is the estimated  $e \rightarrow \gamma$  background in the nominally selected dataset. The value is computed as the yield in the second column multiplied by the scale. The values in the sixth column as used for the background subtraction (Tab. .20-.21) or estimation fo the systematic uncertainty (Tab. .22-.23). The seventh column is yields of the weighted signal MC ( $W\gamma \rightarrow e\nu\gamma$ ) in the nominally selected conditions, it is quoted for comparison purposes, to estimate how significant is  $e \rightarrow \gamma$  background compared to the signal.

Table .20:  $e \rightarrow \gamma$  background. Barrel. Fits with  $M_T^W$  cut applied

bin lims	DY+jets nom. sel.	Data $e \rightarrow \gamma$ enr.	DY+jets $e \rightarrow \gamma$ enr.	scale	$e \rightarrow \gamma$ yield	SigMC ( $W\gamma \rightarrow e\nu\gamma$ )
15-20	1917±63	6395±149	3300±83	1.94±0.0667	3715±177	5857±110
20-25	1175±49	5141±235	2987±79	1.72±0.091	2023±137	2868±77
25-30	543±33	6489±122	3418±84	1.9±0.0591	1030±71	1411±54
30-35	166±18	7257±105	4215±94	1.72±0.0461	286±33	915±43
35-45	134±16	18534±144	11597±158	1.6±0.0251	215±27	1247±51
45-55	186±20	7417±97	4134±94	1.79±0.0473	335±37	820±41
55-65	130±16	1426±48	685±38	2.08±0.136	272±39	654±37
65-75	86±13	473±29	286±24	1.65±0.177	143±27	440±30
75-85	42±9	174±19	165±19	1.05±0.168	45±12	295±25
85-95	20±6	140±14	66±12	2.1±0.445	42±16	234±22
95-120	38±9	156±16	94±14	1.65±0.307	63±19	318±26
120-500	36±9	64±11	67±12	0.957±0.246	34±12	429±30

Table .21:  $e \rightarrow \gamma$  background. Endcap. Fits with  $M_T^W$  cut applied

bin lims	DY+jets nom. sel.	Data $e \rightarrow \gamma$ enr.	DY+jets $e \rightarrow \gamma$ enr.	scale	$e \rightarrow \gamma$ yield	SigMC ( $W\gamma \rightarrow e\nu\gamma$ )
15-20	458±31	2004±159	1805±61	1.11±0.096	508±55	2253±68
20-25	402±29	2613±77	2432±72	1.07±0.0451	432±36	1177±49
25-30	216±21	3719±102	3527±85	1.05±0.0388	228±23	574±34
30-35	123±16	5228±78	5374±109	0.973±0.0247	120±16	445±31
35-45	173±19	11873±114	12355±164	0.961±0.0158	166±18	638±37
45-55	223±21	5286±75	4212±94	1.25±0.0334	280±28	287±24
55-65	182±19	1010±38	813±41	1.24±0.0787	226±28	237±22
65-75	82±13	327±22	299±25	1.09±0.121	89±17	194±21
75-85	68±13	167±17	184±21	0.907±0.141	61±15	137±18
85-95	40±10	107±22	82±14	1.29±0.35	52±19	81±14
95-120	48±11	88±11	97±15	0.901±0.188	43±13	166±20
120-500	22±7	36±6	54±11	0.662±0.184	15±6	145±18

Table .22:  $e \rightarrow \gamma$  background. Barrel. Fits without  $M_T^W$  cut applied

bin lims	DY+jets nom. sel.	Data $e \rightarrow \gamma$ enr.	DY+jets $e \rightarrow \gamma$ enr.	scale	$e \rightarrow \gamma$ yield	SigMC ( $W\gamma \rightarrow e\nu\gamma$ )
15-20	1917±63	11771±321	7491±125	1.57±0.0503	3012±138	5857±110
20-25	1175±49	10162±201	6933±120	1.47±0.0387	1722±85	2868±77
25-30	543±33	12055±173	7526±125	1.6±0.0353	869±57	1411±54
30-35	166±18	15580±138	9753±144	1.6±0.0275	265±30	915±43
35-45	134±16	39220±218	27310±242	1.44±0.015	193±24	1247±51
45-55	186±20	16343±135	10411±149	1.57±0.0261	293±31	820±41
55-65	130±16	3256±65	1722±60	1.89±0.0765	247±33	654±37
65-75	86±13	938±39	600±36	1.56±0.115	135±23	440±30
75-85	42±9	405±24	274±24	1.48±0.162	63±16	295±25
85-95	20±6	156±19	125±16	1.25±0.226	25±9	234±22
95-120	38±9	189±18	155±18	1.22±0.188	46±13	318±26
120-500	36±9	96±13	89±14	1.08±0.226	38±12	429±30

Table .23:  $e \rightarrow \gamma$  background. Endcap. Fits without  $M_T^W$  cut applied

bin lims	DY+jets nom. sel.	Data $e \rightarrow \gamma$ enr.	DY+jets $e \rightarrow \gamma$ enr.	scale	$e \rightarrow \gamma$ yield	SigMC ( $W\gamma \rightarrow e\nu\gamma$ )
15-20	458±31	3798±158	4004±92	0.948±0.0452	434±35	2253±68
20-25	402±29	5631±103	5586±109	1.01±0.027	405±31	1177±49
25-30	216±21	8755±138	8528±132	1.03±0.0228	222±22	574±34
30-35	123±16	12865±120	13762±175	0.935±0.0148	115±15	445±31
35-45	173±19	29009±176	29847±254	0.972±0.0102	168±19	638±37
45-55	223±21	12339±114	10099±145	1.22±0.021	273±27	287±24
55-65	182±19	2012±50	1700±59	1.18±0.0511	215±25	237±22
65-75	82±13	646±32	606±36	1.07±0.0842	87±16	194±21
75-85	68±13	260±19	316±28	0.823±0.0957	56±12	137±18
85-95	40±10	139±15	148±19	0.944±0.16	38±11	81±14
95-120	48±11	115±13	185±21	0.626±0.104	30±8	166±20
120-500	22±7	54±8	85±14	0.632±0.149	14±5	145±18

## .10 APPENDIX: Electron-photon invariant mass.

### Data vs MC plots

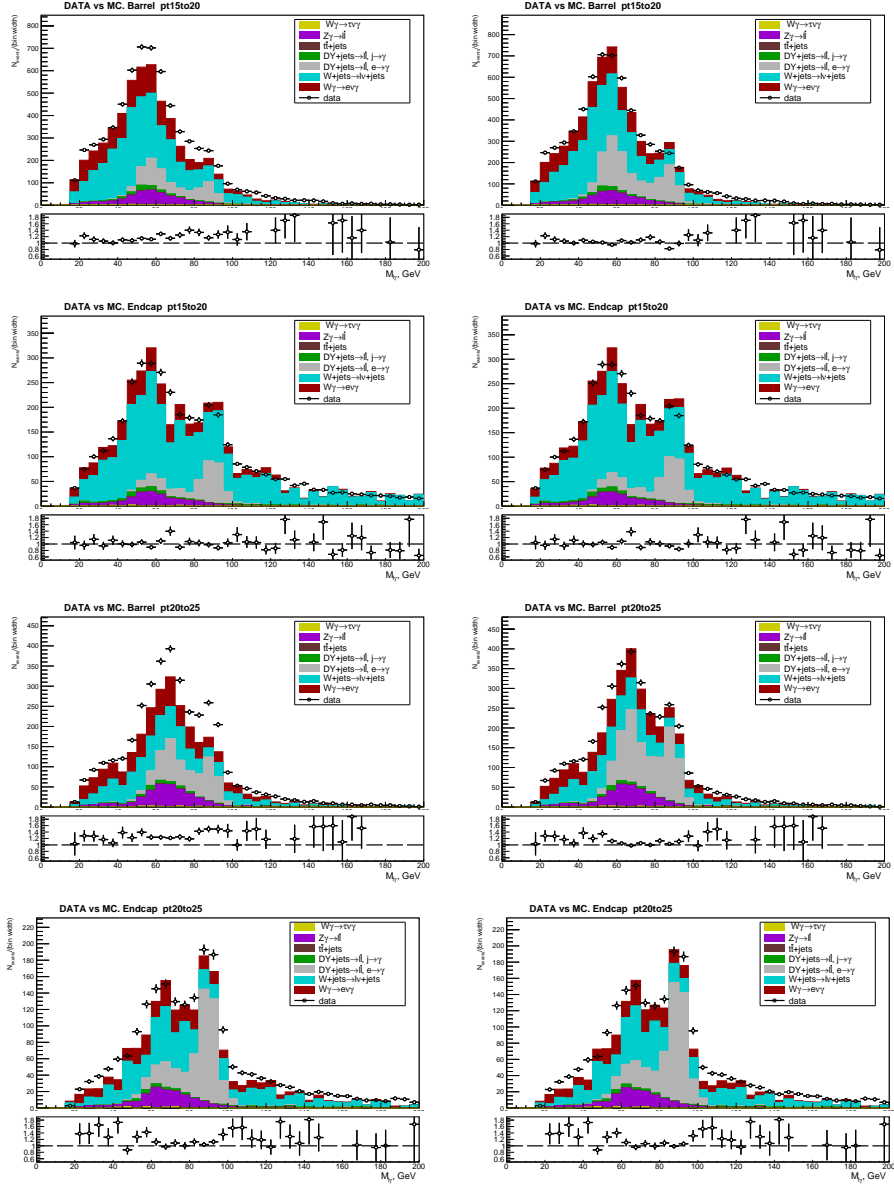


Figure .104:  $M_{e\gamma}$  distribution, data vs MC. Bins 15 – 20 – 25 GeV. Left: all MC samples are normalized to luminosity of data, PU weight and SFs, right:  $DY+jets(e \rightarrow \gamma)$  also normalized to  $e \rightarrow \gamma$  background estimates.

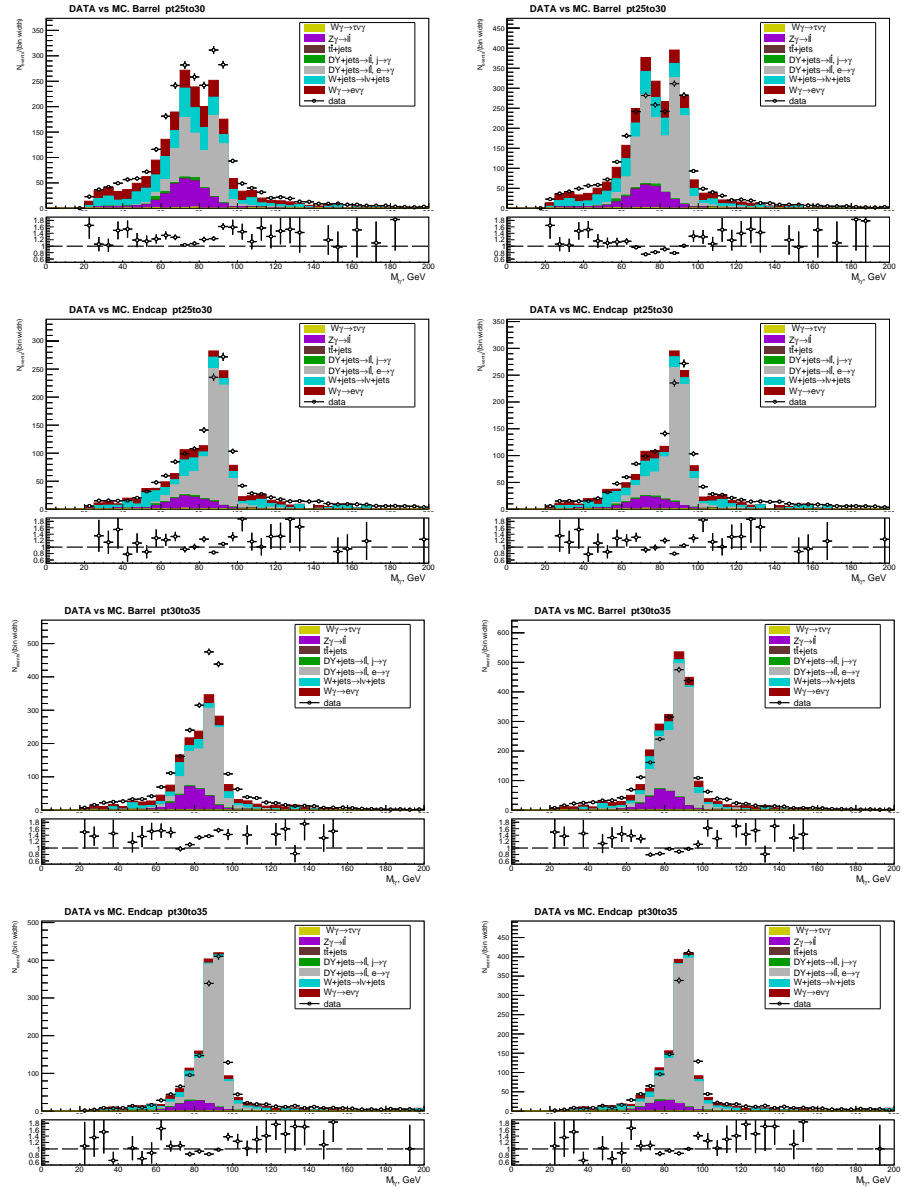


Figure .105:  $M_{e\gamma}$  distribution, data vs MC. Bins  $25 - 30 - 35$  GeV. Left: all MC samples are normalized to luminosity of data, PU weight and SFs, right:  $DY+jets(e \rightarrow \gamma)$  also normalized to  $e \rightarrow \gamma$  background estimates.

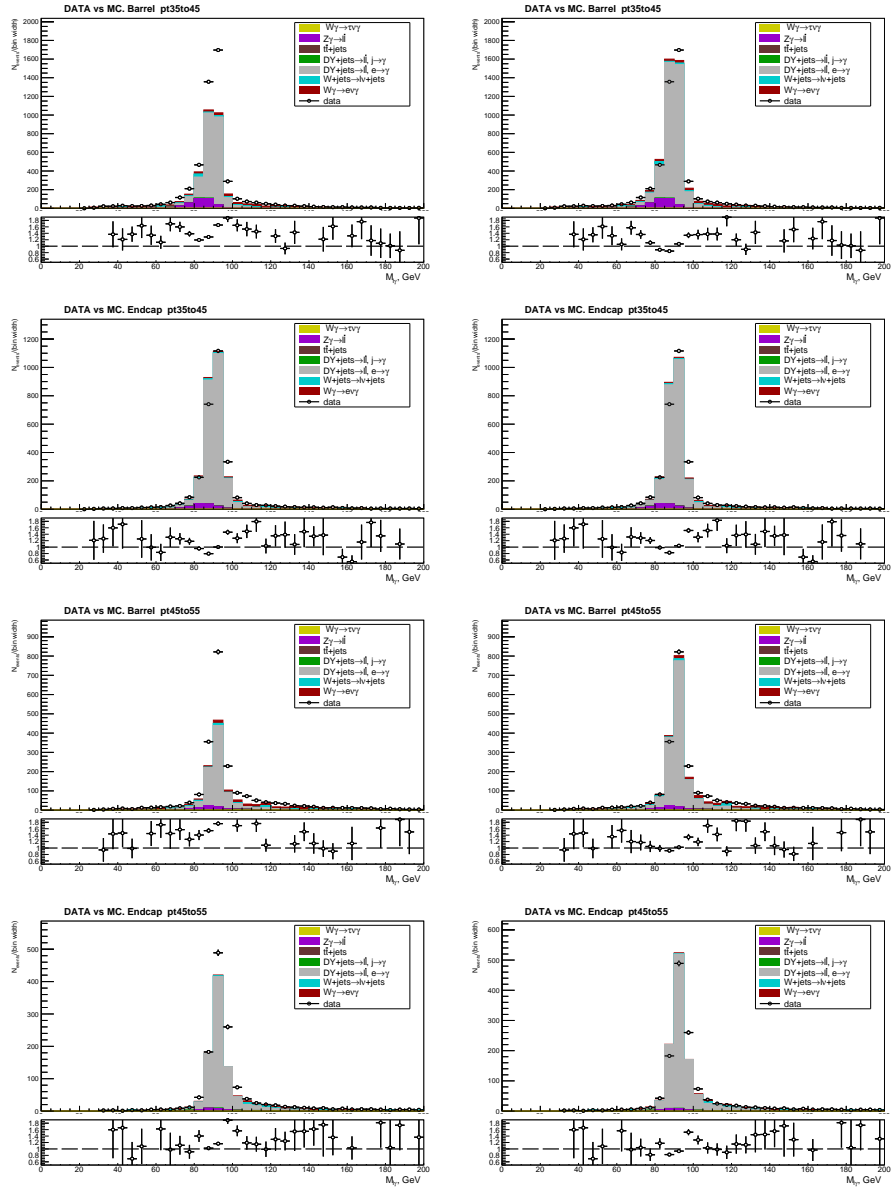


Figure .106:  $M_{e\gamma}$  distribution, data vs MC. Bins  $35 - 45 - 55$  GeV. Left: all MC samples are normalized to luminosity of data, PU weight and SFs, right:  $DY+jets(e \rightarrow \gamma)$  also normalized to  $e \rightarrow \gamma$  background estimates.

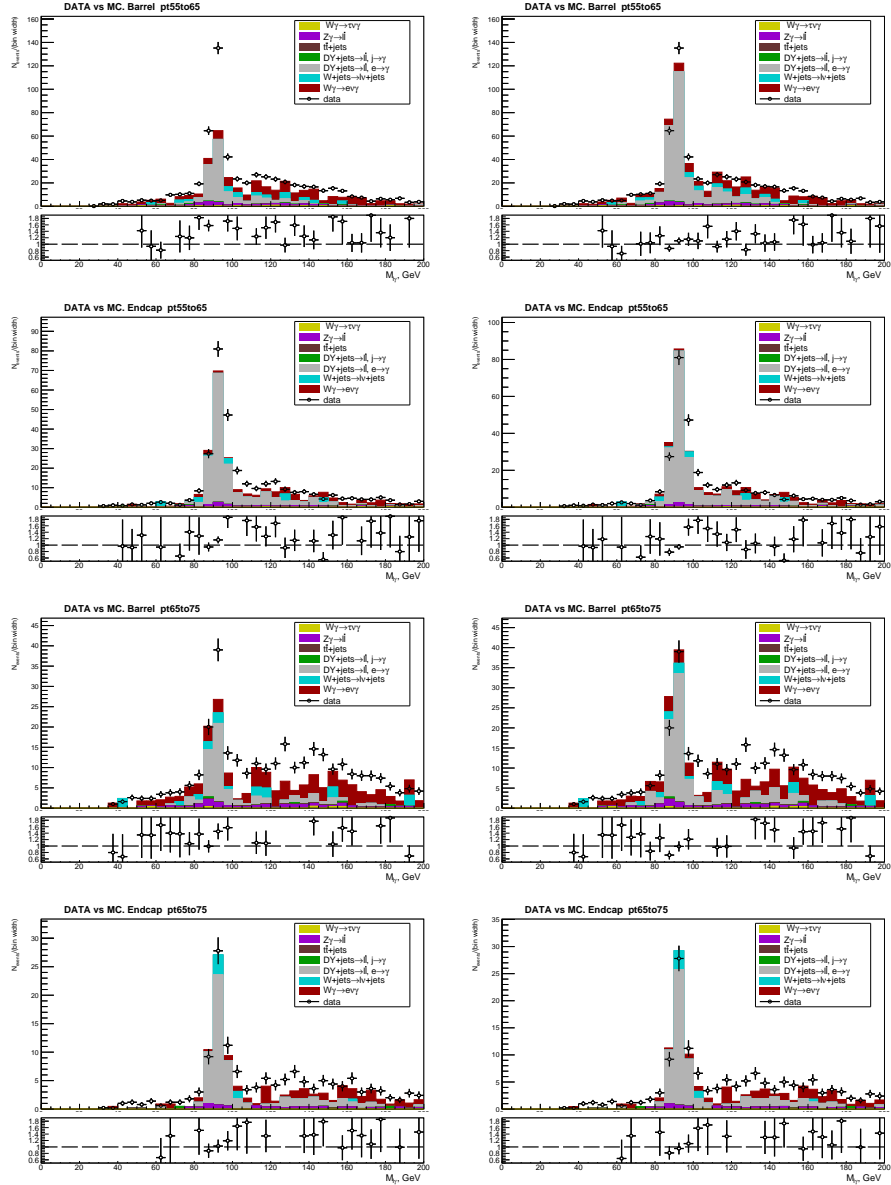


Figure .107:  $M_{e\gamma}$  distribution, data vs MC. Bins 55 – 65 – 75 GeV. Left: all MC samples are normalized to luminosity of data, PU weight and SFs, right: DY+jets( $e \rightarrow \gamma$ ) also normalized to  $e \rightarrow \gamma$  background estimates.

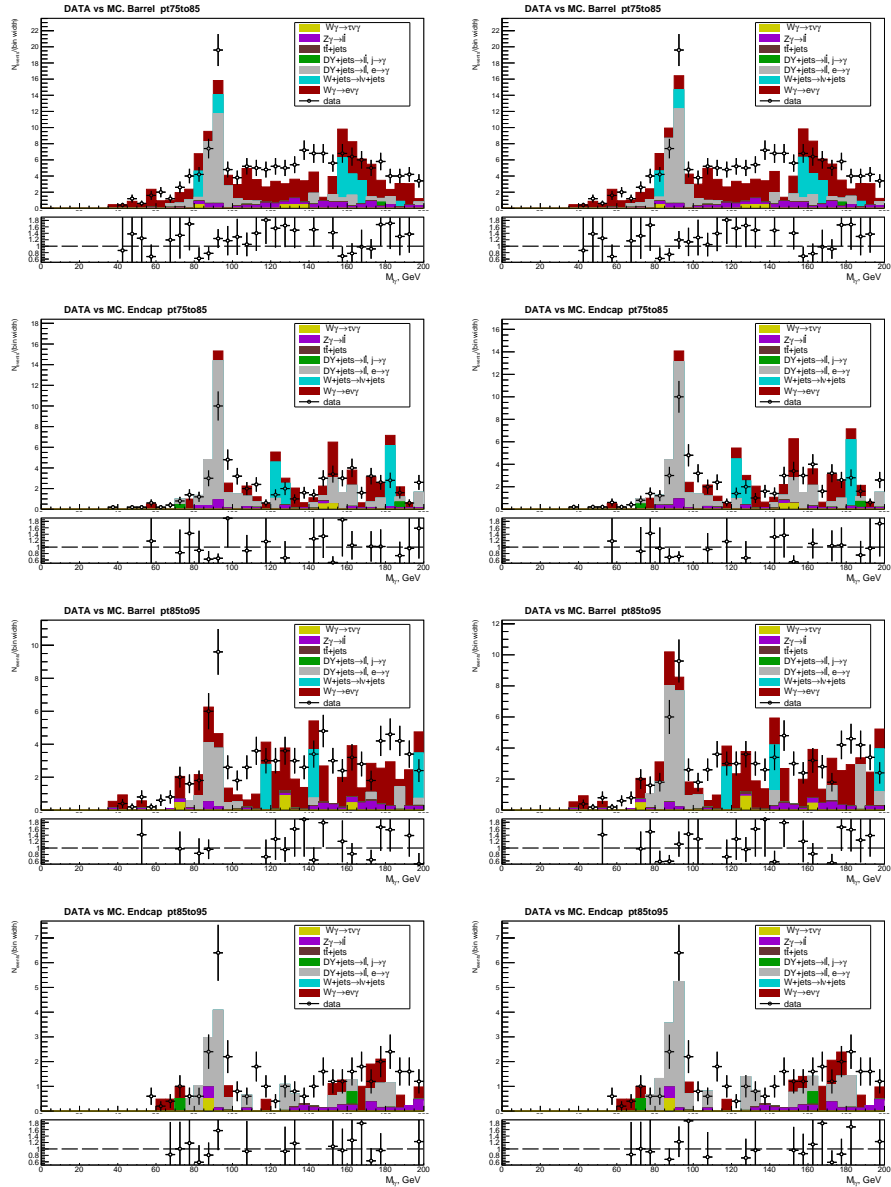


Figure .108:  $M_{e\gamma}$  distribution, data vs MC. Bins 75 – 85 – 95 GeV. Left: all MC samples are normalized to luminosity of data, PU weight and SFs, right: DY+jets( $e \rightarrow \gamma$ ) also normalized to  $e \rightarrow \gamma$  background estimates.

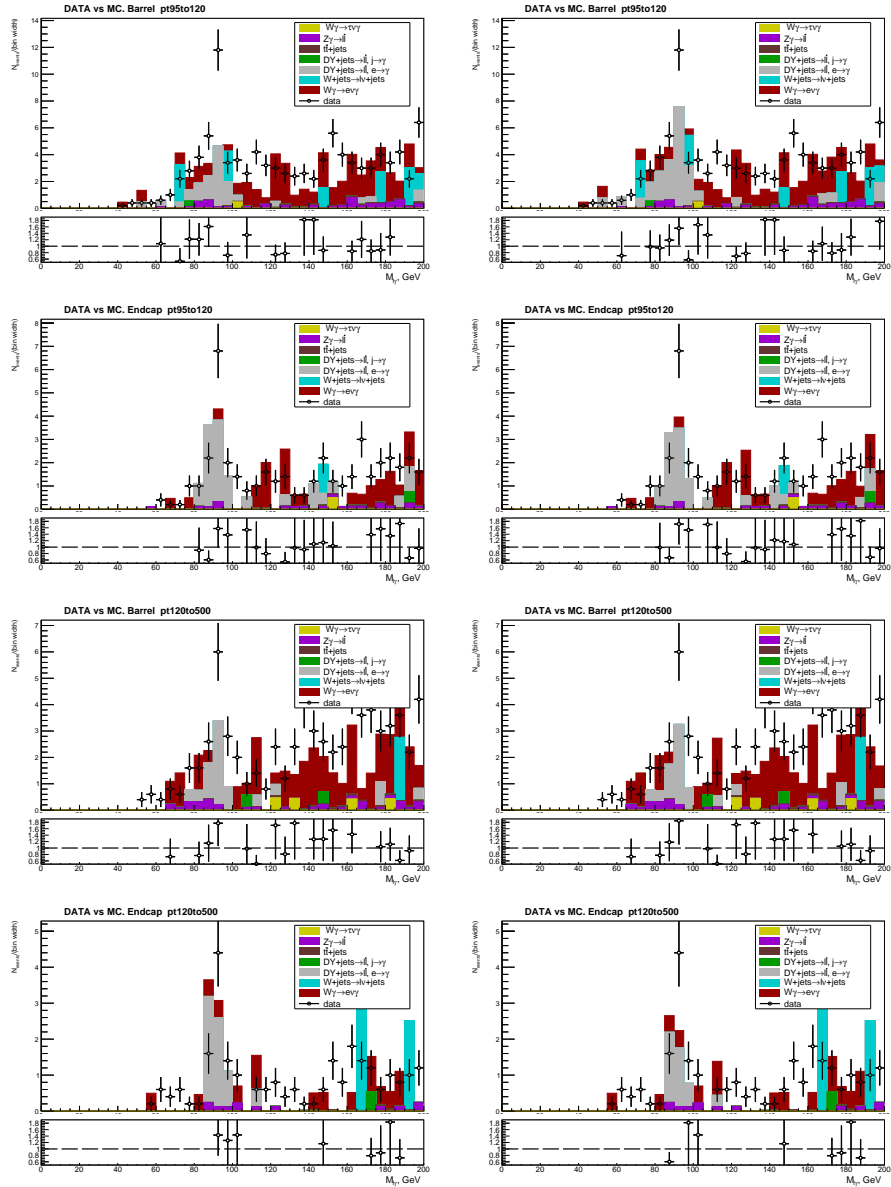


Figure .109:  $M_{e\gamma}$  distribution, data vs MC. Bins 95 – 120 – 500 GeV. Left: all MC samples are normalized to luminosity of data, PU weight and SFs, right: DY+jets( $e \rightarrow \gamma$ ) also normalized to  $e \rightarrow \gamma$  background estimates.

## .11 APPENDIX: Correlation Matrices for Different Sources of the Systematic Uncertainties

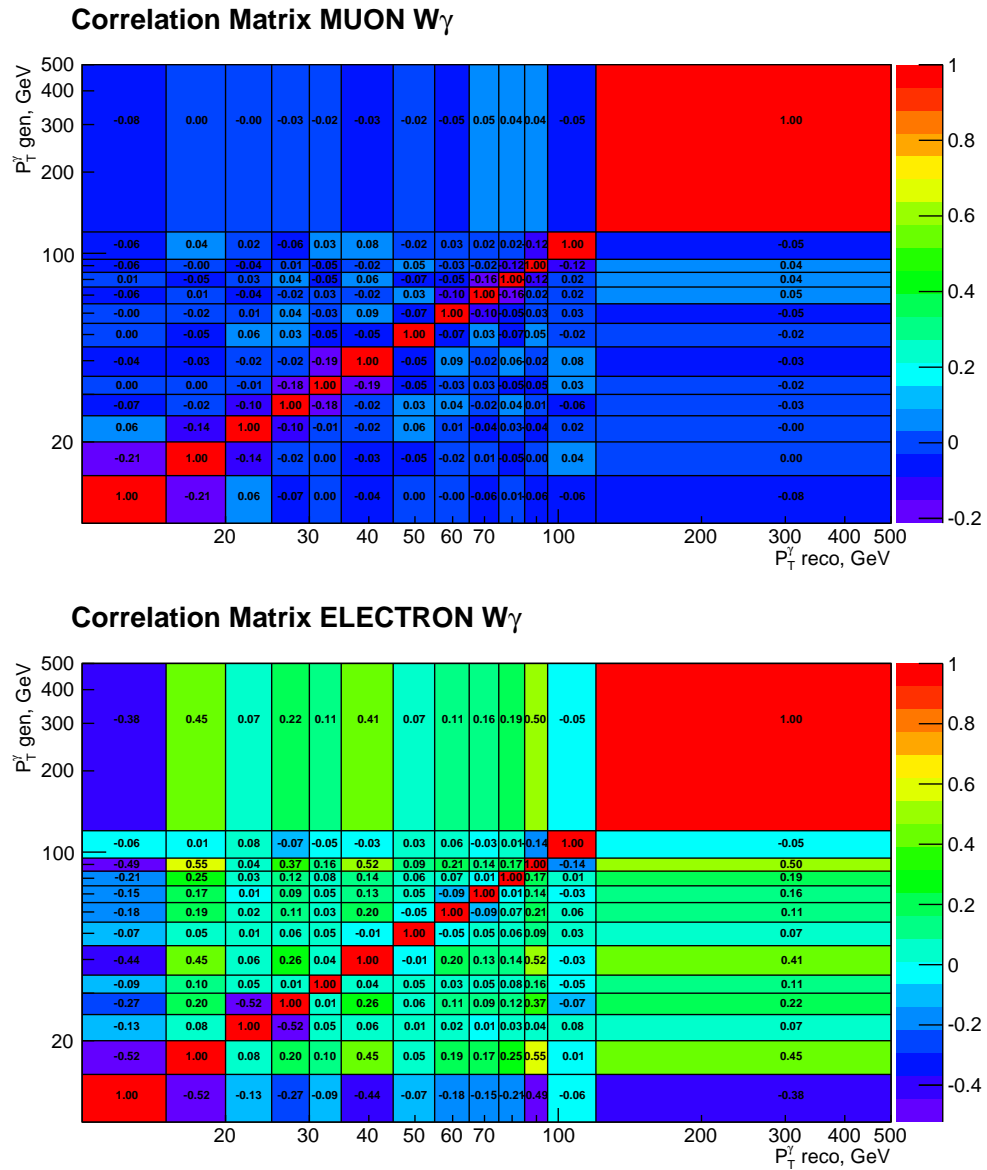


Figure .110: Correlation Matrices for systematic error due to the difference between  $I_{ch}^\gamma$  and  $\sigma_{inj}^\gamma$  fit results.

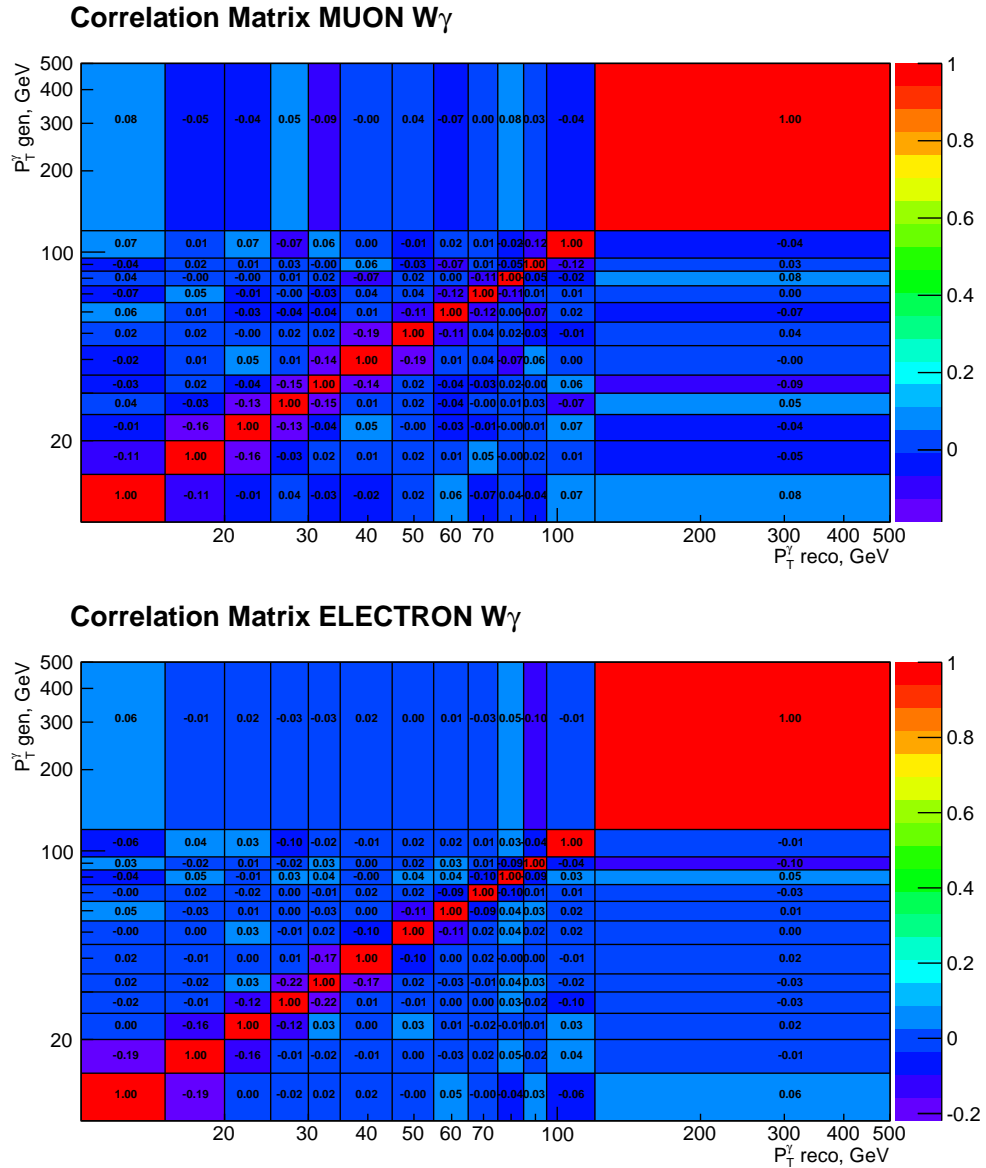


Figure .111: Correlation Matrices for systematic error due to real- $\gamma$  background subtraction.

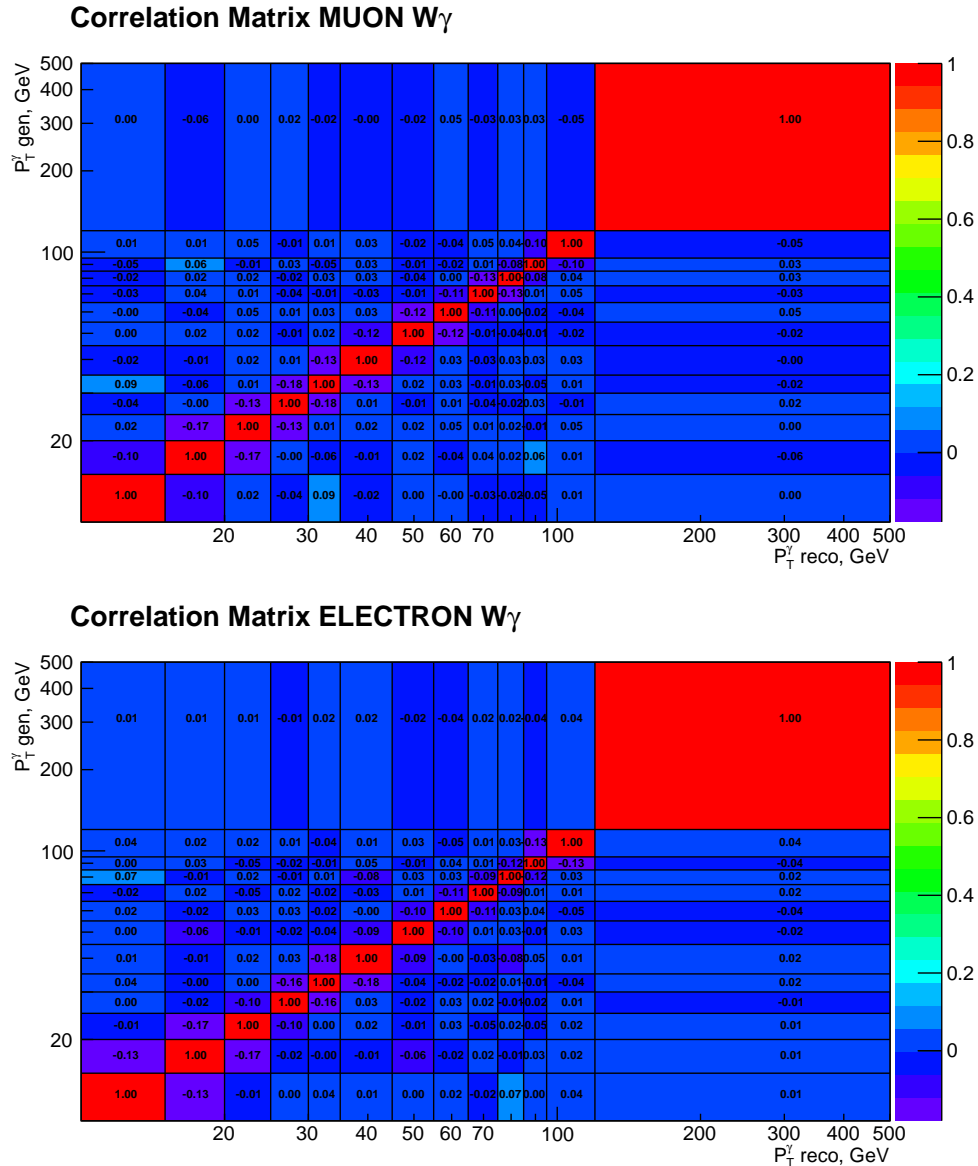


Figure .112: Correlation Matrices for systematic error due to uncertainty on the  $Z\gamma$  MC sample normalization.

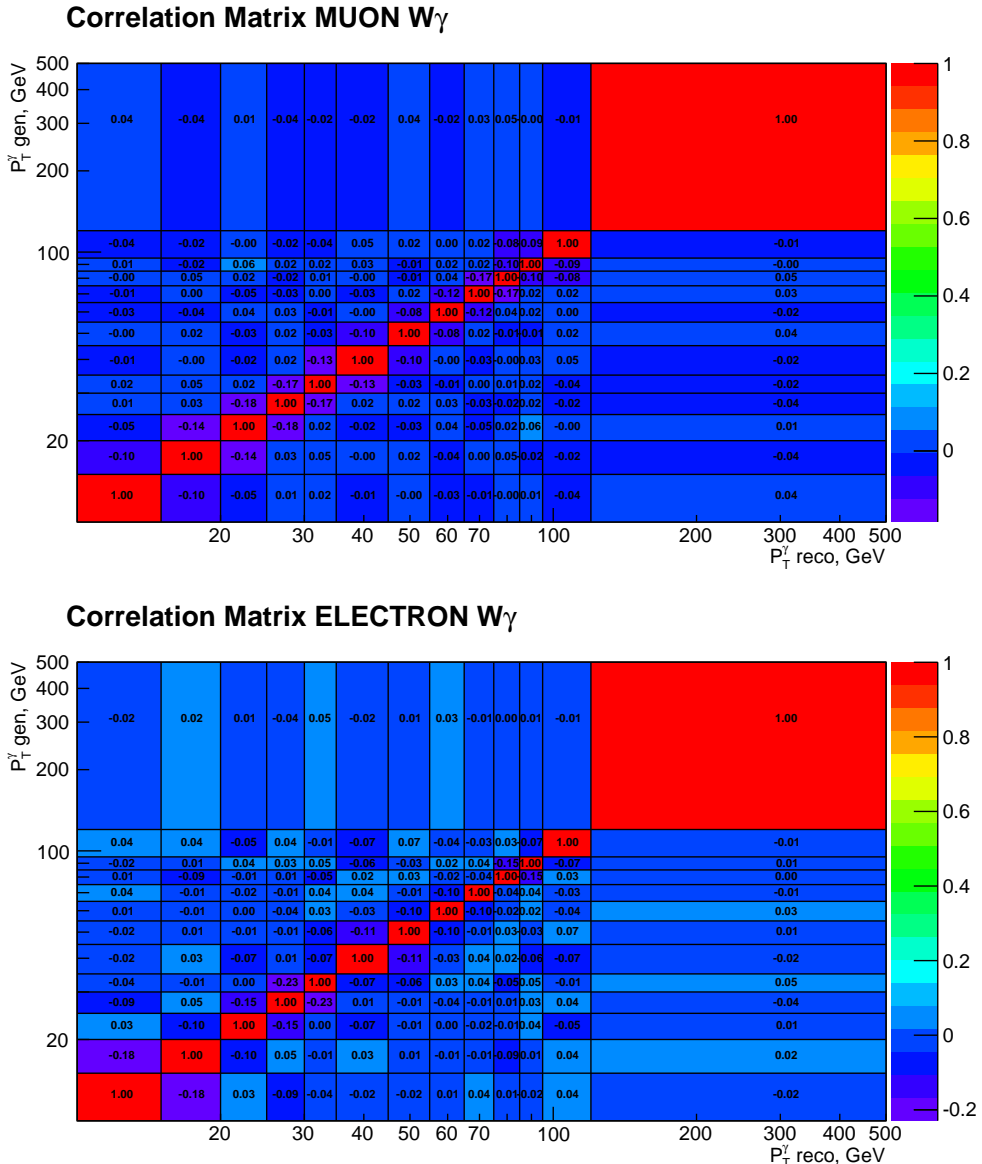


Figure .113: Correlation Matrices for systematic error due to signal MC statistics for unfolding.

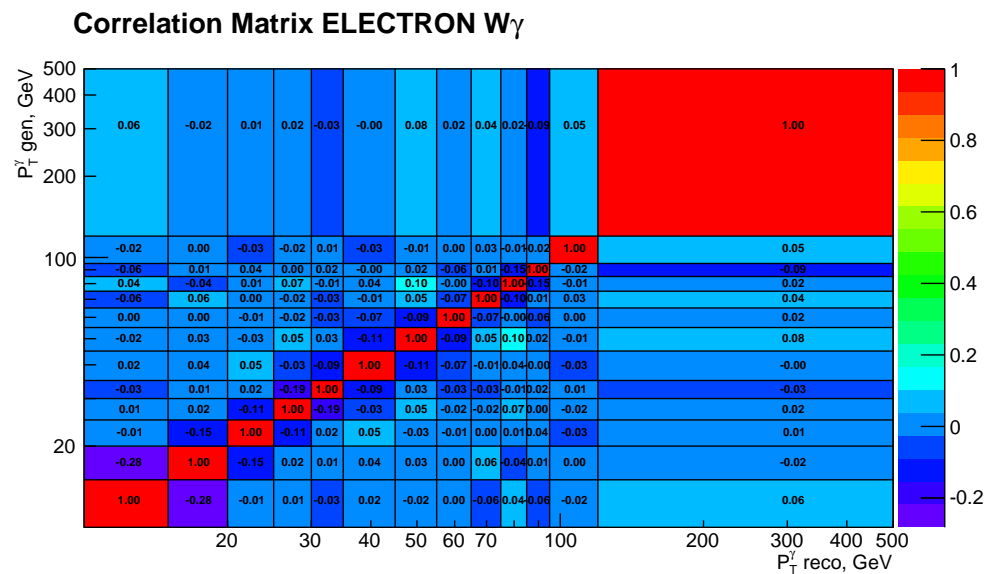


Figure .114: Correlation Matrix for systematic error due to statistics of different samples for  $e \rightarrow \gamma$  background estimation.

## .12 APPENDIX: Code and Software

The CMS software (CMSSW) [9] is the tool developed to process all CMS responses, reconstruct particles and prepare data in a condition convenient for the final physics measurements. CMSSW is mostly written on C++ and python programming languages. It has hundreds of contributors that use GITHUB [26] to share their work. All CMS physics measurements use CMSSW.

The procedure of the tracker alignment and validation described in Ch. 4 is also a part of the CMSSW although the Millepede-II algorithm itself is implemented in the external software tool.

The samples for the physics measurements are stored in a format of ROOT trees. The ROOT tree contains multiple parameters for each entry and allows easy access to all parameters. These properties makes it convenient to use ROOT trees for particle physics measurements where, usually, one entry corresponds to one event. The ROOT trees provided by reconstruction algorithms of CMSSW are referred as “tuples”. Tuples are further processed by different large physics subgroups that prepare “ntuples”. Ntuples store only information that is necessary for a specific class of measurements and arrange it in a more convenient way for this specific class of measurements.

The author of this dissertation used ntuples prepared by Central Taiwan University and Kansas State University groups mostly for various diboson and triboson measurements. The code of the program that prepares the ntuples is available at [25].

The code for the CMS  $W\gamma$  measurement at  $\sqrt{s} = 8$  TeV was written by the author of this dissertation using C++ language, ROOT and RooFit [53] packages, *RooUnfold* [55] class for the detector resolution unfolding, and *RooCMSShapePdf* [52]

for  $e \rightarrow \gamma$  background estimation. Auxiliary shell scripts are used to run the chain of C++ programs corresponding to separate physics measurement steps. The code is available at [26].

Several cross check were performed with other collaborators to make sure the code is free of major errors. Especially the event selection and background estimation for the electron channel is fully implemented by both Kansas State University group and the author of this dissertation in separate frameworks. These procedures are carefully cross checked between two developers.

## .13 APPENDIX: ZGamma Check

For the  $Z\gamma$  check, the same procedures we use for the  $W\gamma$  measurement, we also use for the  $Z\gamma$  measurement except those that are not applicable. Figure .115 shows the data vs MC distribution of  $Z\gamma$ -selected samples. The selected sample mostly consists of  $Z\gamma$  signal event and DY+jets background. DY+jets background is a source of jets $\rightarrow \gamma$  background and is estimated the same way as it is done for our nominal  $W\gamma$  measurement.

The templates are derived from  $Z\gamma \rightarrow \mu\mu\gamma$  sample, therefore, the  $Z\gamma$  check in the muon channel is not a valid physics measurement but a closure check because the templates for the jets $\rightarrow \gamma$  background estimation procedure are largely overlap with the fitted data. At the same time, the  $Z\gamma$  check in the electron channel is a valid physics measurement. Fit results on data and pseudodata (MC mixtures) show good agreement for both channels (Fig. .116-.119). The fit plots themselves are available in App. .14-.15.

Major systematic uncertainties are estimated the same way as it is done for  $W\gamma$  measurement and are listed in Tab. .24-.25. Measured cross section values compared to the MC-based cross section are listed in the Tab. .26-.27. Fig. .120 shows an agreement between muon and electron channels, agreement with the MC-based cross section and with the approved  $Z\gamma$  measurement with CMS at  $\sqrt{s} = 8$  TeV [17].

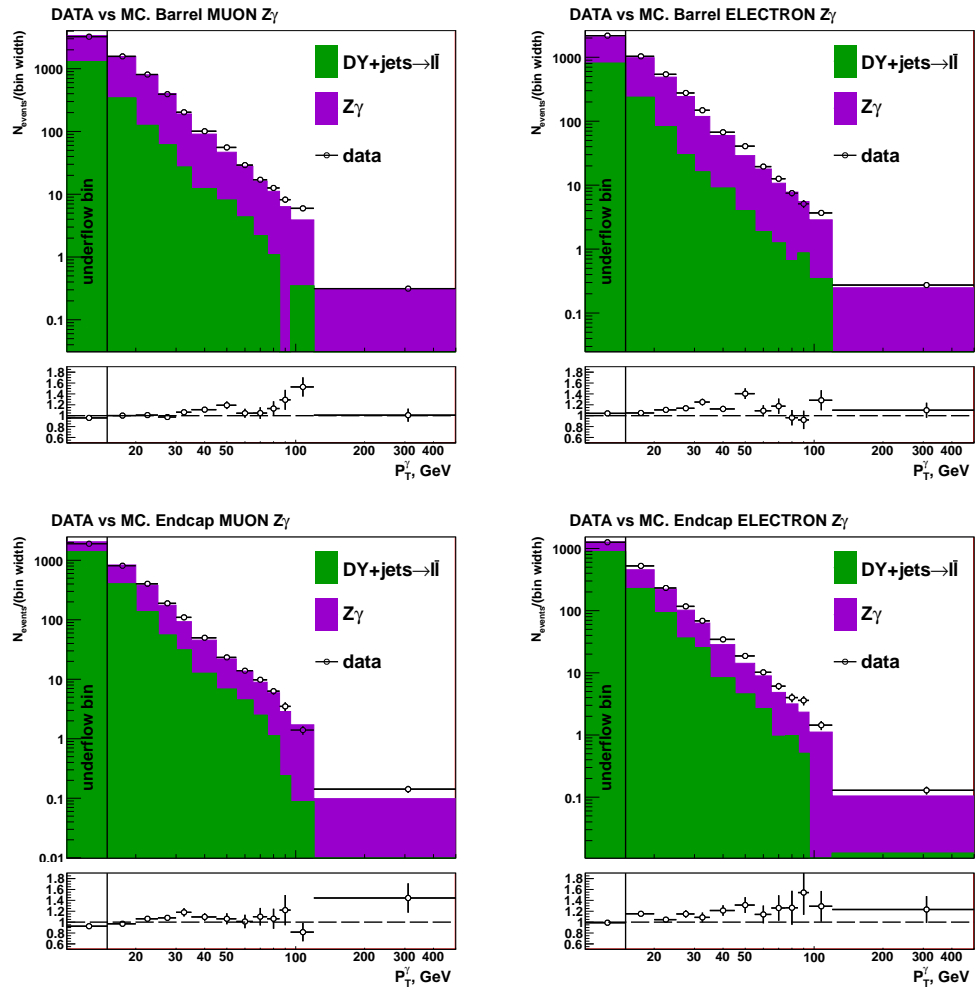


Figure .115: Data vs MC plots. Left column - muon channel, right column - electron channel. Top to bottom: barrel and endcap photons

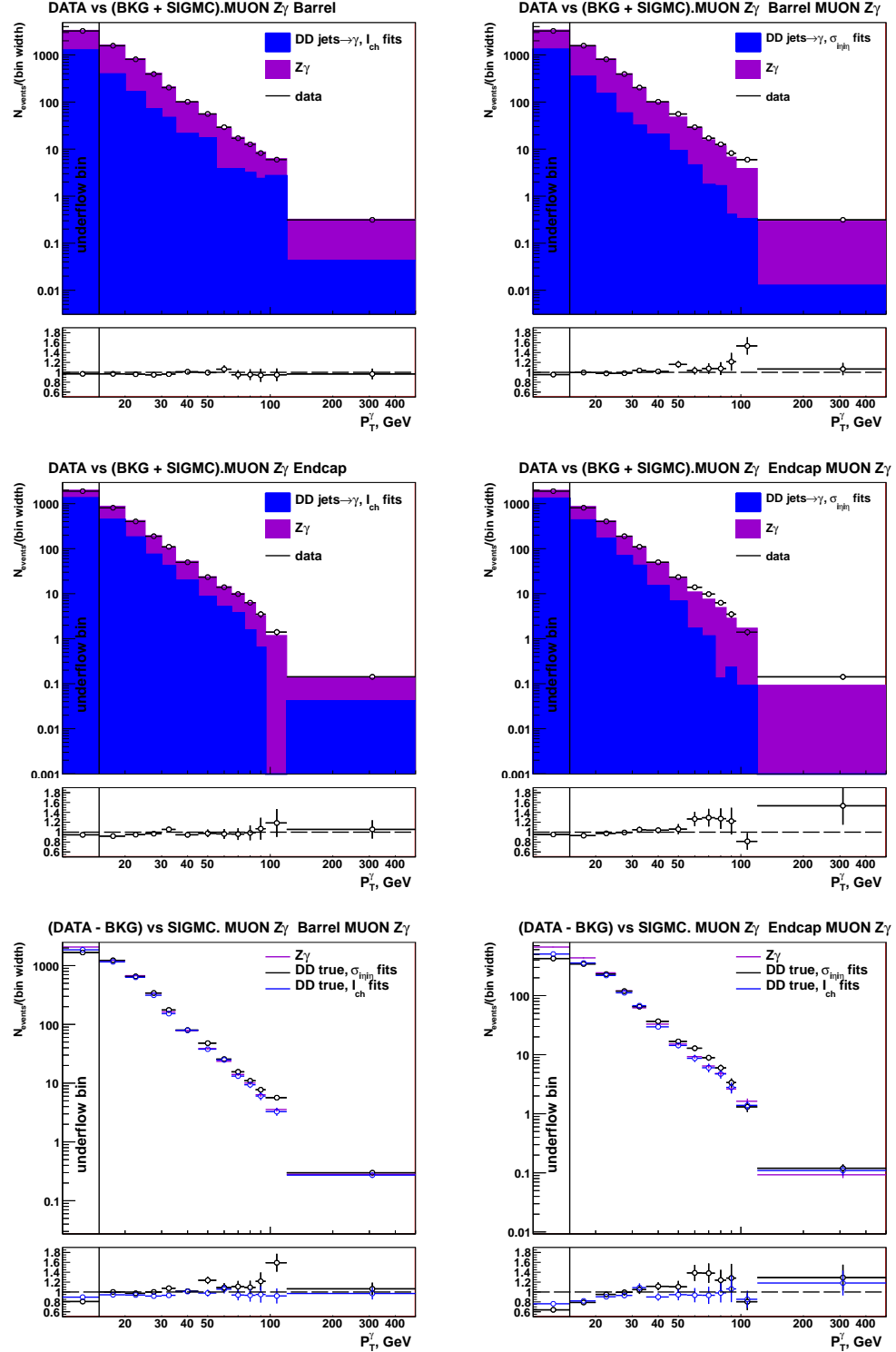


Figure .116:  $Z\gamma$  check. Muon channel. Top and middle: data vs fake- $\gamma$  background derived from the template method + real- $\gamma$  background predicted by dedicated MC samples + signal MC, with  $I_{ch}$  and  $\sigma_{inj}$  used as fit variables. Bottom: data yields after full background subtraction vs signal MC.  $I_{ch}$  vs  $\sigma_{inj}$  fit results.

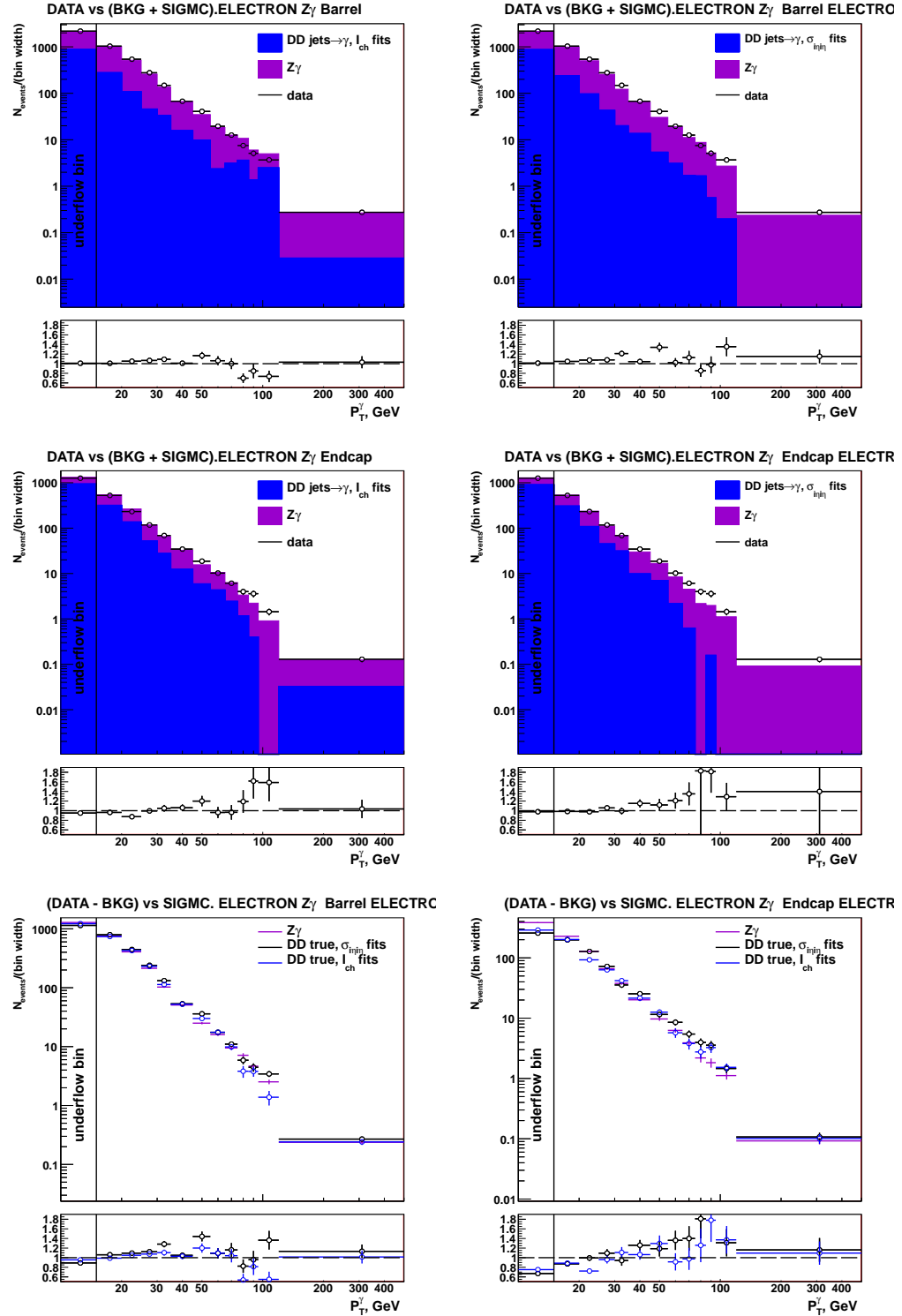


Figure .117:  $Z\gamma$  check. Electron channel. Top and middle: data vs fake- $\gamma$  background derived from the template method + real- $\gamma$  background predicted by dedicated MC samples + signal MC, with  $I_{ch}$  and  $\sigma_{inj}$  used as fit variables. Bottom: data yields after full background subtraction vs signal MC.  $I_{ch}$  vs  $\sigma_{inj}$  fit results.

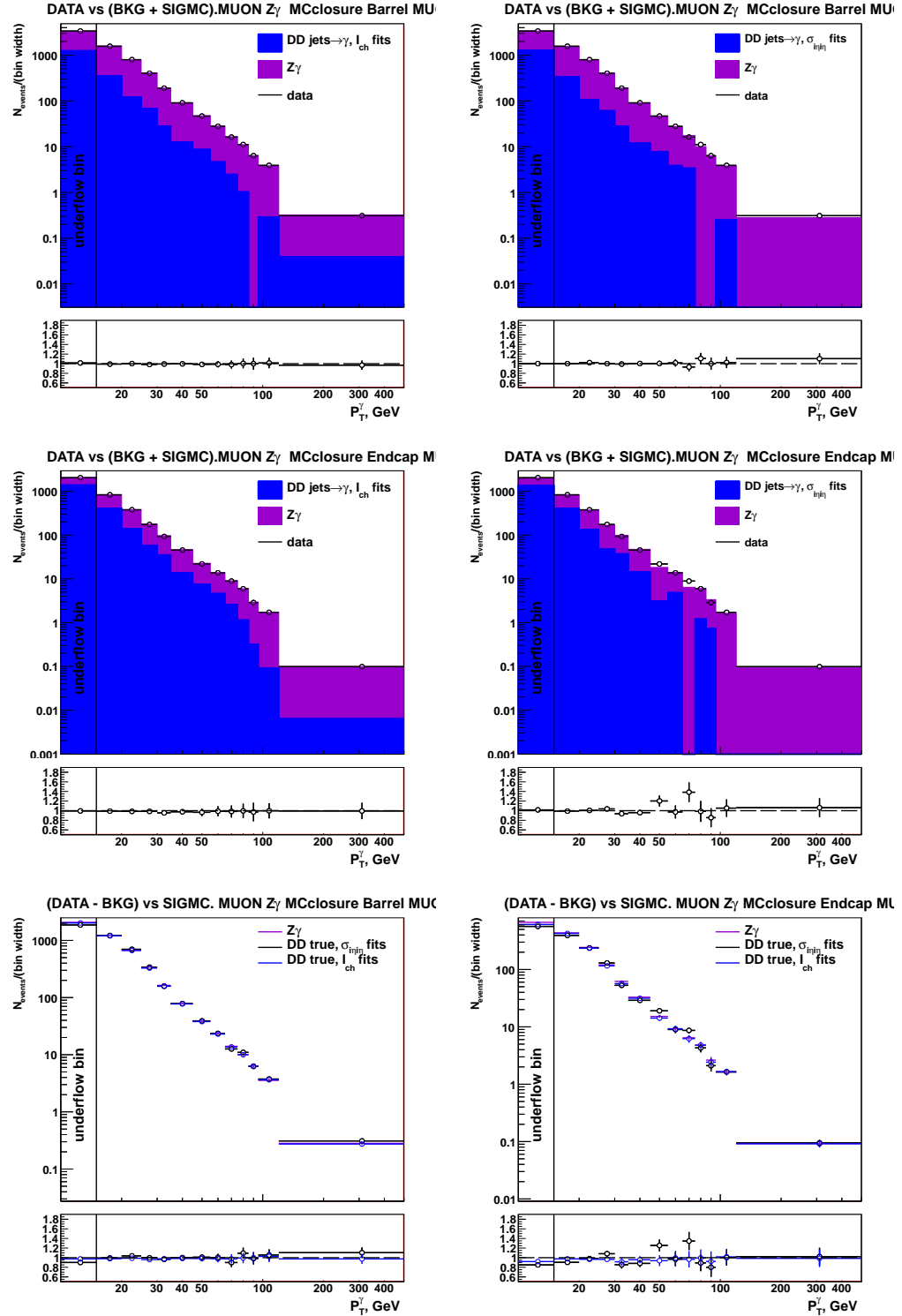


Figure .118:  $Z\gamma$  MC closure check. Muon channel. Top and middle: pseudodata vs fake- $\gamma$  background derived from the template method + real- $\gamma$  background predicted by dedicated MC samples + signal MC, with  $I_{ch}$  and  $\sigma_{ij\eta}$  used as fit variables. Bottom: pseudodata yields after full background subtraction vs signal MC.  $I_{ch}$  vs  $\sigma_{ij\eta}$  fit results.

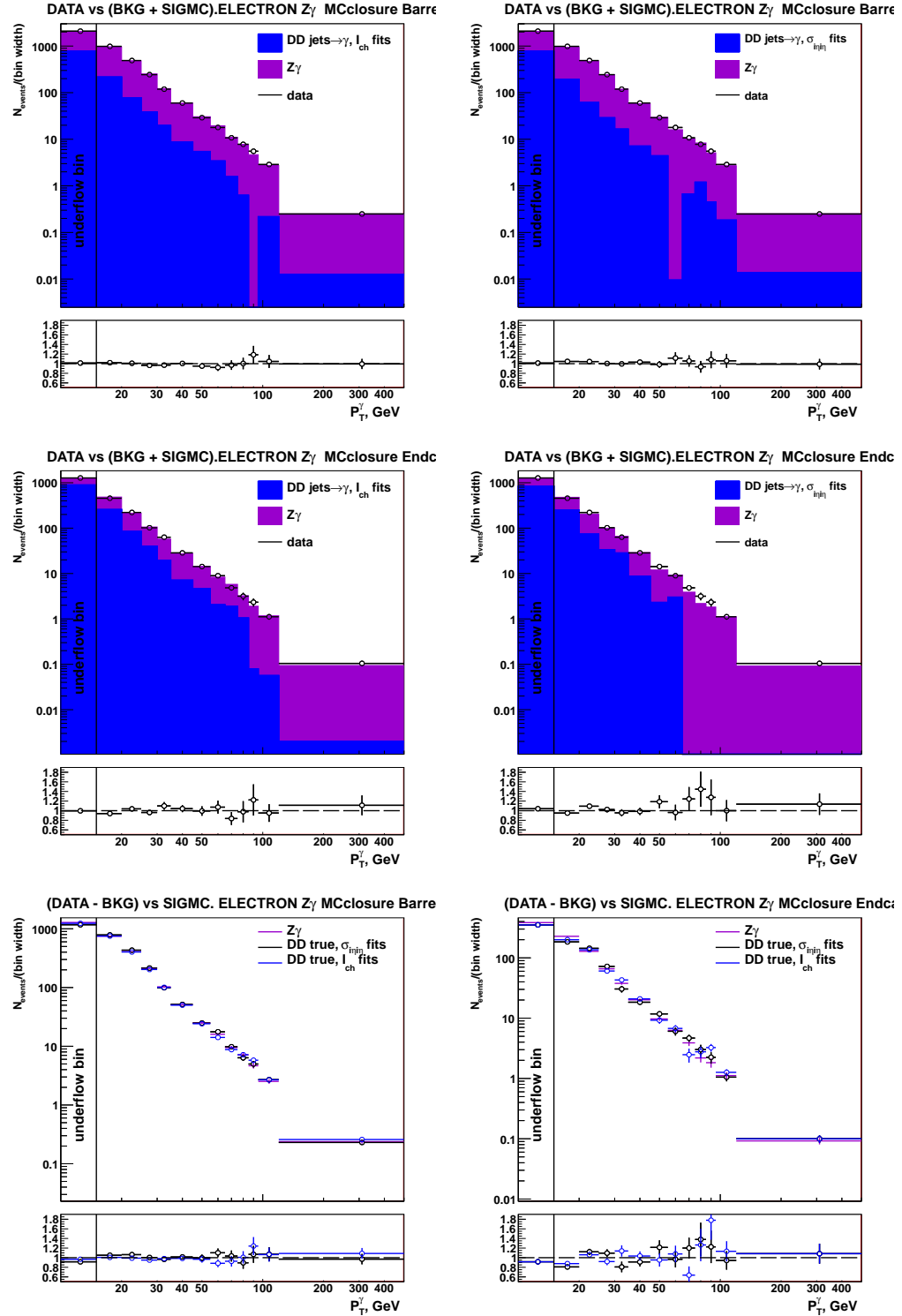


Figure .119:  $Z\gamma$  MC closure check. Electron channel. Top and middle: pseudodata vs fake- $\gamma$  background derived from the template method + real- $\gamma$  background predicted by dedicated MC samples + signal MC, with  $I_{ch}$  and  $\sigma_{ij}$  used as fit variables. Bottom: pseudodata yields after full background subtraction vs signal MC.  $I_{ch}$  vs  $\sigma_{ij}$  fit results.

Table .24: Relative errors [%]. MUON  $Z\gamma$ 

bin lims	err stat	syst $ N_{Ich} - N_{sigi\eta} $	$Z\gamma$ MC norm	$A \times \epsilon$ MC stat	syst lumi	unf MC stat	syst total	syst + stat total
total	1	1	1	0	3	1	3	3
15-20	2	2	2	1	3	2	4	5
20-25	2	2	3	1	3	2	5	5
25-30	3	3	4	2	3	3	7	8
30-35	4	6	5	3	3	5	10	10
35-45	4	3	6	3	3	4	9	9
45-55	6	8	8	4	3	6	14	15
55-65	7	5	7	5	3	7	13	14
65-75	9	7	8	6	3	9	16	18
75-85	10	8	6	7	3	10	16	19
85-95	12	8	8	9	3	12	19	23
95-120	11	10	6	8	3	11	18	21
120-500	8	5	9	7	3	9	16	18

Table .25: Relative errors [%]. ELECTRON  $Z\gamma$ 

bin lims	err stat	syst $ N_{Ich} - N_{sigi\eta} $	$Z\gamma$ MC norm	$A \times \epsilon$ MC stat	syst lumi	unf MC stat	syst total	syst + stat total
total	1	1	1	0	3	1	3	4
15-20	2	3	3	1	3	2	5	6
20-25	3	2	3	1	3	3	5	6
25-30	4	3	4	2	3	4	7	8
30-35	5	4	5	3	3	6	10	11
35-45	5	4	6	3	3	5	10	11
45-55	6	6	6	4	3	7	11	13
55-65	9	7	8	5	3	9	15	17
65-75	10	8	8	7	3	11	18	20
75-85	14	11	12	9	3	16	25	28
85-95	15	9	6	10	3	17	23	28
95-120	10	5	6	9	3	11	16	19
120-500	9	3	7	8	3	10	15	17

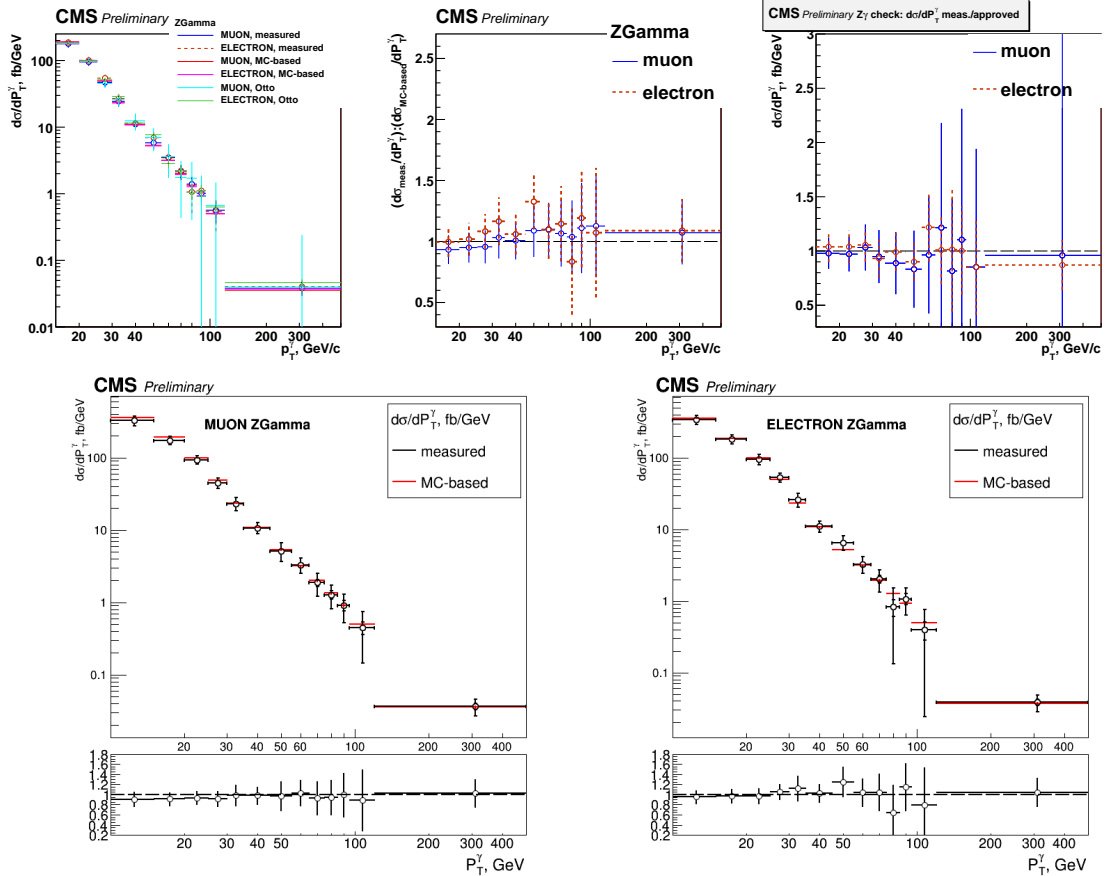


Figure .120:  $Z\gamma$  differential cross section. Top, left to right: the  $Z\gamma$  differential cross section; the ratio of measured over the MC-based  $Z\gamma$  differential cross section; the ratio of the measured over published  $Z\gamma$  differential cross section. Bottom: the  $Z\gamma$  measured differential cross section overlaid with the MC-based one and the ratio plots, the muon channel (left) and the electron channel (right).

Table .26: Cross section and errors. MUON  $Z\gamma$ 

bin lims	$d\sigma/dP_T$ MC based	$d\sigma/dP_T$ meas.
total	2085	$1985 \pm 18 \pm 62$
15-20	191	$178 \pm 3 \pm 8$
20-25	100	$98 \pm 2 \pm 5$
25-30	49	$43 \pm 1 \pm 3$
30-35	24	$23 \pm 1 \pm 2$
35-45	11	$11 \pm 0 \pm 1$
45-55	5.3	$5.2 \pm 0.3 \pm 0.7$
55-65	3.2	$3.4 \pm 0.2 \pm 0.4$
65-75	2.0	$2.1 \pm 0.2 \pm 0.3$
75-85	1.3	$1.5 \pm 0.1 \pm 0.2$
85-95	0.9	$1.1 \pm 0.1 \pm 0.2$
95-120	0.50	$0.56 \pm 0.06 \pm 0.10$
120-500	0.036	$0.040 \pm 0.003 \pm 0.006$

Table .27: Cross section and errors. ELECTRON  $Z\gamma$ 

bin lims	$d\sigma/dP_T$ MC based	$d\sigma/dP_T$ meas.
total	2061	$2091 \pm 24 \pm 70$
15-20	188	$180 \pm 4 \pm 9$
20-25	99	$101 \pm 3 \pm 6$
25-30	50	$51 \pm 2 \pm 4$
30-35	23	$25 \pm 1 \pm 2$
35-45	11	$12 \pm 1 \pm 1$
45-55	5.2	$6.5 \pm 0.4 \pm 0.7$
55-65	3.2	$3.3 \pm 0.3 \pm 0.5$
65-75	1.9	$2.3 \pm 0.2 \pm 0.4$
75-85	1.3	$1.2 \pm 0.2 \pm 0.3$
85-95	0.9	$1.1 \pm 0.2 \pm 0.3$
95-120	0.50	$0.66 \pm 0.07 \pm 0.11$
120-500	0.037	$0.042 \pm 0.004 \pm 0.006$

## .14 APPENDIX: Template Fit Plots, $Z\gamma$ , Data

This appendix contains fit results of jets $\rightarrow\gamma$  background estimation for the  $Z\gamma$  check (App. .13). The templates are derived from  $Z\gamma\rightarrow\mu\mu\gamma$  sample, therefore, the  $Z\gamma$  check in the muon channel is a closure check but the  $Z\gamma$  check in the electron channel is a valid physics measurement.

On each of the plots, the black histogram is data, green is a real- $\gamma$  template, blue is a fake- $\gamma$  template, and red is the fit function. The fits are part of the procedure of jets $\rightarrow\gamma$  background estimation.

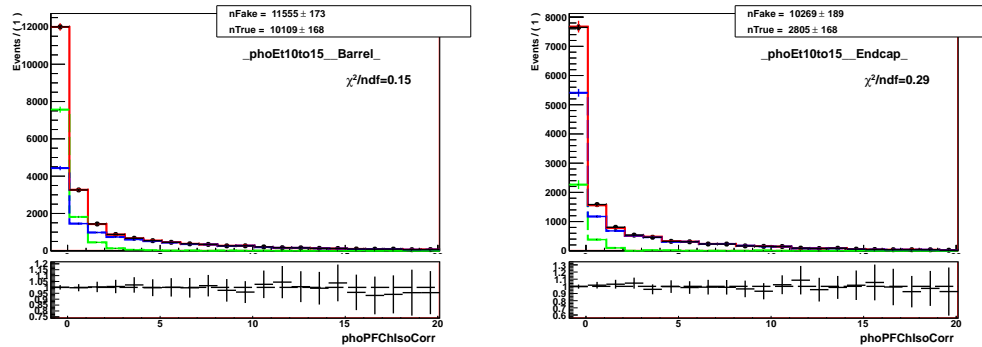


Figure .121: Fits of  $I_{ch}^{\gamma}$  templates,  $Z\gamma$ , muon channel, underflow bin.

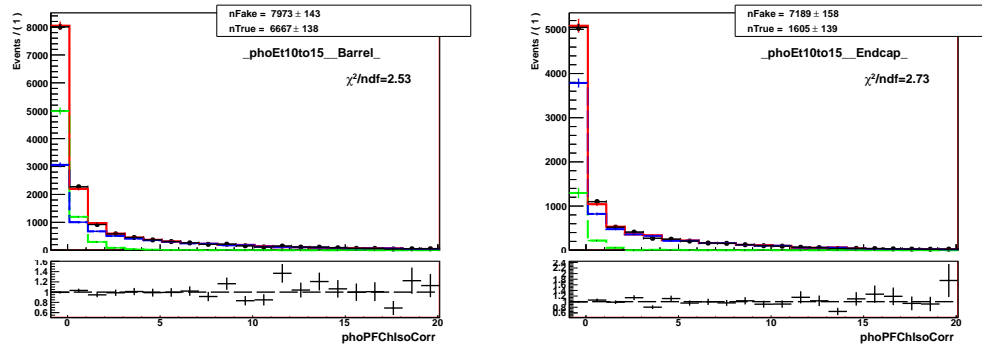


Figure .122: Fits of  $I_{ch}^{\gamma}$  templates,  $Z\gamma$ , electron channel, underflow bin.

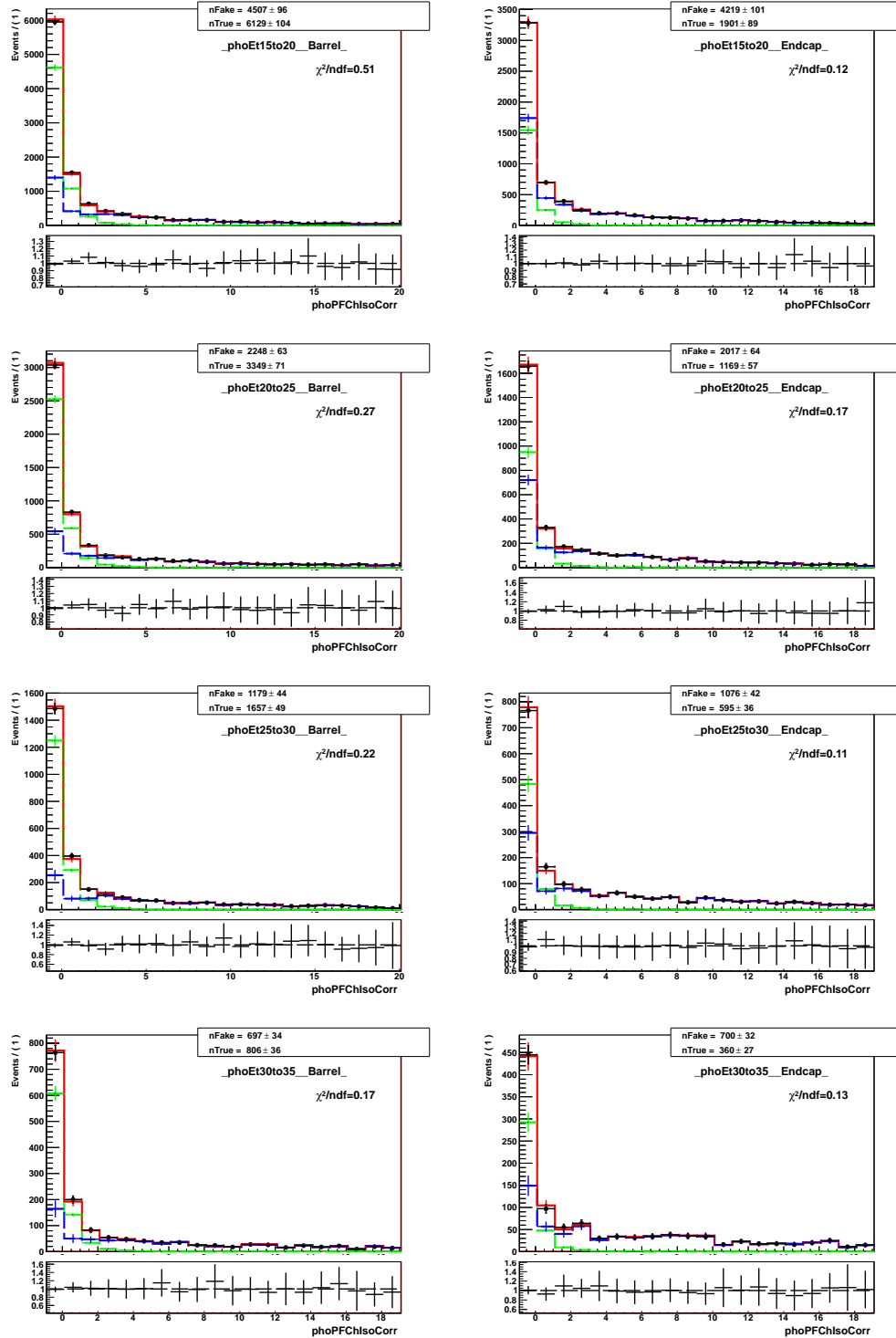


Figure .123: Fits of  $I_{ch}^{\gamma}$  templates,  $Z\gamma$ , muon channel.

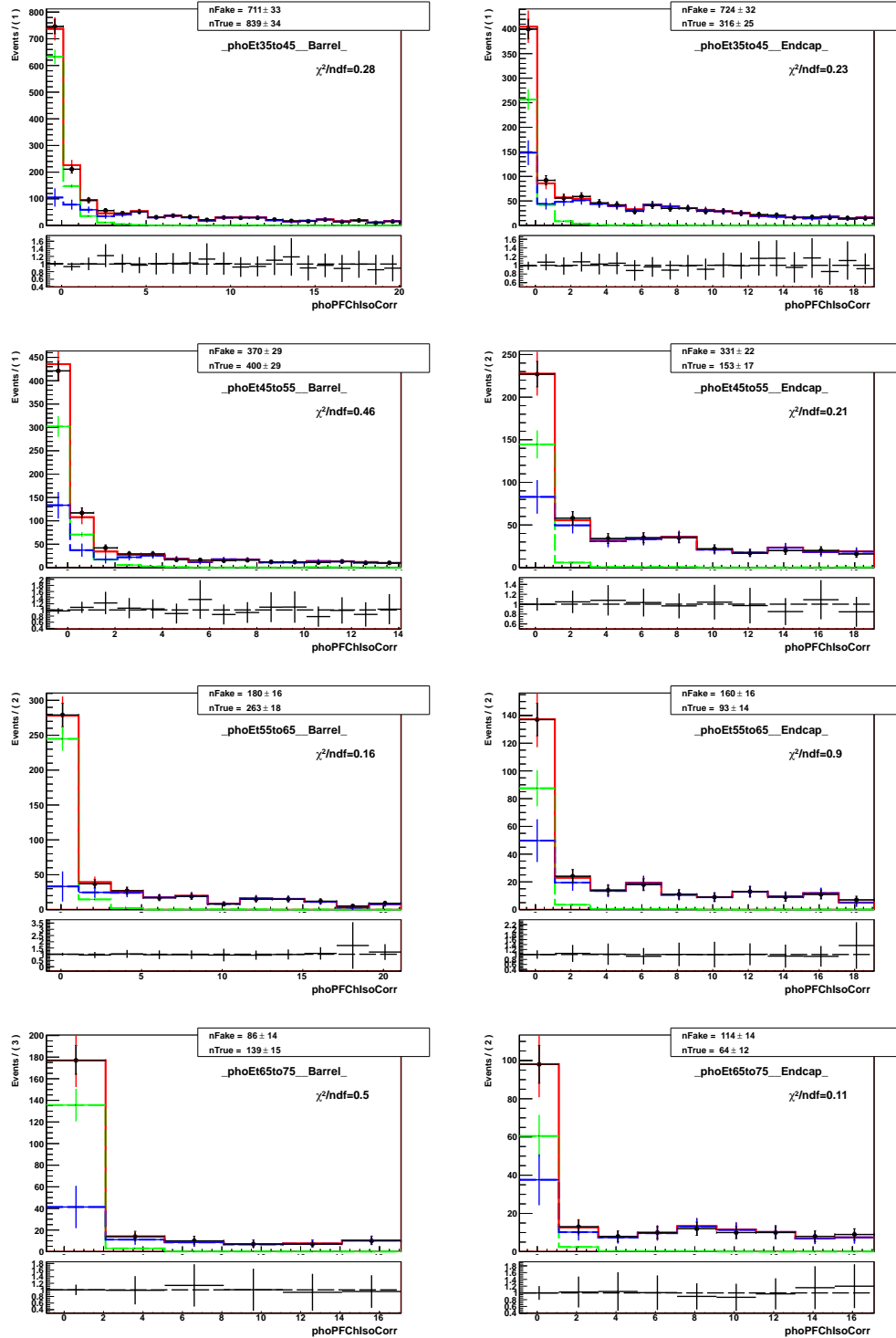
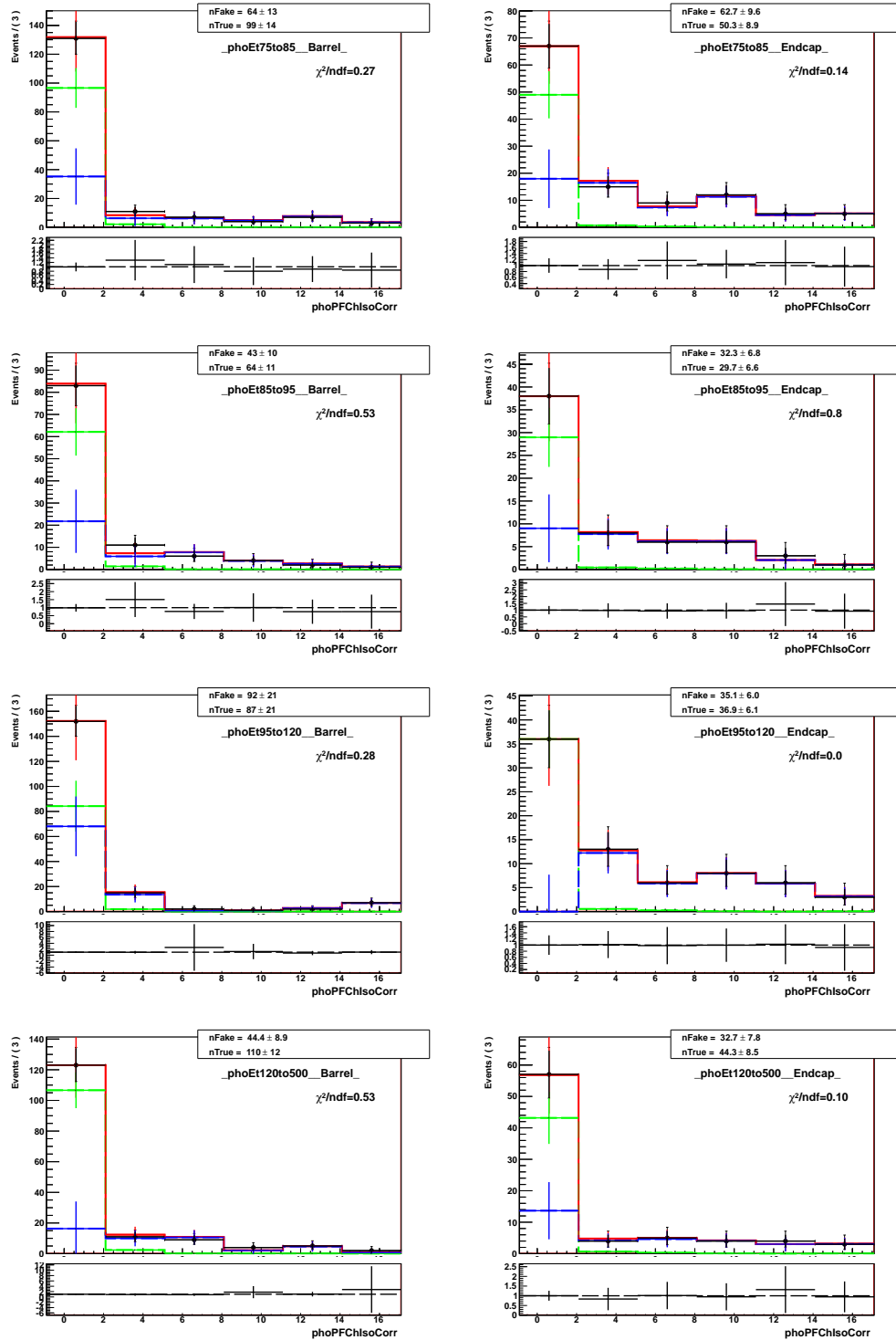


Figure .124: Fits of  $I_{ch}^{\gamma}$  templates,  $Z\gamma$ , muon channel.

Figure .125: Fits of  $I_{ch}^{\gamma}$  templates,  $Z\gamma$ , muon channel.

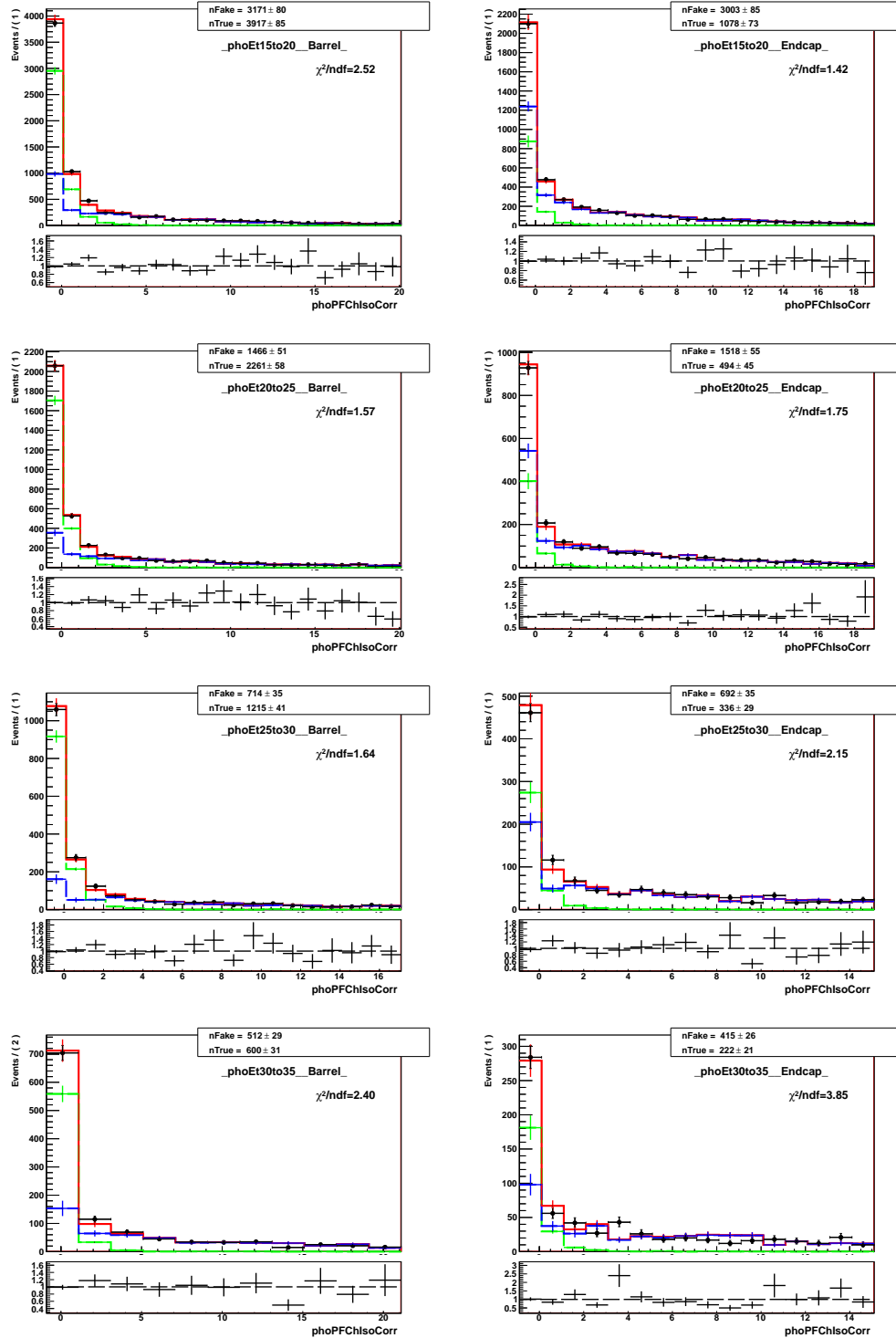


Figure .126: Fits of  $I_{ch}^{\gamma}$  templates,  $Z\gamma$ , electron channel.

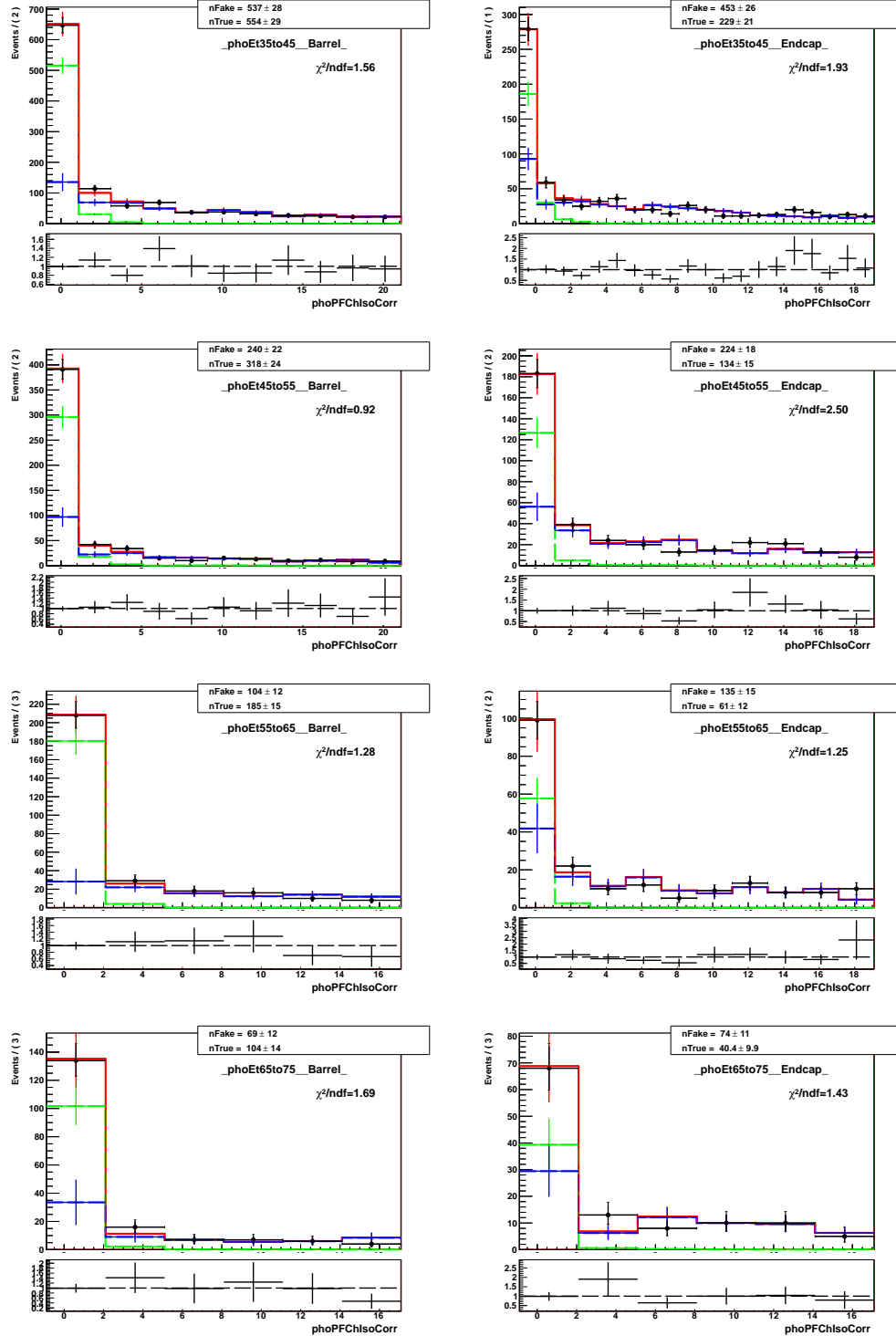


Figure .127: Fits of  $I_{ch}^{\gamma}$  templates,  $Z\gamma$ , electron channel.

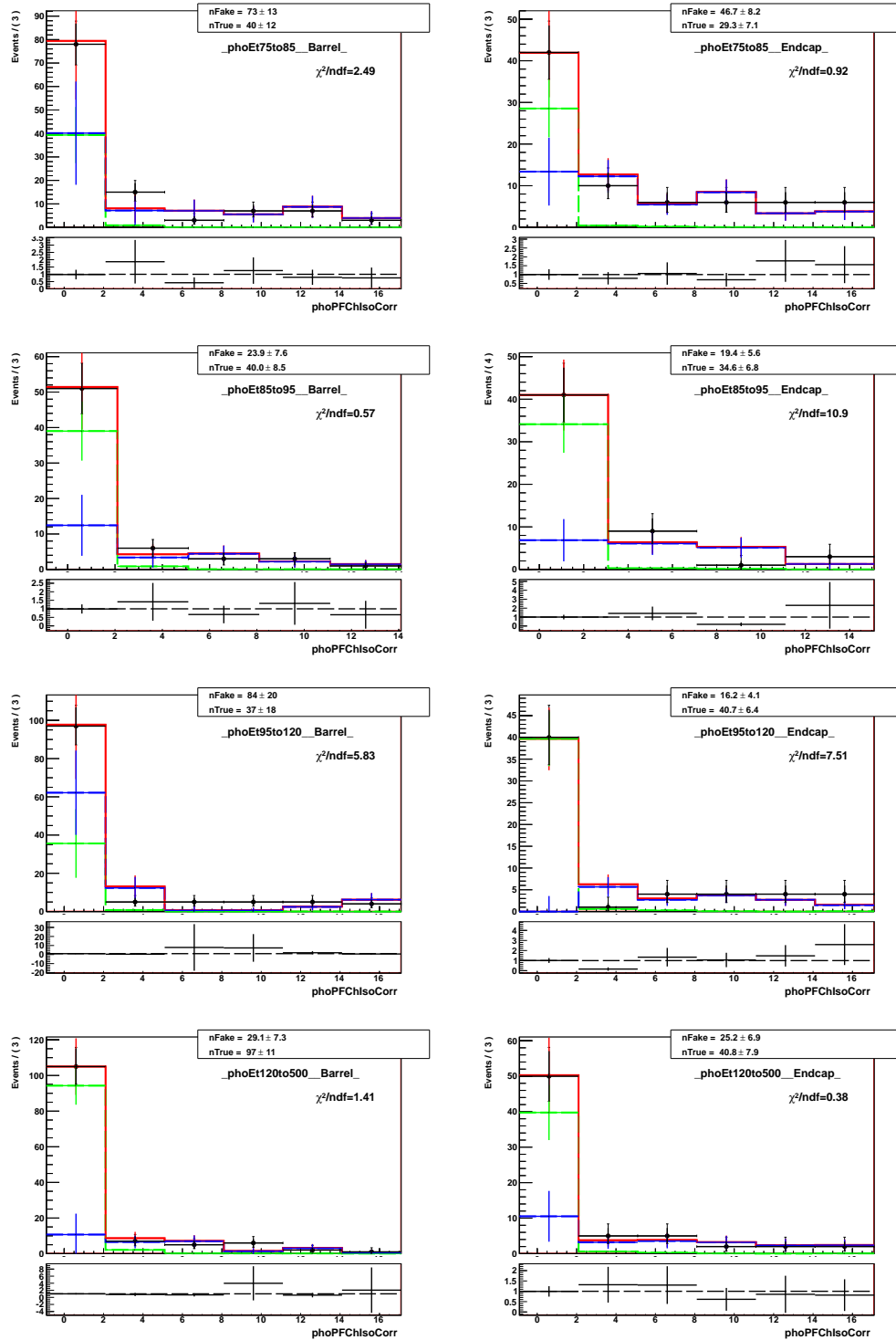
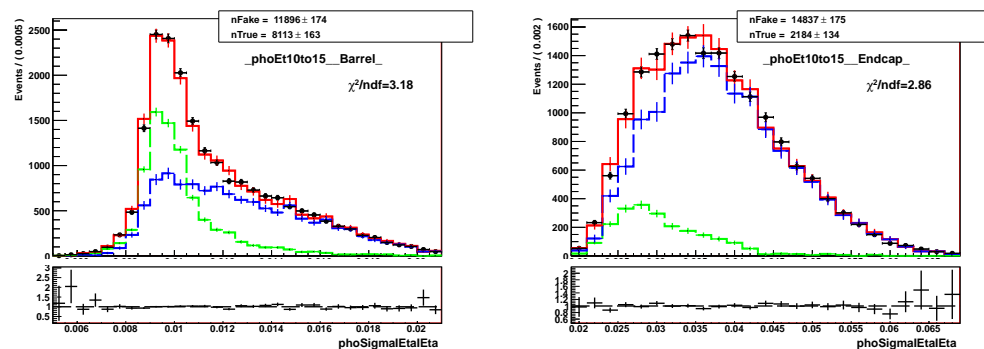
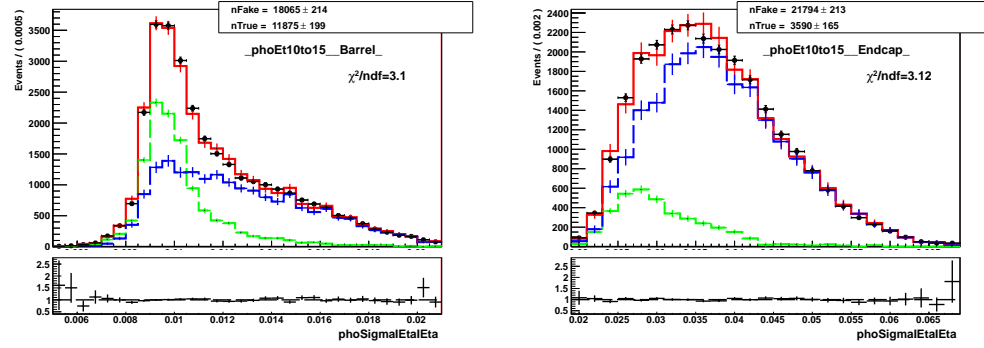


Figure .128: Fits of  $I_{ch}^{\gamma}$  templates,  $Z\gamma$ , electron channel.



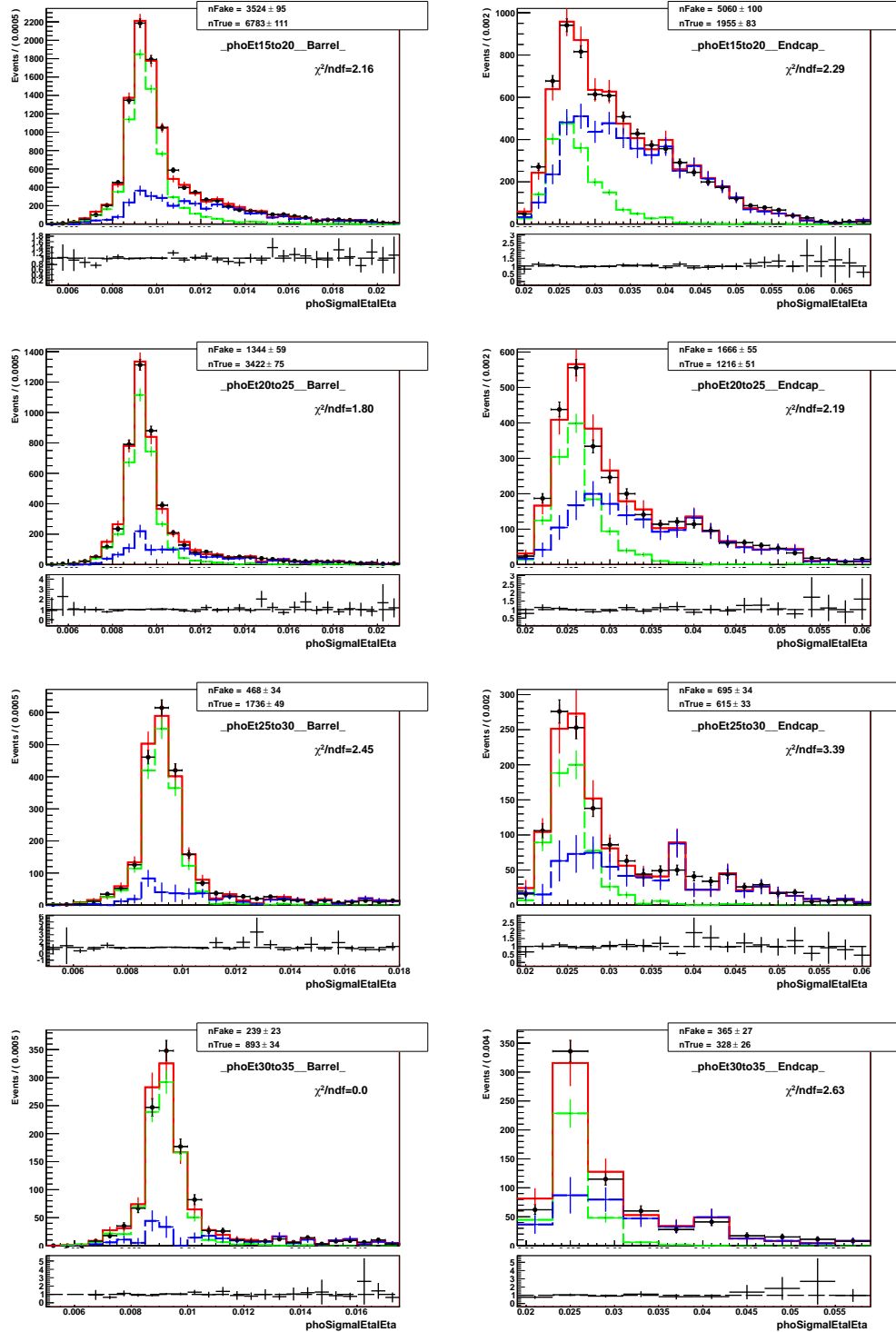


Figure .131: Fits of  $\sigma_{ijij}$  templates,  $Z\gamma$ , muon channel.

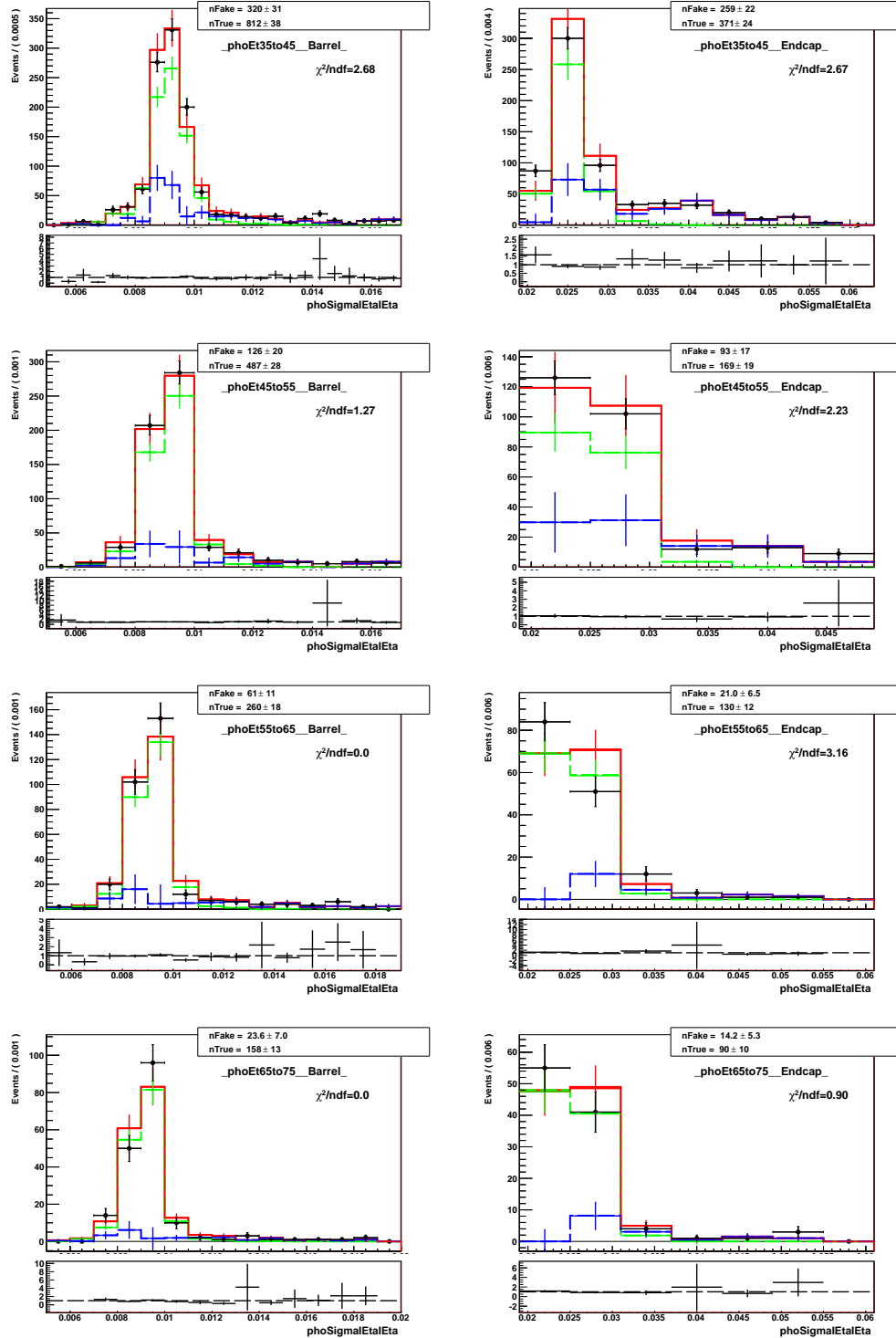


Figure .132: Fits of  $\sigma_{\eta\eta\eta}$  templates,  $Z\gamma$ , muon channel.

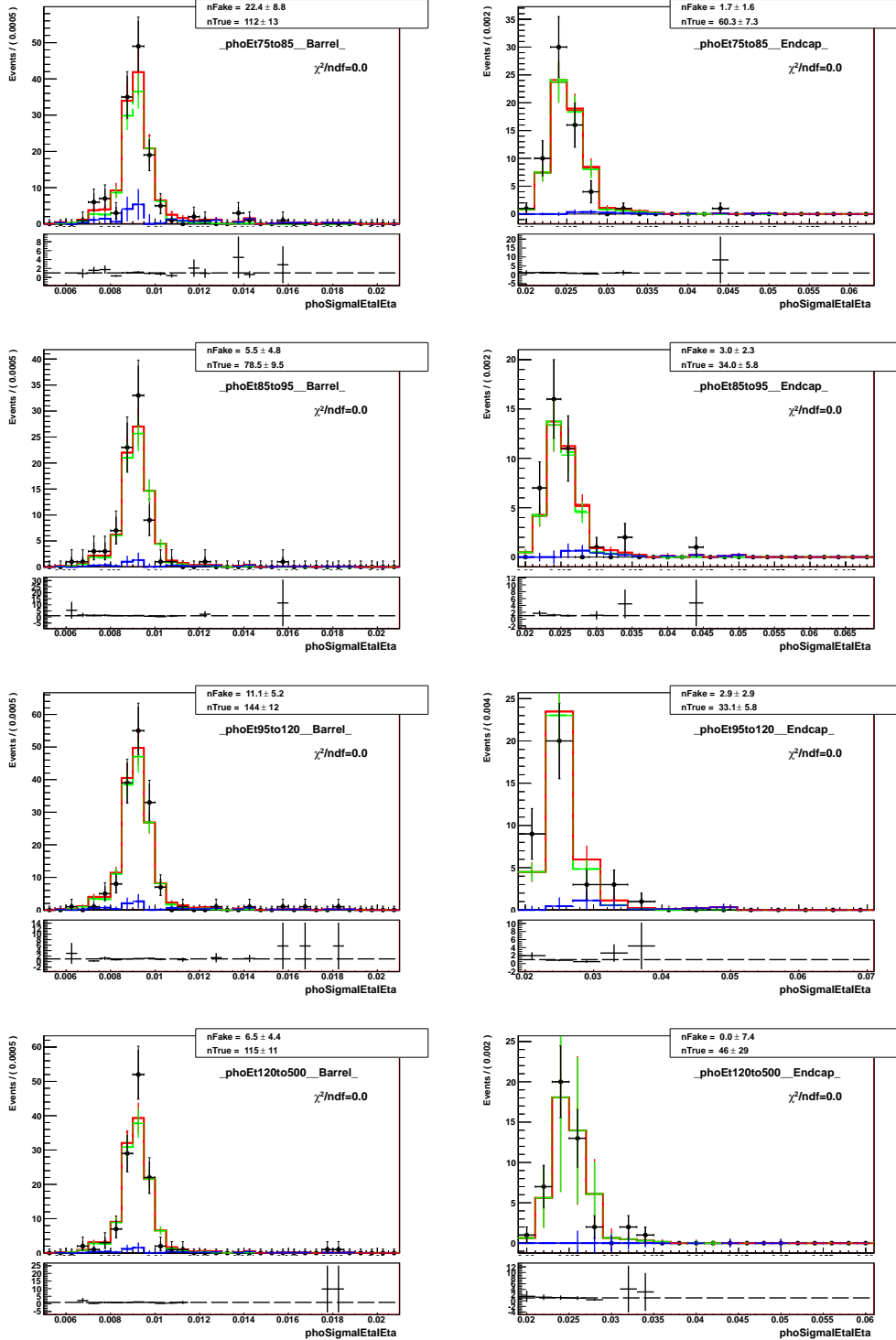


Figure .133: Fits of  $\sigma_{ijij}$  templates,  $Z\gamma$ , muon channel.

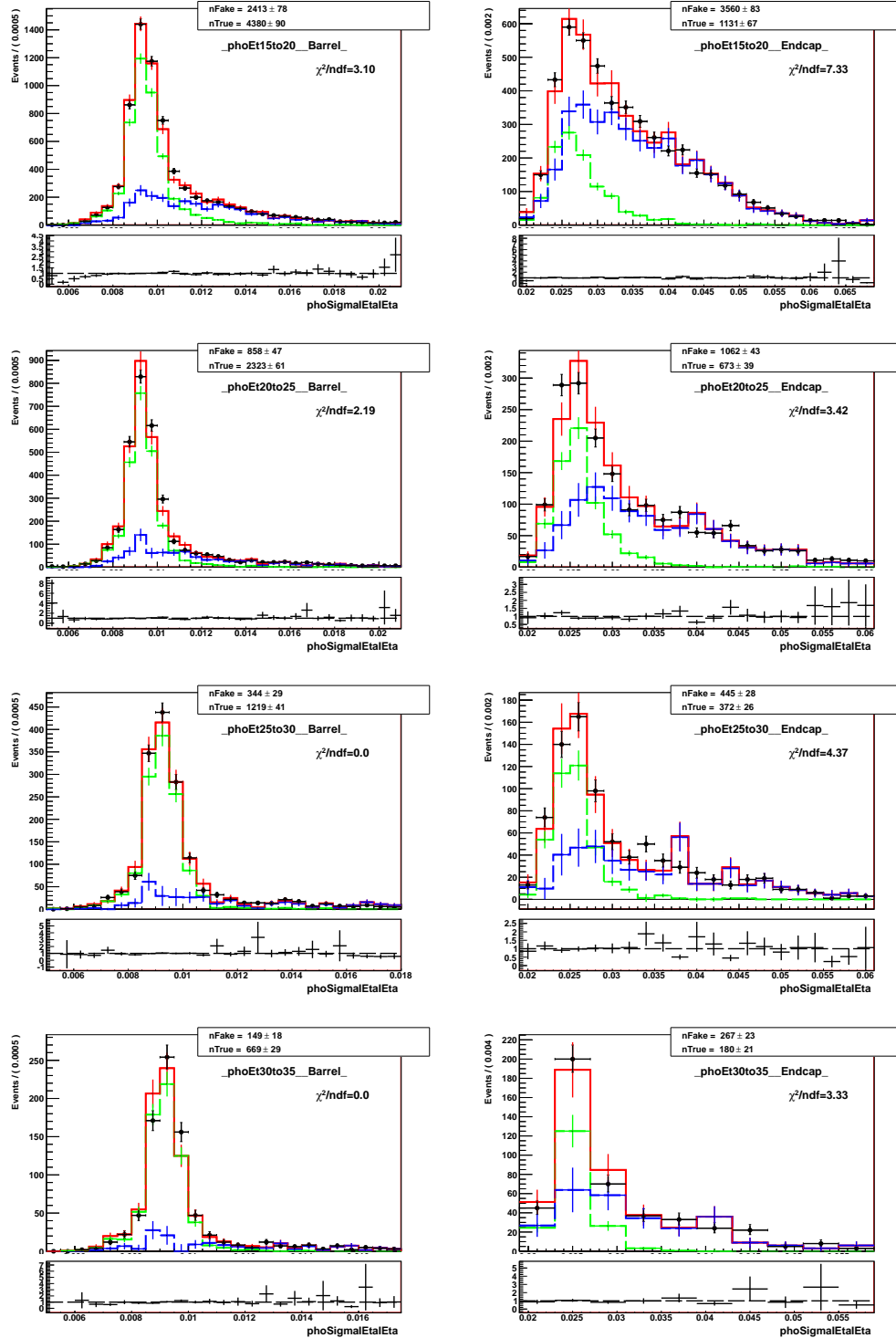


Figure .134: Fits of  $\sigma_{\eta\eta\eta}$  templates,  $Z\gamma$ , electron channel.

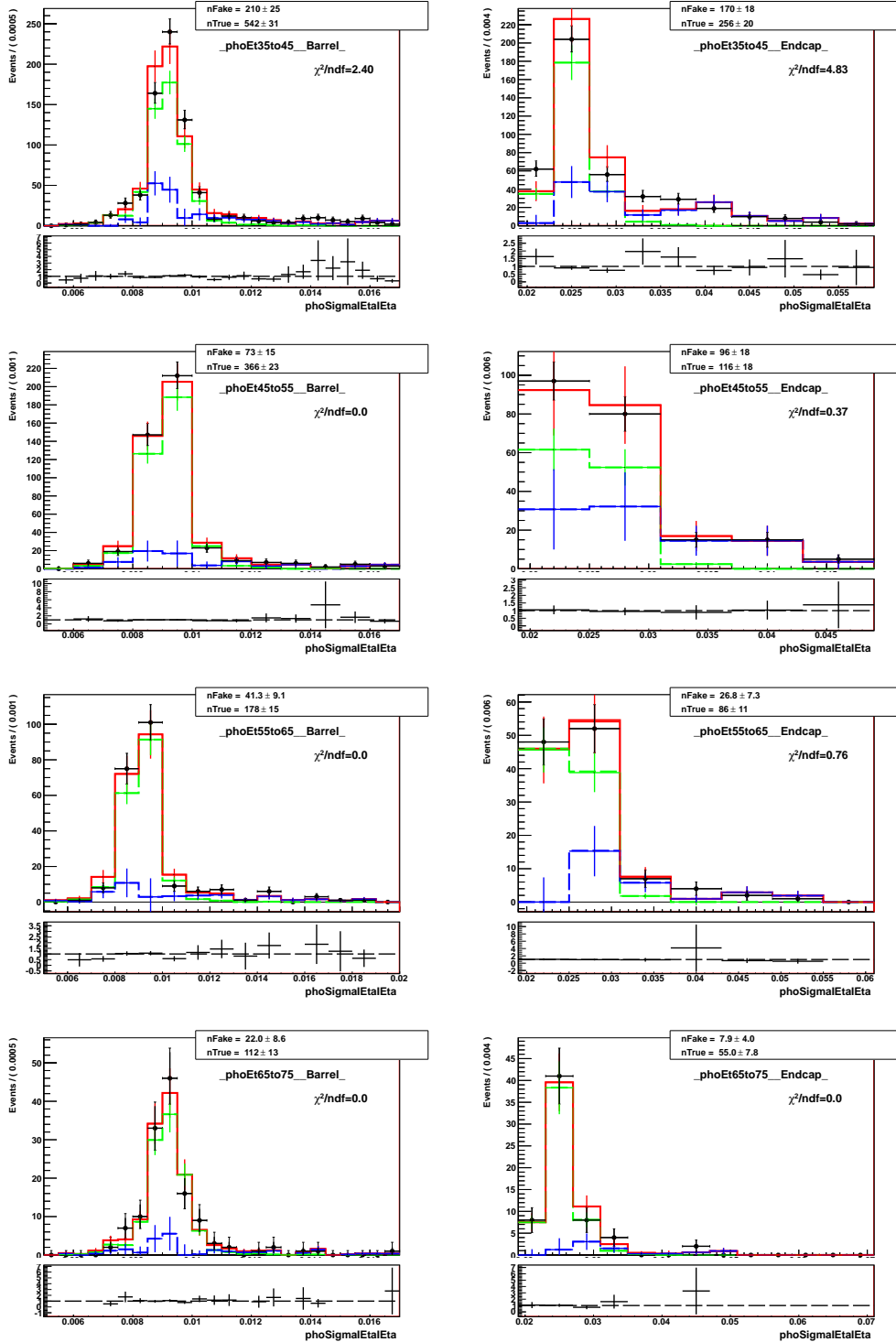


Figure .135: Fits of  $\sigma_{i\eta i\eta}$  templates,  $Z\gamma$ , electron channel.

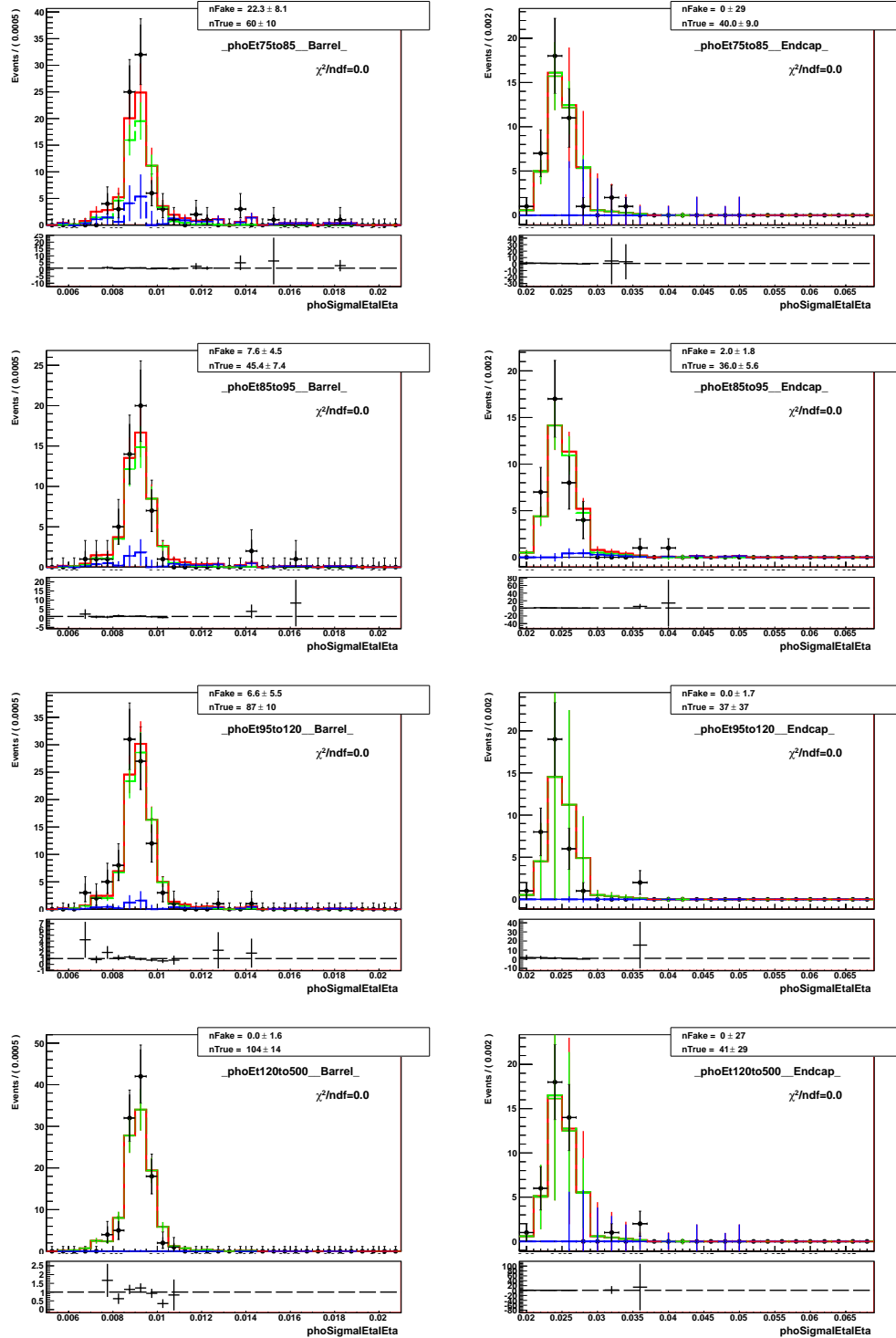


Figure .136: Fits of  $\sigma_{i\eta i\eta}$  templates,  $Z\gamma$ , electron channel.

## .15 APPENDIX: Template Fit Plots, $Z\gamma$ , MC Closure

This appendix contains fit results of jets $\rightarrow\gamma$  background estimation performed on pseudodata prepared as MC samples DY+jets and  $Z\gamma$  with  $Z\gamma$  selection conditions applied. The samples are appropriately weighted and mixed together.

On each of the plots, the black histogram is pseudodata, green is a real- $\gamma$  template, blue is a fake- $\gamma$  template, and red is the fit function. Cyan is a histogram of DY+jets MC sample in a given channel. The fits on pseudodata is performed for the MC closure check.

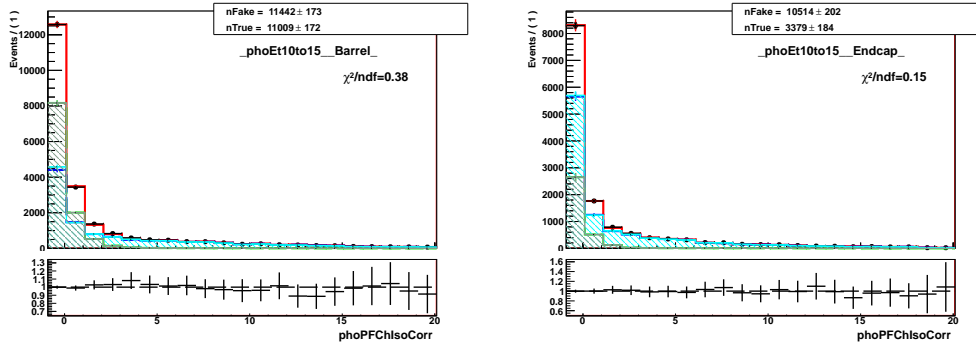


Figure .137: Fits of  $I_{ch}^\gamma$  templates, pseudodata (MC mixtures),  $Z\gamma$ , muon channel, underflow bin (10 – 15 GeV).

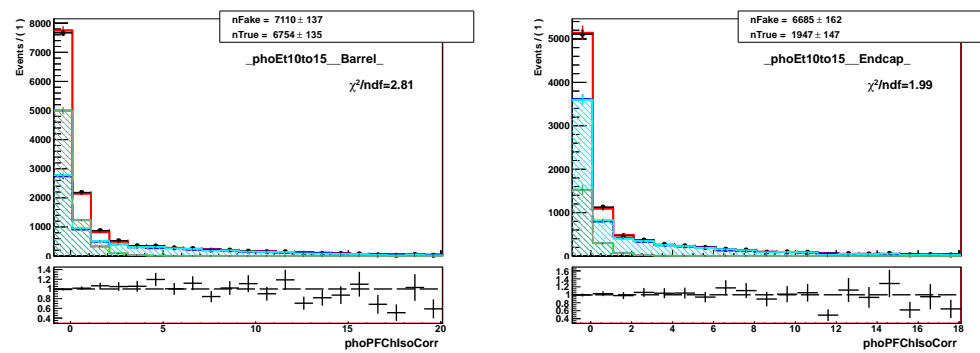


Figure .138: Fits of  $I_{ch}^\gamma$  templates, pseudodata (MC mixtures),  $Z\gamma$ , electron channel, underflow bin ( $10 - 15$  GeV).

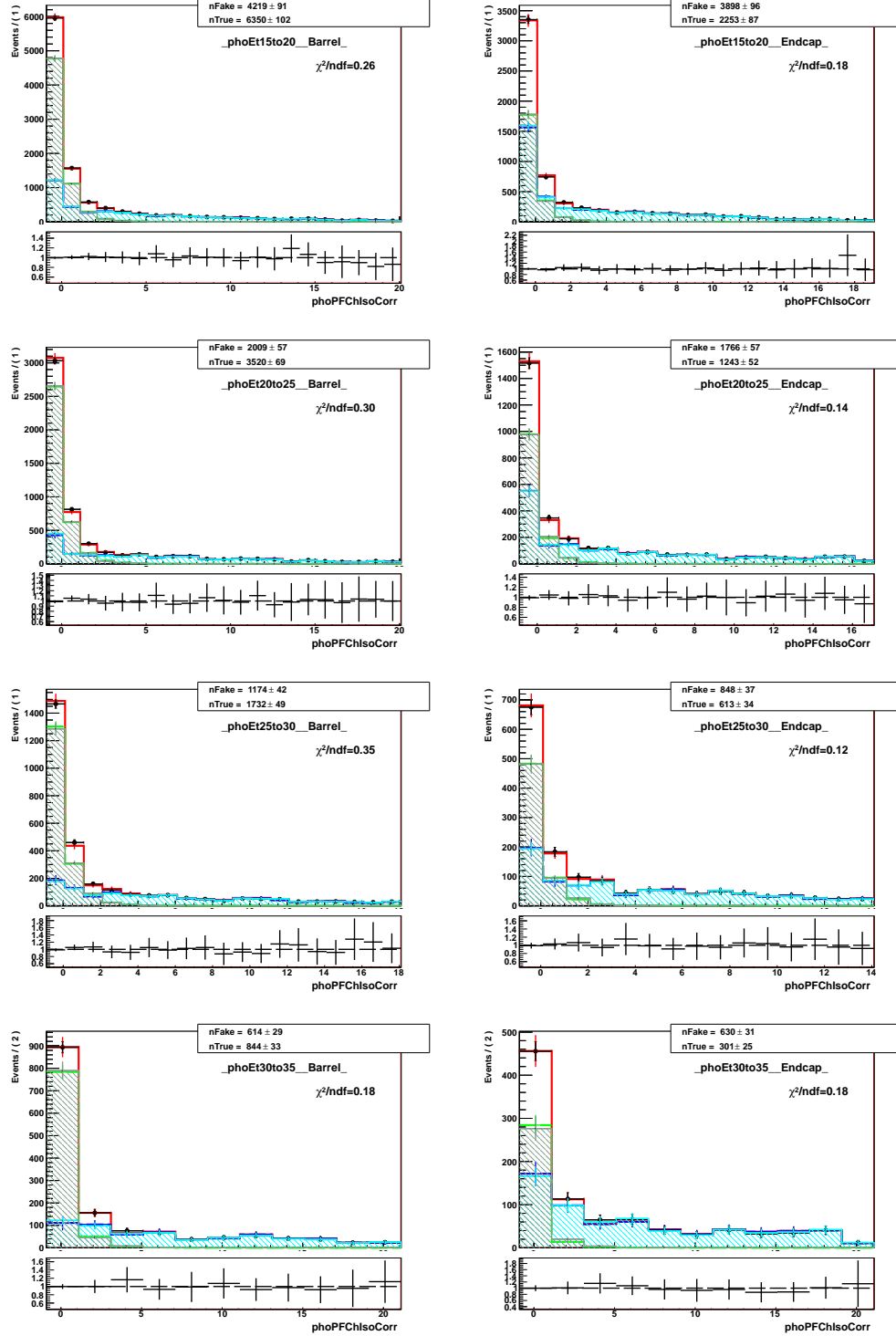


Figure .139: Fits of  $I_{ch}^{\gamma}$  templates, pseudodata (MC mixtures),  $Z\gamma$ , muon channel.

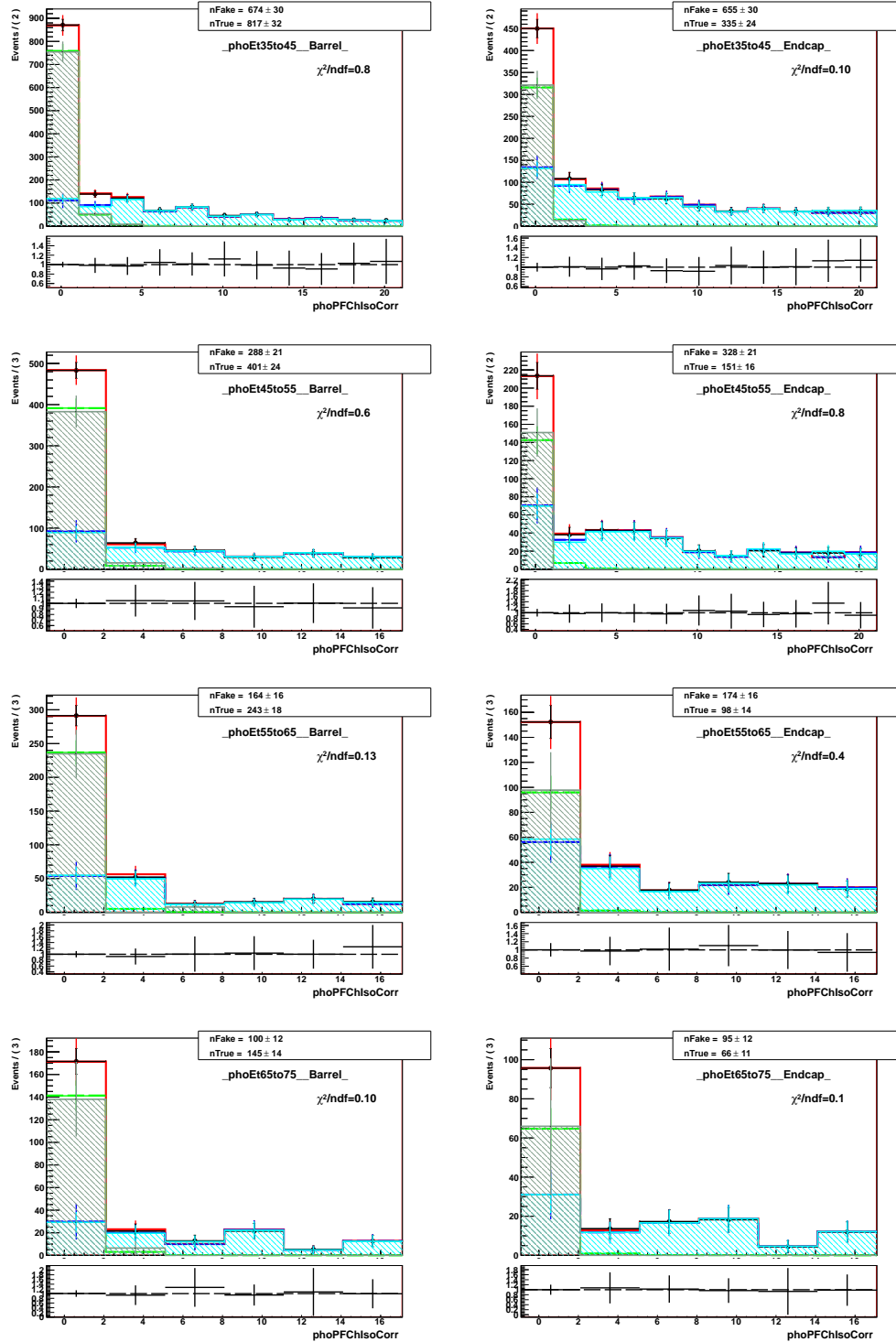


Figure .140: Fits of  $I_{ch}^{\gamma}$  templates, pseudodata (MC mixtures),  $Z\gamma$ , muon channel.

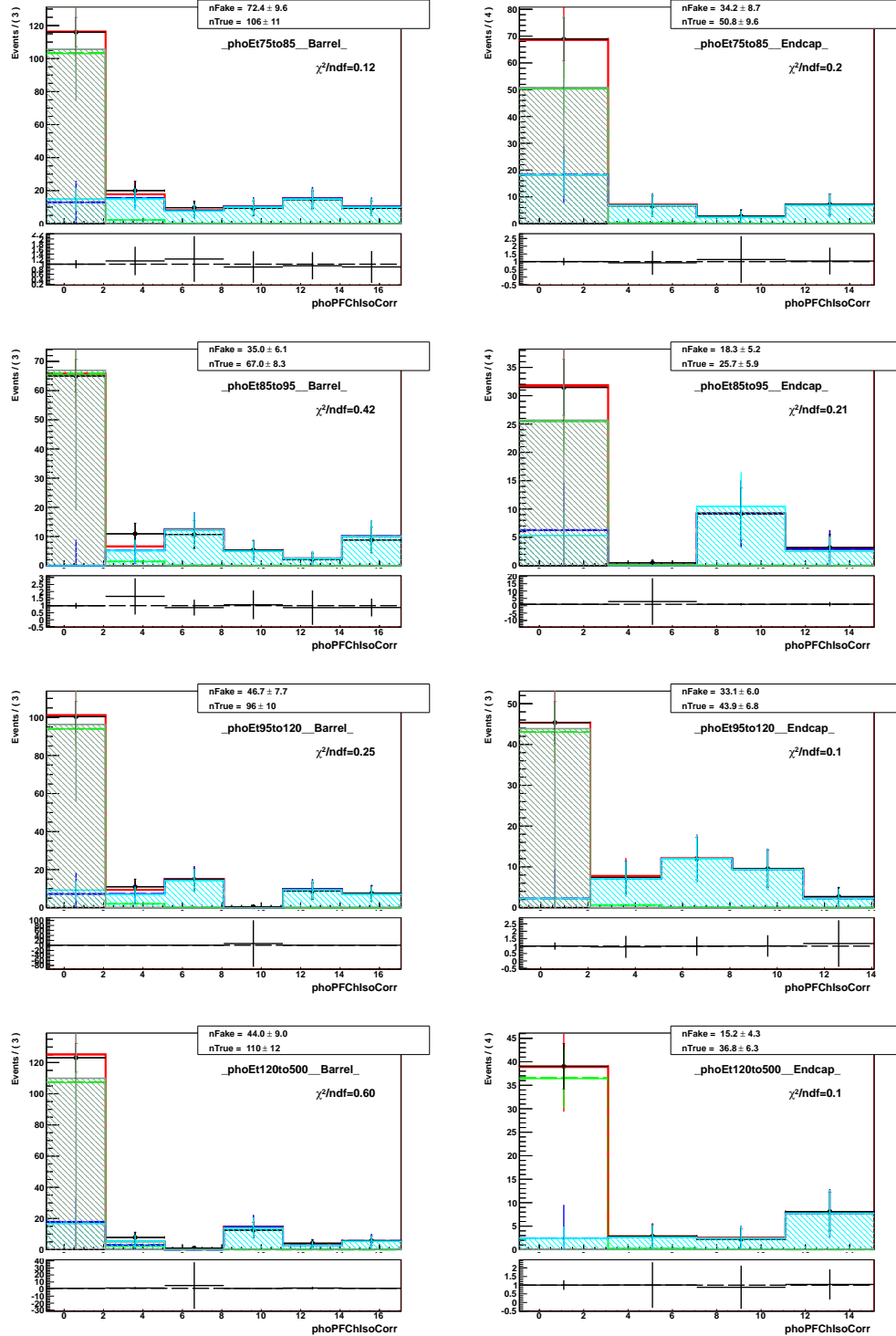


Figure .141: Fits of  $I_{ch}^{\gamma}$  templates, pseudodata (MC mixtures),  $Z\gamma$ , muon channel.

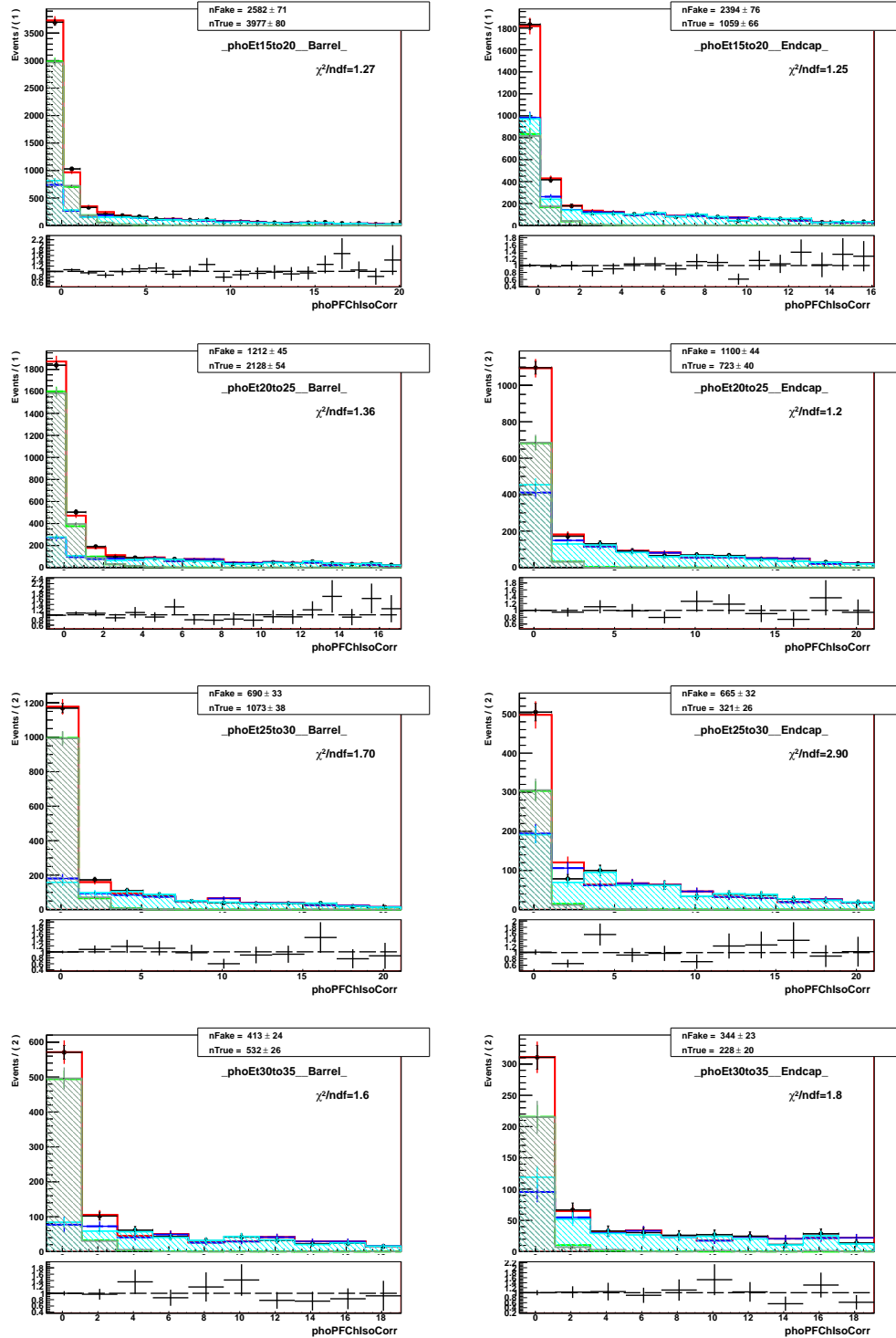


Figure .142: Fits of  $I_{ch}^{\gamma}$  templates, pseudodata (MC mixtures),  $Z\gamma$ , electron channel.

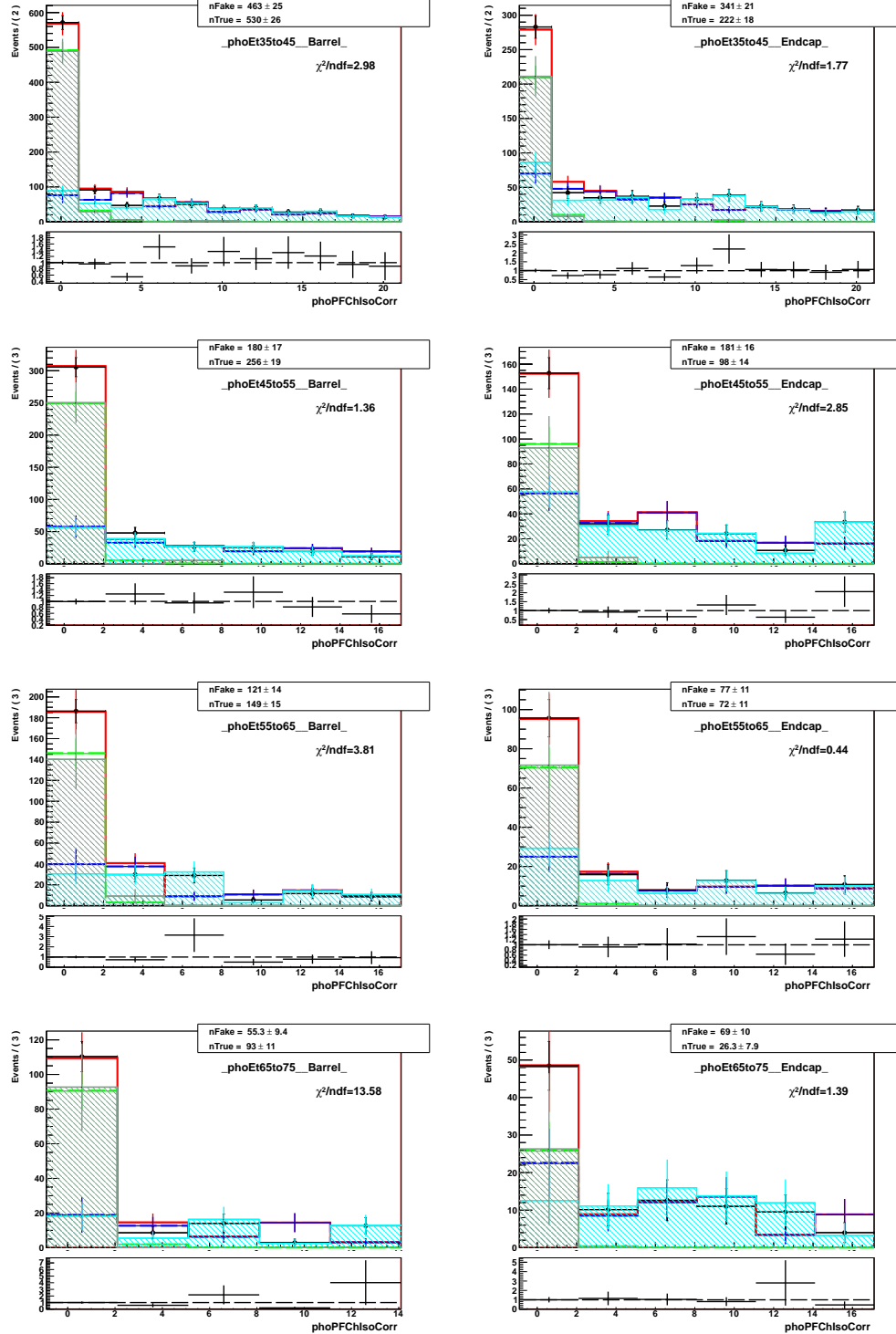


Figure .143: Fits of  $I_{ch}^{\gamma}$  templates, pseudodata (MC mixtures),  $Z\gamma$ , electron channel.

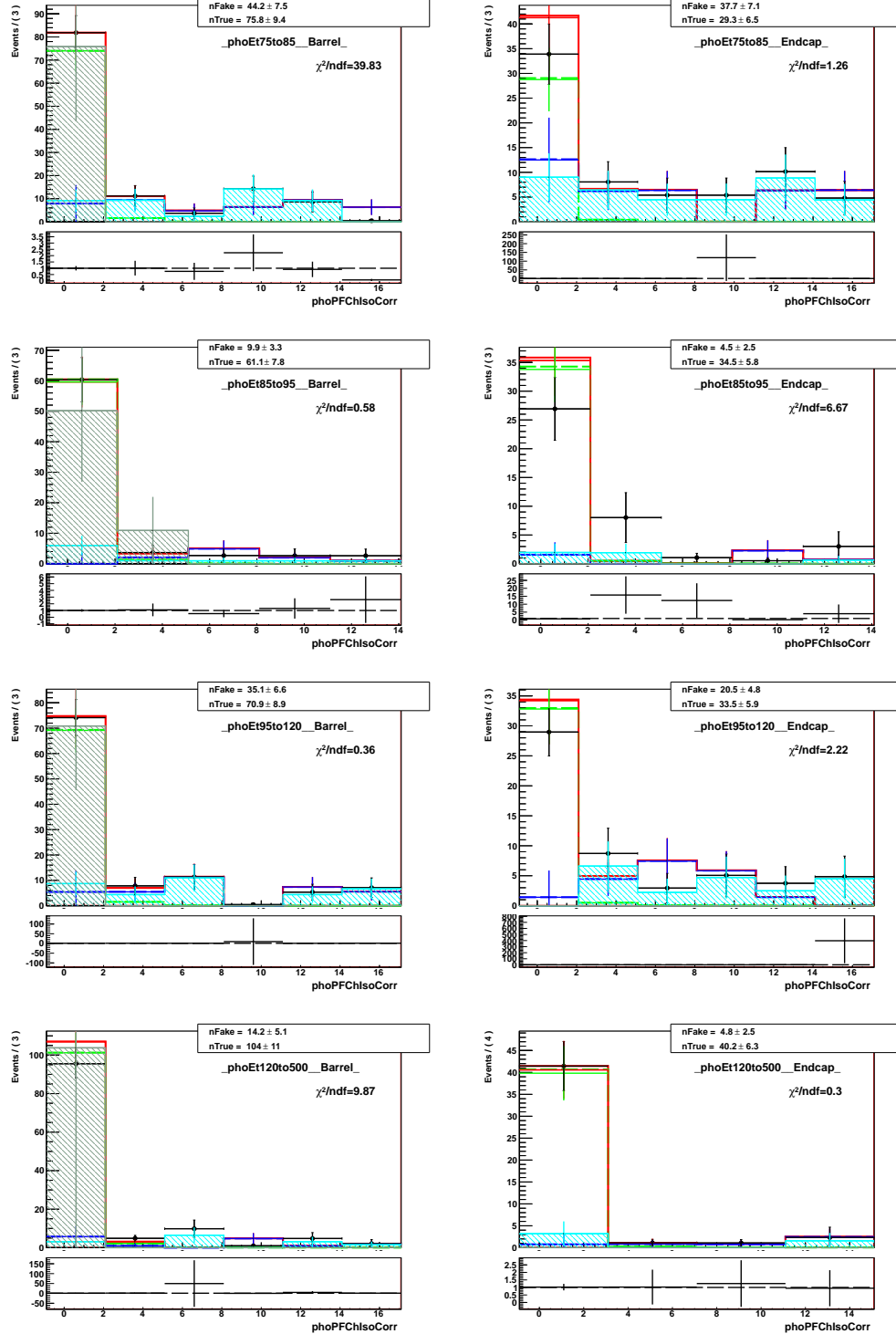


Figure .144: Fits of  $I_{ch}^{\gamma}$  templates, pseudodata (MC mixtures),  $Z\gamma$ , electron channel.

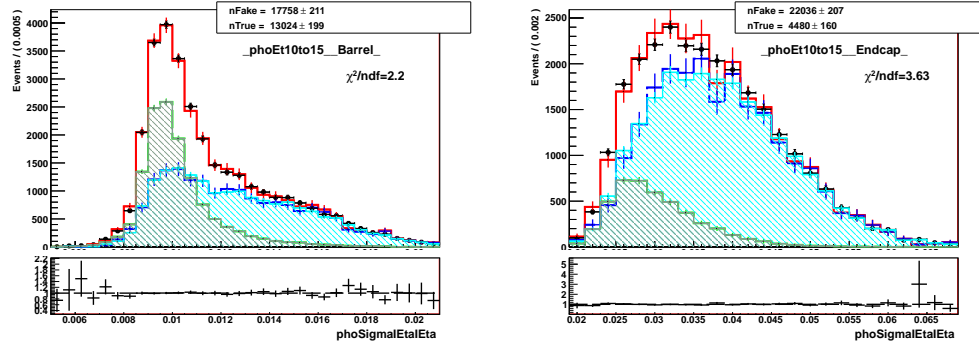


Figure .145: Fits of  $\sigma_{i\eta i\eta}$  templates, pseudodata (MC mixtures),  $Z\gamma$ , muon channel, underflow bin (10 – 15 GeV).

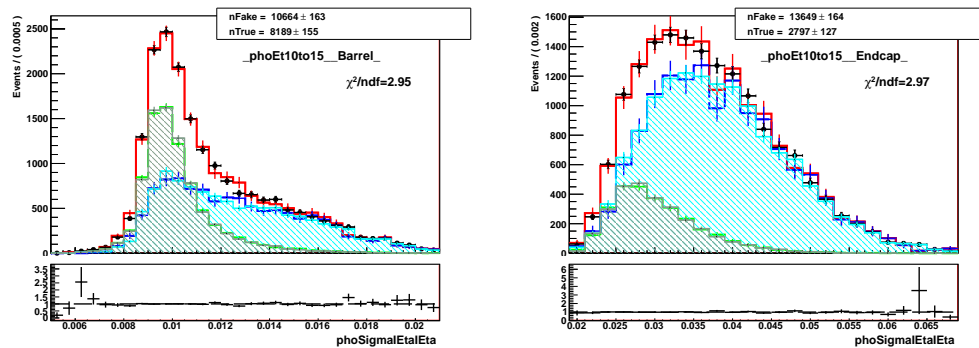


Figure .146: Fits of  $\sigma_{i\eta i\eta}$  templates, pseudodata (MC mixtures),  $Z\gamma$ , electron channel, underflow bin (10 – 15 GeV).

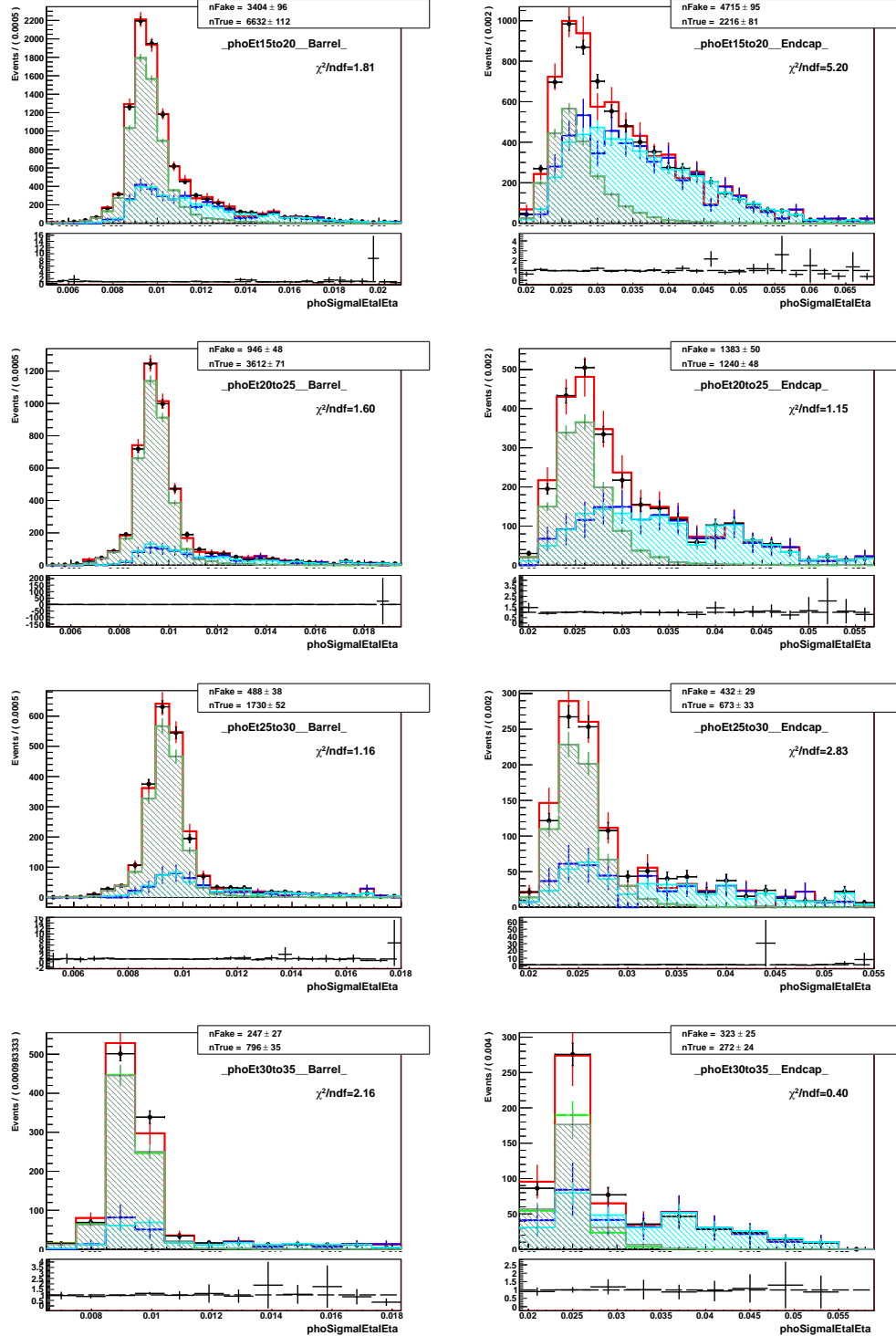


Figure .147: Fits of  $\sigma_{ijij\eta}$  templates, pseudodata (MC mixtures),  $Z\gamma$ , muon channel.

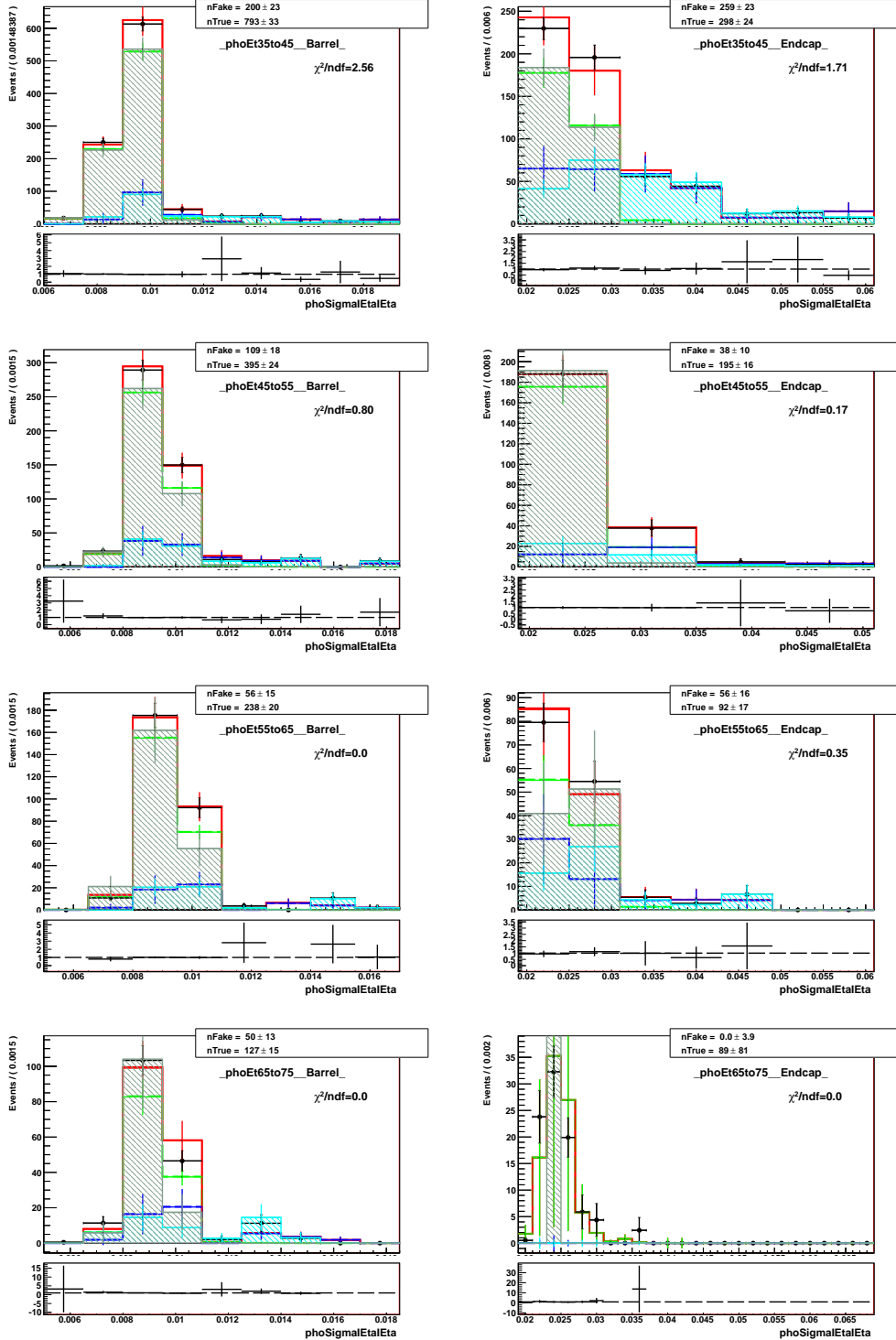


Figure .148: Fits of  $\sigma_{ijij\eta}$  templates, pseudodata (MC mixtures),  $Z\gamma$ , muon channel.

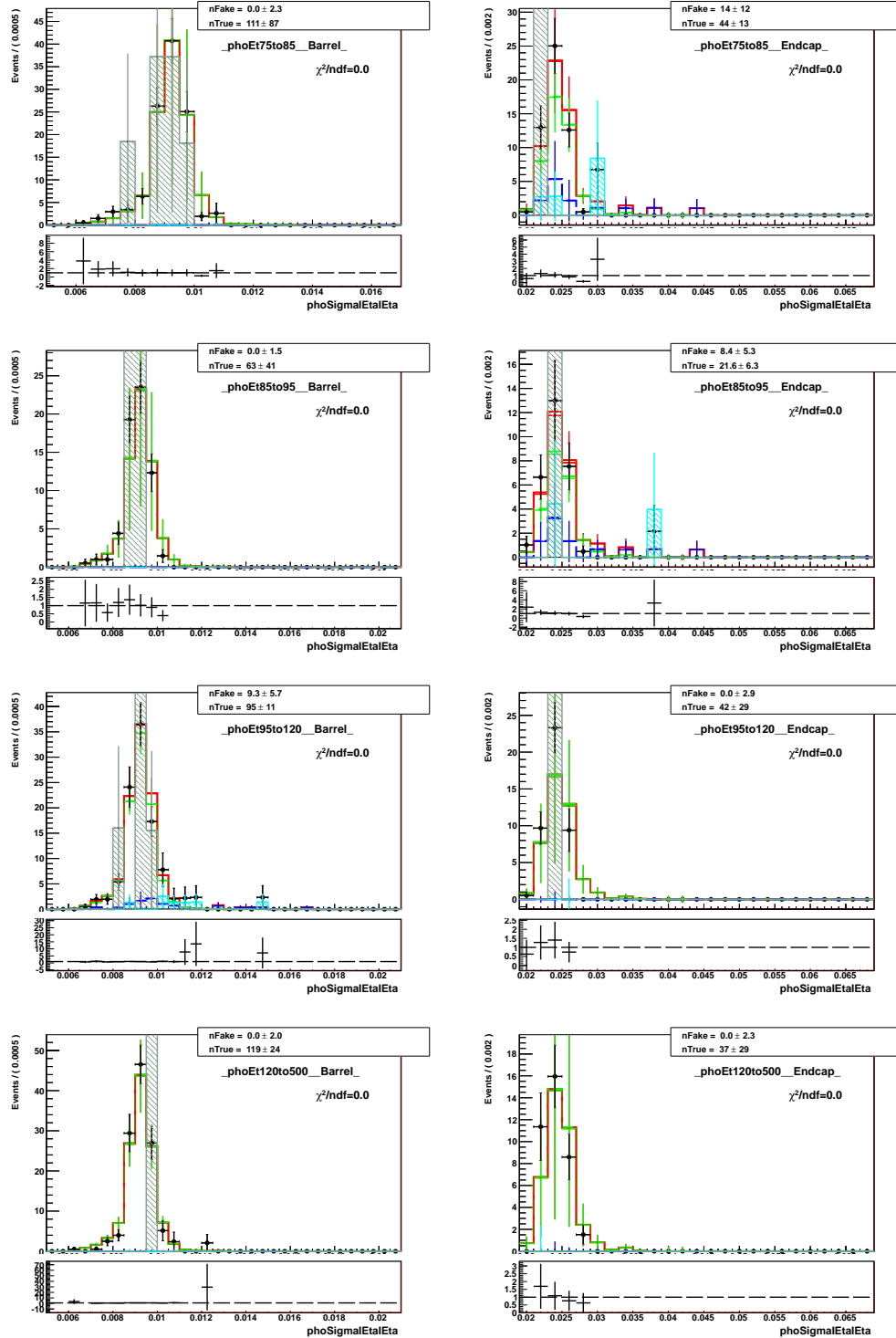


Figure .149: Fits of  $\sigma_{ijij\eta}$  templates, pseudodata (MC mixtures),  $Z\gamma$ , muon channel.

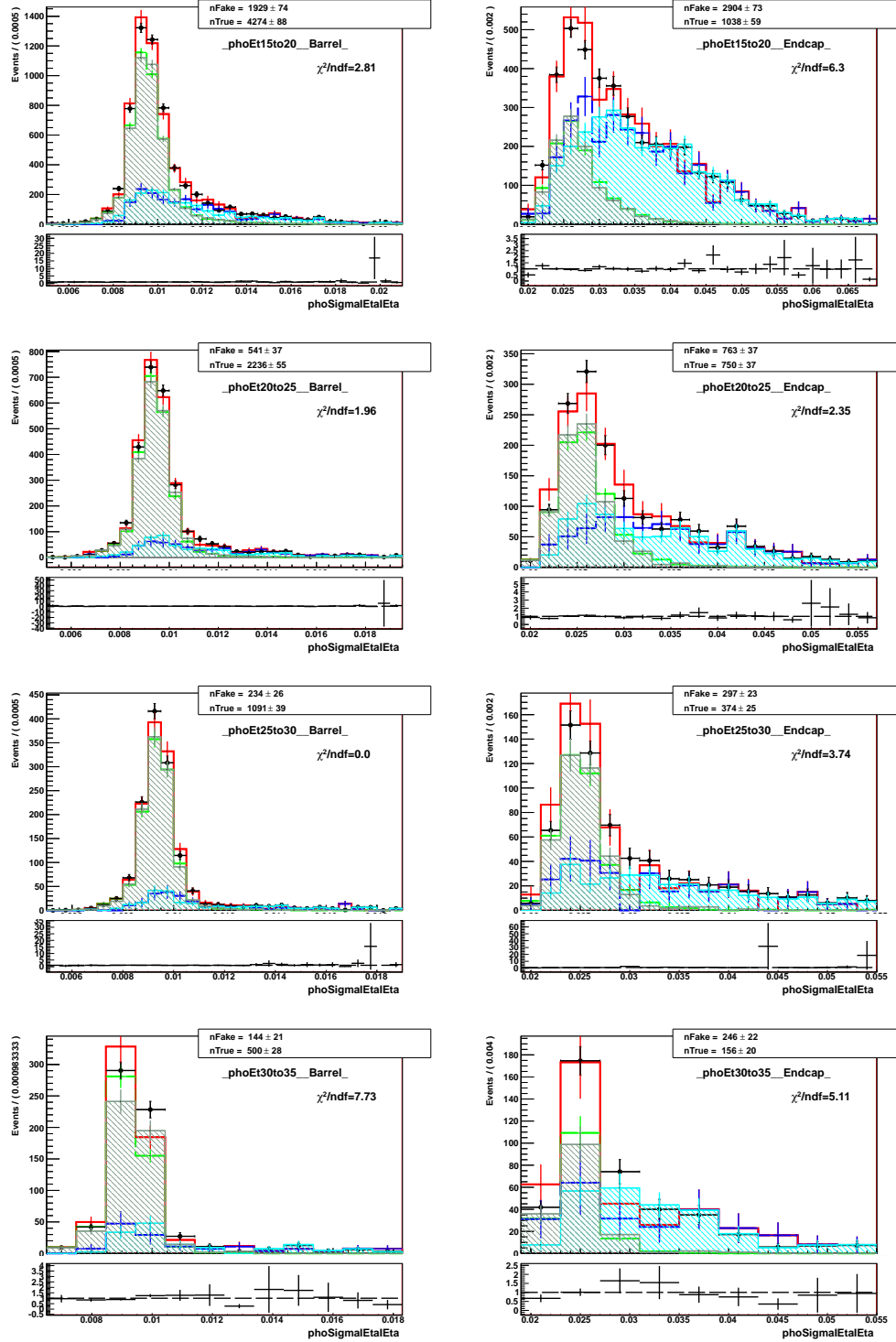


Figure .150: Fits of  $\sigma_{150}$  templates, pseudodata (MC mixtures),  $Z\gamma$ , electron channel.

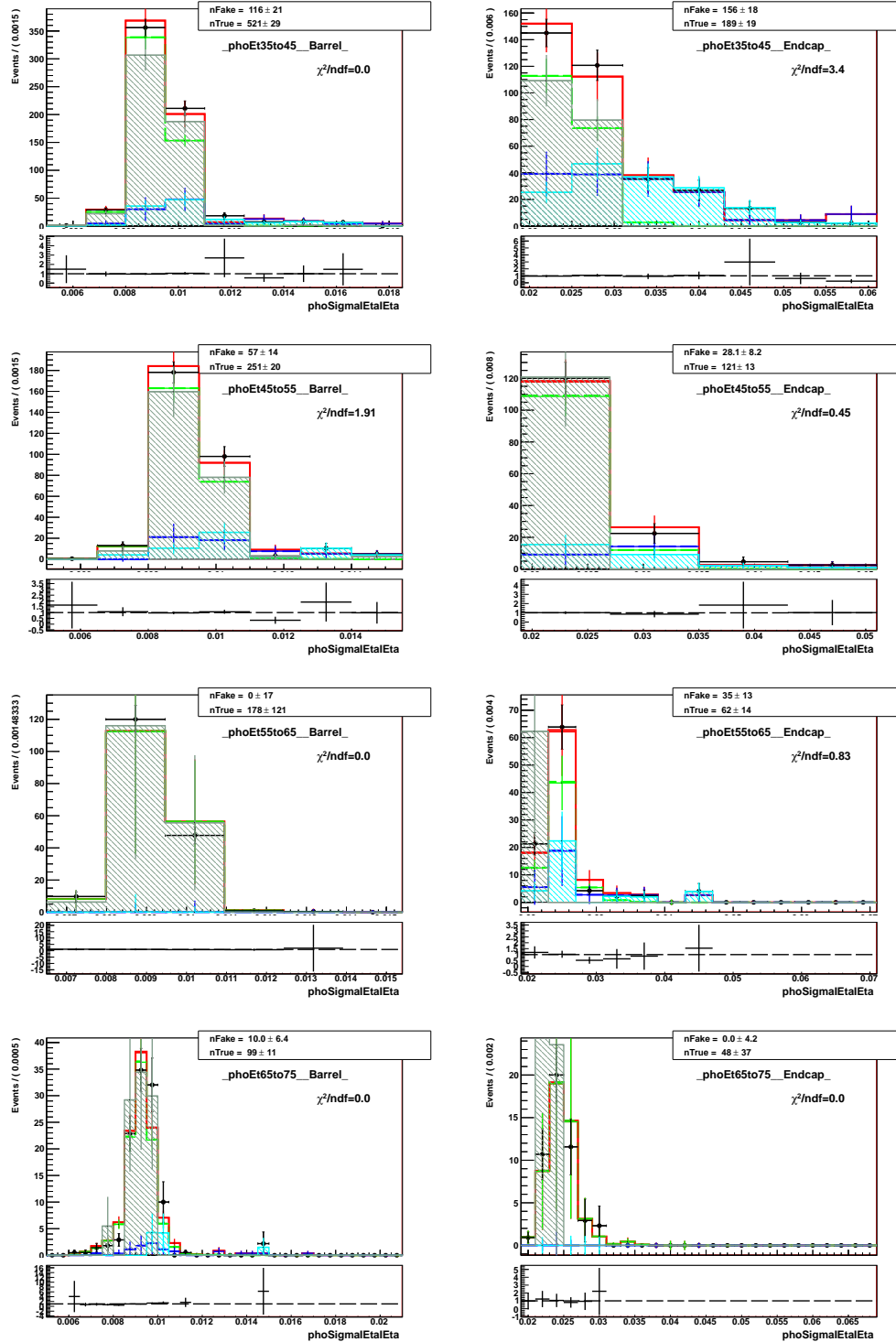


Figure .151: Fits of  $\sigma_{1111}$  templates, pseudodata (MC mixtures),  $Z\gamma$ , electron channel.

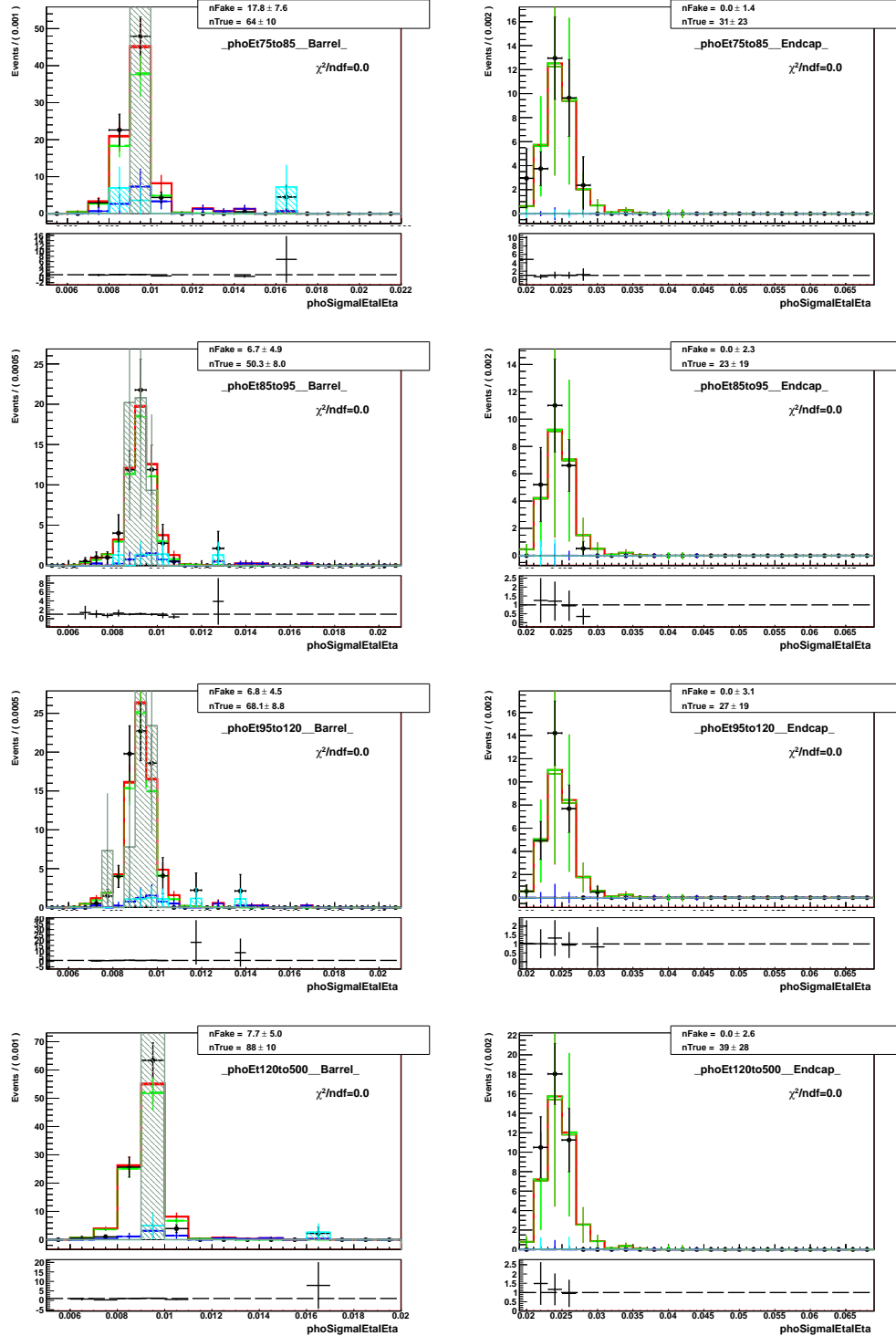


Figure .152: Fits of  $\sigma_{1111}$  templates, pseudodata (MC mixtures),  $Z\gamma$ , electron channel.

# Bibliography

- [1] F. Meier Aeschbacher. Hunting down suspicious results: recent improvements in the alignment of the cms tracker detector, 2010. Available as an internal CMS presentation at: <https://indico.cern.ch/event/243940/contributions/1562955/attachments/416194/578159/>
- [2] F. Meier Aeschbacher. *Measurement of the  $\Lambda_b^0$  baryon lifetime using the Compact Muon Solenoid experiment at Cern's Large Hadron Collider.* PhD thesis, ETH Zurich, 2013.
- [3] Cms tracker detector performance results 2015: Alignment. Available at: <https://twiki.cern.ch/twiki/bin/view/CMSPublic/TkAlignmentPerformance2015>.
- [4] ATLAS VW ( $V=W,Z \rightarrow jj$ ) using 4.6 fb $^{-1}$  of 7 TeV pp collisions JHEP 01 (2015) 049.
- [5] CMS TDR.
- [6] CMS 7 TeV Zg nunug.
- [7] CMS 8 TeV WW lnulnu.
- [8] Available at: <https://inspirehep.net/record/837874/plots>.
- [9] Cmssw.

- [10] CMS VW ( $V=W,Z \rightarrow jj$ ) using 5.0 fb $^{-1}$  of 7 TeV pp collisions Eur.Phys.J. C73 (2013) 2283.
- [11] CMS WW using 4.9 fb $^{-1}$  of 7 TeV pp collisions Eur. Phys. J. C 73 (2013) 2610.
- [12] CMS WW using 19.4 fb $^{-1}$  of 8 TeV pp collisions Submitted to EPJC.
- [13] ATLAS Collaboration. Observation of a new particle in the search for the standard model higgs boson with the atlas detector at the lhc. *Phys. Lett. B*, 716(1):1–29, 2012. Available at: <https://arxiv.org/abs/1207.7214>.
- [14] CMS collaboration. Alignment of the cms tracker with large hadron collider data.
- [15] CMS collaboration. Description and performance of track and primary-vertex reconstruction with the cms tracker. Available at: <https://arxiv.org/abs/1405.6569>.
- [16] CMS collaboration. Wgg, 8 tev.
- [17] CMS collaboration. Zg, 8 tev.
- [18] CMS Collaboration. Observation of a new boson at a mass of 125 gev with cms experiment at the lhc. *Phys. Lett. B*, 716(1):30–61, 2012. Available at: <https://arxiv.org/abs/1207.7235>.
- [19] Wikipedia article. cross section (physics). Available at: [https://en.wikipedia.org/wiki/Cross\\_section\\_%28physics%29](https://en.wikipedia.org/wiki/Cross_section_%28physics%29).
- [20] Do Combination of  $W\gamma$ , WW, WZ and VW using 8.6 fb $^{-1}$  of 2 TeV  $p\bar{p}$  collisions Phys.Lett. B718 (2012) 451–459.
- [21] D'agostini unfolding.

- [22] website: <http://cds.cern.ch/record/1621583/files/>.
- [23] Available at: <https://twiki.cern.ch/twiki/bin/view/CMSPublic/LumiPublicResults>.
- [24] Available at: <http://cds.cern.ch/journal/CERNBulletin/2014/24/News%20Articles/170660>
- [25] ggntuplizer.
- [26] Github.
- [27] L. Gray. *A measurement of the  $Z\gamma$  Cross Section and Limits on anomalous Gauge Couplings at  $\sqrt{s} = 7$  TeV Using CMS*. PhD thesis, University of Wisconsin - Madison, 8 2012.
- [28] D. Griffiths. *Introduction to Elementary Particles*. WILEY-VCH, 2008.
- [29] Martin Halzen. *Quarks and leptons*.
- [30] Hard scattering. Available at: <http://iopscience.iop.org/article/10.1088/0034-4885/70/1/R02>.
- [31] Hip algorithm.
- [32] LEP Combination of WW and single W using 0.7 fb<sup>-1</sup> per experiment of  $e^+e^-$  collisions at WW pair production energies arXiv:1302.3415.
- [33] CERN brochure, <http://cds.cern.ch/record/1165534/files/CERN-Brochure-2009-003-Eng.pdf>.
- [34] Available at: <https://twiki.cern.ch/twiki/bin/view/CMSPublic/LumiPublicResults>.
- [35] LHC TDR.
- [36] Available at: <http://home.cern/topics/large-hadron-collider>.

- [37] Available at: [https://www-do.fnal.gov/results/publications\\_talks/thesis/snyder/html/nodis.html](https://www-do.fnal.gov/results/publications_talks/thesis/snyder/html/nodis.html)
- [38] MadGraph generator.
- [39] MCFM generator.
- [40] Millepede ii algorithm.
- [41] mycode.
- [42] Nasa website. Available at: <https://science.nasa.gov/astrophysics/focus-areas/what-is-dark-energy>.
- [43] Particle data group. Available at: [pdg.lbl.gov](http://pdg.lbl.gov).
- [44] <https://inspirehep.net/record/925379/files/PFT-09-001-pas.pdf>.
- [45] Schroeder Peskin. *Introduction to Quantum Field Theory*.
- [46] A. Pich. *The Standard Model of Electroweak Interactions*, 2007. Updated version of the lectures given at the 2006 European School of High Energy Physics (Aronsborg, Sweden, 18 June - 1 July 2006) and at the 4th CERN - CLAF School of High Energy Physics (Vina del Mar, Chile, 18 February - 3 March 2007). Available at: <https://arxiv.org/abs/0705.4264>.
- [47] 7TeV Wg ATLAS paper.
- [48] 7TeV Wg CMS paper.
- [49] ATLAS WW using 20.3 fb<sup>-1</sup> of 8 TeV pp collisions Submitted to JHEP.
- [50] website: [https://inspirehep.net/record/1235541/files/LHC\\_all.png](https://inspirehep.net/record/1235541/files/LHC_all.png).
- [51] website: <https://muon.files.wordpress.com/2014/01/cms-sigma-vs-e.png>.

[52] Roocmsshapepdf.

[53] Roofit.

[54] Root.

[55] Roounfold.

[56] PhD thesis. Senka's thesis, CMS Wg- $\chi$ munug, 7 TeV.

[57] UNKNOWN [TEMPORARY]. Source of sm figure [temporary]. Available at:  
<http://www.isgtw.org/spotlight/go-particle-quest-first-cern-hackfest>.

[58] aTGC paper, LEP parametrization.

[59] LO (1969) theory paper.

[60] NLO theory paper.

[61] NNLO theory paper.

[62] Available at: <https://twiki.cern.ch/twiki/bin/view/CMSPublic/PhysicsResultsSMPaTGC#>